THREE-DIMENSIONAL LASER WRITING OF MID-INFRARED WAVEGUIDE CIRCUITS IN LITHIUM NIOBATE CRYSTAL

Huu Dat Nguyen

UNIVERSITAT ROVIRA i VIRGILI

Three-Dimensional Laser Writing of Mid-Infrared Waveguide Circuits in Lithium Niobate Crystal

HUU DAT NGUYEN

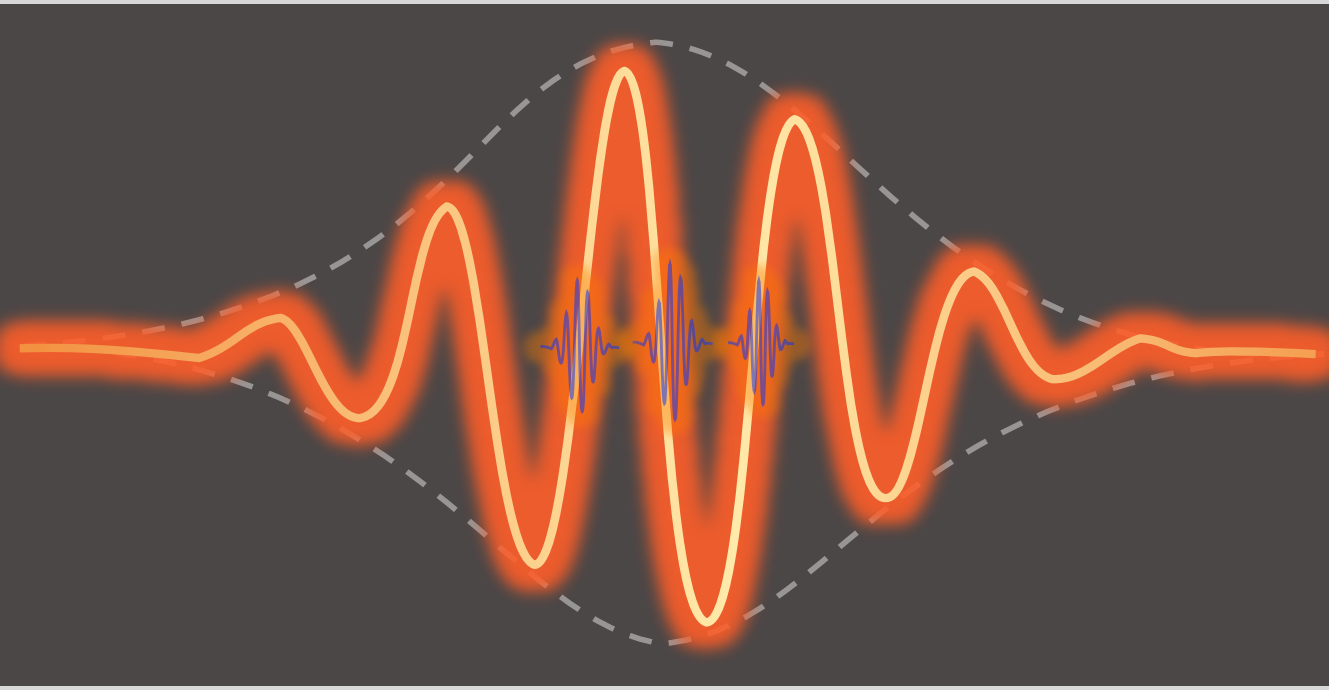

DOCTORAL THESIS
2017

Huu Dat nguyen

THREE-DIMENSIONAL LASER WRITING OF MID-INFRARED WAVEGUIDE CIRCUITS IN LITHIUM NIOBATE CRYSTAL

DOCTORAL THESIS

Supervised by: Dr Airán Ródenas Seguí

Dr. Maria Cinta Pujol Baiges

Doctoral program in Nanoscience, materials and chemical engineering

Physics and Crystallography of Materials (FiCMA)

Department of Physical and Inorganic Chemistry

UNIVERSITAT ROVIRA i VIRGILI

Tarragona - 2017

UNIVERSITAT ROVIRA I VIRGILI

DEPARTAMENT DE QUÍMICA FÍSICA I INORGÀNICA

Campus Sescelades
Marcel·lí Domingo, s/n
43007 Tarragona
Tel. +34 977 55 81 37
Fax +34 977 55 95 63
www.quimica.urv.es

WE STATE that the present research work, entitled "Three-Dimensional Laser Writing of Mid-Infrared Waveguide Circuits in Lithium Niobate Crystal", presented by Huu- Dat Nguyen for the award of the degree of Doctor, has been carried out under our supervision at the Department of Physical and Inorganic Chemistry of this university, and that it fulfils all the requirements to be eligible for the International Doctorate Award.

Tarragona, 6 June 2017

Doctoral Thesis Supervisor

Dr. Airán Ródenas Seguí

Doctoral Thesis Supervisor

Dr. Maria Cinta Pujol Baiges

Acknowledgement

My first special thanks would be to my supervisors, Dr. Airán Ródenas Seguí and Dr. Maria Cinta Pujol Baiges who have been giving me huge supports and guidance on both scientific matters and personal issues. Without their help and encouragement I might not have been able to finish the thesis in the scheduled time.

Secondly, I would like to acknowledge professors Razvan Stoian and Ciro D'Amico (Hubert Curien Laboratory, the Jean Monnet University of Saint –Etienne, France) for their enormous help during my research stays at their institute; And Javier Vázquez de Aldana (Universidad de Salamanca, Spain) for the kind support during my research visit.

I would like to thank all members of the FiCMA group, professors: Quico and Magdalena; technicians: Nicole, Agustí, and Gemma; and other colleagues: Sasha, Ali, Josep Maria, Eric, Josué, Irina, Marc, Arnau, Esrom, and Javier for all the supports, the kindness, and the companionship I have received during my time here.

I would like to thank the technicians at the *Unitat de Microscopia of SRCiT*: Lukas, Mariana, Rita, Mercè and Núria, for their help with characterisation equipment.

I also want to take this chance to give thanks to all my friends, particularly Duc Quang Hoang who has been always giving me valuable advices, and generous supports.

Lastly and most importantly, I would like to take this opportunity to give the best wishes to my parents (Huu Mo Nguyen, and Thi Tho Nguyen), my brother and his wife (Huu Hoang Nguyen, Thi Loan Nguyen), my sister and her husband (Thi Yen Nguyen, Bao Cuong Bach), my nieces and nephews (Bee, Chip, Na, Bon, and a new coming baby). I am always grateful for the love and inspiration that they have been giving me endlessly.

Tarragona, Spain.
July - 2017

Dat Nguyen

List of publications and conferences

Paper I

Huu-Dat Nguyen, Airán Ródenas, Javier R. Vázquez de Aldana, Javier Martínez, Feng Chen, Magdalena Aguiló, Maria Cinta Pujol, and Francesc Díaz, *Heuristic modelling of laser written mid-infrared LiNbO3 stressed-cladding waveguides.* Optics Express, 2016. **24**(7): p. 7777-7791.

Paper II

Huu-Dat Nguyen, Airán Ródenas, Javier R. Vázquez de Aldana, Guillermo Martín, Javier Martínez, Magdalena Aguiló, Maria Cinta Pujol and Francesc Díaz, *Low-loss 3D-laser-written mid-infrared LiNbO3 depressed-index cladding waveguides for both TE and TM polarizations.* Optics Express, 2017. **25**(4): p. 3722-3736.

Other publications

Paper III

Muhammad Ali Butt, **Huu-Dat Nguyen**, Airán Ródenas, Carolina Romero, Pablo Moreno, Javier R. Vázquez de Aldana, Magdalena Aguiló, Rosa Maria Solé, Maria Cinta Pujol, and Francesc Díaz, *Low-repetition rate femtosecond laser writing of optical waveguides in KTP crystals: analysis of anisotropic refractive index changes.* Optics Express, 2015. **23**(12): p. 15343-15355.

Conferences

1. **Huu-Dat Nguyen**, Airán Ródenas, Javier Martínez, Javier V. de Aldana, Guillermo Martín, Cinta Pujol, and Francesc Díaz, (February, 2016). *Unveiling the index changes in laser-written waveguides inside $LiNbO_3$ for the mid-infrared range: towards on-chip chemi-photonic sensors.* Poster presentation at 7th International Symposium on Optical Materials, Lyon, France.

2. **Huu-Dat Nguyen**, Airán Ródenas, Javier R. Vázquez de Aldana, Javier Martinez, Feng Chen, Magdalena Aguiló, Maria Cinta Pujol, and Francesc Díaz, (June, 2016). *3D femtosecond laser-written depressed cladding waveguides on $LiNbO_3$: Optimization of birefringent stress-induced guiding properties in the mid-infrared light.* Oral presentation at XIV Congreso Nacional de Materiales, Gijon, Spain.

Three-Dimensional Laser Writing of Mid-Infrared Waveguide Circuits in Lithium Niobate crystal

Huu-Dat Nguyen

2017

Contents

Contents

Abstract

Lithium Niobate ($LiNbO_3$) is a well-known dielectric material with extensive characteristics: excellent electro-optic, piezo-electrical, piezo-optic, and non-linear optical properties, and a broad transparency from the visible to the mid-infrared range. Three-dimensional ultrafast Laser-Written (3DLW) depressed-index cladding waveguides (CLWs) in $LiNbO_3$ have offered potential applications in mid-infrared integrated photonic active devices. However, development of mid-infrared $LiNbO_3$-CLWs has met a serious bottleneck. The fundamental problem is related to the high complexity of laser-written structures which originates from the anisotropy of the material and the stress-induced effects. For this reason, low-loss single-mode mid-infrared guiding for both orthogonal polarisations has not yet been achieved. All reported mid-infrared $LiNbO_3$-CLWs have been limited to propagation losses of ~3 dB/cm, which is far from the value for practical uses. In this Thesis, the complex mid-infrared refractive index (RI) profiles of $LiNbO_3$-CLWs microstructured under various 3DLW conditions are reported for the first time. The RI profiles were evaluated by a comprehensive finite element method based simulation model along with a heuristic mode-matching approach. The extracted index profiles allow for the first time to design high performance $LiNbO_3$-devices using CLW circuit architectures. CLWs were fabricated in transversal writing geometry and under two thermal accumulation regimes: the low-repetition rate (1 kHz) and the critical-repetition rate regime (100 KHz). Single-mode guiding for both polarised lights with low propagation of 0.5 dB/cm has been achieved for the first time to our knowledge. Both straight and s-bend structures were successfully implemented. Simple functional devices such as beam splitters were designed, demonstrating that straightforward on-chip applications in mid-infrared light generation (i.e. using PPLN) and mid-infrared sensing (i.e. using Mach-Zehnder interferometers) are now feasible. Lastly, a novel 3DLW approach was developed using the longitudinal laser writing scheme, which has certain advantages over the transversal scheme, due to the cylindrical symmetry of the modification profiles.

1

Introduction

This chapter describes the interest of the mid-IR photonic field, and the scope of the thesis.

Contents

1.1. Mid-infrared photonics: the field of interest

Astronomical studies:

Emission of infrared radiation (i.e. heat) is known to occur to any object with non-zero temperature. The wavelength range at which the object irradiates corresponds to its temperature. By observing the spectral range from 1 μm to 100 μm, faraway objects with a wide range of temperatures from tens to several thousands Kelvin can be probed [1]. The mid-infrared (IR) range (referred to thermal infrared) is typically defined between 2 μm and 20 μm, which is within the peak emissions of many astronomical objects [1, 2]. Specifically, terrestrial or telluric planets such as the earth emit with high peak brightness at the wavelength region between 3.5 μm and 4 μm known as the astronomical "L" band rather than at the near-IR region [3]. In the meantime, host stars have peak brightness at a much shorter wavelength range (typically at the visible). This makes considerable brightness contrast for their differentiation. Detection of these mid-IR sources therefore has provided a powerful tool for exploring telluric planets around the solar system and nearby exoplanets. Moreover, further source of information from bio-markers: i.e. water, methane, carbon dioxide and ozone can be collected though spectroscopic observations [1]. This further expands the potential of mid-IR range to applications in the fields of astrochemistry and astrobiology.

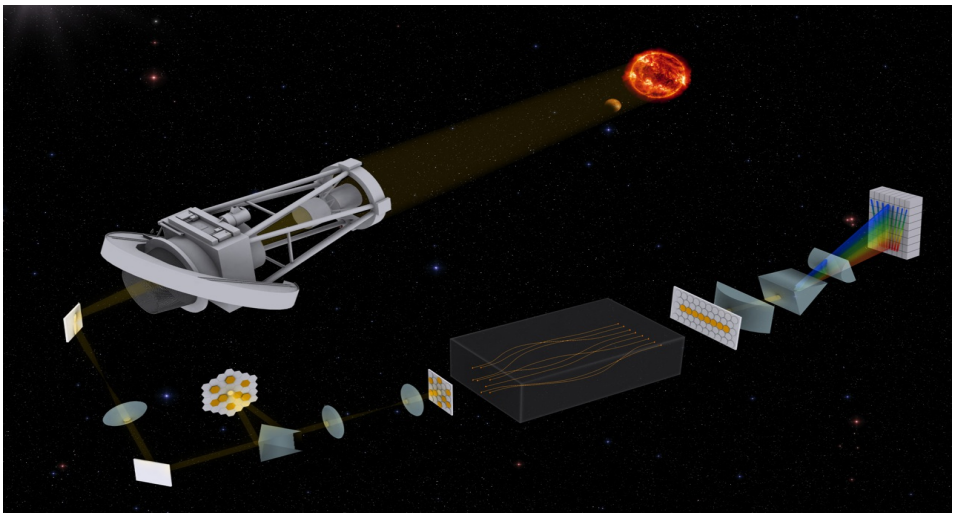

Fig. 1.1. Illustration of an astronomical detection process using mid-IR integrated photonic interferometers. Light from a celestial object is collected by the telescope, directed through mirrors and lenses to integrated photonic pupil-remapping interferometers, and finally recorded by detectors for high-contrast imaging [4].

During the last decade, astronomical instrumentation has been increasingly developed by the advanced photonic technologies [2, 5-10]. The technologies enable integration of entire optical circuits with miniaturised components: i.e. beam splitters, combiners, interferometers [8, 11-16] and spectrographs [17] into centimeter-scaled devices. The small size allows the photonic devices to be easily stabilised in a steady temperature condition and improve their performance. As an example, the Fig. 1.1 illustrates the process for exploring exoplanets enabled by direct detection techniques such as interferometry [4]. Light from celestial targets is collected by a telescope and directed to integrated photonic pupil-remapping interferometers for high-contrast imaging. It is targeted to employ in detections of young planetary mass companions in the nearest star-forming regions.

Chemical/ biochemical monitoring

The mid-IR wavelength window is an extremely useful spectral range which contains fingerprint/ fundamental vibrational absorption of many important molecules [18]. Fig. 1.2 shows mid-IR spectral regions where specific molecules have unique radiation and absorption features depending on their chemical composition [18-20]. In this mid-IR region, photons have much less energy than those in the ultraviolet and visible range. The incident photons excite vibrations in molecules which can be characterised by observing transitions from one vibrational energy level to another.

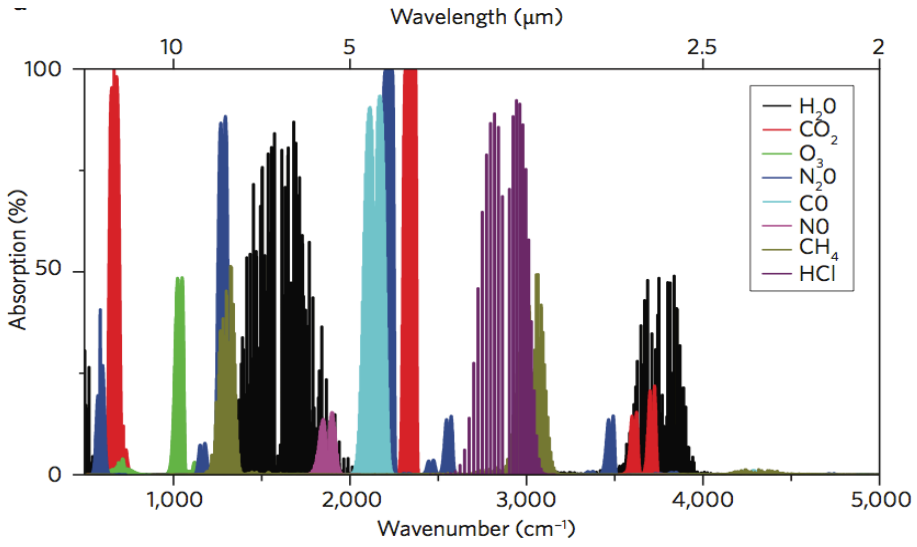

Fig. 1.2. Characteristic mid-IR absorption spectra of common molecules [18]

The unique fingerprint/ spectra of chemical or biochemical molecules therefore can be identified by photonic sensing devices operated at the mid-IR range. When compared to the visible and near-IR ranges, the mid-IR spectral region has demonstrated its advantages for enhanced performance in a number of fields: chemical/ bio-chemical sensing [18], medical diagnosis [20], and environmental screening [21].

1.2. The scope of the thesis

In order to collect useful information from the mid-IR source, high-performance mid-IR integrated photonic instruments are typically required. For realisation of the complex photonic architectures, optical waveguides are initially developed as the fundamental building-blocks.

In this thesis, Lithium Niobate ($LiNbO_3$) is chosen as the host material due to its extensive characteristics including excellent electro-optic, piezo-electric, piezo-optic and non-linear optical properties, together with a broad transparency from the visible to mid-IR range [22]. Due to the advantage of potential mid-IR guiding, the work involves exploration of cladding waveguide structures which are arbitrarily fabricated in 3-dimensional (3D) geometry, using the 3D ultrafast laser writing (3DLW) technique. Implementation of mid-IR waveguides inside a volume of $LiNbO_3$ crystal thereby has a wide range of uses: novel integrated non-linear frequency conversion chips, electro-optic interferometric spectrometers, as well as applications in chemical and bio-medical fields, atmospheric research, high-resolution on-chip vibrational spectroscopy, and astrophotonic instrumentation [23-26].

Challenges of the field

The tight focusing of ultrafast near-IR laser pulses inside $LiNbO_3$ is known to induce a non-linear photo-ionisation process which ultimately results in a spatially localised lattice distortion at micron and nano-scale [27-29]. The irreversible changes involve lattice defects and amorphisation, typically leading to a modification in the refractive indices (RI) of the material. The modification can be judiciously exploited to construct 3D waveguide architectures. In general, two fundamental types of RI modification have been reported with the 3DLW technique in $LiNbO_3$: (1) the so-called Type I modification which results in a RI increase within the laser focal volume; and (2) the Type II modification which involves negative-RI change occurred at the laser focal

volume. In addition, strong stress-optic fields are always present at surrounds of the localised laser focal volume due to the lattice amorphisation and defect generation, involving collateral piezo-optic index changes [23, 30]. The stress-optic fields can expand several microns away from the laser-written structures and must be taken into account when computing RI profiles of optical waveguides.

Depressed-index CLWs are typically fabricated by transversally writing tubular structures in the regime for producing Type II index changes, which therefore act as depressed-RI claddings for sustaining light propagating modes (leaky modes) within its un-modified core. Since the waveguiding core volume is un-modified/un-irradiated by the laser pulses, it preserves all the important optical properties of the pristine crystalline material. This is a clear advantage of this approach over the ion implantation of 3DLW in the Type I regime in which the laser-modified volume is used as a waveguiding core. The light guiding properties of CLWs depend on the magnitude of the negative RI change ($-\Delta n$) produced at the laser-written tracks, and on the size and spatial width of the cladding arrangement [31]. Full RI profiles of a cladding structure are the combination of (i) the local RI changes Δn^{local} at the laser-modified tracks and (ii) the anisotropic piezo-optic RI fields Δn^{stress} induced at their surrounds, which strongly depend on particular 3DLW parameters: pulse duration, pulse energy, repetition rate, scan speed, wavelength, polarisation, and focusing optics, as well as crystallographic orientation of the anisotropic $LiNbO_3$ crystal.

As a result of the high complexity of the laser-written structures which originates from the anisotropy of the material and the stress-induced effects, there exists a fundamental bottleneck for obtaining CLWs in $LiNbO_3$ capable of single-mode low-loss guiding for both orthogonal polarisations at the mid-IR wavelengths. To the best of our knowledge, all $LiNbO_3$ CLWs reported for operation at wavelengths longer than 3000 nm have been limited to guiding for mostly one polarisation, and propagation losses (PLs) of ~3 dB/cm [23, 28, 29, 32-41]. These high PLs are far from the value for practical applications, that is <0.5 dB/cm as required for high performance of mid-IR integrated photonic devices at cm's scale. In pursuit of improving the optical performance of CLWs, thermal treatments have been additionally performed to reduce the anisotropic micro-stress fields induced during the laser writing process [23, 42, 43]. However, an underlying mechanism of the changes in mid-IR waveguide profiles under different thermal annealing conditions has

not been fully understood, mainly due to the difficulty in measuring RI changes of sub-micron volume at this long wavelength range. To date, most experimental reports on CLWs were based on fabrication trial and error methodologies [11, 32, 44-50], with no information on the RI profiles and therefore no proper understanding of the waveguide properties.

The main content of the thesis is briefly concluded as following:

In the chapter 2: Relevant properties of the $LiNbO_3$ material are introduced, along with its state-of-the-art applications.

In the chapter 3: A brief introduction to fundamental technique of 3D ultrafast laser fabrication in $LiNbO_3$ crystal is described.

In the chapter 4: Experimental techniques and all relevant methodologies for characterisation of the fabricated waveguides are described.

In the chapter 5: A finite element method –based simulation model is introduced. It is for the first time to our knowledge, a comprehensive model is built taking into account realistic profiles of the complex laser-modified CLWs. It involves both arbitrary changes of refractive index at the laser-written volume and anisotropic stress-induced refractive index fields at the surrounds of the laser-irradiated volume.

In chapter 6: The development of $LiNbO_3$-CLWs with the low repetition rate (1 kHz) laser systems is described. High performance of $LiNbO_3$-CLWs at the mid-IR range was obtained with lowest propagation losses (<0.5 dB/cm) ever reported to the best of our knowledge. The dependence of the CLW properties with respect to thermal annealing treatments is also thoroughly studied. Other integrated photonic instruments such as directional beam splitters and Mach-Zehnder structures were also numerically analysed based on the experimentally obtained straight waveguide component.

In the chapter 7: The development of $LiNbO_3$-CLWs with the intermediate repetition rate (100 kHz) laser is further explored. Again the CLWs were obtained with high optical performance (propagation losses < 0.5 dB/cm) without thermal annealing post process as required in the low repetition rate regime. A novel longitudinal laser writing geometry is also exploited, capable of realising symmetric laser-modified profiles and therefore periodic lattice-like structures (i.e. hexagonal geometry) and helical structures.

Reference

1. L. Labadie and O. Wallner, *Mid-infrared guided optics: a perspective for astronomical instruments.* Opt. Express, 2009. **17**(3): p. 1947-1962.
2. A. Arriola, S. Gross, M. Ams, T. Gretzinger, D. Le Coq, R. P. Wang, H. Ebendorff-Heidepriem, J. Sanghera, S. Bayya, L. B. Shaw, M. Ireland, P. Tuthill, and M. J. Withford, *Mid-infrared astrophotonics: study of ultrafast laser induced index change in compatible materials.* Opt. Mat. Express, 2017. **7**(3): p. 698-711.
3. M. Nikku, B. Adam, and C. Thayne, *Model Atmospheres for Massive Gas Giants with Thick Clouds: Application to the HR 8799 Planets and Predictions for Future Detections.* The Astrophysical Journal, 2011. **737**(1): p. 34.
4. N. Jovanovic, P. G. Tuthill, B. Norris, S. Gross, P. Stewart, N. Charles, S. Lacour, M. Ams, J. S. Lawrence, A. Lehmann, C. Niel, J. G. Robertson, G. D. Marshall, M. Ireland, A. Fuerbach, and M. J. Withford, *Starlight demonstration of the Dragonfly instrument: an integrated photonic pupil-remapping interferometer for high-contrast imaging.* Mon. Not. R. Astron. Soc. , 2012. **427,** : p. 806–815.
5. R. R. Thomson, R. J. Harris, T. A. Birks, G. Brown, J. Allington-Smith, and J. Bland-Hawthorn, *Ultrafast laser inscription of a 121-waveguide fan-out for astrophotonics.* Optics Letters, 2012. **37**(12): p. 2331-2333.
6. T. A. Birks, I. Gris-Sánchez, S. Yerolatsitis, S. G. Leon-Saval, and R. R. Thomson, *The photonic lantern.* Advances in Optics and Photonics, 2015. **7**(2): p. 107-167.
7. N. Jovanovic, S. Gross, C. Miese, A. Fuerbach, J. Lawrence, and M. Withford. *Direct Laser Written Multimode Waveguides for Astronomical Applications*. in *Advanced Photonics & Renewable Energy*. 2010. Karlsruhe: Optical Society of America.
8. F. Malbet, P. Kern, I. Schanen-Duport, J. P. Berger, K. Rousselet-Perraut, and P. Benech, *Integrated optics for astronomical interferometry.* Astron. Astrophys. Suppl. Ser., 1999. **138**(1): p. 135-145.
9. F. Eisenhauer, G. Perrin, W. Brandner, C. Straubmeier, A. Richichi, S. Gillessen, J. P. Berger, S. Hippler, A. Eckart, M. Schöller, S. Rabien, F. Cassaing, R. Lenzen, M. Thiel, Y. Clénet, J. R. Ramos, S. Kellner, P. Fédou, H. Baumeister, R. Hofmann, E. Gendron, A. Boehm, H. Bartko, X. Haubois, R. Klein, K. Dodds-Eden, K. Houairi, F. Hormuth, A. Gräter, L. Jocou, V. Naranjo, R. Genzel, P. Kervella, T. Henning, N. Hamaus, S. Lacour, U. Neumann, M. Haug, F. Malbet, W. Laun, J. Kolmeder, T. Paumard, R. R. Rohloff, O. Pfuhl, K. Perraut, J. Ziegleder, D. Rouan, and G. Rousset. *GRAVITY: getting to the event horizon of Sgr A**. 2008.
10. Arriola, A., Norris, B., Cvetojevic, N., Gross, S., Lawrence, J., Withford, M., and Tuthill, P. *First on-sky demonstration of a compact fully-integrated photonic waveguide nulling interferometer*. in *2016 Conference on Lasers and Electro-Optics (CLEO)*. 2016.
11. S. Gross, N. Jovanovic, A. Sharp, M. Ireland, J. Lawrence, and M. l. J. Withford, *Low loss mid-infrared ZBLAN waveguides for future astronomical applications.* Opt. Express, 2015. **23**: p. 7946-7956.

12. A. Arriola, S. Mukherjee, D. Choudhury, L. Labadie, and R. R. Thomson, *Ultrafast laser inscription of mid-IR directional couplers for stellar interferometry.* Optics Letters, 2014. **39**(16): p. 4820-4822.
13. M. Benisty, J. P. Berger, L. Jocou, P. Labeye, F. Malbet, K. Perraut, and P. Kern, *An integrated optics beam combiner for the second generation VLTI instruments.* A&A, 2009. **498**(2): p. 601-613.
14. Hanot, C., Mennesson, B., Martin, S., Liewer, K., Loya, F., Mawet, D., Riaud, P., Absil, O., and Serabyn, E., *Improving Interferometric Null Depth Measurements using Statistical Distributions: Theory and First Results with the Palomar Fiber Nuller.* The Astrophysical Journal, 2011. **729**(2): p. 110.
15. H. Hsiao, K. A. Winick, and J. D. Monnier. *A Mid-Infrared Integrated Optic Astronomical Beam Combiner for Stellar Interferometry*. in *Frontiers in Optics 2009/Laser Science XXV/Fall 2009 OSA Optics & Photonics Technical Digest*. 2009. San Jose, California: Optical Society of America.
16. H. Hsiao, K. A. Winick, J. D. Monnier, and J. P. Berger, *An infrared integrated optic astronomical beam combiner for stellar interferometry at 3-4 μm.* Optics Express, 2009. **17**(21): p. 18489-18500.
17. N. Cvetojevic, J. S. Lawrence, S. C. Ellis, J. Bland-Hawthorn, R. Haynes, and A. Horton, *Characterization and on-sky demonstration of an integrated photonic spectrograph for astronomy.* Optics Express, 2009. **17**(21): p. 18643-18650.
18. A. Schliesser, N. Picque, and T. W. Hansch, *Mid-infrared frequency combs.* Nat Photon, 2012. **6**(7): p. 440-449.
19. B. C. Smith, *Fundamentals of Fourier Transform Infrared Spectroscopy, Second Edition*. 2011: CRC Press. i-xiii.
20. R. W. Waynant, I. K. Ilev, and I. Gannot, *Mid–infrared laser applications in medicine and biology.* Philosophical Transactions of the Royal Society of London. Series A: Mathematical, Physical and Engineering Sciences, 2001. **359**(1780): p. 635.
21. Muda, R., Lewis, E., Keeffe, S. O., Dooly, G., and Clifford, J., *Detection of high level carbon dioxide emissions using a compact optical fibre based mid-infrared sensor system for applications in environmental pollution monitoring.* Journal of Physics: Conference Series, 2009. **178**(1): p. 012008.
22. A. M. Prokhorov and I. S. Kuz'minov, *Physics and chemistry of crystalline lithium niobate*. 1990, Bristol, Angleterre: A. Hilger.
23. R. He, Q. An, Y. Jia, G. R. Castillo-Vega, J. R. Vázquez de Aldana, and F. Chen, *Femtosecond laser micromachining of lithium niobate depressed cladding waveguides.* Opt. Mater. Express, 2013. **3**: p. 1378-1384.
24. S. Heidmann, N. Courjal, and G. Martin, *Double polarization active Y-junctions in the L-Band, based on Ti:LiNbO$_3$ Waveguides: polarization and contrast performances.* Opt. Lett., 2012. **37**(16): p. 3318-3320.
25. G.Martin, S. Heidmann, J.-Y. Rauch, L. Jocou, and N. Courjal, *Electro-optic fringe locking and photometric tuning using a two-stage Mach-Zehnder lithium niobate waveguide for high-contrast mid-infrared interferometry.* Opt. Eng., 2014. **53**(3): p. 034101.
26. F. Thomas, S. Heidmann, M. de Mengin, N. Courjal, G. Ulliac, A. Morand, P. Benech, E. Le Coarer, and G. Martin, *First Results in Near and Mid IR Lithium Niobate-Based Integrated Optics Interferometer Based on SWIFTS-Lippmann Concept.* J. Lightwave Technol., 2014. **32**(22): p. 3736–3742.

27. A. Rodenas, G. Zhou, D. Jaque, and M. Gu, *Direct laser writing of three-dimensional photonic structures in Nd:yttrium aluminum garnet laser ceramics.* Appl. Phys. Lett., 2008. **93**(15): p. 151104.
28. A. Rodenas, G. A. Torchia, G. Lifante, E. Cantelar, J. Lamela, F. Jaque, L. Roso, and D. Jaque, *Refractive index change mechanisms in femtosecond laser written ceramic Nd:YAG waveguides: micro-spectroscopy experiments and beam propagation calculations.* Appl. Phys. B, 2009. **95**(1): p. 85–96.
29. A. Rodenas, *Direct femtosecond laser writing of 3D photonic structures in rare-earth doped lithium niobate*. 2009, Universidad Autónoma de Madrid.
30. H. Karakuzu, M. Dubov, and S. Boscolo, *Control of the properties of micro-structured waveguides in lithium niobate crystal.* Opt. Express, 2013. **21**: p. 17122-17130.
31. J. Hu and C. R. Menyuk, *Understanding leaky modes: slab waveguide revisited.* Adv. Opt. Photonics, 2009. **1**: p. 58–106.
32. R. He, Q. An, Y. Jia, G. R. Castillo-Vega, J. R. Vázquez de Aldana, and F. Chen, *Femtosecond laser micromachining of lithium niobate depressed cladding waveguides.* Optical Materials Express, 2013. **3**(9): p. 1378-1384.
33. Q. An, Y. Ren, Y. Jia, J. Rodríguez Vázquez de Aldana, and F. Chen, *Mid-infrared waveguides in zinc sulfide crystal.* Opt. Mat. Express, 2013. **3**: p. 466-471.
34. A. Rodenas, G. A. Torchia, G. Lifante, E. Cantelar, J. Lamela, F. Jaque, L. Roso, and D. Jaque, *Refractive index change mechanisms in femtosecond laser written ceramic Nd:YAG waveguides: micro-spectroscopy experiments and beam propagation calculations.* Applied Physics B, 2009. **95**(1): p. 85-96.
35. H. Karakuzu, M. Dubov, S. Boscolo, L. A. Melnikov, and Y. A. Mazhirina, *Optimisation of microstructured waveguides in z-cut $LiNbO_3$ crystals.* Opt. Mat. Express, 2014. **4**(3): p. 541-552.
36. H. D. Nguyen, A. Ródenas, J. R. Vázquez de Aldana, J. Martínez, F. Chen, M. Aguiló, M. C. Pujol, and F. Díaz, *Heuristic modelling of laser written mid-infrared $LiNbO_3$ stressed-cladding waveguides.* Opt. Express, 2016. **24**(7): p. 7777-7791.
37. Q. An, Y. Ren, Y. Jia, J. R. Vázquez de Aldana, and F. Chen, *Mid-infrared waveguides in zinc sulfide crystal.* Opt. Mater. Express, 2013. **3**: p. 466-471.
38. A. Rodenas, L. M. Maestro, M. Ramirez, G. A. Torchia, L. Roso, F. Chen, and D. Jaque, *Anisotropic lattice changes in femtosecond laser inscribed Nd^{3+}:MgO:$LiNbO_3$ optical waveguides.* J. Appl. Phys., 2009. **106**: p. 013110.
39. B. McMillen and Y. Bellouard, *On the anisotropy of stress-distribution induced in glasses and crystals by non-ablative femtosecond laser exposure.* Opt. Express 2015. **23**: p. 86-100.
40. H. Karakuzu, M. Dubov, S. Boscolo, L. A. Melnikov, and Y. A. Mazhirina, *Optimisation of microstructured waveguides in z-cut $LiNbO_3$ crystals.* Opt. Mater. Express, 2014. **4**: p. 541-552.
41. H. D. Nguyen, A. Ródenas, J. R. Vázquez de Aldana, G. Martín, J. Martínez, M. Aguiló, M. C. Pujol, and F. Díaz, *Low-loss 3D-laser-written mid-infrared $LiNbO_3$ depressed-index cladding waveguides for both TE and TM polarizations.* Optics Express, 2017. **25**(4): p. 3722-3736.
42. R. He, Q. An, J. R. Vázquez de Aldana, Q. Lu, and F. Chen, *Femtosecond – laser micromachined optical waveguides in $Bi_4Ge_3O_{12}$ crystals.* Applied Optics, 2013. **52**(16): p. 3713-3718.

43. J. Martınez de Mendıvil, D. Sola, J. R. Vazquez de Aldana, G. Lifante, A. H. de Aza, P. Pena, and J. I. Pen, *Ultrafast direct laser writing of cladding waveguides in the $0.8CaSiO_3$-$0.2Ca_3(PO4)_2$ eutectic glass doped with Nd^{3+} ions.* J. Appl. Phys., 2015. **117**: p. 043104.
44. A. G. Okhrimchuk and A. V. Shestakov, *Depressed cladding, buried waveguide laser formed in a YAG:Nd^{3+} crystal by femtosecond laser writing.* Opt. Lett., 2005. **30**(17): p. 2248-2250.
45. A. Okhrimchuk, V. Mezentsev, A. Shestakov, and I. Bennion, *Low loss depressed cladding waveguide inscribed in YAG:Nd single crystal by femtosecond laser pulses* Opt. Express, 2012. **20**(4): p. 3832-3843.
46. J. R. Macdonald, S. J. Beecher, P. A. Berry, G. Brown, K. L. Schepler, and A. K. Kar, *Efficient mid-infrared Cr:ZnSe channel waveguide laser operating at 2486 nm.* Opt. Lett., 2013. **38**(13): p. 2194-2196.
47. Y. Ren, G. Brown, A. Ródenas, S. Beecher, F. Chen, and A. K. Kar, *Mid-infrared waveguide lasers in rare-earth-doped YAG.* Opt. Lett., 2012. **37**(16): p. 3339-3341.
48. H. Karakuzu, M. Dubov, and S. Boscolo, *Control of the properties of micro-structured waveguides in lithium niobate crystal.* Opt. Express, 2013. **21**(14): p. 17122-17130.
49. J. Martınez de Mendıvil, D. Sola, J. R. Vazquez de Aldana, G. Lifante, A. H. de Aza, P. Pena, and J. I. Pena, *Ultrafast direct laser writing of cladding waveguides in the $0.8CaSiO_3$-$0.2Ca_3(PO_4)_2$ eutectic glass doped with Nd^{3+} ions.* J. Appl. Phys., 2015. **117**: p. 043104.
50. R. He, Q. An, J. R. Vázquez de Aldana, Q. Lu, and F. Chen, *Femtosecond-laser micromachined optical waveguides in $Bi_4Ge_3O_{12}$ crystals.* Applied Optics, 2013. **52**(16): p. 3713-3718.

2

Lithium Niobate mid-infrared photonics

This chapter describes physical properties of Lithium Niobate which are relevant for mid-infrared photonics, and the state-of-the-art of its applications.

Contents

2.1. Introduction

Lithium Niobate is one of the most widely used ferroelectric materials for integrated electro-optic devices and non-linear optical applications. It is a man-made crystal which was synthesised in a single crystal form and investigated for its crystalline structure and physical properties in 1966 for the first time [1-5]. Lithium Niobate appears naturally optically birefringent and has the chemical formula (in the stoichiometric state) of $LiNbO_3$. The basic physical properties of $LiNbO_3$ are listed in the Table 2.1. Lithium Niobate exhibits an extensive range of characteristics including large pyro-electric, piezo-electric, electro-optic and photo-elastic coefficients. As a result of extensive study and large scale manufacture of high-quality wafers, Lithium Niobate is often recognised as the silicon of the non-linear optics.

Table 2. 1. Basic physical properties of Lithium Niobate [6]

Chemical formula	$LiNbO_3$
Crystallographic system	Trigonal
Space group	*R3c*
Transparent window	0.4 μm – 5 μm
Density	4.612 $g.cm^{-3}$
Melting point	1553 K
Curie temperature	1483 K
Thermal expansion coefficients [7]	
X, Y axis	1.54×10^{-5} K^{-1}
Z axis	0.75×10^{-5} K^{-1}
Mechanical hardness	5 Mohs
Thermal conductivity [8]	$\kappa \approx 2.67$ $W.m^{-1}.K^{-1}$
Specific heat capacity [8]	$Cp \approx 714$ $J.kg^{-1}.K^{-1}$
Molecular weight	147.9 $g.mol^{-1}$
Solubility	Insoluble in H_2O

2.2. Physical properties of Lithium Niobate

2.2.1. Crystallographic structure

Below the Curie temperature of 1483 K, Lithium Niobate is in ferroelectric phase and exhibits spontaneous crystal polarisation $P_S \approx 70$ $\mu C.cm^{-2}$ [9] which is around one order of magnitude larger than most of the ferroelectric materials; due to the non-central charge positioning of the lithium and niobium cations [10, 11]. In this ferroelectric state,

$LiNbO_3$ is a non-centrosymmetric crystal and belongs to the trigonal space group ($R3c$) and point group of 3m . This makes $LiNbO_3$ an uniaxial crystal with a three-fold rotational symmetry about its crystallographic c-axis. As shown in Fig. 2.1.a. the crystal structure consists of planar sheets of oxygen anions in a distorted hexagonal close-packed configuration. The face sharing oxygen octahedra are stacked in a screw-like form along the crystallographic axis and filled with either lithium (Li) or niobium (Nb) ions, while the oxygen tetrahedral interstices remain vacant. In the positive polar direction (along the crystallographic c direction), the atoms are arranged at the interstices in the following order: Li, Nb, vacancy, Li, Nb, vacancy… [6].

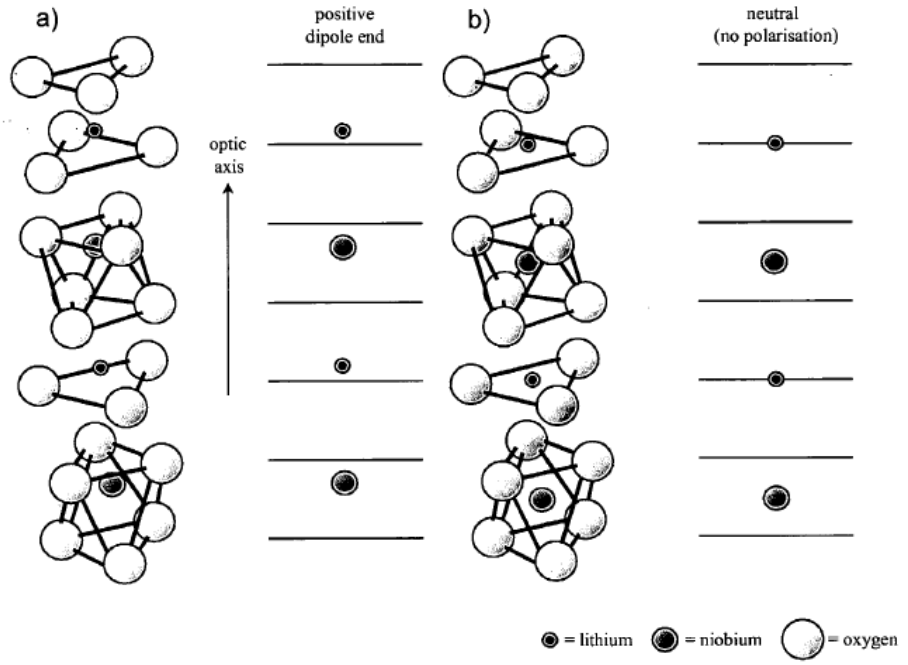

Fig. 2.1. Crystallographic structure of Lithium Niobate in (a) ferroelectric and (b) paraelectric phase [12]. The optic axis is parallel to the c crystallographic direction.

Above the Curie temperature, the crystal becomes paraelectric (space group $R\bar{3}c$) and non-polar, due to the movement of the Li and Nb ions into a centrosymmetric configuration. In this paraelectric phase, the Li ion positions in one of the oxygen planes that is c/4 away from the Nb ion; and the Nb ion is centred between the oxygen layers.

As the temperature decreases through the Curie temperature, the crystal experiences a phase transition when the elastic forces dominate and force the Li and Nb ions into new

positions relative to the oxygen octahedra (Fig. 2.1.b). This shift of ions results the charge separation, causing $LiNbO_3$ to exhibit the spontaneous polarisation which gives rise to many unique properties discussed in next sections.

2.2.2. Linear Optical properties

Regarding optical transmission, $LiNbO_3$ shows a good transmission within the near-infrared up to 5 µm wavelength, whereas large absorption occurs at the wavelength below 0.4 µm and above 5 µm [13].

$LiNbO_3$ is classified as negative uniaxial birefringent crystal in which its extraordinary refractive index, n_e (electric field polarised parallel to the optical axis) is lower than its ordinary refractive index, n_o (electric field polarised perpendicular to the optical axis). In the Cartesian coordinate system (x,y,z), the z axis is defined to be parallel to the c-axis, known as the optic axis; the x axis is chosen to coincide with any of the two a or b axes; while the y axis is chosen by the rule of right handed which hence lies along the plane perpendicular to the crystallographic axis [6].

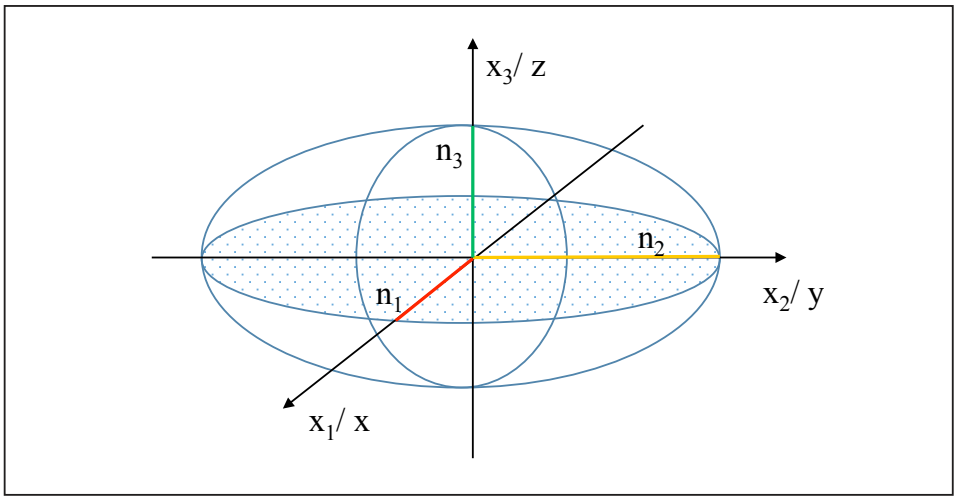

Fig. 2.2. Schematic of an indicatrix with negative uniaxial: $n_o > n_e$ (ordinary index: $n_o = n_1 = n_2$; extraordinary index: $n_e = n_3$)

In order to conceptualise the birefringence in the corresponding coordinate system, an indicatrix is constructed in a form of an ellipsoid whose shape represents the real part of refractive indices for light traveling through the respective axes of the crystal (Fig. 2.2.). The indicatrix is described in an elliptical expression:

$$\left(\frac{x_1}{n_1}\right)^2 + \left(\frac{x_2}{n_2}\right)^2 + \left(\frac{x_3}{n_3}\right)^2 = 1. \quad (2.01)$$

Which can be simplified in terms of a tensor b_{ij}:

$$b_{11}x_1^2 + b_{22}x_2^2 + b_{33}x_3^2 = 1. \quad (2.02)$$

$$Or \qquad \sum_{ij=1}^{3} b_{ij}x_i x_j = 1. \quad (2.03)$$

The birefringence of $LiNbO_3$ is relatively large [13], which makes it suitable for many integrated electro-optical non-linear optical applications. The congruent $LiNbO_3$ has the extraordinary index, n_e ranging from 2.34 to 2.8 and ordinary index, n_o ranging from 2.2 to 2.25, over the visible window. The dependence of these refractive indices on wavelength of the incident electromagnetic wave and temperature is expressed in the Sellmeier equation [14]:

$$n_o^2 = 4.9048 + \frac{1.178\,x10^5 + 2.314\,x10^{-2}F}{\lambda^2 - (2.1802\,x10^2 - 2.9671\,x10^{-5}F)^2} - 2.7153x10^{-8}\lambda^2 + 2.1429x10^{-8}F$$

$$n_e^2 = 4.5820 + \frac{0.9921x10^5 + 5.271\,x10^{-2}F}{\lambda^2 - (2.1090x10^2 - 4.9143x10^{-5}F)^2} - 2.194x10^{-8}\lambda^2 + 2.297x10^{-8}F$$

Where λ is the wavelength of incident light and F is temperature dependent function: $F = (T-T_o)(T+T_o+546)$, with T_o =297.5 K is the reference temperature. Fig. 2.3 displays the refractive index dispersion of lithium niobate at $T=T_o$= 297.5 K.

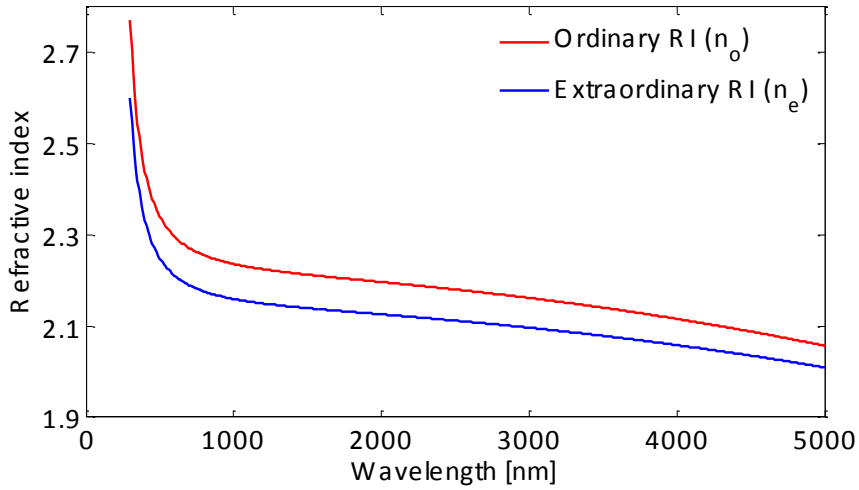

Fig. 2.3. Refractive index dispersion of Lithium Niobate.

2.2.3. Non-linear optical properties

The non-linear effect is one of the main advantageous properties which enables $LiNbO_3$ to have a broad field of applications such as conversion of optical frequency. When an electromagnetic wave propagates through a transparent medium, the driving electric field accelerates the loosely bound valence electrons, and distorts the shape of the electron distribution. The distortion of the electron distribution is referred to as the electrical polarisation, P and is given in a function of the applied electric field, E:

$$P_\chi = \varepsilon_0\left(\chi^{(1)}E + \chi^{(2)}E^2 + \chi^{(3)}E^3 + \ldots\right). \quad (2.04)$$

Where the $\chi^{(n)}$ are the electric susceptibility tensors of rank (n+1) and ε_0 is the permittivity of the medium (in this case, Lithium Niobate) in vacuum. In a linear regime, the restorative electrostatic forces that act to maintain the electron distribution are much greater than the distorting forces induced by a low intensity of the propagating electric field. Therefore, higher order terms of the equation 2.04 do not play a significant role in adding to the polarisation and can be eliminated. The linear equation is written as:

$$P_\chi = \varepsilon_0\chi^{(1)}E. \quad (2.05)$$

However, at high electric field strengths, these high order terms have crucial contributions to the polarisation, and the medium now has a non-linear response to the electric field. Considering the applied electric field is in a form of two frequency components $E = E_0 \cos\omega_1 t + E_0 \cos\omega_2 t$, the right site of the equation 2.04 using only the first two terms will result in forms of $\omega_1 + \omega_2$, $\omega_1 - \omega_2$, $2\omega_1$, $2\omega_2$ leading to a range of non-linear effects such as second harmonic generation, difference frequency generation, sum frequency generation, etc. The values of the incident electromagnetic field and the values of the non-linear coefficients $\chi^{(2)}$ are responsible for the strength of the non-linear interaction within the crystal. The second order susceptibility $\chi^{(2)}$ is expressed in the below equation relating to the non-linear coefficient tensor, d_{ij} which is measured experimentally:

$$2d_{ij} = \chi^{(2)} \quad (2.06)$$

In centrosymmetric crystals, d is zero, which explains why the non-linear effects only happen in non-centrosymmetric crystals such as $LiNbO_3$ in its ferroelectric phase.

2.2.4. Piezo-optic effect

This thesis work involves numerical simulation of changes in refractive index with respect to stress fields induced by thermal expansion of laser-damaged volume. The relation between this induced stress and the corresponding refractive index change is referred to the piezo-optic effect of the material; or the photo-elastic effect when considering strain instead of stress.

Before going to discuss these effects, it is worth to introduce concepts of stress and strain. The stress is defined as a distributed force on an internal or external unit area of a body and composed of nine components in arbitrary coordinate system as illustrated in Fig. 2.4 [15].

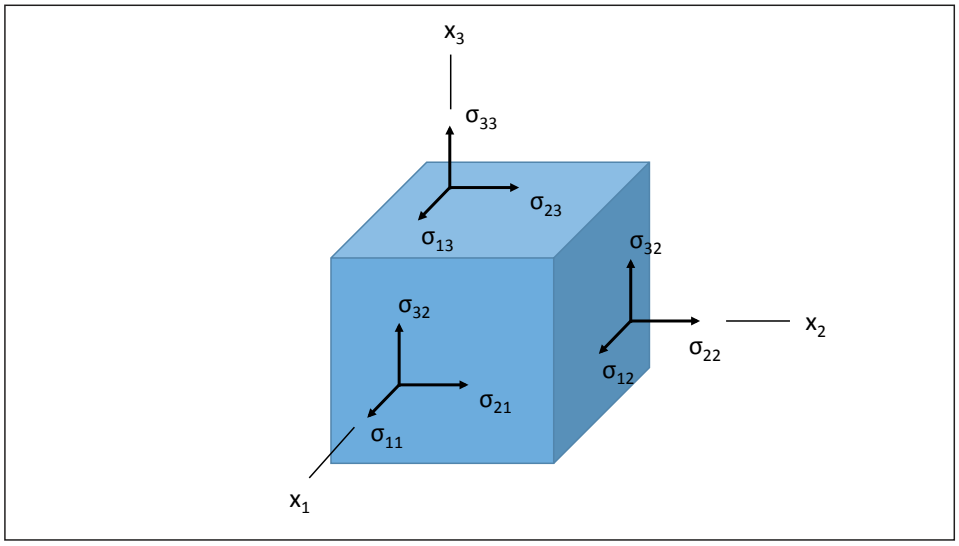

Fig. 2.4. Schematic of stress distributed on a solid body.

The stress tensor is given:

$$\sigma_{ij} = \begin{bmatrix} \sigma_{11} & \sigma_{12} & \sigma_{13} \\ \sigma_{21} & \sigma_{22} & \sigma_{23} \\ \sigma_{31} & \sigma_{32} & \sigma_{33} \end{bmatrix} \tag{2.07}$$

In this notation, the first subscript refers to the direction of the force, while the second indicates the normal to the face on which the force acts. For static equilibrium, each force is balanced equally by an opposite force on the reverse side of the body. This makes the stress tensor symmetric with $\sigma_{12} = \sigma_{12}$; $\sigma_{13} = \sigma_{31}$; and $\sigma_{23} = \sigma_{32}$. Therefore, six independent components of the stress are specified with three tensile stresses (if values

are positive) or compressive stresses (if the values are negative): σ_{11}, σ_{22}, and σ_{33}, and three shear components: σ_{12}, σ_{13}, and σ_{23}.

The applied stress to a solid body in the equilibrium state causes it to undergo deformation whose measure is labelled as strain, ϵ. Similar to the stress, components of strain include normal and shear strain. The normal strain is a measure of length change, ∂u of a stressed element in a direction parallel to the normal stress [16]:

$$\epsilon_i = \frac{\partial u_i}{\partial x_i} \tag{2.08}$$

While the shear strain is a measure of distortion of the stressed element [16]:

$$\epsilon_{ij} = \epsilon_{ji} = \frac{1}{2}\left(\frac{\partial u_i}{\partial x_j} + \frac{\partial u_j}{\partial x_i}\right) \tag{2.09}$$

The relationship between the stress and the strain in an elastic regime can be formulated by the Hooke's law [15, 16]:

$$\epsilon_{ij} = c_{ijkl}\sigma_{kl} \tag{2.10}$$

Where c_{ijkl} is the fourth rank elastic stiffness tensor which has 3^4=81 elements. With the symmetry of the shear stress/strain ($\sigma_{ij} = \sigma_{ji}$; $\epsilon_{ij} = \epsilon_{ji}$), it is convenient to contract the notation: $\sigma_{11} = \sigma_1$; $\sigma_{22} = \sigma_2$; $\sigma_{33} = \sigma_3$; $\sigma_{12} = \sigma_4$; $\sigma_{13} = \sigma_5$; and $\sigma_{23} = \sigma_6$; and similarly for ϵ. Additionally, the elastic tensor can be reduced to c_{ij} containing 36 elements.

Referring to the piezo-optic effect, when the solid material is subjected to a stress, the respective refractive indices n_i are expected to change; giving changes to the original indicatrix. The difference between the original indicatrix tensor, b_{ij} and the changed indicatrix tensor, b'_{ij} is described:

$$\Delta b_{ij} = b'_{ij} - b_{ij} \tag{2.11}$$

As the theory of elasticity proposed by Pockels [17], the change in refractive index described in the indicatrix tensor can be quantified as a function of the corresponding stress:

$$\Delta b_{ij} = \pi_{ijkl}\,\sigma_{kl} \tag{2.12}$$

Where σ_{kl} is the second rank stress tensor and π_{ijkl} is the fourth rank tensor of piezo-optic coefficients which has 81 elements. Similarly, due to the symmetry of the stress/strain, the tensor can be contracted to a simplified form:

$$\Delta b_i = \sum_{i,j=1}^{6} \pi_{ij}\sigma_j \tag{2.13}$$

Or in a version of strain tensor, ϵ:

$$\Delta b_i = \sum_{i,j=1}^{6} p_{ij}\epsilon_j \tag{2.14}$$

Where p_{ij} is the photoelastic tensor which relates to the piezo-optic tensor by the equation:

$$p_{ij} = \pi_{ij}\, c_{ij} \tag{2.15}$$

Now, the change in the indicatrix tensor can be described:

$$\Delta b_i = b'_i - b_i = \frac{n_i^2 - n_i'^2}{n_i^2 n_i'^2} \cong \frac{(n_i - n_i')(n_i + n_i')}{n_i^4}$$

$$\cong \frac{-\Delta n_i\, 2n_i}{n_i^4} = -\frac{2\Delta n_i}{n_i^3} \tag{2.16}$$

Therefore, the change in refractive index with respect to the applied stress is formulated by combining the equation 2.12 and 2.15:

$$\Delta n_i^{stress} = -\frac{n_i^3}{2}\sum_{i,j=1}^{6} \pi_{ij}\sigma_j \tag{2.17}$$

Here, Lithium Niobate crystalline structure is classified as a trigonal symmetry, point group of 3m, giving the elastic stiffness tensor (c_{ij}) 6x6 matrix which is symmetrical along its diagonal, while the photoelastic (p_{ij}) and piezo-optic (π_{ij}) matrices are described in Fig. 2.5.

The experimental coefficients of elastic stiffness and piezo-optic effect are taken from [18] (as listed in the Table 2.2)

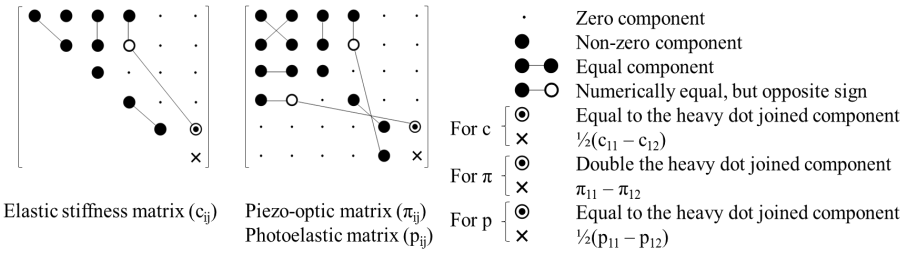

Fig. 2.5. Representation of elastic stiffness, piezo-optic and photoelastic matrices for Lithium Niobate of a trigonal symmetry, class 32, 3m. [15].

Table 2.2: Elastic stiffness, c and piezo-optic, $\boldsymbol{\pi}$ coefficients of Lithium Niobate

Elastic	c_{11}	c_{12}	c_{13}	c_{14}	c_{33}	c_{44}		$\times 10^9$ Nm^{-2}
	205.4	57.2	74	7.9	249	60.9		[18]
Piezo-optic	π_{11}	π_{12}	π_{13}	π_{31}	π_{33}	π_{14}	π_{41}	π_{44}
	-0.43	0.15	0.78	0.5	0.32	-0.8	-0.9	2.0 [18]

2.3. State-of-the art $LiNbO_3$ photonics for mid-IR applications

With the unique properties, $LiNbO_3$ has been used as a host material in a wide range of mid-IR applications. The first SWIFTS-Lippmann interferometer has been implemented for the near and mid-IR operation, by focused ion beam in Lithium Niobate [19]. It gives potential applications in electro-optic modulation of interferogram and high-resolution spectroscopy. Integrated Mach-Zehnder interferometer modulators have been fabricated on silicon-on-Lithium-Niobate platform for operation at a wavelength of 3.39 μm [20]. In this work, large areas of thin, monocrystalline silicon was transferred to bulk $LiNbO_3$ substrates, so as to offer silicon-based platform for exploiting the Pockels or linear electro-optic effect in the mid-IR range. Other report has demonstrated the method to obtain high-contrast mid-IR interferometry using two-stage Mach-Zehnder $LiNbO_3$ waveguides at 3.39 μm wavelength [21]. Integrated-optic inteferometric beam combiners in $LiNbO_3$ have been reported for operation in astronomical L band (3 μm – 4 μm) [22]. The device was desirable for application in stellar interferometry. Other work has been done also for electro-optic beam combiners using active Y junction, operated for double polarization at 3.39 μm wavelength [23]. In the line of astrophotonic devices, 3D three telescopes beam combiners, electro-optic beam combiners and high spectral resolution integrated interferometers have additionally demonstrated [24]. The use of periodically poled Lithium Niobate (PPLN) also provides great opportunities for mid-IR upconversion spectroscopy using a laser frequency comb [25] and mid-IR laser sensor for gas detection [26].

Reference

1. S. C. Abrahams, W. C. Hamilton, and J. M. Reddy, *Ferroelectric Lithium Niobate. 4. Single crystal neutron diffraction study at 24 °C.* Journal of Physics and Chemistry of Solids, 1966. **27**(6): p. 1013-1018.
2. S. C. Abrahams, H. J. Levinstein, and J. M. Reddy, *Ferroelectric Lithium Niobate. 5. Polycrystal X-ray diffraction study between 24 °C and 1200 °C.* Journal of Physics and Chemistry of Solids, 1966. **27**(6): p. 1019-1026.
3. S. C. Abrahams, J. M. Reddy, and J. L. Bernstein, *Ferroelectric Lithium Niobate. 3. Single crystal X-ray diffraction study at 24 °C.* Journal of Physics and Chemistry of Solids, 1966. **27**(6): p. 997-1012.
4. K. Nassau, H. J. Levinstein, and G. M. Loiacono, *Ferroelectric Lithium Niobate. 1. Growth, domain structure, dislocations and etching.* Journal of Physics and Chemistry of Solids, 1966. **27**(6): p. 983-988.
5. K. Nassau, H. J. Levinstein, and G. M. Loiacono, *Ferroelectric Lithium Niobate. 2. Preparation of single domain crystals.* Journal of Physics and Chemistry of Solids, 1966. **27**(6): p. 989-996.
6. A. M. Prokhorov and I. S. Kuz'minov, *Physics and chemistry of crystalline Lithium Niobate*. 1990, Bristol, Angleterre: A. Hilger.
7. Y. S. Kim and R. T. Smith, *Thermal Expansion of Lithium Tantalate and Lithium Niobate Single Crystals.* Journal of Applied Physics, 1969. **40**(11): p. 4637-4641.
8. K. K. Wong, *Properties of Lithium Niobate*. 2002: INSPEC/Institution of Electrical Engineers.
9. M. E. Lines and A. M. Glass, *Principles and Applications of Ferroelectrics and Related Materials*. Oxford Classic Texts in the Physical Sciences. 2001, Oxford: Oxford University Press. 694.
10. R. S. Weis and T. K. Gaylord, *Lithium Niobate: Summary of physical properties and crystal structure.* Applied Physics A, 1985. **37**(4): p. 191-203.
11. T. Volk and M. Wöhlecke, *Lithium Niobate: Defects, Photorefraction and Ferroelectric Switching*. Springer Series in Materials Science. Vol. 115. 2009: Springer-Verlag Berlin Heidelberg.
12. Weis, R. S. and Gaylord, T. K., *Lithium niobate: Summary of physical properties and crystal structure.* Applied Physics A, 1985. **37**(4): p. 191-203.
13. M. Lawrence, *Lithium Niobate integrated optics.* Reports on Progress in Physics, 1993. **56**(3): p. 363.
14. G. Kötitz, *Properties of Lithium Niobate. EMIS datareviews series no. 5. INSPEC, The Institution of Electrical Engineers, London and New York 1989, 364 S., 99 Tab., ISBN 0-85296-482X.* Crystal Research and Technology, 1990. **25**(6): p. 720-720.
15. J. F. Nye, *Physical Properties of Crystals: Their Representation by Tensors and Matrices*. 1985: Clarendon Press.
16. W. Young, R. Budynas, and A. Sadegh, *Roark's Formulas for Stress and Strain, 8th Edition*. 2011: McGraw-Hill Education.
17. T. S. Narasimhamurty, *Photoelastic and electro-optic properties of crystals*. 1981: Plenum Press.
18. Andrushchak, A. S., Mytsyk, B. G., Laba, H. P., Yurkevych, O. V., Solskii, I. M., Kityk, A. V., and Sahraoui, B., *Complete sets of elastic constants and*

photoelastic coefficients of pure and MgO-doped lithium niobate crystals at room temperature. Journal of Applied Physics, 2009. **106**(7): p. 073510.

19. F. Thomas, S. Heidmann, M. de Mengin, N. Courjal, G. Ulliac, A. Morand, P. Benech, E. Le Coarer, and G. Martin, *First Results in Near and Mid IR Lithium Niobate-Based Integrated Optics Interferometer Based on SWIFTS-Lippmann Concept.* Journal of Lightwave Technology, 2014. **32**(22): p. 4338-4344.
20. J. Chiles and S. Fathpour, *Mid-infrared integrated waveguide modulators based on silicon-on-lithium-niobate photonics.* Optica, 2014. **1**(5): p. 350-355.
21. G. Martin, S. Heidmann, J. Y. Rauch, L. Jocou, and N. Courjal, *Electro-optic fringe locking and photometric tuning using a two-stage Mach–Zehnder lithium niobate waveguide for high-contrast mid-infrared interferometry.* Optical Engineering, 2014. **53**(3): p. 034101-034101.
22. H. Hsiao, K. A. Winick, J. D. Monnier, and J. P. Berger, *An infrared integrated optic astronomical beam combiner for stellar interferometry at 3-4 μm.* Optics Express, 2009. **17**(21): p. 18489-18500.
23. S. Heidmann, N. Courjal, and G. Martin, *Double polarization active Y junctions in the L band, based on Ti:$LiNbO_3$ Lithium Niobate waveguides: polarization and contrast performances.* Optics Letters, 2012. **37**(16): p. 3318-3320.
24. G. Martin, J. R. Vázquez de Aldana, A. Rodenas, C. d'Amico, and R. Stoian. *Recent results on photonic devices made by laser writing: 3D 3T near IR waveguides, mid-IR spectrometers and electro-optic beam combiners*. 2016.
25. T. A. Johnson and S. A. Diddams. *Mid-IR Frequency Comb Upconversion Spectroscopy*. in *Conference on Lasers and Electro-Optics 2010*. 2010. San Jose, California: Optical Society of America.
26. T. Töpfer, K. P. Petrov, Y. Mine, D. Jundt, R. F. Curl, and F. K. Tittel, *Room-temperature mid-infrared laser sensor for trace gas detection.* Applied Optics, 1997. **36**(30): p. 8042-8049.

3

3D ultrafast laser writing in $LiNbO_3$

This chapter briefly describes the technique of 3D ultrafast laser writing of optical waveguides in $LiNbO_3$ crystals.

Contents

3.1. Introduction

The conventional approach for microfabricating optical waveguides in $LiNbO_3$ is the use of lithographic techniques such as ion in-diffusion, ion implantation and soft photon exchange [1-3]. However, these techniques are limited to a two-dimensional (2D) layout which does not allow fully exploiting three-dimensional (3D) circuit architectures. The 3D designs would allow for a great improvement in functionality for most of integrated electro-optic devices that involve multi-channel beam combination, particularly in the field of astrophotonics and telecommunications. The emergence of high-reliability industrial-grade ultrafast pulse lasers and the continued development of the 3D direct laser writing technique (from now on, 3DLW) has offered a versatile and efficient tool for the 3D fabrication of complex waveguide structures in solids within short timescales of only minutes or hours [4-6].

An "*ultrafast laser*" is commonly referred to as laser which emits pulses with time durations in the range of tens or hundreds of femtoseconds (fs: 10^{-15} s) to a few picoseconds (ps: 10^{-12} s). Femtosecond ultraviolet excimer lasers were initially used for ablation of polymethylmethacrylate (PMMA) in the late 1980s [7, 8]. Later on, tightly focused fs near-infrared laser pulses were employed to locally modify the refractive index of transparent materials (glass) at Hirao's group [9] and Mazur's group [10] in the mid 1990s. Up until now, 3DLW technique has been increasingly employed to microstructuring photonic devices on many materials and particularly on $LiNbO_3$ crystals [11-17].

When a transparent optical material is exposed to tightly focused ultrafast laser pulses with powers above the modification threshold (typically ~25 $GW.cm^{-2}$) [18], it experiences a non-linear photoionization process, giving rise to a final localised refractive index modification within the focal volume, with dimensions in the order of micrometer to nanometric dimensions depending on the focusing optics and laser writing parameters [6]. Once the material is laser-scanned with high-precision motion stages an arbitrary 3D modified refractive index path can be realised thanks to the highly non-linear photo-modification process which only produces material changes at the peak intensity focal volume coordinates. This solves the problem of the traditional photolithography which is limited to manufacturing surface planar devices. Details on the mechanism and technique of the 3DLW are given in the next sections.

3.2. Three-dimensional direct ultrafast laser writing

3.2.1. Fundamentals of ultrafast laser-material interaction with transparent dielectrics

In this section, we summarise the basics of the 3DLW technique associated light-matter interaction process and the underlying material modification mechanisms, as reviewed from available relevant literature. The internal modification of a dielectric material under exposure to the tightly focused ultrafast pulses is described by the nonlinear laser-material interaction process which can be divided into three fundamental processes: (1) generation of a free electron plasma, (2) energy relaxation, and (3) material modification [6].

(1) Generation of a free electron plasma: conventional absorption caused by long pulsed (longer than nanoseconds) or continuous wave (CW) lasers primarily involves linear single-photon absorption which requires the photon energies to exceed the bandgap energy of the material, resulting in electron excitation from the valence band to the conduction band [19]. Therefore, for these types of laser, light with photon energies smaller than the material bandgap cannot efficiently excite conduction band electrons inside the bulk material [Fig. 3.1(a) and (b)]. Damage occurs from a phase transformation of the dielectric material through the conventional heat deposition. In practice this means that with CW or long pulse lasers, the inscription of highly localised micron or submicron voxels is almost impossible. In other words, 3D laser writing is not feasible. Conversely, at the focus of the ultrafast laser pulse beam, an extremely high density of photons is both spatially and temporally localised, which can excite valence band electrons through the nonlinear absorption of multiple photons [9, 10]. In such case, the interaction of the transparent material with the ultrafast laser pulse only happens at the focal volume where the photon density is sufficient high to trigger the multiphoton absorption; whereas out-of-focus multiphoton absorption is almost zero. This significant advantage allows the ultrafast laser to internally modify the transparent material in a 3D printing fashion [Fig. 3.1(c)].

The nonlinear photo-ionisation consists on multiphoton ionisation and/or tunnelling ionisation mechanisms, depending on the frequency and intensity of the focused laser beam [6, 20, 21]. At low intensity and high frequency, the dominant mechanism is the

multiphoton ionisation as shown in Fig. 3.1(d). In order to bridge the material bandgap the number of incident photons (m) must satisfy: $m \cdot h\nu > E_g$, with h is the Planck constant, ν is the frequency of incident light and E_g is bandgap of the material [6].

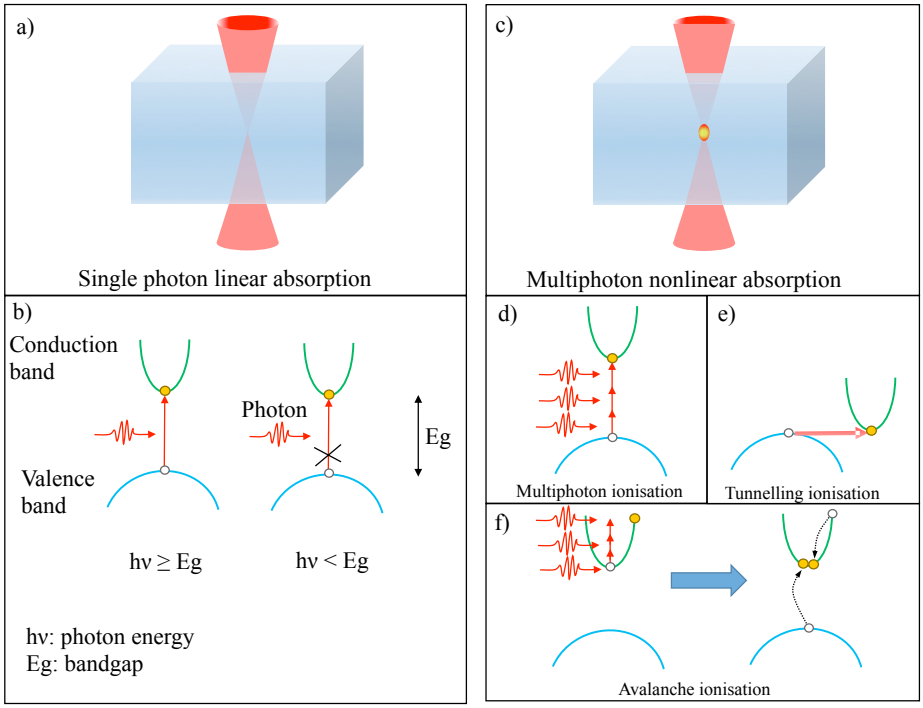

Fig. 3.1. Diagram of linear photon absorption and multiphoton nonlinear absorption produced by focused long pulsed laser and ultrashort laser respectively [6].

Tunnelling ionisation takes place when the laser pulse is at high intensity and low frequency [Fig. 3.1(e)]. At this strong electromagnetic field, the band structure of the material is distorted; resulting a reduction in the gap between the valence band and the conduction band [6]. Here, the direct transition of an excited electron from the valence band to the conduction band takes place through the quantum tunnelling of electrons.

However, there also exists a third fundamental process called avalanche photo-ionization, in which the nonlinearly excited conduction-band electrons are further excited until they gain enough kinetic energy to excite other bound electrons [22]. Since the avalanche ionisation relies linearly on the laser intensity, there is a small dependence between the optical breakdown threshold and the bandgap energy of the material which makes the fs laser microfabrication feasible in a wide range of materials [6].

Formation of plasma at the focal volume occurs once the density of the excited electrons is high enough (~1029 particle/m^3) [23, 24].

(2) Energy relaxation and (3) material modification: Once the free electron plasma is generated through the nonlinear photonionisation and avalanche ionisation, its energy is transferred to the lattice in a timescale of the order of several ps [6]. This results in a permanent modification of the material which is typically recognised by three types of changes [9]: a smooth graded refractive index change (typically at low pulse energy) [25], birefringent refractive index modification (typically at moderate pulse energy) [26-28], and generation of localised amorphization caused by "micro-explosions" (at high pulse energy) [29]. There is a series of factors undergoing the regime of these structural changes; including the laser fabrication variables: e.g. pulse energy, pulse duration, laser repetition rate, incident wavelength, polarisation, scan velocity, focusing optics, and spatiotemporal beam shaping; and properties of the processing material: e.g. bandgap, crystallographic structure, crystal orientation and thermal conductivity.

Within the framework of this thesis, the change in refractive index of a Lithium Niobate crystal induced by given laser fabrication conditions will be the main focus. The locally modified volume of the material as a result of the tightly focused ultrafast pulses produces refractive index changes not only within the focal volume but also at its surrounds, this leads to a wide range of possibilities for writing photonic structures with different properties and optical designs.

3.2.2. The ultrafast laser writing technique

A standard ultrafast laser writing setup is illustrated in Fig. 3.2. The fabrication system involves a laser source with beam control elements and focusing optics. Microscope objectives or aspheric lenses are usually used to tightly focus the collimated beam onto the sample, which is mounted on high resolution motorised stages. By controlling the stages with a programmed script on a computer, the sample can be translated in a 3D configuration resulting in 3D laser-modified microstructures. The beam control/beam shaping elements usually consist of an electro-optic or acoustic optic device for down tuning the repetition rate, a temporal/spatial pulse shaper, a variable attenuator, a waveplate to control the polarization of the beam, and a shutter. In order to real time monitor the laser-material interaction process, a charge coupled device (CCD) camera is

placed above the objective lens to collect images from the sample, usually a reflection image of the process is used, although transmission is also useful or even a phase contrast microscope can be installed to better observe in real time the type of refraction index changes taking place at the focal volume of the writing beam.

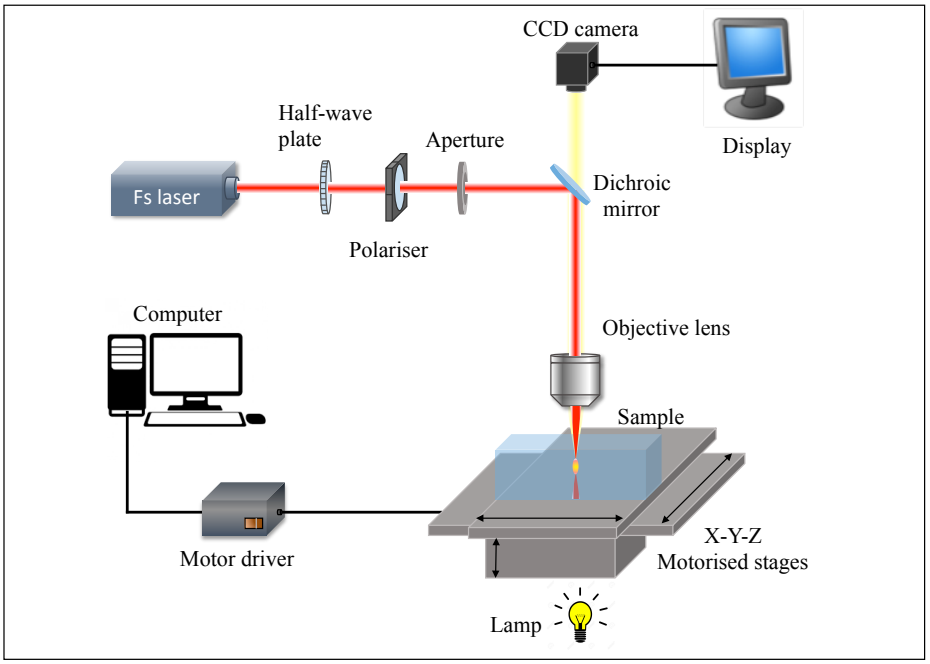

Fig. 3.2. Schematic example of a 3D ultrafast laser writing system.

3.2.2.1. Writing geometry: longitudinal and transversal scan

The standard writing geometry for 3DLW technique is typically divided into two scenarios: (i) transversal and (ii) longitudinal scan [6] (Fig. 3.3). They are defined by the direction with which the sample is moved relative to the propagation direction of the writing beam.

(i) The transversal writing scheme: the sample is scanned transversely/perpendicularly with respect to the direction of the incident laser propagation. This allows fabrication of arbitrary waveguide geometries and lengths. Structures are typically made within a depth range of <1 mm which is more than enough for exploiting 3D photonic designs. However, the main disadvantage of the transversal writing geometry is the asymmetry of the laser-modified profiles in the writing cross-section. This is due to the characteristic difference between the lateral and in-depth focal volume sizes, that is, the elongation of

the Gaussian focus denoted by the aspect ratio between the depth of focus (d_0) and the transversal laser spot size (ω_0) and which is inversely proportional to the focusing numerical aperture (NA): *aspect ratio* = $d_0/\omega_0 \sim n/NA$ [6]. In the specific case of fabrication in $LiNbO_3$ crystals (refractive index at λ=1µm: $n_o \approx 2.2$), using focusing objectives with NA in the range of 0.2 to 0.85, the focal laser volume typically appears with aspect ratio of asymmetry in the range between 10 and 2. The large aspect ratio asymmetry therefore results in an elliptical profile of the laser-modified volume. This asymmetrically elliptical profile is furthermore a strong source of anisotropic stress generated during the laser modification. The resultant effect on waveguide property therefore is the anisotropic guiding performance which is studied and discussed in details in Chapter 5.

To overcome the asymmetry/ elongation of the laser profile, focusing objectives with high NA can be used. This however limits the working distance and the effective depth of modification inside the material. Another approach to reduce the elongation of the modified region is to use beam shaping techniques [30]. A slit shaping technique has been tested on $LiNbO_3$ sample, however, it resulted in complicated behaviours due to the complex anisotropic properties of the crystal. It is therefore not included in this thesis.

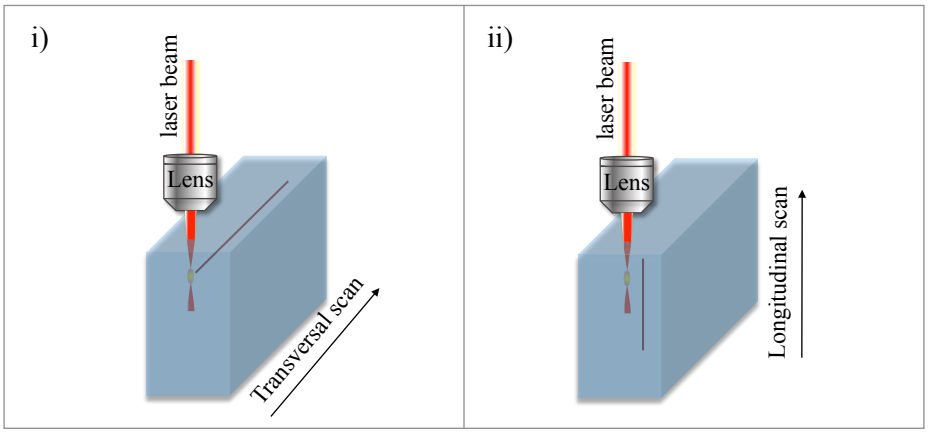

Fig. 3.3. Schematic illustration of the two standard laser writing geometries: (i) transversal writing scheme and (ii) longitudinal writing scheme.

(ii) The longitudinal writing scheme: the sample is scanned parallel to the propagation direction of the incident beam. The advantage of this writing geometry is the potentially symmetric profile of the modification channels, given the focal spot is symmetric. It is

therefore promising for developing waveguides with minimised anisotropic effects. However, the limitation of this approach is the difficulty in fabricating long waveguides with homogeneous properties, due to the limited depth of focus, optical aberrations at different depths, varying absorption levels at different depths, and the required high intensity laser pulses with varying intensity as a function of depth. To minimise these issues, it is essential to choose appropriate focusing objectives, and finely adjust the alignment of the laser beam to sample an translation stages axis, particularly in the case of highly sensitive, birefringent $LiNbO_3$ crystals where minimal changes in focusing conditions results in large changes in the resulting written structures. Further details and results are given in Chapter 7.

3.2.3. Repetition rate – thermal regimes

The pulse repetition rate is a fundamental parameter that allows controlling the thermal regime on which the laser processing is done. The low and high repetition rates are those for which zero or high thermal accumulation occurs between consecutive pulses, and consequently affect the laser modification process to a very high degree [31-33]. The thermal accumulation at the laser focal volume and its surroundings is primarily dependent on the material heat capacity and thermal conductivity, and on the spatial profile of the laser beam. The term *high*-repetition rate within the context of heat accumulation, is therefore used in the case that the time interval between two consecutive pulses is significantly faster than the time it takes for the generated heat to diffuse out of the focal volume. In the case all heat is fully dissipated after each laser pulse and before the next incoming pulse, the laser-writing process is said to be performed under a *low*-repetition rate.

The heat diffusion time denotes the thermal cycle of the material upon exposure to a single laser pulse. The effective cooling time (τ_{eff}) can be approximated from the laser spot size (d_{spot}) and thermal diffusivity (D_{th}) of the material as [34]: $\tau_{eff} = \frac{d_{spot}^2}{D_{th}}$. In the case of $LiNbO_3$, τ_{eff} lies within the range of 0.5 – 100 μs, for focal spot sizes of 1 – 10 μm, respectively. With high repetition rate in the range of 1 MHz and 100 MHz, the time interval between the pulses falls in the range of 1 μs to 10 ns, which are significantly faster than the (τ_{eff}) value. On the other hand, the low repetition rate of 1 kHz results in the time interval of 1 ms, that is much longer than the heat diffusion time (τ_{eff}) of the

$LiNbO_3$ material. Example of the thermal regimes of the low and high repetition rate is visually illustrated in Fig. 3.4.

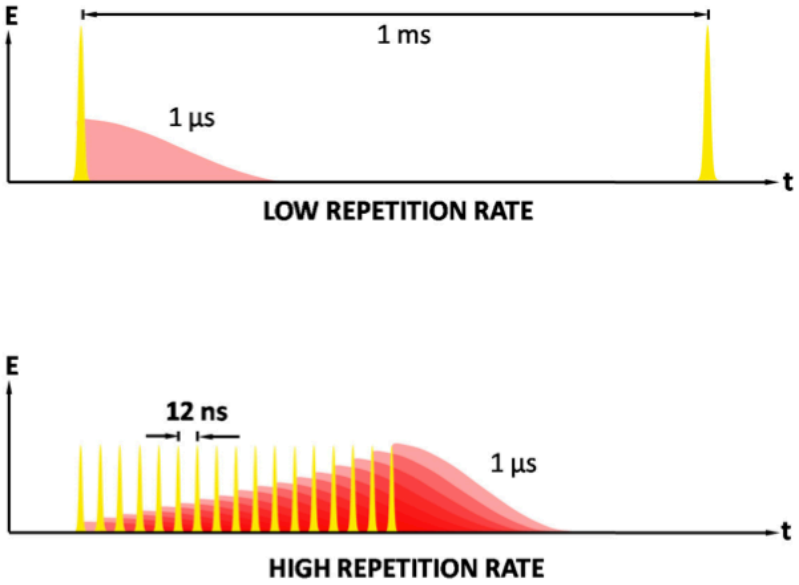

Fig. 3.4. Illustration of thermal regimes in low (1 kHz) and high (1 MHz) repetition rate laser [34].

As a result of using a high repetition rate, the accumulated heat anneals the material within laser focal volume and its surrounds. This effectively reduces level of stress generated during the laser processing as well as the number of lattice defects. However, it was also reported that the use of high repetition rate increases both dimension [31-33, 35] and degree of material changes [33], of the modified volume.

An advantageous thermal regime for certain types of waveguides could be the *critical regime*, $f_{cr}=1/\tau_{eff}$ [33], where thermal accumulation takes place but to a sufficiently small level such that temperatures reached at the focal volume are just high enough to anneal out optical defects and minimise lattice stress, while maintaining the small size features characteristic of the *cold* low-repetition rate regime. From the practical point of view, writing structures around the critical repetition rate would allow the achievement of small features sizes and high index changes while using a high pulse repetition rate which allows for ultrafast fabrication times of just minutes, instead of hours as it is the case for low repetition rates. With the aim of taking advantage of this thermal regime,

CLWs were studied in the intermediate repetition rate of 100 kHz. Details are presented in Chapter 7.

3.3. Laser-written waveguides in Lithium Niobate

3.3.1. Types of refractive index modifications

As previously discussed, the material changes induced by the ultrafast laser pulses inside a transparent material are highly dependent on the laser processing parameters and nature of the target material. In Lithium Niobate, two types of refractive index (RI) modifications (Δn^{local}) have been agreed by researches only attending to the sign of the real part of the index change, $\pm\Delta n^{local}$. It is important to note that only permanent index changes are considered, that is, changes which allow to construct waveguides which can be extensively used for photonic applications for minimal time extensions of one year or so without any change to their guiding properties. Attending to these conditions, two main types of index changes are defined:

(i) Type I modification ($+\Delta n^{local}$) involves a smooth positive refractive index change in the laser-induced volume of the bulk material [Fig. 3.5(a)]. In this case the low energy pulse is deposited in the focal volume resulting a low damage level. This weak damage renders a RI increase in the affected volume. It has been noticed that the change occurs only to the extraordinary index, whereas the ordinary index of $LiNbO_3$ remains unchanged or slightly decreased [11, 12]. The origin of this extraordinary index increase is supposedly referred to a main mechanism: creation of lattice defects at the focal region that reduce the spontaneous polarisation of the $LiNbO_3$ crystal [12]. Other mechanisms such as the photorefractive effect or changes in chemical composition due to ions diffusion have also been considered, however no clear conclusions were demonstrated [12]. In this configuration waveguides are formed in the positive refractive index region which is defined to be within the focal volume and not on its surrounding. This type of modification regime therefore allows to write step-index or graded-index optical waveguides, which feature similar properties to those of standard optical fibers.

(ii) Type II modification ($-\Delta n^{local}$) involves negative changes in both indices of refraction at the focal volume. This level of damage is achieved by using higher laser intensities than in the case of Type I index changes, and therefore collateral affects in the surroundings of the focal volume are always present. The main collateral effect is the

appearance of piezo-optic induced RI changes surrounding the Type II laser-damaged region, which are known to be induced by the stress fields surrounding modified volumes [Fig. 3.5(b)].

Within the lattice defect model, as a result of the high energy laser pulse the $LiNbO_3$ crystal experiences a strong disorder in its crystallographic structure, leading to a volume increase. As the first approximation, this increase in the volume/ decrease in the density corresponds to the refractive index decrease as described in the Clausius-Mosotti equation [12]:

$$\frac{n^2-1}{n^2+1}=\frac{\alpha_M}{V_M} \tag{3.1}$$

where α_M is the molar polarizability of the material and V_M is the volume change. At the same time a stress field is built up in the surrounding material where the piezo-optic effect governs the index changes [33]. In this Thesis, the built-up stress field is numerically studied using a thermal expansion model (discussed in the next chapter).

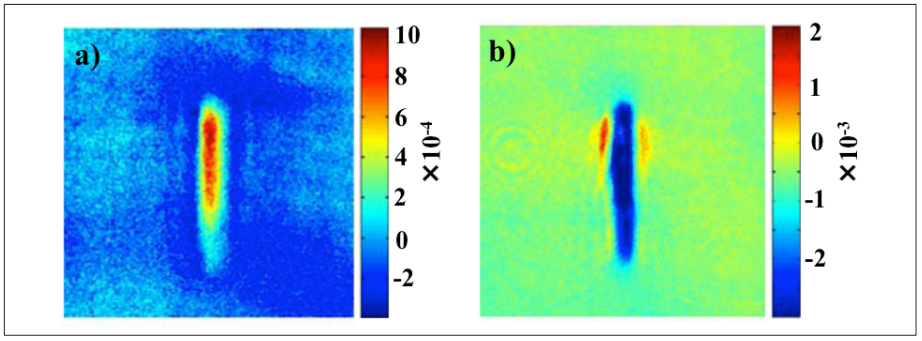

Fig. 3.5. Refractive index modification in Lithium Niobate x-cut sample using a fixed pulse energy of 0.2 μJ: a) Type I modification (increased refractive index at the focal volume) produced by 220fs pulse, and b) Type II modification (negative refractive index change at the focused volume and piezo-optic index change at the sides) produced by 1.1ps pulse. (figure taken from Burghoff *et al*. [12]).

3.3.2. Types of laser written optical waveguides

Depending on the types of modifications (Type I or Type II), different types of waveguides can be designed. 3DLW optical waveguides are generally classified into three configurations:

(i) Step-index or graded-index waveguides: the light guidance is confined in the positive RI laser-radiated volume (the written track). As shown in Fig. 3.7(a), the RI

increased region is typically produced by translating the $LiNbO_3$ material with low energy fs-laser fluence, or sometimes by multi-scanning of the laser beam for enhancement of index contrast or for the design of rectangular core shapes. This increased region acts as a waveguide core for light propagation [Fig. 3.7(b)]. Due to the advantage of the direct laser-written guiding-structures, the type I waveguide is suitable for passive devices such as beam splitters/combiners with Y-junctions and directional light couplers [6, 36, 37]. However, in this configuration the index modification only occurs to the extraordinary index of $LiNbO_3$ (up until present experimental reports), therefore the waveguide supports only the corresponding polarised light. The limit to one polarisation does not allow its application in phase-matched frequency conversion where 2D light guidance is required, unless a periodically poled PPLN crystal is used. Additionally, this type of waveguide is not completely stable and can disappear after a certain life time of various years depending on writing conditions, and can be removed under thermal treatment at 423 K or more for a few hours; which is therefore not advantageous for high-power applications [37].

(ii) Double-track stress-induced waveguide: associated with the type II modification, this type of waveguide typically involves a pair of negative laser- induced RI tracks which confines light in between where the positive stress-optic index changes take place. This stress-induced region results from the volume expansion of the irradiated zone caused by a strong energy fs-laser pulse. The fabrication of these type of waveguides in rare earth ions doped $LiNbO_3$ crystals were studied for the first time in by Ródenas *et al*. [33]. Combining micro-spectroscopic analysis with beam guiding characterizations, it was shown how lattice defects and stress fields can be imaged, explaining the guiding mechanism, as shown in Fig. 3.6. The combination of compressive stress adjacent to the laser-damaged tracks produces a homogenously increased RI volume which is described under the piezo-optic effect. Light is therefore well guided within this region [see Fig. 3.6(c)].

There are some advantageous features of this type of waveguide geometry over the type I step-index waveguide configuration: (1) Since the waveguide core is not directly affected by the laser irradiation, some properties of the bulk crystal might be well preserved; which are crucial for many applications [38, 39]. (2) Controlling of the RI changes is more straightforward than the type I, and the insight mechanism is well

established with recent data available in a wide range of materials [37]. (3) Light guidance for both orthogonal polarisations is possible, though there is still a big variation in the two modes depending on the material properties [37]. (4) The written structures are more stable against time and thermal annealing, allowing for the development of stable and robust photonic devices.

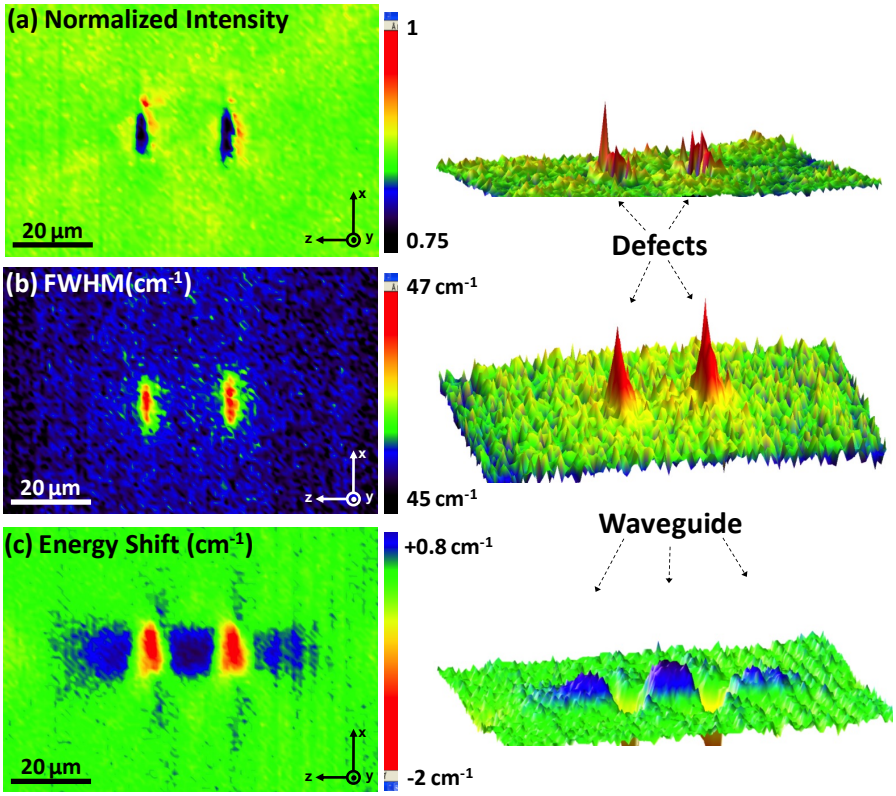

Fig. 3.6. Micro-spectroscopic study of Type II modifications and Stress-optic double-track Nd^{3+}:$LiNbO_3$ waveguides, taken from Ródenas *et al*. [33]. Spatial distribution of the intensity (a), FWHM (b), and energy shift (c) of the main luminescence peak within the non-polarised $^4F_{3/2} \rightarrow {}^4I_{9/2}$ emission band of Nd^{3+} ions, located at around 11114 cm^{-1}. Three-dimensional plots are also shown, which allow visualizing the magnitude of spectral changes relative to the noise level in the measurements.

There are also some disadvantages when compared to Type I step-index waveguides: (1) in order to guide light damage tracks must be inscribed, which inevitably results in propagation losses due to scattering of light from the Type II tracks. In order to avoid it, these tracks can be further separated, but this also collaterally diminishes the induced stress-field and therefore the mode becomes less confined, which is again detrimental to

avoid scattering losses; (2) due to the weak index changes that can be achieved by means of stress-optic index changes these type of waveguide do not allow for tight bends and therefore are not a good option to design 3D waveguide circuit architectures, as it is the case for step-index waveguides based on the Type I index change. The application of these types of waveguides is therefore restricted to straight waveguides designs; (3) lastly, due to the weak confinement of these waveguides, guiding within the mid-infrared regime could not be reported with this type of waveguides so far. In order to design waveguides capable of sustaining mid-infrared light propagation for both polarization, a third type of waveguide design is therefore needed, which is the one developed within this Thesis: cladding waveguides.

(iii) Cladding waveguide (so-called depressed-index cladding waveguide, from now on CLW): It is built on the basis of the type II index modification mechanism, however, instead of having only two tracks the cladding waveguide is constructed by numerous tracks forming a cladding layer around an un-modified core which can guide light in the form of leaky modes [40].

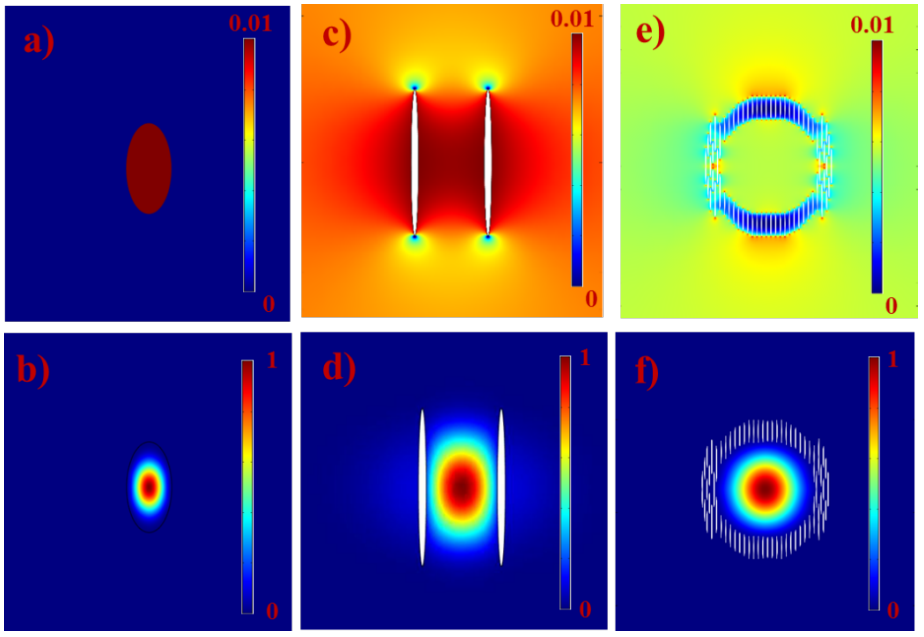

Fig. 3.7. Three configurations of 3DLW optical waveguides, simulated by means of FEM software. Top layer shows the index profiles, and bottom layer shows the near-field mode distributions: (a)-(b) an idealised step-index waveguide (Type I modification type); (c)-(d) a Type II double-track stress-optic waveguide; and (e)-(f) a cladding waveguide where both stress-optic index changes and Type II modifications at tracks occur.

The Fig. 3.7(e) and (f) depicts an example of the cladding waveguide in which formation of low-index laser-induced tracks as well as the piezo-optic RI change make a well-confined circular barrier for light propagation inside. Different cross-sectional shapes of waveguide geometry can be created by arranging the tracks with desirable order. Practically, circular geometry is more favourable due to its suitability for light coupling from objective lens or optic fibres. The spatial thickness and size of the cladding structure together with magnitude of the negative RI change in the cladding are the fundamental properties of this type of waveguide determining its performance. Compared to the type II configuration, the depressed cladding waveguide has a better control over the un-modified core where the unique properties of the $LiNbO_3$ crystal are well preserved. The other advantage of the cladding guiding geometry is its ability of having 2D guidance in the cross-section. However, in Lithium Niobate there is a huge challenge to obtain identical light guidance in both orthogonal polarisations due to its anisotropic nature of refractive index changes in the laser-written tracks and asymmetrically induced stress-optic fields at the surrounds.

3.4. Design approaches to mid-infrared waveguides in Lithium Niobate

Using the standard double-track stress-optic waveguiding approach, the longest operating wavelength in a 3D laser written waveguide in Lithium Niobate crystal was limited to around 1 μm, reported by Burghoff *et al*. [13]. With the emergence of the laser-inscribed cladding waveguide regime, Kroesen *et al*. recently succeeded in obtaining wave guidance in $LiNbO_3$ at the near-IR at 1.55 μm, demonstrating its better waveguiding performance (in terms of propagation losses and waveguide anisotropy) over the dual-track approach [14]. However, the development of low propagation loss (~0.5 dB/cm) laser-written $LiNbO_3$ CLWs for the mid-IR range is strongly limited by the reported difficulty of achieving propagation losses below 3 dB/cm at wavelengths longer than ~3 μm. The first report on $LiNbO_3$ mid-infrared CLWs was with insertion losses of ~5 dB for a single mode CLW of 1 cm long and characterised at 4 μm wavelength [15]. Apart from the experimental works, a numerical calculation of confinement loss on $LiNbO_3$ crystal was systematically performed, showing that guiding of 3.5 μm light is achievable with the lowest propagation loss of 1 dB/cm theoretically [16]. However, these theoretical works did not take into account the inherent stress-optic index fields that crucially influence the waveguiding behaviour of this type of laser-

fabricated CLWs [17, 34, 41, 42]. It has been observed that the $LiNbO_3$ CLW experiences a strong anisotropic behaviour resulted from the complex asymmetric stress fields built up at the side of the laser-irradiated tracks. This is one of the most difficult challenges that needs to be tackled and whose solution requires a deeper understanding of the real refractive index changes that occur at the mid-IR range. Successful achievement of low-loss single-mode mid-infrared waveguiding on $LiNbO_3$ operated for both orthogonal polarisation would bring a real deal to development of true high performance devices such as stellar interferometry [43-45], and on-chip modulation [46].

Reference

1. D. Jaque, E. Cantelar, and G. Lifante, *Lattice micro-modifications induced by Zn diffusion in Nd:$LiNbO_3$ channel waveguides probed by Nd^{3+} confocal micro-luminescence.* Applied Physics B, 2007. **88**(2): p. 201-204.
2. D. Castaldini, P. Bassi, S. Tascu, P. Aschieri, M. P. De Micheli, and P. Baldi, *Soft-Proton-Exchange Tapers for Low Insertion-Loss $LiNbO_3$ Devices.* Journal of Lightwave Technology, 2007. **25**(6): p. 1588-1593.
3. G. B. Montanari, P. De Nicola, S. Sugliani, A. Menin, A. Parini, A. Nubile, G. Bellanca, M. Chiarini, M. Bianconi, and G. G. Bentini, *Step-index optical waveguide produced by multi-step ion implantation in LiNbO3.* Optics Express, 2012. **20**(4): p. 4444-4453.
4. S. Juodkazis, V. Mizeikis, and H. Misawa, *Three-dimensional microfabrication of materials by femtosecond lasers for photonics applications.* Journal of Applied Physics, 2009. **106**(5): p. 051101.
5. S. Nolte, S., M. Will, M., J. Burghoff, J., and A. Tuennermann, *Femtosecond waveguide writing: a new avenue to three-dimensional integrated optics.* Applied Physics A, 2003. **77**(1): p. 109-111.
6. R. Osellame, G. Cerullo, and R. Ramponi, *Femtosecond Laser Micromachining: Photonic and Microfluidic Devices in Transparent Materials*. 2012: Springer Berlin Heidelberg.
7. R. Srinivasan, E. Sutcliffe, and B. Braren, *Ablation and etching of polymethylmethacrylate by very short (160 fs) ultraviolet (308 nm) laser pulses.* Applied Physics Letters, 1987. **51**(16): p. 1285-1287.
8. S. Küper and M. Stuke, *Femtosecond uv excimer laser ablation.* Applied Physics B, 1987. **44**(4): p. 199-204.
9. K. Davis, K. Miura, N. Sugimoto, and K. Hirao, *Writing waveguides in glass with a femtosecond laser.* Opt. Lett., 1996. **21**: p. 1729-1731.
10. E. N. Glezer, M. Milosavljevic, L. Huang, R. J. Finlay, T. H. Her, J. P. Callan, and E. Mazur, *Three-dimensional optical storage inside transparentmaterials.* Optics Letters, 1996. **21**(24): p. 2023-2025.
11. J. Burghoff, H. Hartung, S. Nolte, and A. Tünnermann, *Structural properties of femtosecond laser-induced modifications in $LiNbO_3$.* Applied Physics A, 2007. **86**(2): p. 165-170.
12. J. Burghoff, S. Nolte, and A. Tünnermann, *Origins of waveguiding in femtosecond laser-structured $LiNbO_3$.* Applied Physics A, 2007. **89**(1): p. 127-132.
13. J. Burghoff, C. Grebing, S. Nolte, and A. Tünnermann, *Efficient frequency doubling in femtosecond laser-written waveguides in lithium niobate.* Applied Physics Letters, 2006. **89**(8): p. 081108.
14. S. Kroesen, W. Horn, J. Imbrock, and C. Denz, *Electro–optical tunable waveguide embedded multiscan Bragg gratings in lithium niobate by direct femtosecond laser writing.* Optics Express, 2014. **22**(19): p. 23339-23348.
15. R. He, Q. An, Y. Jia, G. R. Castillo-Vega, J. R. Vázquez de Aldana, and F. Chen, *Femtosecond laser micromachining of lithium niobate depressed cladding waveguides.* Optical Materials Express, 2013. **3**(9): p. 1378-1384.
16. H. Karakuzu, M. Dubov, S. Boscolo, L. A. Melnikov, and Y. A. Mazhirina, *Optimisation of microstructured waveguides in z-cut $LiNbO_3$ crystals.* Optical Materials Express, 2014. **4**(3): p. 541-552.

17. A. Ródenas, L. M. Maestro, M. O. Ramírez, G. A. Torchia, L. Roso, F. Chen, and D. Jaque, *Anisotropic lattice changes in femtosecond laser inscribed Nd^{3+}:MgO:$LiNbO_3$ optical waveguides.* Journal of Applied Physics, 2009. **106**(1): p. 013110.
18. H. Li, F. Zhou, X. Zhang, and W. Ji, *Bound electronic Kerr effect and self-focusing induced damage in second-harmonic-generation crystals.* Optics Communications, 1997. **144**(1): p. 75-81.
19. D. S. Bradshaw and D. L. Andrews, *Laser-modified one- and two-photon absorption: Expanding the scope of optical nonlinearity.* Physical Review A, 2013. **88**(3): p. 033807.
20. B. C. Stuart, M. D. Feit, S. Herman, A. M. Rubenchik, B. W. Shore, and M. D. Perry, *Nanosecond-to-femtosecond laser-induced breakdown in dielectrics.* Physical Review B, 1996. **53**(4): p. 1749-1761.
21. Chris, B. S., Andr, C. B., and Eric, M., *Laser-induced breakdown and damage in bulk transparent materials induced by tightly focused femtosecond laser pulses.* Measurement Science and Technology, 2001. **12**(11): p. 1784.
22. R. R. Gattass and E. Mazur, *Femtosecond laser micromachining in transparent materials.* Nat Photon, 2008. **2**(4): p. 219-225.
23. N. Bloembergen, *Laser-induced electric breakdown in solids.* IEEE Journal of Quantum Electronics, 1974. **10**(3): p. 375-386.
24. B. C. Stuart, M. D. Feit, A. M. Rubenchik, B. W. Shore, and M. D. Perry, *Laser-Induced Damage in Dielectrics with Nanosecond to Subpicosecond Pulses.* Physical Review Letters, 1995. **74**(12): p. 2248-2251.
25. K. Miura, J. Qiu, H. Inouye, and T. Mitsuyu, *Photowritten optical waveguides in various glasses with ultrashort pulse laser.* Applied Physics Letters, 1997. **71**(23): p. 3329-3331.
26. L Sudrie, M Franco, B Prade, and A Mysyrowicz, *Writing of permanent birefringent microlayers in bulk fused silica with femtosecond laser pulses.* Optics Communications, 1999. **171**(4b).
27. Y. Shimotsuma, P. G. Kazansky, J. Qiu, and K. Hirao, *Self-Organized Nanogratings in Glass Irradiated by Ultrashort Light Pulses.* Physical Review Letters, 2003. **91**(24): p. 247405.
28. C. Hnatovsky and R. S. Taylor, *Pulse duration dependence of femtosecond-laser-fabricated nanogratings in fused silica.* Applied Physics Letters, 2005. **87**(1): p. 014104.
29. S. Juodkazis, K. Nishimura, S. Tanaka, H. Misawa, E. G. Gamaly, B. Luther-Davies, L. Hallo, P. Nicolai, and V. T. Tikhonchuk, *Laser-Induced Microexplosion Confined in the Bulk of a Sapphire Crystal: Evidence of Multimegabar Pressures.* Physical Review Letters, 2006. **96**(16): p. 166101.
30. R. Osellame, S. Taccheo, M. Marangoni, R. Ramponi, P. Laporta, D. Polli, S. De Silvestri, and G. Cerullo, *Femtosecond writing of active optical waveguides with astigmatically shaped beams.* Journal of the Optical Society of America B, 2003. **20**(7): p. 1559-1567.
31. C. B. Schaffer, A. Brodeur, J. F. Garcia, and E. Mazur, *Micromachining bulk glass by use of femtosecond laser pulses with nanojoule energy.* Opt. Lett., 2001. **26**(2): p. 93-95.
32. R. Osellame, N. Chiodo, V. Maselli, A. Yin, M. Zavelani-Rossi, G. Cerullo, P. Laporta, L. Aiello, S. De Nicola, P. Ferraro, Finizio, A., and G. Pierattini,

Optical properties of waveguides written by a 26 MHz stretched cavity Ti:sapphire femtosecond oscillator. Opt. Express, 2005. **13**(2): p. 612-620.

33. L. Shah, A. Y. Arai, S. M. Eaton, and P. R. Herman, *Waveguide writing in fused silica with a femtosecond fiber laser at 522 nm and 1 MHz repetition rate* Opt. Express, 2005. **13**(6): p. 1999-2006.
34. A. Rodenas, *Direct femtosecond laser writing of 3D photonic structures in rare-earth doped lithium niobate*. 2009, Universidad Autónoma de Madrid.
35. S. Nolte , M. Will , J. Burghoff, and A. Tünnermann, *Ultrafast laser processing: New options for three-dimensional photonic structures.* Journal of Modern Optics, 2004. **51**(16): p. 2533-2542.
36. G. Marshall, A. Politi, J. Matthews, P. Dekker, M. Ams, M. Withford, and J. O'Brien, *Laser written waveguide photonic quantum circuits.* Opt. Express, 2009. **17**: p. 12546-12554.
37. F. Chen and J. R. Vázquez. de Aldana, *Optical waveguides in crystalline dielectric materials produced by femtosecond-laser micromachining.* Laser & Photonics Reviews, 2014. **8**(2): p. 251-275.
38. A. Rodenas, G. A. Torchia, G. Lifante, E. Cantelar, J. Lamela, F. Jaque, L. Roso, and D. Jaque, *Refractive index change mechanisms in femtosecond laser written ceramic Nd:YAG waveguides: micro-spectroscopy experiments and beam propagation calculations.* Applied Physics B, 2009. **95**(1): p. 85-96.
39. C. Zhang, N. Dong, J. Yang, F. Chen, J. R. Vazquez de Aldana, and Q. Lu, *Channel waveguide lasers in Nd:GGG crystals fabricated by femtosecond laser inscription.* Optics Express, 2011. **19**(13): p. 12503-12508.
40. J. Hu and C. R. Menyuk, *Understanding leaky modes: slab waveguide revisited.* Advances in Optics and Photonics, 2009. **1**(1): p. 58-106.
41. A. Ródenas, G. A. Torchia, G. Lifante, E. Cantelar, J. Lamela, F. Jaque, L. Roso, and D. Jaque, *Refractive index change mechanisms in femtosecond laser written ceramic Nd:YAG waveguides: micro-spectroscopy experiments and beam propagation calculations.* Applied Physics B, 2009. **95**(1): p. 85-96.
42. B. McMillen and Y. Bellouard, *On the anisotropy of stress-distribution induced in glasses and crystals by non-ablative femtosecond laser exposure.* Optics Express, 2015. **23**(1): p. 86-100.
43. H. Hsiao, K. A. Winick, and J. D. Monnier. *A Mid-Infrared Integrated Optic Astronomical Beam Combiner for Stellar Interferometry*. in *Frontiers in Optics 2009/Laser Science XXV/Fall 2009 OSA Optics & Photonics Technical Digest*. 2009. San Jose, California: Optical Society of America.
44. F. Thomas, S. Heidmann, M. de Mengin, N. Courjal, G. Ulliac, A. Morand, P. Benech, E. Le Coarer, and G. Martin, *First Results in Near and Mid IR Lithium Niobate-Based Integrated Optics Interferometer Based on SWIFTS-Lippmann Concept.* Journal of Lightwave Technology, 2014. **32**(22): p. 3736-3742.
45. G. Martin, S. Heidmann, J. Y. Rauch, L. Jocou, and N. Courjal, *Electro-optic fringe locking and photometric tuning using a two-stage Mach–Zehnder lithium niobate waveguide for high-contrast mid-infrared interferometry.* Optical Engineering, 2014. **53**(3): p. 034101-034101.
46. J. Chiles and S. Fathpour. *On-Chip Modulation in the Mid-Infrared with Silicon-on-Lithium-Niobate Photonics*. in *CLEO: 2015*. 2015. San Jose, California: Optical Society of America.

4

Waveguides preparation and optical characterization

This chapter describes the experimental techniques that were used to characterise the laser-written sample chips and the used methodology for measuring the passive optical performance of single waveguides.

Contents

4.1. Introduction

This chapter introduces all the techniques which were used for obtaining the results presented throughout this thesis. It briefly describes the preparation process, structural characterisation, and the mid-IR waveguiding characterisation of the waveguides. Among the techniques, bright-field optical transmission microscopy and confocal reflection microscopy were used in parallel for characterising overall structures of the laser-written tracks. Phase contrast microscopy was used to characterise individual tracks with contrast enhanced images with respect to standard bright-field transmission imaging. Environmental scanning electron microscopy (ESEM) in both Secondary Electrons (SE) and Back-Scattered detection (BSD) modes, and atomic force microscopy (AFM), were used to obtain high resolution images of single laser-written tracks without the need to deposit metallic coatings on the samples, and hence precisely measure observable surface material or topological changes with nanometric resolution.

With regard to the passive optical waveguiding characterisation of the waveguides, an optical setup for free-space in- and out-coupling of laser radiation into the waveguides and for the IR imaging of the out-put near-field waveguide's output modes, was built for the mid-IR range, around 3.394 μm and 3.680 μm with a HeNe laser and a diode ICL laser, respectively. Polarizing linear filters were also used in order to characterise each orthogonal mode. Measurement of the propagation losses was carried out by measuring the waveguide insertion loss, and estimating the Fresnel and Coupling losses (CL) so as to obtain the total propagation losses by subtraction to the total IL. The calculation of the CL involves analysing the near-field intensity spatial distribution of the output waveguide modes, and calculating its overlap integral with the free space optical focal spots.

4.2. Sample preparation

The work in this thesis involves the use of commercial $LiNbO_3$ crystals (Altechna). The samples were polished at high quality optical grade before laser processing. Typically, the 3D laser-written (3DLW) Cladding Waveguides (CLWs) are not continuous up to the sample facets, due to the sample surface border aperturing of the femtosecond laser beam at the top surface, implying that the waveguides cannot be written up to the very sample facets inside it. The distance from the CLW facets to the sample surface is

usually of around a 100 μm, depending on the focusing depth and the focusing numerical aperture. For this reason, a second polishing process was always carried out to make sure that the CLW facets are present on the sample surface. A cutting process also required to reveal deeply buried structures in the case of samples fabricated by longitudinal writing scenario.

4.3. Microscopic characterisation

This section introduces the techniques used to characterise the laser-modified μ-structures inside $LiNbO_3$ samples. These techniques are only able to provide qualitative information, but also quantitative results of the modified CLW structures can be obtained by means of approximations by a model described in Chapter 5.

4.3.1. Optical transmission microscopy

Laser-written embedded microstructures inside $LiNbO_3$ crystals can be qualitatively characterised by means of transmitted light microscopy, as a means for the fast assessment of the spatial extension and degree of damage of those. In this thesis, most of the bright-field transmission images were routinely taken using a Leica DM2500 microscope, shown in Figure 4.1.

In the sample, as a result of the laser-induce refractive index (RI) changes along long straight or curved regions produce a diffraction image which resembles well the local RI modifications in the visible range [see Fig. 4.1 inset]. Collectively, the imaged patterns have bright or dark shapes depending the type of the laser-modification, but also on the type of illumination which is performed, either in Koehler illumination configuration or with a tightly condenser apertured beam. Due to this, the best way to systematically compare different types of fabricated structures such as waveguides, is by performing bright-field imaging on the same conditions always. In the case that Type I modifications are present, since the modified volume has a RI increase it can act as a waveguide therefore producing a brighter image given the right focusing and illumination conditions are achieved. On the contrary, in the case of Type II modifications, features are rather seen as dark regions were light is not transmitted due to the decrease of RI and to their highly scattering properties [example in Fig. 4.1. inset]. This optical characterisation only provides qualitative information on the laser-written features within the visible range, but it greatly serves a a fast tool for the assessment of

the type of fabricated microstructures. In order to obtain quantitative estimations of the RI changes within the IR range, more complex experiments need to be done, as it will be explained in the next sections as well as by modelling, as introduced in Chapter 5.

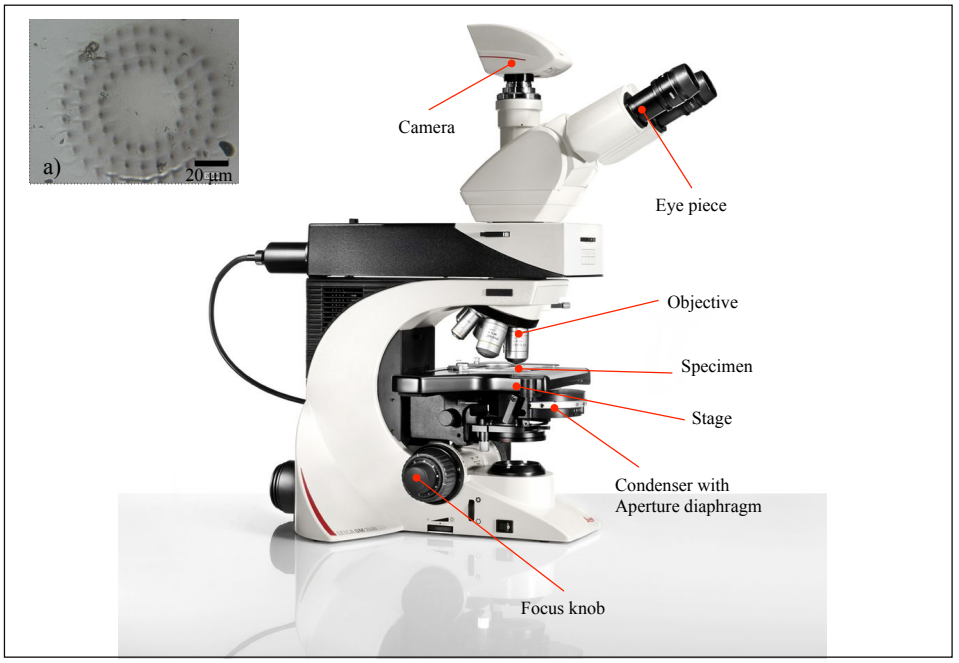

Fig. 4.1. Schematic of optical transmission Leica DM2500 microscope and an image example of a type II laser-written circular cladding waveguide structure (inset a).

4.3.2. Phase contrast microscopy

The addition of phase-contrast optical components to the standard bright-field microscope is employed as a technique to obtain contrast-enhanced images of the laser-written microstructures in the $LiNbO_3$ transparent samples. A phase contrast microscope was available in one of the used 3DLW setups, so that the laser modification process could be observed in real time. Fig. 4.2 shows a cut-away diagram of an upright phase contrast microscope, together with a schematic illustration of the optical train.

In this system, the microstructures termed as a phase object diffract and shift in phase the incident light waves. The phase shift/ contrast can be transformed into amplitude differences that are easily visualised in the eyepieces. The modern phase contrast microscope enables samples containing small internal modified features to be detected and imaged with enhanced contrast by means of post-acquisition image processing.

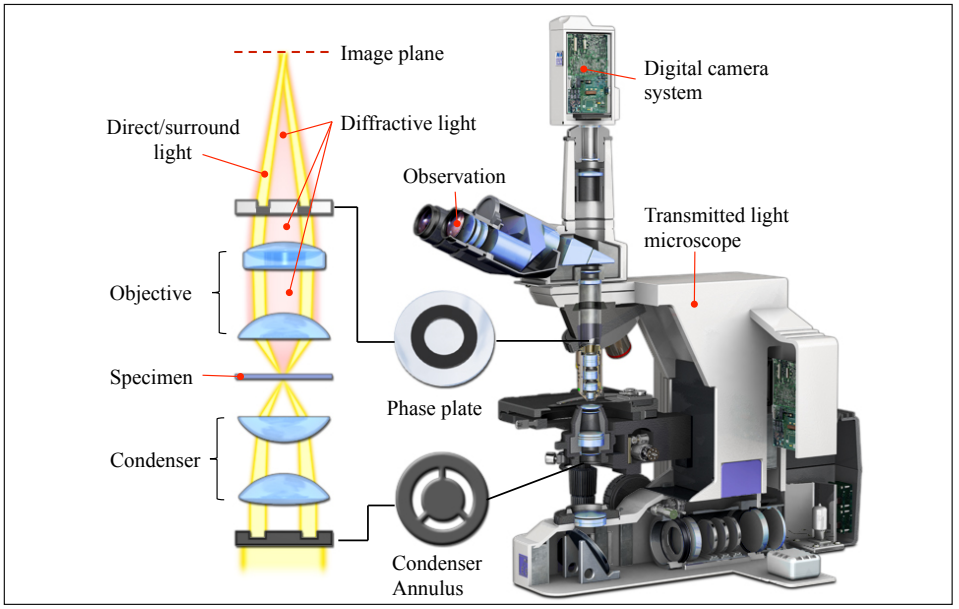

Fig. 4.2: Cut-away diagram of a phase contrast microscope and illustration of the optical train.

The phase-contrast imaging scheme is also illustrated in Fig. 4.3. Partially coherent illumination is collected through a collector lens and focused on a specialised annulus which is placed at the front focal plane of a condenser. The specimen therefore can be illuminated by defocused/ parallel light waves emanating from the transparent annular ring. Upon passing through the specimen/ phase object, the incident wavefront that is present in the illuminating beam is divided into two following components. (1) The primary component is an un-deviated/un-diffracted planar wavefront, referred to as surround light (S-wave), which passes through and around the specimen without interacting with it. (2) The second component is a deviated/diffracted spherical wavefront, referred to as diffracted light (D-wave) which is scattered and retarded in phase by phase gradients present in the specimen/ the RI modified structures. After leaving the specimen plane, the surround and diffracted lights are collected by the objective and subsequently segregated by a phase plate. The diffracted light crosses a thicker part of the phase plate, resulting a shift in phase compared to the surround light. Ultimately, a phase contrast image is formed at the intermediate image plane upon interference of the two wavefronts. The resultant wave is typically referred to as the particle wave (P-wave), which is mathematically described as P = S+D. Contrast of the

phase contrast image depends on the relative difference in intensity/ amplitudes between the particle (P) and surround (S) waves, which allows to be visualised in the eyepieces.

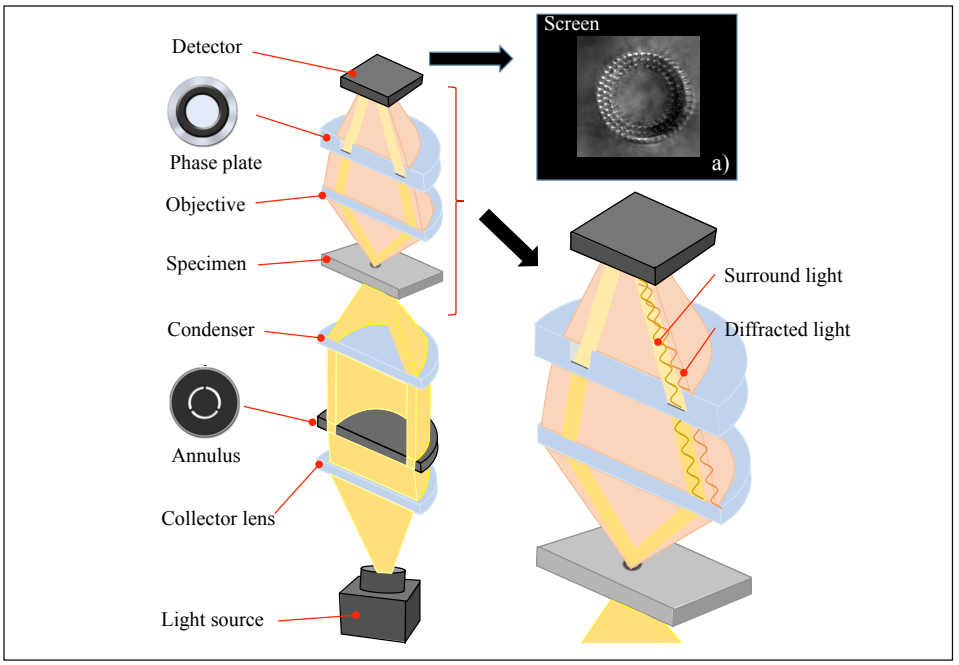

Fig. 4.3. Schematic illustration of phase contrast imaging in a typical phase contrast microscope. Inset (a) is the phase contrast image of a Type II laser-modified structure.

In the phase contrast microscopy, the phase shift (δ) which is the difference in location of an emergent wavefront between the phase object and its surrounding medium, is of paramount importance for quantifying the phase object [1]. The phase shift directly relates to the change in optical path length (Δ_{OPL}) of waves passing through the phase object, denoting as $\delta = 2\pi\Delta_{OPL}/\lambda$. In classical optics, the change in optical path length (Δ_{OPL}) is a product of the difference in RI (Δn) and thickness (Δt) of the object with respect to its background: $\Delta_{OPL} = \Delta n \times \Delta t$. Since the thickness of the entire sample is constant in this case, the argument remains only the RI change or RI contrast (Δn).

Specifically, the $LiNbO_3$ sample consists of RI modified structures in which the RI contrast is denoted by $\Delta n = n_1 - n_0$, with n_1 is the local RI of singe features, and n_0 is the RI of the surrounding bulk material. When coherent light passes through the features, the wave is either increased or decreased in its velocity proportionally to the RI contrast. In the case of the Type I modification, the local RI of the features is greater than the RI of the surrounding bulk material ($\Delta n>0$), the wave is reduced in its velocity while

passing through the features and retarded in its relative phase. Therefore, the features appear in a darker shape than their background. In contrast, the Type II modification results in a decrease of RI contrast ($\Delta n<0$), the wave is advanced in phase upon exiting the features and therefore images appear brighter features as illustrated in Fig. 4.4. inset (a). The phase contrast images can be further enhanced by image post-processing in ImageJ software.

4.3.3. Confocal reflection microscopy

The laser-written waveguides were inspected by confocal reflection microscopy for their surface quality which is a crucial factor determining the effectiveness of external light coupling. Surface topography of the samples is characterised by confocal imaging in a Sensofar PLμ 2300 confocal microscope. Fig. 4.4 illustrates the confocal reflection system, in which images are formed by collecting reflected beams from the illuminated sample surface through a magnifying objective.

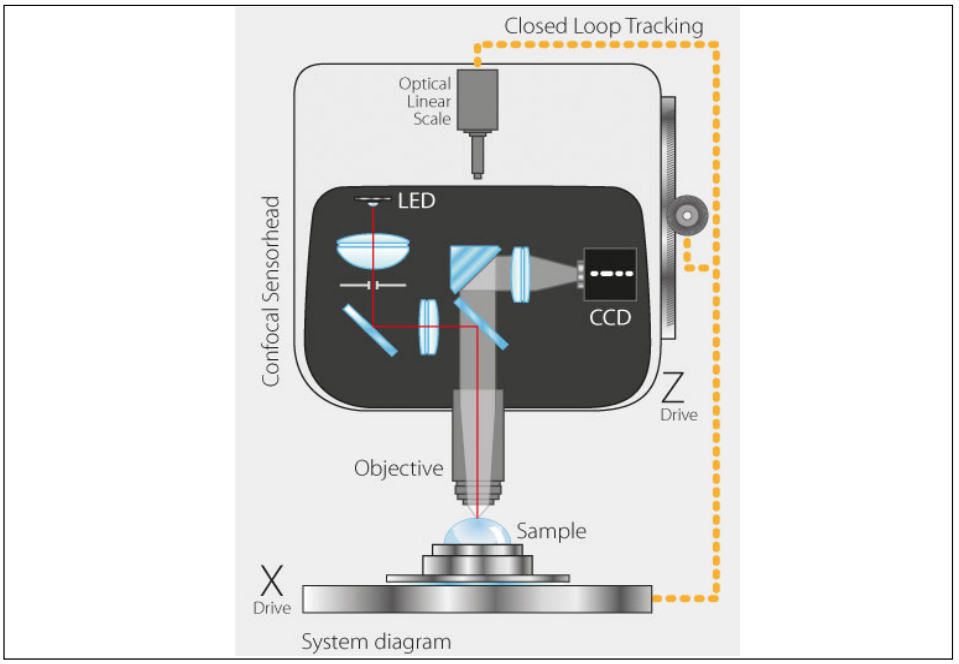

Fig. 4.4. Diagram of the Sensofar® confocal reflection microscope.

Due to the topography, each beam arrives at the surface of the sample in different points located at different heights. The plane that is perpendicular to the beam and contains the surface of the sample is called the focal plane. Thus, as the beam arrives to the sample,

numerous focal planes are formed. Every focal plane reflects the light which again crosses the objective lens and the dichroic mirror until it reaches the detector pinhole. Those rays coming from different focal planes, that are focused just before the detector pinhole are called the in-focus light rays (i.e. confocal). Thus only the in-focus light rays can pass through the pinhole before reaching the detector [2]. The sample is scanned vertically (z-direction) in steps so that every point on the surface passes through the focus.

4.3.4. Environmental scanning electron microscopy

Environmental scanning electron microscope (ESEM) was chosen to characterise the CLWs due to its capability of studying in detail the microstructures in the non-conductive $LiNbO_3$ sample without prior sample preparation such as conductive coating. In the ESEM system, interaction of electrons extracted from an electron column with atoms in the sample results in a variety of signals [Fig. 4.5 (a)]. By scanning the focused electron beam on the sample surface, signals are collected to construct images which contain quantitative and qualitative information of the sample morphology as well as composition [3].

As the incident electrons penetrate into the sample, they excite atoms from the sample. The excited atoms emit different types of electrons which are monitored by detectors [Fig. 4.5 (b)]. Two fundamental groups of electrons are typically observed, including secondary electrons and backscattered electrons [3]. The number of these electrons depends on the angle between the incident electron beam and the sample surface, the distance to their detectors, as well as the properties of the sample material.

(i) Secondary electrons (SEs): are the electrons that have been directly ejected from the sample atoms upon interactions with the primary electrons of the incident beam. These SE usually have very low energy, and therefore mainly escape from a shallow region at the sample surface. As a result, the SEs offer high resolution imaging of the sample topography.

(ii) Backscattered electrons (BSEs): are primarily the incident electrons that have been scattered back out of the sample after elastic collisions with nuclei of the sample atoms. The BSEs have much higher energy than the SEs, therefore result in information from a

deep region inside the sample. The number of BSEs depends on not only the angle of the incident electrons, but also composition and density of the sample.

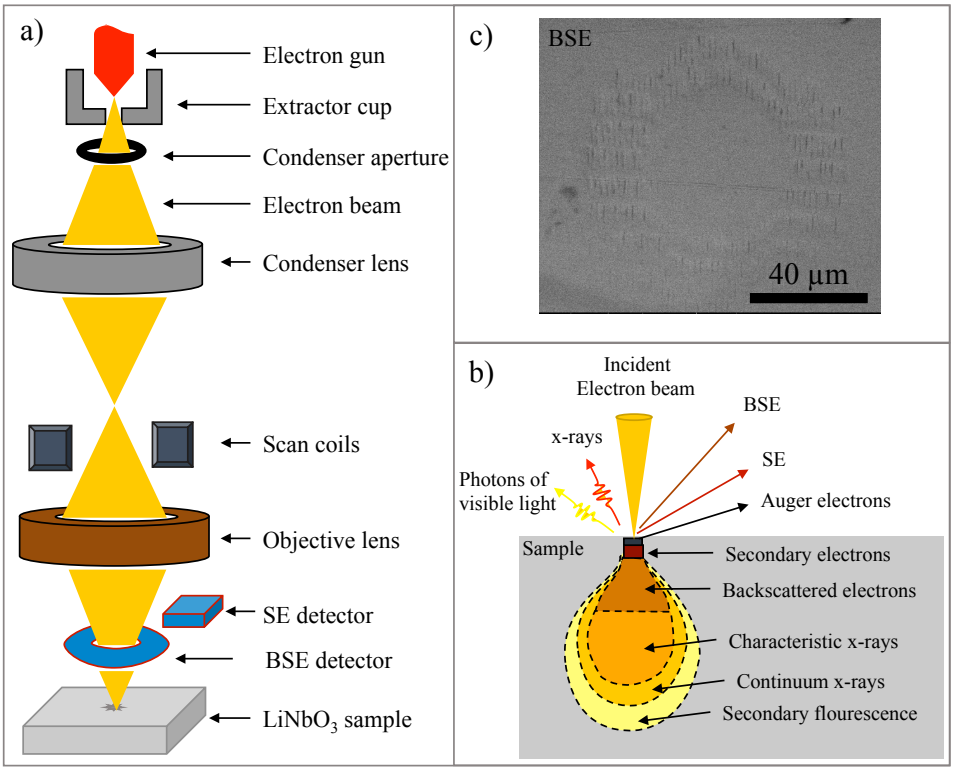

Fig. 4.5. Schematic illustration of a simplified SEM system (a), observation of electron emissions (b) and an example of backscattered electron image of a laser-written CLW structure (c).

Since the $LiNbO_3$ sample is not conductive, the ESEM measurement was usually performed at low vacuum and high voltage to reduce the charging. Features of the RI structures in the sample are collectively imaged by both secondary electron and backscattered electron modes. The measurement was done on an ESEM - FEI Quanta 600. Fig. 4.5 (c) shows an example of BSE image of the CLW structure fabricated by 3D direct laser writing.

4.3.5. Atomic force microscopy

For measuring real dimensions of single laser-modified features in $LiNbO_3$ sample with high resolution, the work involves the use of the atomic force microscope (AFM), which is one type of the scanning probe microscopy (SPM) instruments. It allows to visualise topographic objects of nano-scale dimensions with extremely high resolution.

The mechanism of the AFM is entirely different from the optical microscopes and other characterisation instruments including the scanning electron microscope. In the AFM system, a sharp nano-scaled tip on a cantilever is used to raster-scan across the sample surface [4]. The interaction of the tip with the sample surface induces a deflection of the cantilever. The deflected action is recorded by a laser beam which is focused on the backside of the cantilever [Fig. 4.6]. Images are collectively formed by the recorded laser signal in response to the surface topography of the sample. A 3D AFM image of etched tracks on the $LiNbO_3$ sample is demonstrated in Fig. 4.6. inset (a).

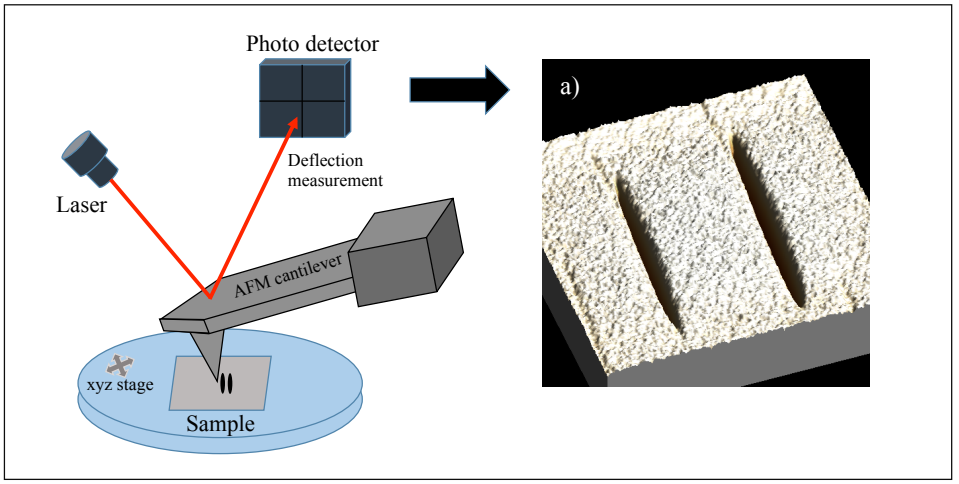

Fig. 4.6. Schematic illustration of AFM characterisation, and an example of 3D image taken from an etched $LiNbO_3$ sample (inset a).

Since the AFM only provide information of the sample surface, the $LiNbO_3$ sample is etched with nitric acid solution with 20 % concentration at room temperature to selectively reveal the laser-modified microstructures in a topographic form. The etching was processed for 30 s which was believed to be enough for tens of nanometter depth revelation of the laser-modified structures. Longer time might over etch the unmodified region, hence might result in no accuracy for measuring the laser-written structures. More details of the etch rate were reported in the reference and therein [5]. The etched sample was raster-scanned in a square area of 80 µm. The characterisation was carried out by a Keysight 5500 AFM microscope.

4.4. Optical guiding characterisation

The section introduces the methodology for quantifying the passive mid-infrared optical performance of the laser-fabricated CLWs. It involves experimental techniques and data post-processing methods for obtaining characteristic guided modes and loss values of the waveguides.

4.4.1. Output mode near-field intensity

Mid-IR guiding properties of CLWs were characterised using a laboratory optical setup as illustrated in Fig. 4.7. The setup involves a linearly polarised interband cascade laser - ICL (Nanoplus) emitting at the wavelength of 3680 nm and with a mounted collimating output lens. Two mirrors were arranged in different heights and at different vertical planes, so that the collimated laser beam was delivered with almost linear polarization of 45^{o} with respect to the two horizontal and vertical axes, this allowed the excitation of the two orthogonal polarization components of the waveguides propagation modes: the "horizontal" (i.e. quasi-TE, from now on simply TE) and "vertical" (i.e. quasi-TM, from now on TM) polarization components, by means of using a linear polariser before the waveguide input lens. Since the waveguides typically have a non-zero birefringence, in order to select the polarization of the waveguides output modes an analyser (linear polariser) was also used after the output coupling lens before detecting elements. In this way strict propagation losses could be measured for each given orthogonal polarization components, and the polarised output modes could also be imaged. The sample was mounted on a micro-positioning Thorlabs stage with 4-axis manual microcontrollers. Input light was typically launched into the waveguide by an aspheric lens with 0.18 NA. Additionally, a pinhole was placed before the input lens so as to finely adjust the beam diameter and optimise the input coupling spot size into waveguides minimizing input coupling losses so as to obtain overall better propagation loss calculations (as explained in the following). The images of the near-field waveguide's modes were obtained by using an out-coupling aspheric lens with 0.64 NA and a FLIR SC700 mid-IR camera. To calibrate the camera field of view (FOV) and evaluate the resolution, a calibration target (R1DS1P - Positive 1951 USAF Test Target, Ø1") was used.

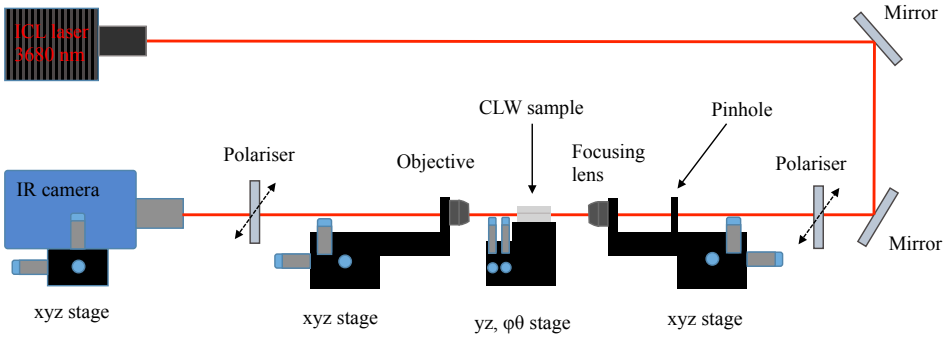

Fig. 4.7. Schematic illustration of the optical guiding setup for characterisation of CLWs at the mid-IR wavelength.

Output near-field intensity images of the waveguides were stored in a digital matrix form, so that the waveguide's output mode field diameters (MFDs) at $1/e^2$ intensity, and their losses could be calculated, as explained in the next section.

4.4.2. Calculation of the waveguide mode size

All waveguides in this thesis were designed to have approximately circular waveguiding cores, so that their guided modes had intensity profiles closely resembling Gaussian ones. This allows to use first order mathematical approximations for the case of Gaussian fields, such as for calculating overlap integrals. The size of these modes therefore can be calculated using the common expression from fiber technology, of the mode field diameters (MFDs). By definition, the MFD of a single guided mode waveguide is the diameter at which the power density is reduced to $1/e^2$ of its maximum value. Here, the power density is proportional to the square of the electric and magnetic field strengths which are extracted from the digital images.

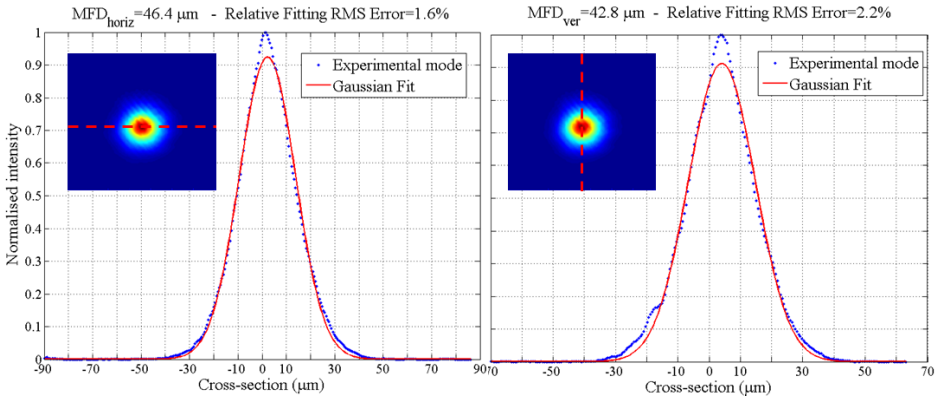

Fig. 4.6. Example of a Gaussian fitting of near-field intensity vertical and horizontal cross-sections of the TE mode of a CLW characterised at the mid-IR at 3.68 µm wavelength.

For a close approximation of the MFDs, the Gaussian function (Eq 4.1) [6] was used to fit with the experimental data.

$$I(x) = I_0 e^{-\frac{(x-a)^2}{2\sigma^2}} \tag{4.1}$$

Where, I_0 is the maximum power intensity which is the height of the curve's peak, a is the central position of the peak, x is the cross-sectional spatial variable and σ is the standard deviation of the function, which can be referred to as the Gaussian root mean square (RMS) width.

The MFDs therefore can be calculated from the standard deviation:

$$\text{MFD} = 4\,\sigma \tag{4.2}$$

Fig. 4.6 shows an example of the vertical and horizontal cross-sections Gaussian fit results for the near-field TE polarised (i.e. horizontally polarised) mode of a 50 um diameter core CLW. Both horizontal and vertical cross-sections were well fitted in the Gaussian function with low RMS fitting error of ~2%.

4.4.3. Measurement of the waveguide's propagation losses (PLs)

The passive optical performance of the waveguides was determined by measuring their propagation losses (PLs). Throughout this thesis, the PLs of the CLWs were characterised by an indirect method which involves measuring the waveguide's insertion losses (ILs). The ILs are defined by the losses resulted from insertion of the waveguiding element in a light transmission channel. Therefore, the experimental measurement of the ILs is a straightforward procedure done by taking the logarithm of the output power (P_{out}) of the waveguide over the input power (P_{in}) of the incident beam:

$$IL = -10 \cdot log_{10}\left(\frac{P_{out}}{P_{in}}\right) \tag{4.3}$$

The total value of the ILs must be the results of different loss processes, including the coupling losses (CLs) between the external beam and the waveguide, the reflection losses (Fresnel losses, FLs) at both input and output end-faces of the waveguide, and the inner propagation losses (PL) of the waveguide [7]. Therefore the following relationship holds for these different types of losses:

$$\text{IL} = \text{CL} + \text{FL} + \text{PL} \tag{4.4}$$

The coupling loss (CL): the input coupling efficiency between the input laser beam and a given waveguide, was always optimised by the use of appropriate input focusing lens with low numerical aperture (NA), and with the fine adjustment of a pinhole so as to further tailor the input spot size to match as best as possible th waveguide's fundamental mode. CLs can be calculated by 2D overlap integral of the waveguide mode and the input beam as described in the simplified formula [8]:

$$CL = -10 \cdot log_{10}\left(4\frac{E_i(x,y)^2 \times E_w(x,y)^2}{[E_i(x,y)^2 + E_w(x,y)^2]^2}\right) \quad (4.5)$$

where $E_i(x,y)$ is the electric field of the input beam and $E_w(x,y)$ is the fundamental mode field of the waveguide. It should be noted that the output coupling from the waveguide to an imaging objective was assumed to be zero since we use high NA lenses which fully capture all the waveguide's output cone of light.

The Fresnel loss (FL): Occur when the input beam is coupled to the waveguide, the beam is partly reflected back. This loss from the reflection is called Fresnel loss which is caused by a step change in the refractive index at both interfaces between the waveguide material and air or output medium [9]. The Fresnel loss is given in the formula following:

$$FL = -10 \cdot log_{10}\left(\frac{4n_L n_A}{(n_L n_A)^2}\right)^2 \quad (4.6)$$

Where n_L and n_A are the refractive indices of $LiNbO_3$ and air, respectively. For the case of ordinary refractive index at wavelength of 3680 nm:

$$FL_o = -10log\left(\frac{4 \cdot 2.1309 \cdot 1}{(2.1309 \cdot 1)^2}\right)^2 = 1.214\ dB \quad (4.7)$$

For the case of extraordinary refractive index at wavelength of 3680 nm:

$$FL_e = -10log\left(\frac{4 \cdot 2.07 \cdot 1}{(2.07 \cdot 1)^2}\right)^2 = 1.125\ dB \quad (4.8)$$

Propagation loss (PL): The PLs of waveguides, which originate due to absorption or scattering within the channel waveguide, can be finally calculated by subtracting the CLs and the FLs to the measured total ILs:

$$PL = IL - CL - FL \quad (4.9)$$

Reference

1. D. B. Murphy and M. W. Davidson, *Fundamentals of Light Microscopy and Electronic Imaging*. 2012: Wiley.
2. B. R. Masters, *Confocal Microscopy and Multiphoton Excitation Microscopy: The Genesis of Live Cell Imaging*. 2006: SPIE Press.
3. L. Reimer, *Scanning Electron Microscopy: Physics of Image Formation and Microanalysis*. 1998: Springer-Verlag Berlin Heidelberg.
4. G. Haugstad, *Atomic Force Microscopy: Understanding Basic Modes and Advanced Applications*. 2012: John Wiley & Sons, Inc.
5. H. Bhugra and G. Piazza, *Piezoelectric MEMS Resonators*. 2017: Springer International Publishing.
6. W. S. C. Chang, *Principles of Lasers and Optics*. 2005: Cambridge University Press.
7. R. C. Alferness, T. Tamir, W. K. Burns, J. F. Donelly, I. P. Kaminow, H. Kogelnik, F. J. Leonberger, A. F. Milton, T. Tamir, and R. S. Tucker, *Guided-Wave Optoelectronics*. 2013: Springer Berlin Heidelberg.
8. R. G. Hunsperger, *Integrated Optics: Theory and Technology*. 2009: Springer New York.
9. M. Weik, *Fiber Optics Standard Dictionary*. 1997: Springer US.

5

Modelling of mid-IR $LiNbO_3$ cladding waveguides

This chapter describes the use of numerical simulation models for estimation of full RI profiles of mid-IR cladding waveguides in $LiNbO_3$. The realistic estimation of the RI profiles helps better understanding of guiding behaviours and development of high performance waveguides.

Contents

5.1. Introduction

Mid-IR CLWs typically involve microfabrication of structures containing tens or hundreds of low-index tracks in a large area (~50 μm scale) [1-3]. As the nature of the type II modification, each single track experiences not only the depressed-RI changes within the laser-exposed volume ($-\Delta n^{local}$), but also the anisotropic stress-induced RI changes (Δn^{stress}) at its surrounds [discussed in chapter3]. Due to the high complexity of the laser-written structures, optical properties of the CLWs are usually difficult to predict, particularly at the mid-IR wavelengths. Up to date, most of the experimental reports on CLWs is based on trial and error methodologies [1-9] which are time consuming and not reliable. In this thesis, a comprehensive simulation model is built, taking into account both the depressed-RI changes and the anisotropic stress fields, which are essential for developing high performance mid-IR cladding waveguides, and reliable laser manufacturing of photonic circuits [10-14].

Shown in Fig. 5.1 is algorithm of the modelling process which is described through five main steps:

(1) An initial CLW structure is fabricated with respect to a certain laser writing condition. The CLW is subsequently characterised to obtain structural information of the laser-modified features, and its guiding performance including propagation losses and diameter of near-field guided modes.

(2) The structural data of the CLW is used to build a computational domain/geometry for the finite element method (FEM) simulation in which complex RI fields of the laser-modified features/ elliptical tracks ($-\Delta n^{local}$) and the surrounding stress-optic fields (Δn^{stress}) are quantitatively computed.

(3) An initial assumption is made for the values of depressed-RI changes ($-\Delta n^{local}$) to perform the first computational mode study. Results from the FEM simulation contain theoretical information of PLs and MFDs of the guided CLW.

(4) Matching of the computed with the experimental values of PLs and MFDs is carried out through iterative process, by adjusting the Δn^{local} assumption. A final approximation of the Δn^{local} values is reached when the computed PLs and MFDs are well fitted with the experimentally obtained values.

Once all the proposed parameters have been fulfilled, waveguides are re-designed, following low-loss single mode criteria for both orthogonal horizontally (TE) and vertically (TM) polarised lights.

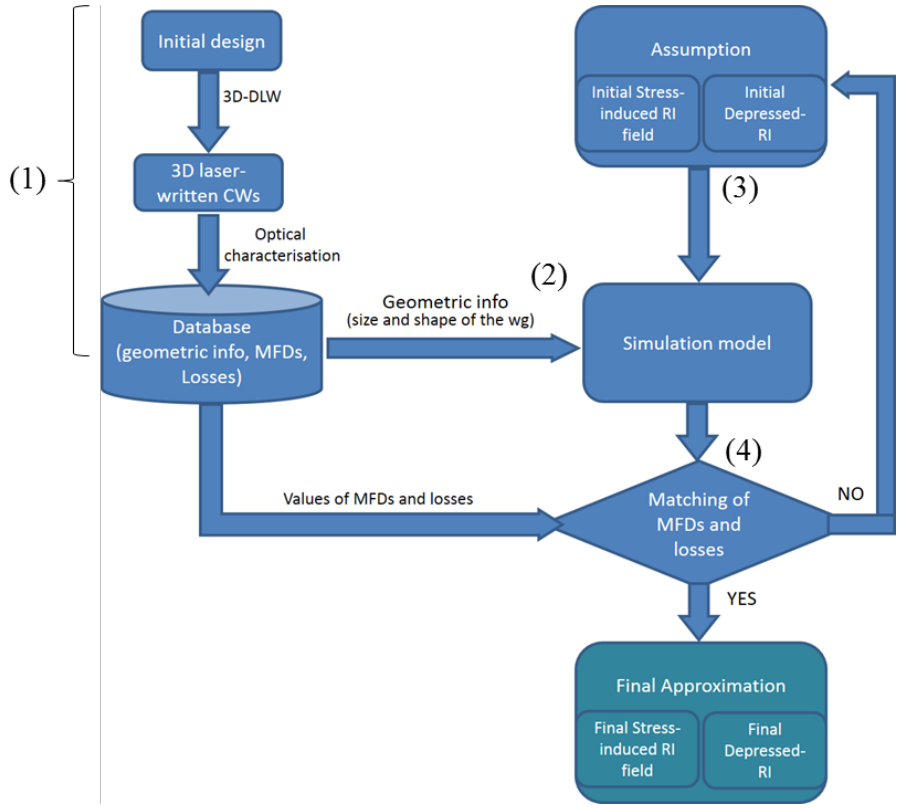

Fig. 5.1. Algorithm of the mode-matching modelling process using FEM simulation.

Furthermore, another separate set of simulation model based on finite difference beam propagation method (FD-BPM), is used to simulate light propagation of the optimised CLWs and further confirm the mode guiding results. In this FD-BPM model, the full RI profiles of CLWs are taken from the FEM model to perform propagation simulation of straight, s-bend CLWs and also directional splitters [results described in chapter 6].

5.2. Numerical modelling techniques

In the first model, the FEM simulation is performed by the commercial COMSOL Multiphysics® software. The technique allows solving partial differential equations in both solid mechanics and electromagnetic waves problems.

In the second model, the FD-BPM simulation is carried out by BeamPROP software which is a part of the RSoft Photonic Component Design Suite®. The computational simulation is solved for light propagation of waveguiding structures.

5.2.1. The finite element method (FEM) based simulation

5.2.1.1. Simulation of anisotropically induced stress fields

It is well accepted that the tight focusing of intense ultrafast laser pulses inside $LiNbO_3$ leads to a localised distortion of the crystal, resulting in a micrometric expansion of the modified volume whose shape resembles the Gaussian laser focus ellipsoid [15, 16]. Therefore, this local volume change induces an anisotropic stress field at its surrounds.

Supposing that the laser-written structures are homogeneous along the writing direction, the simulation of these stress-induced effects can be simplified to 2D cross-sectional geometry, as first reported by M. Will *et al.* in crystalline quartz [17]. Here, the 2D thermal expansion model is used to qualitatively predict the volume expansion of the laser-written region and stress generated at the surrounds. In this simulation model, it is assumed that the volume expansion is mainly due to the elastic distortion [15]. The simulation is governed by the Duhamel-Hooke's law [Eq. (5.01)] which reflects the relation between the strain (ε), stress (σ), tensors and temperature difference (ΔT) in the linear thermal expansion model [18].

$$\sigma_{ij} = \sigma_0 + C_{ijkl} : (\varepsilon_{kl} - \varepsilon_0 - \alpha_{kl}\Delta T) \tag{5.01}$$

Where C_{ijkl} is the fourth order elasticity tensor, ":" stands for the double-dot tensor product, σ_0 and ε_0 are initial stress and strain, $\Delta T = T - T_0$, is the temperature change parameter controlling the volume expansion ($\Delta V/V$), and α_{kl} is the second order linear thermal expansion tensor. As described in chapter 2: section 2.2.4, the elasticity tensor can be completely represented by a known symmetric 6x6 matrix [19], and the linear thermal expansion coefficients are taken from [20]. For the case of the strain tensor, it can be written in terms of the point displacement gradient ∇u :

$$\varepsilon = \frac{1}{2}(\nabla u + \nabla u^T) \tag{5.02}$$

or in form of components as: $$\varepsilon_{mn} = \frac{1}{2}\left(\frac{\partial u_m}{\partial u_n} + \frac{\partial u_n}{\partial u_m}\right) \tag{5.03}$$

In this model, the total computational domain is created with a circular shape; which is convenient for the use of boundary conditions (perfectly matched layers –PMLs) which will be introduced later. The size of the computational domain was chosen to be 600 μm diameter; which is large enough to not only cover the entire structure of the typical cladding waveguide (< 300 μm), but also have room to apply the PMLs which can efficiently minimise non-real solutions. A fixed constraint is set at an outer boundary of this entire domain, and a displacement constraint is assigned to the laser-written domains where the expansion starts. The temperature difference (ΔT) is used as a primary control parameter that can be adjusted to match the simulated results with the experimental data, for example a pair of laser-written tracks whose stress field has been experimentally studied [12, 15].

This simulation strongly relies on the shape of the modified volume which, as mentioned in chapter 3, varies depending on the parameters of laser writing system (pulse duration, energy, repetition rate, and focusing optics, among others), as well as the crystal composition and the crystallographic orientation. For this, the fabricated structures should be microscopically characterised to obtain their geometrical dimensions which are used in the simulation model. Throughout this model, the modified volume is assumed to have ideal elliptical shapes.

5.2.1.2. Calculation of the complex refractive index profiles

Under exposure to the ultrafast laser beam, the $LiNbO_3$ material experiences RI changes not only inside the exposed volume (Δn^{local}), but also at its surround (Δn^{stress}). Therefore, the complete RI profile (Δn) is combination of Δn^{local} and Δn^{stress} which are both considered in the followings.

(1) Δn^{stress}: Assuming that the stress field is the only responsible mechanism that produces RI changes at the surrounds of the laser-inscribed tracks, the stress-induced RI change can be readily calculated by the piezo-optic effect, the equation 2.15 is recalled from chapter 2, section 2.2.4.

$$\Delta n_i^{stress} = -\frac{n_i^3}{2}\sum_{i,j=1}^{6}\pi_{ij}\sigma_j \tag{5.04}$$

Specifically, the Δn^{stress} of $LiNbO_3$ in our case is calculated by the following formula:

$$\Delta n_x^{stress} = -\frac{no^3}{2}\left(\pi_{11}\sigma_x + \pi_{12}\sigma_y + \pi_{13}\sigma_z\right) \quad (5.05)$$

$$\Delta n_y^{stress} = -\frac{no^3}{2}\left(\pi_{21}\sigma_x + \pi_{22}\sigma_y + \pi_{23}\sigma_z\right) \quad (5.06)$$

$$\Delta n_z^{stress} = -\frac{ne^3}{2}\left(\pi_{31}\sigma_x + \pi_{32}\sigma_y + \pi_{33}\sigma_z\right) \quad (5.07)$$

Where the values of the piezo-optic (π_{ij}) matrix are taken from [19]. The components of the induced stress (σ_j) are derived from the thermal expansion model that is computed beforehand.

(2) Δn^{local}: Within the laser-modified volume, in $LiNbO_3$ a decrease of RI is reportedly associated with a reduction in density caused by the crystalline lattice damage and amorphization [12, 15], as mentioned in chapter 3. The magnitude of the RI decrease primarily correlates to the volume increase though the Clausius-Mosotti equation [15] and was estimated within a range of 0.001 to 0.01 for the visible light [12, 15], both with ordinary and extraordinary RI. However, the exact number of these values is still a subject of research, due to the fact that the physical processes in which the $LiNbO_3$ lattice undergoes when exposed to different types of tightly focused ultrafast laser pulse are not fully understood. Additionally, there is a lack of available techniques capable of directly measuring the RI values of medium-high index materials with a sub-μm spatial resolution, as it is the case in the type of laser written structures which are analysing in this thesis. Furthermore, the RI change values measured at the visible, near-IR, or mid-IR wavelength ranges would be significantly different since these wavelengths involve fundamentally different resonance effects, such as direct bandgap absorption in the UV-visible, absorptions by optical defects, lattice defect, and phonon absorptions in the mid-IR.

For these reasons, the simulation model is built to predict the RI changes of the laser-written waveguide structures at the mid-IR range relying on input experimental data measured at the desired device working wavelength (typically 3.68 μm within this thesis work) so as to obtain a realistic modelling within the spectral region of interest. The initial RI changes given by the model first iteration are therefore used as input variables that later are refined in an iterative process so as to match experimental waveguiding characterization results (propagation losses-PLs and/or mode field diameters-MFDs).

These RI changes at the laser-modified tracks (Δn^{local}) combine with the stress-induced RI fields at the surrounds (Δn^{stress}) to form highly spatially varying RI profiles of the whole waveguide structures which can then be further used for analysis of waveguiding properties (described in the next section).

5.2.1.3. FEM simulation of near field waveguide mode

For analysis of the waveguiding modes, the electromagnetic waves model using frequency domain was studied under the wave equation for electric field vector E [21, 22]:

$$\nabla\times(\mu_r^{-1}\nabla\times E) - k_0^2\left(\varepsilon_r - \frac{j\sigma}{\omega\varepsilon_0}\right)E = 0 \tag{5.08}$$

Where k_0 is the wave number of free space which is defined as:

$$k_0 = \omega\sqrt{\varepsilon_0\mu_0} = \frac{\omega}{c_0} \tag{5.09}$$

Here the parameters: μ_0 and ε_0 are the permeability and the permittivity of vacuum. μ_r and ε_r are the permeability and the permittivity of the material, ω is angular frequency, c_0 is speed of light in vacuum and σ is the electrical conductivity.

When using refractive index $n^2 = \varepsilon_r$ with the assumption that $\mu_r = 1$ and σ = 0, the equation (5.08) can alternatively be written as:

$$\nabla\times(\nabla\times E) - k_0^2 n^2 E = 0 \tag{5.10}$$

In mode analysis, this equation is solved for the propagation constant β. The time-harmonic representation of the electric fields includes a complex parameter in the phase and is described with a known propagation in the out-of-plane direction:

$$E(r,t) = Re\left(\tilde{E}(r_T)e^{j\square - j\beta z}\right) = Re\left(\tilde{E}(r_T)e^{j\omega-\alpha z}\right) \tag{5.11}$$

Where the spatial parameter, $\alpha = \delta_z + j\beta = -\lambda$, has an imaginary part ($j\beta$) referring to the propagation constant and an real part (δ_z) representing the damping along the propagation direction. The relation between the propagation constant (β) and effective index (n_{eff}) of the mode is denoted as: $\beta = n_{eff}\, k_0$. Throughout the thesis, mode fields are typically presented with the form of intensity which is proportional to the square of the electric field amplitude.

All simulations in this work are computed for a free space wavelength of 3.68 μm corresponding to the $LiNbO_3$ refractive indices of n_z = 2.0700 and n_y = 2.1309 for extraordinary and ordinary polarised modes, respectively [23]. In order to truncate the computational domain and minimise light reflections from the boundary, isotropic and circular perfectly matched layers (PML) are applied surrounding the cladding waveguide structure. The PML light absorber is defined as a function of refractive index n_{PML} [24, 25]:

$$n_{PML}(r) = n_{o,e} - ik_{max}\left(\frac{r - r_{in}}{L}\right)^2, \quad r_{in} < r \leq r_{in} + L. \qquad (5.12)$$

where r is the radial coordinate, r_{in} and L are the inner radius and thickness of the PML, and k_{max} is the maximum absorption value. All these parameters have been carefully chosen so as to give reliable waveguide modes [26]: k_{max} = 0.002 has been chosen as giving the most effective absorption for the structure, and r_{in} = 150 μm and L = 150 μm are chosen to effectively reduce the computational domain while not affecting the computed modes.

The model is simulated using a designed geometry that matches the fabricated track-cladding structures. For starting, the initial refractive index changes ($\Delta n^{\mathrm{local}}$) assumed at the tracks for the mid-IR range, are of $\Delta n^{\mathrm{local}} = -5 \times 10^{-3}$ for both polarizations. TM and TE modes are studied separately, and iteratively computed while varying the unknown RI change ($\Delta n^{\mathrm{local}}$) of the tracks, in order to match the experimental results. In the first mode analysis, the simulation is set to search for as many modes as possible (~500 modes). From this first simulation it is then possible to refine the effective index and use this value for further simulations in which only 20 modes are looked for, therefore the time consumption for simulation could be reduced.

In the finite element analysis, the entire geometry is broken down into stiffness matrices which contain a series of points or nodes. Equations are solved on each individual point that connected to others in form of triangular mesh elements (an example is shown in Fig. 5.2). The accuracy of the solution therefore depends on the space between the nodes. The smaller the mesh area of the mesh elements is, the closer the nodes will be, and the better approximation of the solution can be achieved. However, the more mesh elements the greater computing power is required.

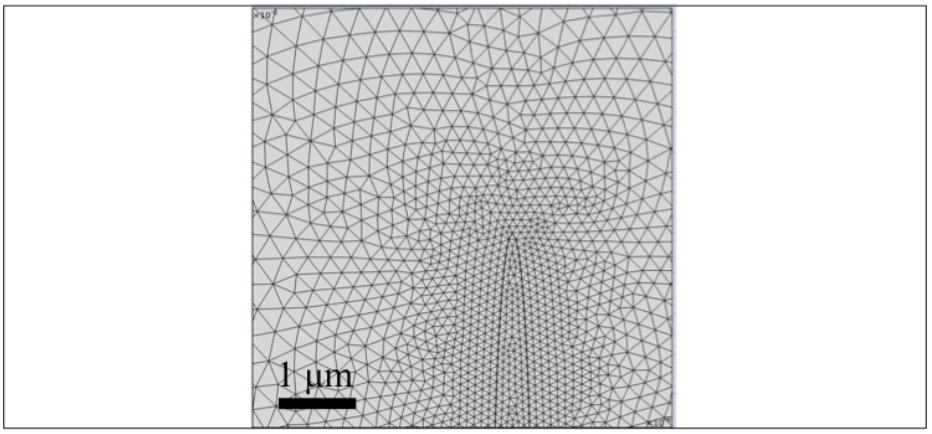

Fig. 5.2. An example of triangular meshed elements used in finite element method based calculation.

In the case of transverse writing scheme, since the laser-written tracks are simulated as elliptical shape with minimum dimensions of typically ~20 μm along the incident (focusing) direction of the laser beam (z-axis, vertical) and ~1 μm along the perpendicular direction (y-axis, horizontal), the finite elements mesh of elliptical tracks is defined with a free triangular mesh of size around 40 nm in the horizontal and 450 nm for the vertical. Inside the cladding area a free triangular mesh of size around 1 μm in both horizontal and vertical directions is used. The rest of domains are defined with free triangular meshes of minimum size 50 nm and maximum size 10 μm.

5.2.2. The finite difference beam propagation method (FD-BPM)

5.2.2.1. Light propagation simulation of cladding waveguides

Light propagation was simulated by BeamPROP software which is a part of the RSoft Photonic Component Design Suite®. The computational simulation is based on finite difference beam propagation method (FD-BPM), details described in [27, 28] and references therein. This particular approach uses the finite difference method to numerically solve the well-known parabolic or paraxial approximation of the Helmholtz equation for monochromatic waves [22].

$$\frac{\partial u}{\partial z} = \frac{i}{2\bar{k}}\left(\frac{\partial^2 u}{\partial_{x^2}} + \frac{\partial^2 u}{\partial_{y^2}} + (k^2 - \bar{k}^2)u\right) \tag{5.13}$$

This is the basic beam propagation method (BPM) equation in 3D model. It can be simplified to 2D term by removing the part with y dependence. Given the propagation

direction along the guiding z axis and an input field, u(x,y,z=0), the equation 5.13 expresses the evolution of the field in the space z>0. Here, the notation $k(x,y,z) = k_0$ n(x,y,z) is the spatially dependent wavenumber, with $k_0 = 2\pi/\lambda$ being the wavenumber in free space; while $\bar{k}$ is a constant number referring to as the reference wavenumber. Therefore, the geometry of the computing problem is completely determined by the RI profile n(x,y,z) which is inputted though segment assignments.

For a straight waveguide, a simple segment is created with total length of 22 mm. The segment is then assigned to the complex RI profile of the designed cladding structure previously generated by COMSOL model and which was processed in Matlab to create a readable BeamPROP matrix file. This methodology allows to apply any specific designated complex RI profile which cannot be done by using simple built-in drawing tools. For large radii bend waveguides (R ≥100 mm) the same procedure is applied and a circular s-bend is added between the input and output straight sections. Scaling and grid sizes are thoroughly considered to assure that correct computations are obtained.

For the simulation of light propagation, the fundamental mode is pre-computed before launching into the waveguide input, while the output power was monitored along the waveguide pathway, using a square monitor of the size of the corresponding waveguide core. All beam propagation figures in this thesis show a 2D intensity distribution across the waveguides, i.e. the near-field intensity distribution inside the CLWs, and the integrated power across the monitor surface, which represents the actual power flux at each point along the waveguide path length. This allows to compare the propagation losses (PLs) of different cladding designs.

Regarding to the boundary condition, the so-called transparent boundary condition (TBC) is applied [29]. The approach is to assure that the field acts as an outgoing plane wave with no back-reflection near the computational boundary. The TBC is proved to be effective in allowing the light waves to freely escape from the computational domain details reported in [29].

5.2.2.2. The FD-BPM for waveguide mode solving

The BPM simulation includes two numerical mode solvers: the iterative method and the correlation method. Though the iterative method is usually a fast technique for obtaining the field shape and propagation constant [30, 31], its computation relies on the so-called

imaginary distance beam propagation method which is therefore not valid for computational structures with an imaginary index or for lossy/leaky modes, which is the case of cladding waveguides [26]. In this simulation work, mode solving was performed by launching an incident Gaussian field into the waveguide input and using correlation method. Since the waveguide structure is assumed to be uniform along the z propagation direction, the input field and the propagating field can be expressed in the correlation function [32]:

$$P(z) = \int \emptyset_{in}^{*}(x)\emptyset(x,z)\,dx \tag{5.14}$$

$$\text{Or } P(z) = \sum_m |A_m|^2\, e^{i\beta_m z} \tag{5.15}$$

Where m is a generalised mode index, A_m is the mode weight coefficients, and β_m is the propagation constants; by definition the highest propagation constant corresponds to the fundamental mode (m=0). By taking the Fourier transform of the correlation function, the mode spectrum can be computed and should have peaks at the modal propagation constants. The eigenvalues or the effective index values for each mode can therefore be obtained from the mode spectrum. The corresponding mode profiles or eigenfunctions can be obtained in a second propagation by beating the propagating field against the known propagation constants via:

$$\phi_m(x) = \frac{1}{L}\int_0^L \phi(x,z)e^{-i\beta_m z} \tag{5.16}$$

For obtaining more accurate effective index values, two following corrections can be applied. The first correction is made for the error caused by solving the paraxial equation instead of the exact Helmholtz equation details reported in [32]. In the second correction, the mode profiles are used to find the propagation constants by substituting the mode profiles into the wave equation. This allows not only finding the imaginary part of the propagation constant, but also correcting the real values; and thus resulting in a more accurate effective index.

5.2.3. Theoretical propagation loss calculation

Solutions of the simulation model involve the effective index of the guided mode which contains the real part and the imaginary component. The imaginary part of the effective index represents the propagation loss of the mode whose proportional calculation is

described following. For a straight waveguide, the theoretical propagation loss of a guided mode is calculated in first order approximation by assuming an exponential decay with the propagation length with the effective medium attenuation coefficient $\alpha = 4\pi \cdot Im(n_{eff})/\lambda$, so that:

$$PLs\left(\frac{dB}{cm}\right) = \frac{40\pi}{ln10.\lambda(\mu m)} Im\left(n_{eff}\right) \times 10^4 \qquad (5.17)$$

Bend losses (BLs) are also estimated by subtracting the PLs of straight waveguides to the total loss obtained in an s-bend waveguide BPM simulation of equal length. By knowing the total extra radiation loss due to bends we then normalise this value to the total arc length of the s-bend in mm, obtaining a BLs value in dB/mm.

5.3. Full RI profiles of microstructured $LiNbO_3$ waveguides

5.3.1. Components of stress-induced RI profile in standard double-track waveguides

The first study involves calculations of laser-induced stress distribution in the standard laser-written double-track waveguides whose micro-stress data were experimentally examined and reported in [12, 15, 33]. In the previous work of Burgoff *et al.* [15], pairs of tracks with separation of several micrometers (~10-50 μm) were fabricated by a chirped pulse amplified laser system, delivering a near-IR wavelength of ~800 nm, sub-picosecond pulse of ~200 fs, and repetition rate of 1 kHz. Using standard focusing lenses (NA: ~0.2-0.6), the induced stress between the double tracks was measured in the order of 10-500 MPa, depending on the selected laser pulse energies (typically ~0.1-0.8 μJ) [12, 15].

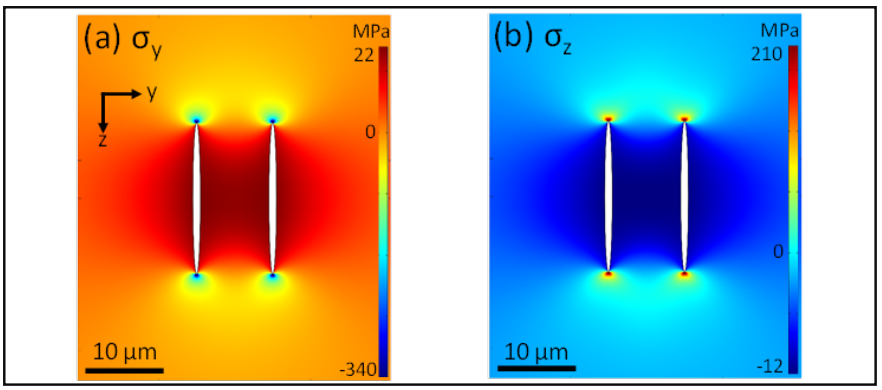

Fig. 5.3. Simulated stress field of the 2-track structure. (a) for the σ_y component (b) for the σ_z component.

In this simulation, the magnitude of the stress fields is numerically adjusted by varying the parameter of the temperature change (ΔT) in the thermal expansion model. In the results shown in Fig. 5.4, it could be observed that for the σ_y stress component, compressive stress spreads at the lateral sides of the tracks, while tensile stress takes place at the apexes [Fig. 5.3(a)]. Conversely, for the σ_z stress component, tensile stress is distributed between the tracks and compressive stress takes place at the tracks apexes [Fig. 5.3 (b), details reported in paper I].

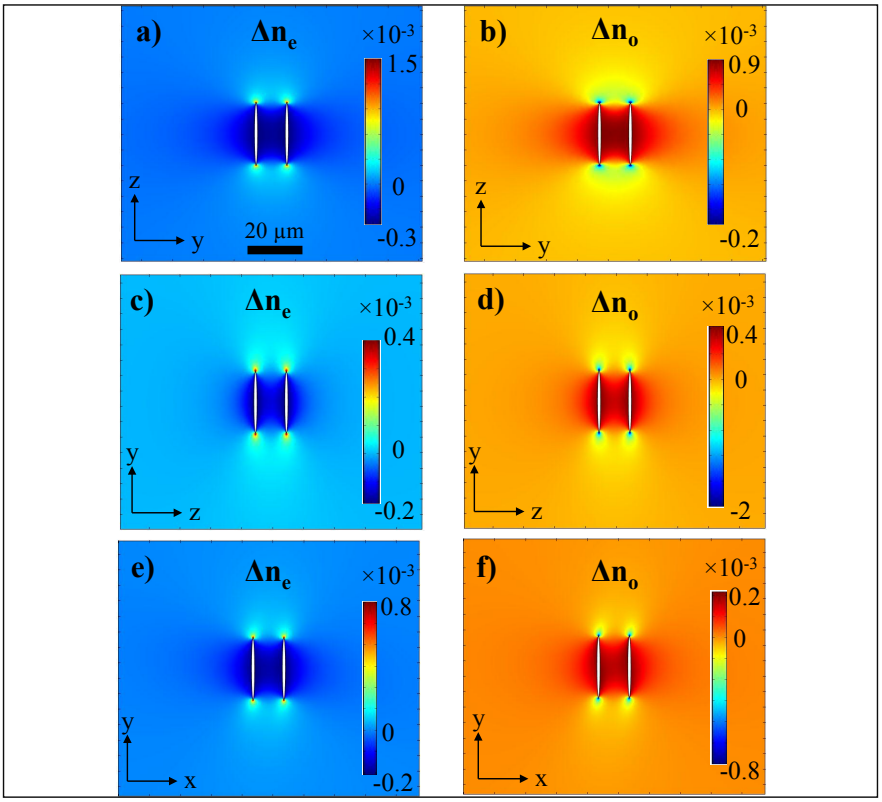

Fig. 5.4. Refractive index distributions in standard double-track laser-written waveguides in $LiNbO_3$. Cross-sectional RI profiles on yz plane (a) and (b); zy plane (c) and (d); and xy plane (e) and (f).

The simulated stress fields are subsequently used to calculate the RI distribution at the surrounds of the laser-modified volume (Δn^{stress}) using the piezo-optic formula (described in chapter 2, section 2.2.4). Fig. 5.4 shows the components of RI distribution of the double-track waveguides with the track dimensions of 1 × 20 μm and separation of 10 μm between the two tracks. As resembled from the computed stress profiles, the

RI distribution shows the RI gradient in both lateral and vertical directions with opposite magnitude sign.

Corresponding to the stress value in the range of 10-500 MPa, theoretically the maximum RI change (Δn^{stress}) is in the order of few 10^{-3}. Different orientations of the crystal (z-cut and y-cut samples) were also studied with the same linear thermal expansion conditions, showing no significant difference in the resulted profiles (Fig. 5.4). However, the magnitude of the Δn^{stress} changes is different for each orientation as a result from the anisotropy of $LiNbO_3$.

5.3.2. RI properties of $LiNbO_3$-CLW in the mid-infrared

While stress-induced RI values at surrounds of the modified tracks (Δn^{stress}) are estimated from the piezo-optic calculation, the depressed-RI changes inside these tracks (Δn^{local}) remain unknown in the mid-infrared range. As already mentioned in the section 5.1, in order to study these Δn^{local} changes CLWs are used due to the nature of their leaky mode guiding which is very sensitive to magnitude of the depressed-RI changes in the cladding.

5.3.2.1. Stress-induced RI profiles – Δn^{stress}

The cladding waveguides are typically designed to have rectangular or circular arrangements. In this thesis, circular cladding arrangement is chosen due to its symmetry which, on one hand, optimises the butt-coupling of input Gaussian beam into the waveguide, and on the other hand, reduces the anisotropy of waveguide performance.

As shown in Fig. 5.4, the examined waveguide has core diameter of 40 μm, surrounded by 79 elliptical tracks (track dimensions of 0.5 μm × 10 μm, with horizontal track separation of 2 μm), and cladding thickness of 10 μm. This structure was obtained by transversely scanning ultrafast laser beam along the x-direction of the z-cut $LiNbO_3$ crystal. In this fabrication, the laser system was set with linearly-polarised pulses of ~120 fs duration, repetition rate of 1 kHz at central wavelength ~795 nm, pulse energy of 0.6 μJ, scan speed of 0.7 mm/s and focused through the xy plane of the sample at a minimum depth of 300 μm using a microscope objective (20x, NA= 0.4). Laser polarization was kept perpendicular to the scanning direction. Results in Fig. 5.4(a) and (b) show a good match of the designed and fabricated patterns. This geometric structure was used to model and calculate the stress distribution induced by the volume expansion

of laser-modified tracks [details in section 5.2]. As it can be seen in Fig. 5.4(c) and (d), a biaxial tensile/compressive $\sigma_{y/z}$ stress field generates at the lateral and vertical sides of the cladding. This complex stress field will produce a strongly anisotropic waveguide behaviour. Magnitude of this stress field can be adjusted by varying the temperature change (ΔT) in the thermal expansion model. By using ΔT= 100K, the maximum compressive and tensile stress is of about 67 MPa and 280 MPa, respectively, which well matched with the experimental values previously presented in [12, 15, 33]. The two components of RI distribution (Δn_y and Δn_z) therefore resemble the stress fields, resulting a range of RI gradient from 0.0016 to 0.015 [Fig. 5.4(e) and (f)]. Additionally, it is noticed that changes of RI at the inner part of the cladding ring are smaller than those outside. This might be due to the fact that the stress field originating from the inside apexes is partly cancelled by the opposite stress from the neighbour tracks, as a result of the circular arrangement. Details on this matter are further discussed in the next section 5.3.3.

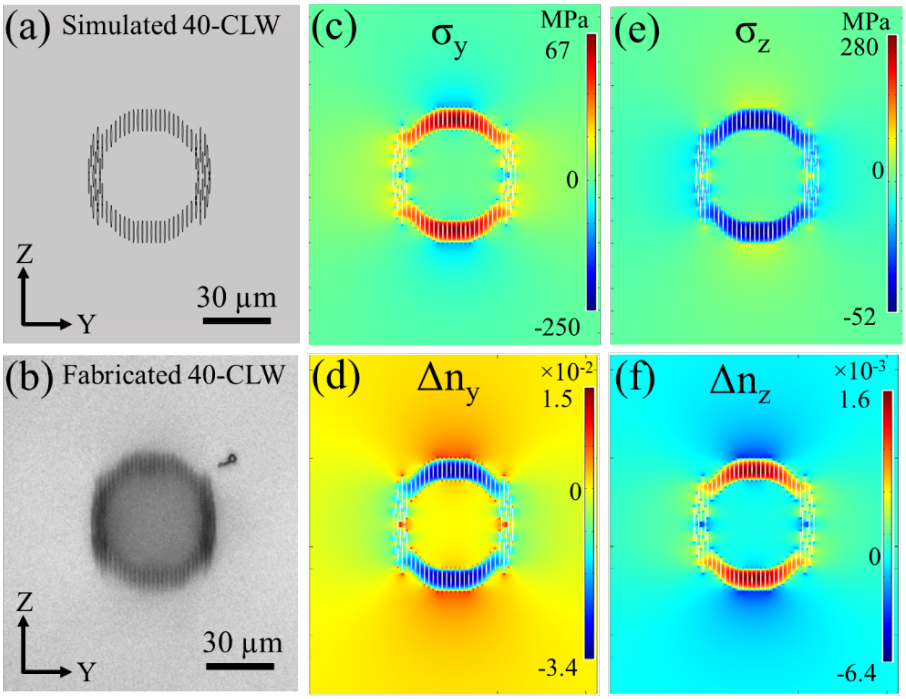

Fig. 5.4: Designed (a) and laser-written structure (b) of cladding waveguide in $LiNbO_3$ with 40 µm core, and its FEM simulated stress profiles (c) (e), and refractive index distributions (d) (f).

5.3.2.2. Combination of Δn^{local} and Δn^{stress}: the origin of waveguide anisotropy in $LiNbO_3$

Assuming the depressed-RI changes inside the laser-modified tracks ($-\Delta n^{local}$) are always negative (type II modification), when combined with the y component of the $-\Delta n_y^{stress}$ at the surrounds which also exhibits negative property in the lateral sides [Fig. 5.5(a)], it is evident that this complex combination of RI profile will be efficient for TE-polarised light guiding. Conversely, combination of negative $-\Delta n^{local}$ and the laterally positive z component of the $+\Delta n_z^{stress}$ [Fig. 5.5(b)] will deteriorate the TM-polarised guiding. This effect does not depend on the $LiNbO_3$ crystallographic axial alignment; it is an anisotropic effect arising solely by the highly asymmetric shape of the laser-written tracks. In order to mitigate this effect, the tracks should be written closer together, however, higher number of tracks will be required to have the same cladding size; which therefore costs the increase of the processing time, and also increases the risk of sample cracking. To compromise these two issues and maintain flexible fabrication parameters which do not entail cracking, the distance between tracks is optimised to 2 µm for all the studied cladding designs.

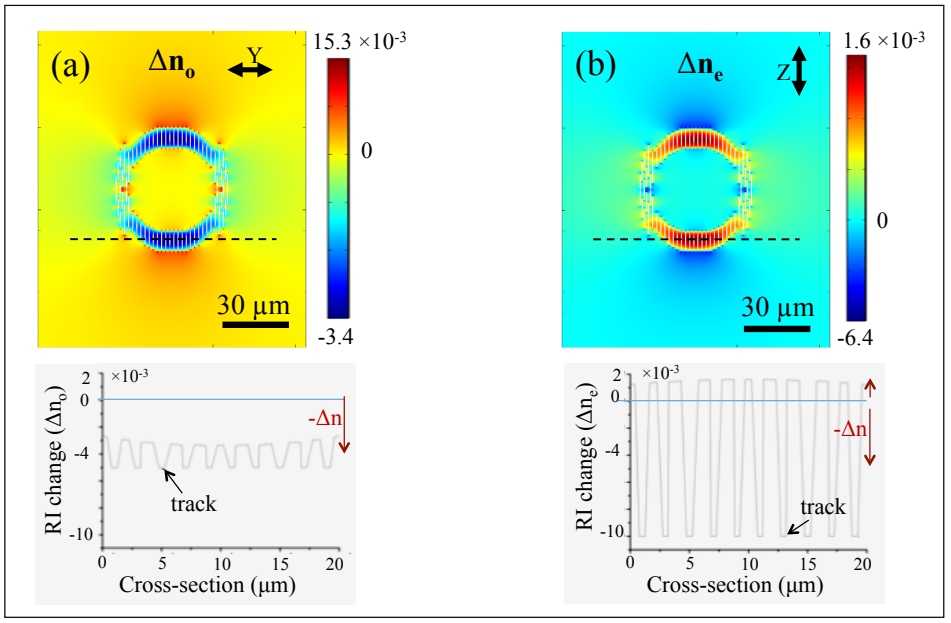

Fig. 5.5: Simulated refractive index profiles of $LiNbO_3$- CLWs, with $\Delta n_{o/y}$ component (a), and $\Delta n_{e/z}$ component (b).

Another factor that contributes to the anisotropy of polarised light guiding in $LiNbO_3$-CLWs, is the anisotropy of the depressed-RI changes (Δn^{local}) of the two ordinary (n_o) and extraordinary (n_e) RI. The evidence of the anisotropic behaviour of the RI changes in $LiNbO_3$ was reported by the work of [15], in which the Δn_o^{local} value was assumed to be half of the value of Δn_e^{local} for the visible light.

5.3.2.3. Estimation of depressed-RI changes in CLWs by heuristic mode-matching approach

In this simulation, an initial assumption is made with depressed-RI changes: Δn_o^{local} = -0.005 and Δn_e^{local} = -0.01, which are then varied in the iterative mode-matching process. This initial assumption of Δn_inside, in combination with the piezo-optic RI distribution (Δn^{stress}) which is simultaneously computed from the thermal expansion model; forms complete RI profiles of the $LiNbO_3$-CLW structure.

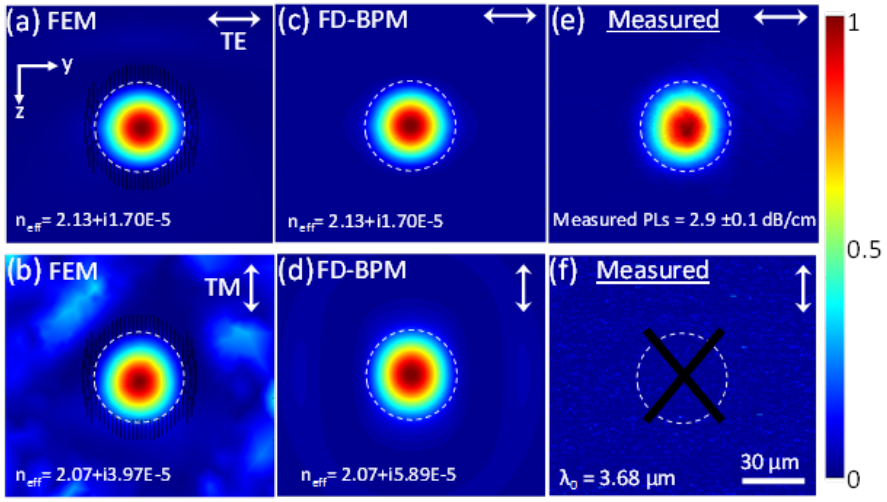

Fig. 5.6. Fundamental mode intensity distribution of the 40 µm diameter core CLW obtained by FEM (a) (b), FD-BPM (c) (d), simulation with initial assumption: Δn_o^{local} = -0.005 and Δn_e^{local} = -0.01, comparing with experimental results (e) (f).

In order to study mode guiding, the electromagnetic waves model is applied, taking into account the calculated RI profiles of the entire CLW structure. The model results solutions of near-field guided modes which can be extracted to calculate PLs and MFDs. These calculated values of PLs and MFDs are iteratively compared with experimental values, while varying the variables: Δn_inside in the assumption, until the computed and

the experimental values match well with each other. The first mode-matching results are presented in [Fig. 5.6, details reported in paper I], comparing the simulated TE and TM fundamental modes by the FEM method [Fig. 5.6(a) and (b)], FD-BPM method [Fig. 5.6(c) and (d)], and experimental results [Fig. 5.6(e) and (f)].

In this first round, the computed effective index of the TE mode was $2.13 + i1.7 \times 10^{-5}$, giving an estimated PLs of 2.5 dB/cm which are slightly lower than the measured value (2.9 ±0.1 dB/cm). Additionally, MFDs of the guided mode were compared as a function of the depressed-RI inside the tracks (Δn^{local}: from -0.001 to -0.01). After the iterative matching of both PLs and MFDs, the best matched result was achieved with $\Delta n_{o/y}^{local} = -0.008 + i7 \times 10^{-4}$, which gives a TE mode effective refractive index of $2.13 + 1.95 \times i10^{-5}$. This TE mode effective index gives a propagation loss of 2.89 dB/cm, in excellent agreement with the measured value of 2.9 ±0.1 dB/cm [Fig. 5.7, details reported in paper I]. It is noticed that the obtained value of $\Delta n_{o/y}^{local}$ is a complex number containing the real part; and the imaginary component which is introduced as the extinction coefficient associating to the absorption and scattering at the track volume.

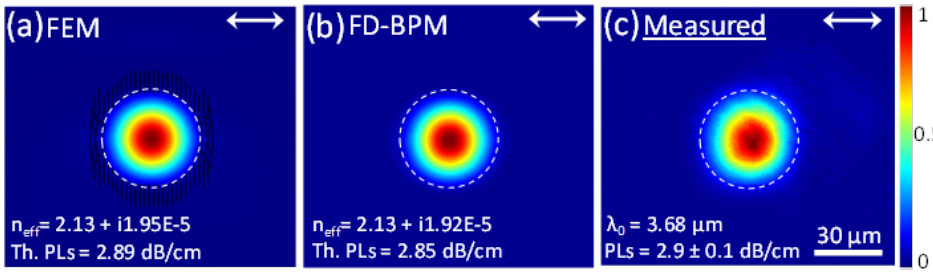

Fig. 5.7. Intensity distribution of TE modes of the 40 µm CLW. (a) FEM, (b) FD-BPM and (c) experiment. Using complex RI change inside the cladding tracks: $\Delta n_{o/y}^{local} = -0.008+i0.0007$.

In the case of vertically polarised light, no TM mode was observed experimentally. This clearly shows the evidence of the anisotropic behaviour that inherently occurs in this type of waveguide in $LiNbO_3$. As mentioned in the previous section, 5.3.2.2, one of the reasons why the CLW does not guide TM light is because of the positive $+\Delta n_{e/z}^{stress}$ component in between the modified tracks. Another reason could be that the negative RI change inside the tracks for vertically polarised (n_e) light is significantly low. The combination of these factors might lead to the fact that the proportion of negative extraordinary-RI contrast in the cladding is not high enough for sustaining a leaky mode

at 3.68 μm light. In the simulation, by using the initial assumption ($\Delta n_{e/z}^{local}$ = -0.01), the computed PLs of the TM mode were around 8.7 dB/cm which is very high and might be at the limit for the technical measurement of the fabricated sample. Since no experimental data were recorded for this case of extraordinary light (TM), the value $\Delta n_{e/z}^{local}$ = -0.01 still remains as an assumption.

5.3.3. Asymmetry of stress effect in circular CLWs

Previously, it has been observed that the stress effect at the inner part of the cladding structure is dimmer than the outer part. In order to study more details and demonstrate this asymmetric effect, a series of separate simulations was performed with increasing the number of tracks in the circular geometry. Fig. 5.8(a) and (b) demonstrate simulation results of a single laser-written track. Typical stress fields observed in this type of individual laser-written structure include symmetric distributions of compressive stress and tensile stress in both lateral and vertical directions. In the second case [Fig. 5.8(c) and (d)], when another track is added to the side in the way that one is vertically lower than the other, the stress at the track apex seems to be partially cancelled by the opposite stress at the lateral side of the neighbour track. The cancelling effect becomes larger when more tracks are added in the same way in which tracks are arranged with a form of a curve. Shown in Fig. 5.8(e) and (f) is the track arrangement in a quarter of the circular geometry. In this geometry, the tracks on the right are typically positioned lower than the one on the left in the vertical axis. As a result, the stress at the track apexes is inherently cancelled by the opposite stress at the lateral sides of the tracks. The last simulation which computes stress distributions in half of the circular geometry [Fig. 5.8(g) and (h)] clearly demonstrates the strongly asymmetric effect of the stress accumulation. The strong stress fields are evident at the upper part of the structure, whereas the stress fields at the lower part are very weak. This kind of asymmetric stress effect is practically good for designing cladding waveguides, when the material inside the cladding/or in the core is not significantly affected/or modified, thus the material properties are preserved.

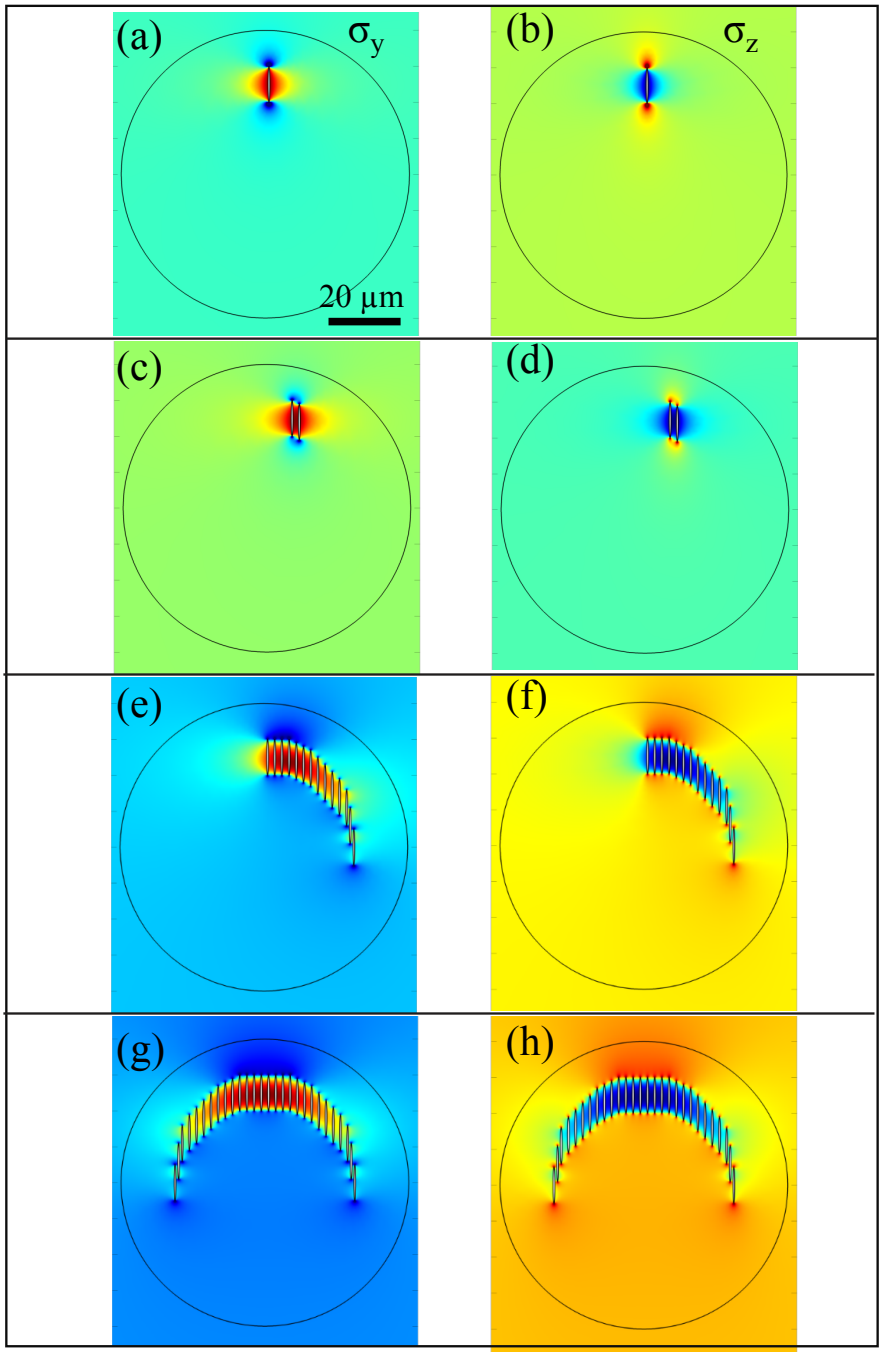

Fig. 5.6. Demonstration of the asymmetric stress effect. Simulated stress fields of tracks in different configurations: 1 track (a) (b), 2 tracks (c) (d), quarter of a circular arrangement (e) (f), and half of a circular arrangement (g) (h).

Reference

1. A. G. Okhrimchuk and A. V. Shestakov, *Depressed cladding, buried waveguide laser formed in a YAG:Nd^{3+} crystal by femtosecond laser writing.* Opt. Lett., 2005. **30**(17): p. 2248-2250.
2. S. Gross, N. Jovanovic, A. Sharp, M. Ireland, J. Lawrence, and M. l. J. Withford, *Low loss mid-infrared ZBLAN waveguides for future astronomical applications.* Opt. Express, 2015. **23**: p. 7946-7956.
3. A. Okhrimchuk, V. Mezentsev, A. Shestakov, and I. Bennion, *Low loss depressed cladding waveguide inscribed in YAG:Nd single crystal by femtosecond laser pulses* Opt. Express, 2012. **20**(4): p. 3832-3843.
4. J. R. Macdonald, S. J. Beecher, P. A. Berry, G. Brown, K. L. Schepler, and A. K. Kar, *Efficient mid-infrared Cr:ZnSe channel waveguide laser operating at 2486 nm.* Opt. Lett., 2013. **38**(13): p. 2194-2196.
5. Y. Ren, G. Brown, A. Ródenas, S. Beecher, F. Chen, and A. K. Kar, *Mid-infrared waveguide lasers in rare-earth-doped YAG.* Opt. Lett., 2012. **37**(16): p. 3339-3341.
6. R. He, Q. An, Y. Jia, G. R. Castillo-Vega, J. R. Vázquez de Aldana, and F. Chen, *Femtosecond laser micromachining of Lithium Niobate depressed cladding waveguides.* Optical Materials Express, 2013. **3**(9): p. 1378-1384.
7. H. Karakuzu, M. Dubov, and S. Boscolo, *Control of the properties of micro-structured waveguides in Lithium Niobate crystal.* Opt. Express, 2013. **21**(14): p. 17122-17130.
8. J. Martınez de Mendıvil, D. Sola, J. R. Vazquez de Aldana, G. Lifante, A. H. de Aza, P. Pena, and J. I. Pena, *Ultrafast direct laser writing of cladding waveguides in the $0.8CaSiO_3$-$0.2Ca_3(PO_4)_2$ eutectic glass doped with Nd^{3+} ions.* J. Appl. Phys., 2015. **117**: p. 043104.
9. R. He, Q. An, J. R. Vázquez de Aldana, Q. Lu, and F. Chen, *Femtosecond-laser micromachined optical waveguides in $Bi_4Ge_3O_{12}$ crystals.* Applied Optics, 2013. **52**(16): p. 3713-3718.
10. A. Rodenas, G. Zhou, D. Jaque, and M. Gu, *Direct laser writing of three-dimensional photonic structures in Nd:yttrium aluminum garnet laser ceramics,.* Appl. Phys. Lett., 2008. **93**(15): p. 151104.
11. A. Rodenas, G. A. Torchia, G. Lifante, E. Cantelar, J. Lamela, F. Jaque, L. Roso, and D. Jaque, *Refractive index change mechanisms in femtosecond laser written ceramic Nd:YAG waveguides: micro-spectroscopy experiments and beam propagation calculations.* Applied Physics B, 2009. **95**(1): p. 85-96.
12. A. Rodenas, *Direct femtosecond laser writing of 3D photonic structures in rare-earth doped Lithium Niobate*, in *Departamento de Física de Materiales*. 2009, Universidad Autónoma de Madrid.
13. A. Rodenas, L. M. Maestro, M. Ramirez, G. A. Torchia, L. Roso, F. Chen, and D. Jaque, *Anisotropic lattice changes in femtosecond laser inscribed Nd^{3+}:MgO:$LiNbO_3$ optical waveguides.* J. Appl. Phys. , 2009. **106**: p. 013110.
14. B. McMillen and Y. Bellouard, *On the anisotropy of stress-distribution induced in glasses and crystals by non-ablative femtosecond laser exposure.* Opt. Express 2015. **23**: p. 86-100.
15. J. Burghoff, S. Nolte, and A. Tünnermann, *Origins of waveguiding in femtosecond laser-structured $LiNbO_3$.* Applied Physics A, 2007. **89**(1): p. 127-132.

16. J. Burghoff, H. Hartung, S. Nolte, and A. Tünnermann, *Structural properties of femtosecond laser-induced modifications in $LiNbO_3$.* Applied Physics A, 2007. **86**(2): p. 165-170.
17. M. Will, J. Burghoff, S. Nolte, A. Tünnermann, F. Wunderlich, and K. Goetz, *Detailed investigations on femtosecond-induced modifcations in crystalline quartz for integrated optical applications.* Proc. SPIE 2005. **5714**: p. 261–270.
18. P. M. Dixit and U. S. Dixit, *Modeling of Metal Forming and Machining Processes by Finite Element and Soft Computing Methods*. 2008: Springer-Verlag London.
19. A. S. Andrushchak, B. G. Mytsyk, H. P. Laba, O. V. Yurkevych, I. M. Solskii, A. V. Kityk, and B. Sahraoui, *Complete sets of elastic constants and photoelastic coefficients of pure and MgO-doped Lithium Niobate crystals at room temperature.* Journal of Applied Physics, 2009. **106**(7): p. 073510.
20. Y. S. Kim and R. T. Smith, *Thermal Expansion of Lithium Tantalate and Lithium Niobate Single Crystals.* Journal of Applied Physics, 1969. **40**(11): p. 4637-4641.
21. M. Koshiba, *Optical Waveguide Theory by the Finite Element Method*. 2011: Springer Netherlands.
22. G. Lifante, *Beam propagation method for design of optical wavegudie devices*. 2016: John Wiley & Sons, Ltd.
23. D. Zelmon, D. Small, and D. Jundt, *Infrared corrected Sellmeier coefficients for congruently grown Lithium Niobate and 5 mol.b.* J. Opt. Soc. Am. B, 1997. **14**: p. 3319-3322.
24. Y. Tsuji and M. Koshiba, *Guided-Mode and Leaky-Mode Analysis by Imaginary Distance Beam Propagation Method Based on Finite Element Scheme.* Journal of Lightwave Technology, 2000. **18**(4): p. 618.
25. H. Karakuzu, M. Dubov, S. Boscolo, L. A. Melnikov, and Y. A. Mazhirina. *Control of the Properties of Micro-Structured Waveguides in Lithium Niobate Crystals*. in *Advanced Solid-State Lasers Congress*. 2013. Paris: Optical Society of America.
26. J. Hu and C. R. Menyuk, *Understanding leaky modes: slab waveguide revisited.* Advances in Optics and Photonics, 2009. **1**(1): p. 58-106.
27. R. Scarmozzino, A. Gopinath, R. Pregla, and S. Helfert, *Numerical techniques for modeling guided-wave photonic devices.* IEEE Journal of Selected Topics in Quantum Electronics, 2000. **6**(1): p. 150-162.
28. R. Scarmozzino and R. M. Osgood, *Comparison of finite-difference and Fourier-transform solutions of the parabolic wave equation with emphasis on integrated-optics applications.* Journal of the Optical Society of America A, 1991. **8**(5): p. 724-731.
29. G. Hadley, *Transparent boundary condition for beam propagation.* Opt. Lett., 1991. **16**: p. 624-626.
30. D. Yevick and B. Hermansson, *New formulations of matrix beam propagation method: Application to rib waveguides.* J. Quantum Electron, 1989. **25**: p. 221.
31. S. Jungling and J. C. Chen, *A study and optimisation of eigenmode calculations using the imaginary-distance beam-propagation method.* J. Quantum Electron, 1994. **30**: p. 2098.
32. M. D. Feit and J. A. Fleck, *Computation of mode properties in optical fiber waveguides by a propagating beam method.* Appl. Optics, 1980. **19**: p. 1154.

33. A. Rodenas, J. A. Sanz Garcia, D. Jaque, G. A. Torchia, C. Mendez, I. Arias, L. Roso, and F. Agullo-Rueda, *Optical investigation of femtosecond laser induced microstress in Neodymium doped Lithium Niobate crystals.* Journal of Applied Physics, 2006. **100**(3): p. 033521.

6

Development of $LiNbO_3$-CLWs with low repetition rate lasers

This chapter describes the process for obtaining low-loss single mode mid-IR $LiNbO_3$-CLWs using low repetition rate laser pulses.

Contents

6.1. Introduction

Implementation of mid-IR integrated photonic devices with high performance requires waveguide components which possess single-mode low-loss (<0.5 dB/cm) guiding typically for both orthogonal TE and TM polarised light. However, there is a real challenge to develop such low-loss mid-IR CLWs on $LiNbO_3$. To our knowledge, all reported mid-IR (>3 μm wavelength) CLWs in $LiNbO_3$ have been limited to PLs of ~3 dB/cm [1-4] which is far from the value for practical applications. This bottom-neck could originate to the fact that at this long wavelength range, the confinement losses of CLWs are way higher than at near-IR or visible range. Furthermore, guiding performance typically favours for one polarisation rather than for the other; due to the anisotropy of the material, and the stress-induced effects.

In this chapter, fabrication of CLWs is processed by low repetition rate regime (1 kHz) in which the generation of stress is more evident than the high repetition rate lasers (>100 kHz). In low-repetition rate systems the time interval between incident pulses is of ~1 ms, which is about three-orders of magnitude longer than the time (1 μs) for the absorbed laser radiation, or the generated heat to diffuse out of the focal volume [5, 6]. As the heat is built up and cooled out every time the pulse arrives, a strong stress field is accumulated around the focal volume.

Therefore, with the help of the comprehensive model which realistically takes into account the stress-induced effect, a progressive approach is proceeded to achieve appropriate microstructure cladding designs as well as fabrication conditions for obtaining propagation losses below 0.5 dB/cm, the level that is typically required for optical circuits of cm´s size.

6.2. Strategies for reducing PLs for both TE and TM modes

In order to achieve the criteria of low-loss single mode mid-IR guiding for both TE and TM polarisations, several approaches have been suggested in the following:

(1) Increase of the waveguide core: in the leaky-mode CLWs, the bigger waveguide cores typically result lower losses due to the less light scattering out of the cladding [1, 4, 7]. However, to some extent the bigger CLW core size increases the excitation of higher order modes for any polarization which is not desirable. Thereby, in order to both

lower the PLs and remain mono-mode operation, several core diameters of circular CLWs are considered in the following section 6.3.3.

(2) Increase of the cladding thickness: Attenuation of leaky modes in CLWs is known to exponentially decrease with the rate of increasing the thickness of the depressed-RI cladding [8]. However, larger cladding structure might complicate the stress-induced RI field and therefore increase the risk of cracking and also the anisotropy. This character is studied in section 6.3.4.

(3) Increase of the RI contrast of the cladding: Based on the model in chapter 5, it is clear that the CLWs performance can be improved by increasing the RI contrast of the cladding. This feature is dependent on the laser fabrication conditions such as pulse energy, pulse energy, focusing optics, and writing velocity, and also orientation of the crystal. Behaviours of the CLWs with regards to the two fundamental parameters: pulse energy and scan speed are examined in section 6.3.5.1.

(4) Erasure of the anisotropic stress-induced effect: In order to have the waveguide supporting for both polarization, it is important to reduce the anisotropic stress, by writing the tracks closer together, or changing the track shape, or designing appropriate cladding arrangements. As discussed in chapter 5, putting the tracks closer can reduce the area of the anisotropic laser-induced stress between them, however it is at risk of sample cracking. To avoid the cracking, the optimised space between the tracks is found to be 2 μm which is used throughout all experiments in the transverse writing scenario in this thesis. Due to the asymmetrically elliptical shape, each track is a source of strong anisotropic stress. Therefore, by changing of the track shape the anisotropic effect can be reduced. However, this requires a beam engineering technique to modify spatial profile of the laser pulse which is beyond the scope of this thesis.

Another the approach for reducing the anisotropic stress is by thermal post-processing. The erasure of stress under thermal treatment is known to enhance waveguide performance in several materials [1, 9, 10]. However, the mechanism of the process is unclear. With the help the simulation model described in chapter 5, comprehensive understanding of the effect of thermal post-processing on CLW properties is discussed in section 6.3.5.2.

6.3. CLWs in transverse writing scheme

6.3.1. Design and modelling

The CLW design and numerical analysis in this chapter are performed by both FEM and FD-BPM techniques as described in chapter 5. Different cladding arrangements examined on particular conditions are adapted by modifying the geometrical domain in the computational models.

6.3.2. Experimental details

As already described in chapter 4, the ultrafast laser fabrication involves transcription of tracks to construct a negative RI (– Δn) circular array which supports leaky modes along the tubular channel [11]. Geometrical coordinates of each individual track were extracted from the 2D design and loaded to a script used in the laser inscription process. Trial of writing single tracks was initially conducted in order to specify the track sizes as a function of laser energy and focusing depth.

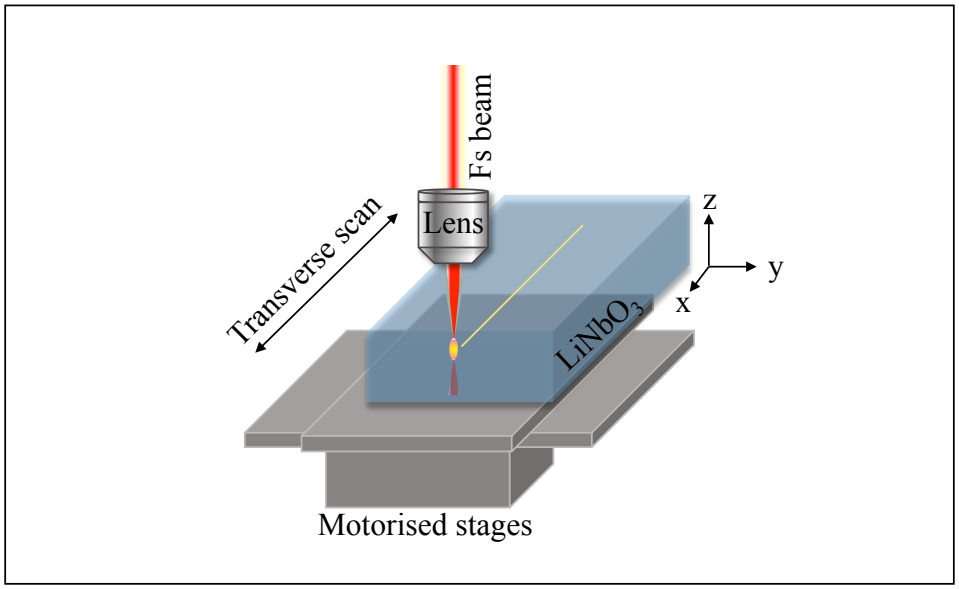

Fig. 6.1. Schematic of the transverse ultrafast laser writing geometry.

In this transverse writing scheme, each track is fabricated by scanning the laser beam along the sample with a constant depth. The modification is strictly dependent on particular parameters of the laser setup and also the orientation of the sample. Throughout this chapter, the orientation of the sample is fixed to xy plane as illustrated

in Fig. 6.1. In this specific scenario, the 3D laser writing (3DLW) is focused along the z-axis and scanned along the x-axis of a z-cut $LiNbO_3$ sample, at a central depth of ~300 μm. A variety of scan speed was used in specific experiments.

The ultrafast laser beam was generated by a Ti:Sapphire regenerative amplified laser system (Spitfire and Tsunami systems, Spectra-Physics) which was set to a low repetition rate of 1 kHz, at a central wavelength of 800 nm. The pulse duration was fixed to ~120 fs, while pulse energy was varied using a calibrated neutral density filter, a half-wave plate and a linear polariser. A high-resolution three-axis motorised stage was used to mount the sample and precisely move the positions corresponding to the programmed script.

Regarding to the laser polarisation, the beam was linearly polarised along the y-axis of the sample (perpendicular to the scanning direction). A 90º rotation of the polarization direction did not produce significant differences in the fabricated structures. Such independence, to our knowledge, is due to the fact that the propagation direction of the femtosecond laser is along the z-axis of the crystal (z-cut sample) and thus the polarisation is mainly contained in the isotropic XY plane.

Thermal post-processing

Thermal treatments of the waveguides were performed in a furnace with open-air condition. A series of seven sequential annealing processes at different peak temperatures was carried out. The first annealing was done at a maximum temperature of 573 K (300 ºC) for 3 hours, with a 2 K per minute ramp for heating up and cooling down. The sequential processes were repeated with increasing peak temperatures of 773, 873, 973, 1073, 1123 and 1173 K (900 ºC). Since the annealing was repeatedly done on the same sample, the final result is an accumulation of heat treatments from all the preceding processes. The sample was analysed by SEM and the waveguides were fully characterised after each annealing step.

6.3.3. Properties of CLWs: core size dependence

Following the criteria of low-loss single mode waveguides, three different CLWs were examined with core diameters of 40 μm (CLW_40), 70 μm (CLW_70) and 100 μm (CLW_100). As shown in Fig. 6.2, the designed patterns and the fabricated structures

look almost identical. Here all the CLWs were fabricated on Z-cut MgO: $LiNbO_3$ sample, under the same laser fabrication conditions as listed in Table 6.1:

Table 6. 1. Laser fabrication parameters for CLW_40, CLW_70 and CLW_100

Repetition rate	1 kHz
Central wavelength	800 nm
Pulse duration	120 fs
Pulse energy	0.6 μJ
Polarisation	Linear
Scan speed	0.7 mm/s
Focusing optics	Microscope objective (20x, NA 0.4)
Depth of focused beam	~300 μm
Sample	MgO: $LiNbO_3$, Z-cut

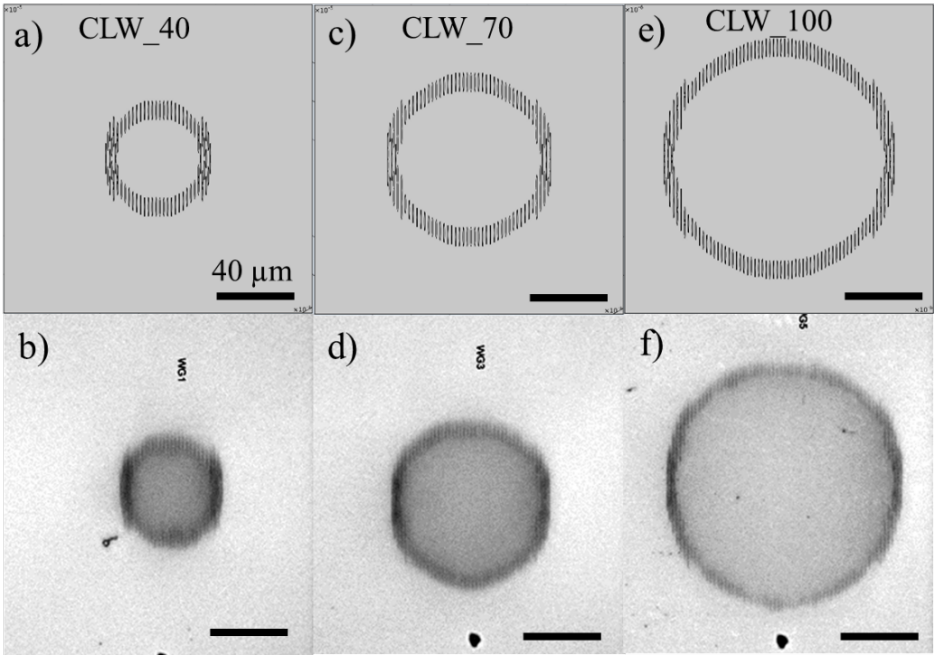

Fig. 6.2. Designed and fabricated structures of CLWs with core diameters of 40 μm (a) and (b); 70 μm (c) and (d); and 100 μm (e) and (f).

Shown in Fig. 6.3 are the guiding results which indicate that the CLW with a small core diameter of 40 μm supports single mode, while the bigger CLWs with core diameters of >70 μm are multimode. Results of the CLW_100 are not recorded since the large mode

area was out of view in the camera. Both the FEM simulations and experiments agree with the results. It is noticed that all the CLWs only support guiding for the TE polarisation. This is a clear evidence of the anisotropy of the depressed-RI CLWs in $LiNbO_3$.

The CLW_40 was measured with propagation losses of 3 dB/cm which is comparable with previous reported values [1, 2, 4], and in line with the observation described in chapter 5. This also confirms that losses below 1 dB/cm at the mid-RI wavelengths appear to be challenging to achieve by the 3DLW techniques in $LiNbO_3$.

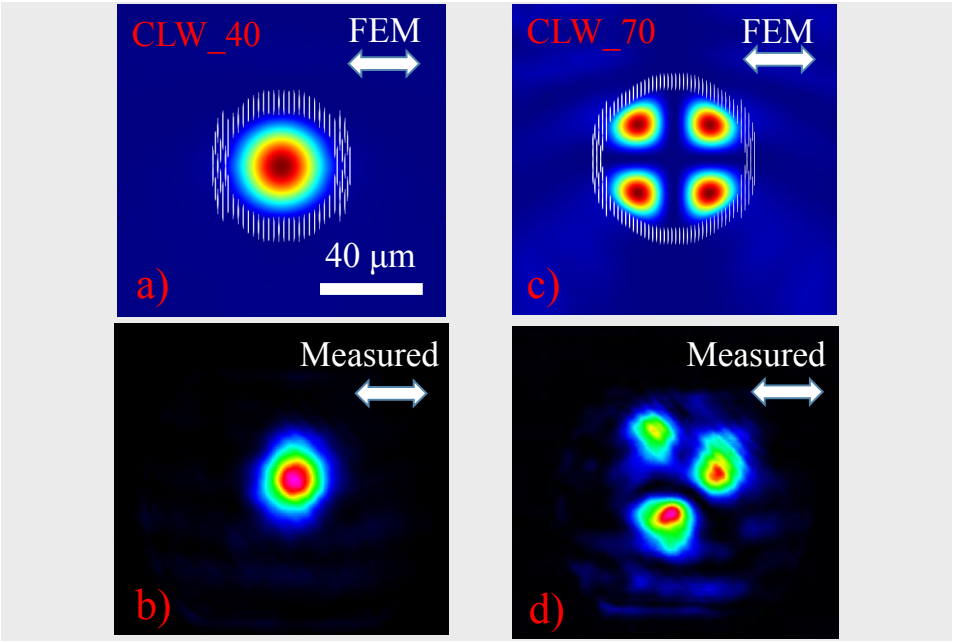

Fig. 6.3. Near-field guided modes of 40 µm core- CLW_40 obtained by FEM (a) and by experiment (b); and 70 µm core- CLW_70 obtained by FEM (c) and by experiment (d).

6.3.4. Properties of CLWs: cladding thickness dependence

As mentioned in the section 6.2, guiding performance of CLWs can be improved by increasing thickness of the circular cladding layer. In this set of experiment, CLWs with cladding thickness of 10 µm and 16 µm were fabricated on Z-cut $LiNbO_3$ sample using the same fabrication conditions [listed in Table 6.2]. As shown in Fig. 6.4(a) and (d), both CLWs have the same core diameter of 50 µm formed by circular arrangement of laser-written tracks. It can be noticed that the writing conditions for this experiment is

different from the one presented in section 6.3.3. It is required to use higher pulse energy of ~1.26 μJ and focusing optics of 40x NA 0.65 instead of ~0.6 μJ pulse energy and 20x, NA 0.4 focusing optics as required in the previous experiment. This difference could be due to the use of a different stock sample. Previously, the $LiNbO_3$ sample was doped with MgO which might cause it to behave differently to the fs laser radiation [5]. In both laser-written structures of the CLW_50 and CLW2R_50, it can be seen that there are extra arrays of tracks appearing at the lower part. This is caused by an aberration effect which renders a second focal point of the laser beam at a certain depth (>300 μm). The effect typically occurs when a high NA (>0.6) objective is used. By adjusting the angle of the incident beam to the sample surface, this effect can be reduced, but it is still hard to avoid.

Table 6. 2. Laser fabrication parameters for CLW_50 and CLW2R_50

Repetition rate	1 kHz
Central wavelength	800 nm
Pulse duration	120 fs
Pulse energy	1.26 μJ
Polarisation	Linear
Scan speed	0.7 mm/s
Focusing optics	Microscope objective (40x, NA 0.65)
Depth of focused beam	~300 μm
Sample	$LiNbO_3$, Z-cut

Regarding to the guiding performance, the thin 10 μm cladding thickness (CLW_50) exhibits mono-mode guiding for only TE polarisation, while guiding of both polarised TE and TM light was obtained by the thick 16 μm cladding thickness (CLW2R_50). In terms of PLs, though the CLW2R_50 is multimode for TE polarisation, its fundamental TE mode exhibits a strong guiding with PLs as low as 0.4 dB/cm which is way lower than the results (3 dB/cm) typically obtained in Mid-IR CLWs in $LiNbO_3$. Additionally, the mono-mode TM guiding was observed in the CLW2R_50, giving PLs of 2.7 dB/cm which is significantly higher than the value for TE mode. It is also worth noticing that in the CLW2R_50 the MFD of the TM mode (~50 μm) is larger than the value of TE mode (~40 μm); or in other words the TE mode is more confined than the TM mode. The reason for this behaviour could be explained by the strong stress-optic effects which are

anisotropically in favour the TE rather than TM polarised light. This anisotropy of guiding performance has a strong relation with the complex RI profile at cladding structure which is comprehensively studied in section 6.3.5.

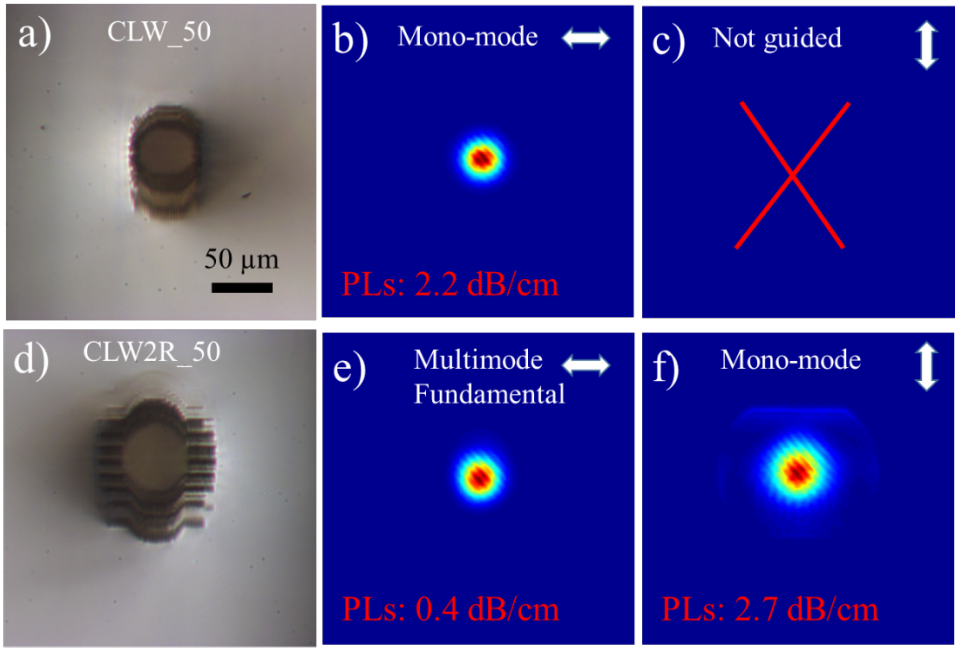

Fig. 6.4. Optical transmission images and guiding modes of CLW2R_50 (a), (b) and (c), and CLW2R_50 (d), (e) and (f).

6.3.5. Properties of CLWs: RI profiles of the cladding layer

Guiding performance of CLWs strongly relies on profiles of the cladding layer in which both (1) the RI magnitude/contrast of each single track and (2) its surrounding RI distribution play a primary role.

(1) Depending on a particular laser setup (pulse duration, energy, focusing optics, scan speed and others), the RI contrast can be adjusted, typically by varying pulse energy and scan speed.

(2) The anisotropic stress-induced RI distribution at surrounds of modified- track volume is technically unable to avoid during the ultrafast laser fabrication. This unwanted stress effect is usually reduced through thermal post-processing [1, 9, 10]. Despite the wide use of the approach, the underlying mechanism of this process is hitherto not fully understood.

Therefore, the focus of this section is on the study of CLWs properties with respect to both laser writing conditions (mainly pulse energy and scan speed), and thermal treatments.

6.3.5.1. Properties of CLWs with respect to laser writing conditions

In this experiment, the CLWs were fabricated with a series of different pulse energy and scan speed, while all other laser fabrication parameters were kept constant (listed in Table 6.3). Here the CLW structure is designed with a large cladding thickness of 16 µm and a core diameter of 50 µm (named CLW2R_50), as previously optimised in section 6.3.4.

Table 6. 3. Laser fabrication parameters for CLW2R_50

Repetition rate	1 kHz
Central wavelength	800 nm
Pulse duration	120 fs
Pulse energy	**0.84 – 2.31 µJ**
Polarisation	Linear
Scan speed	**500 – 750 µm/s**
Focusing optics	Microscope objective (40x, NA 0.65)
Depth of focused beam	~300 µm
Sample	$LiNbO_3$, Z-cut

The CLW structure was characterised by ESEM, showing a clear circular cladding structure [Fig. 6.5(a)]. However, there appeared extra tracks at a beam-focused depth of >300 µm [Fig. 6.5(c)], as a result of the lens aberration which is due to the use of high NA lens (already mentioned in the previous section 6.3.4). These extra tracks were estimated to have dimensions of ~2/3 of the primary tracks. To make a realistic calculation, the simulation model is modified by adding extra tracks to the cladding geometry [Fig. 6.5(b)].

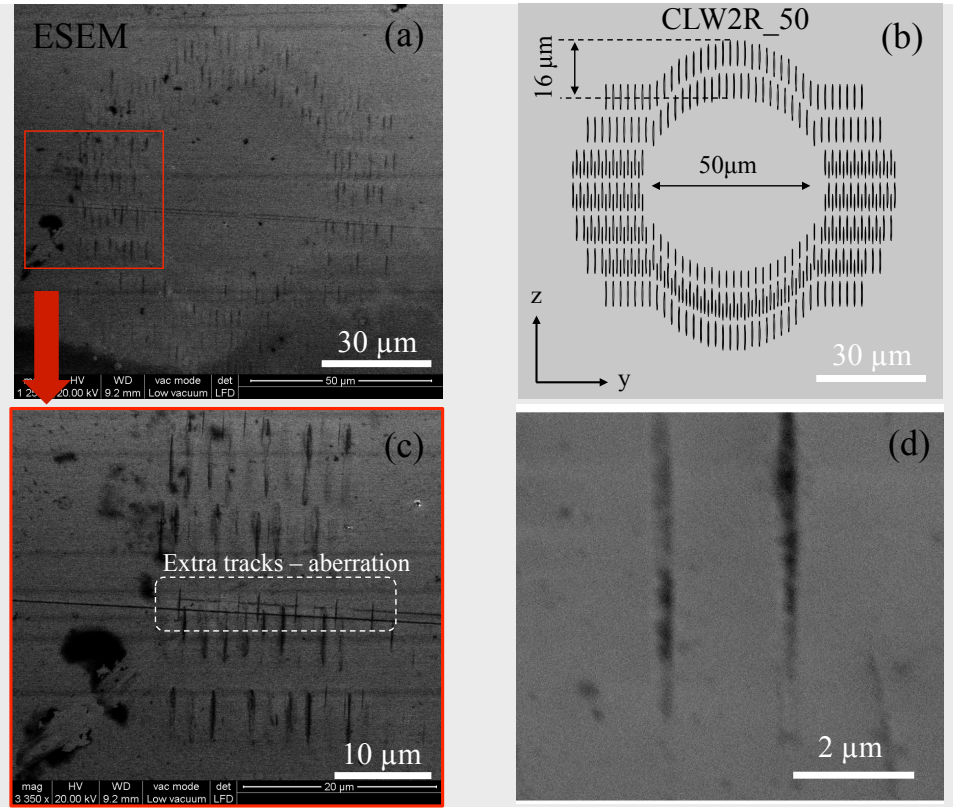

Fig. 6.5. ESEM images of the CLW2R_50 (a), (c) and (d); and its designed structure (b).

Dimensions of single tracks were measured by a high magnification mode in ESEM [Fig. 6.5(d)]. Moreover, in order to confirm the result in sub-micrometer scale, AFM characterisation was further performed, resulting in high-resolution images. As shown in Fig. 6.6, the laser-written tracks appear to have elliptical shapes with dimensions of 0.3 µm along the minor axis, and 7 µm along the major axis (measured by AFM).

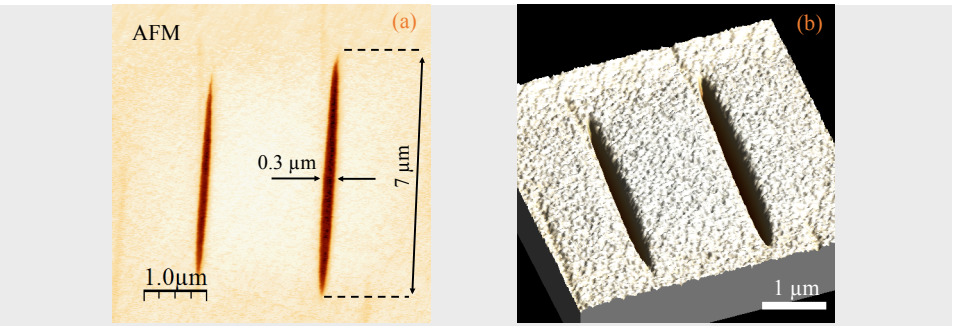

Fig. 6.5. AFM images of laser-written tracks in 2D (a) and 3D (b).

Guiding performance of all the CLWs was characterised with mid-IR light (3.68 μm wavelength). Table 6.4 lists propagation loss results of the as-fabricated CLWs which are divided in two groups: group A and B include the CLWs fabricated with scan speeds of 750 μm/s and 500 μm/s respectively. The CLWs in both groups were written with the pulse energy ranging from 0.84 to 2.31 μJ. All the CLWs exhibits guiding for both orthogonal polarisation. For TM polarised light guiding, the waveguides appear to be mono-mode, with relatively-low PLs. In the case of TE polarised light, since the CLWs are multimode, the PL results were measured for the fundamental mode.

Table 6.4. Propagation losses of the CLW2R_50s fabricated with different laser parameters

	Group A								Group B		
	750 μm/s scan velocity								500 μm/s scan velocity		
	750_ wg1	750_ wg2	750_ wg3	750_ wg4	750_ wg5	750_ wg6	750_ wg7	**750_ wg8**	500_ wg1	500_ wg3	500_ wg5
Pulse energy (μJ)	0.84	1.05	1.26	1.47	x	1.89	2.10	**2.31**	0.84	1.26	1.68
TE-PLs* (dB/cm)	0.68	0.41	0.40	0.33	x	0.27	0.30	**0.20**	0.47	0.39	0.51
TM-PLs (dB/cm)	4.59	3.48	2.70	2.11	x	1.18	1.28	**1.19**	1.67	1.49	1.20

* For TE polarisation, the CLWs are multimode, the PL values were recorded for the fundamental mode

x: broken or not guided

Fig. 6.7 shows guiding results of the CLWs as a function of pulse energy and scan speed.

(1) In terms of TM polarisation: The waveguides show an exponential improvement of guiding performance (exponential decrease of PLs) with regard to the increase of the pulse energy up to 1.89 μJ. No significant improvement of the guiding or the PLs stabilised since the CLWs were fabricated with pulse energy higher than 1.89 μJ. This could be a saturated point where, either the guiding of the pure cladding waveguides is no longer dependent on the RI contrast of laser-written tracks, or the higher pulse energies do not enhance RI contrast of the modified volume any more.

Regarding to the laser scan velocity, the CLWs written with lower scan speed (500 μm/s) clearly enhances the guiding performance compared to the ones fabricated with high scan speed (750 μm/s). In principle, the slower movement of the laser beam means

the more pulses arrive at a certain point in the sample which in turns results a stronger modification. Another reason of this RI contrast enhancement is the larger overlapping of the pulse coverage along the scanning path when the beam moves with low speed.

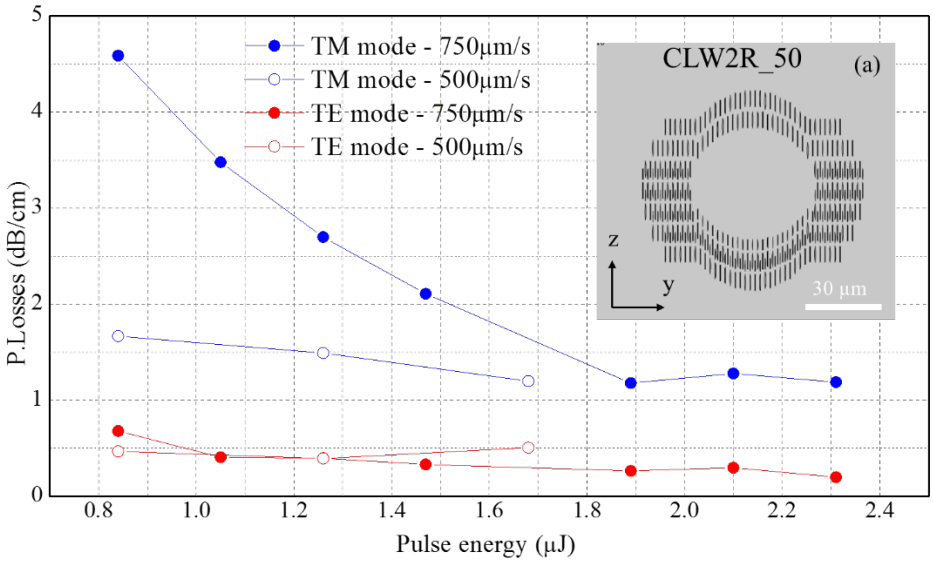

Fig. 6.7. Propagation losses of CLW2R_50 with respect to laser writing parameters: pulse energy and scan speed.

(2) In terms of TE polarisation: PLs of the fundamental mode of all the written CLWs are <0.5 dB/cm which is remarkably low compared with typical values (~3 dB/cm) that others reported until now [1, 2, 4]. The use of low scan speed for fabrication did not a significant improvement of the guiding for TE polarisation. It should be noted that the resulted CLWs are multimode which is not ideal for many photonic integrated applications.

The results here once again confirm that the anisotropic behaviour is always present in the laser-written depressed-index CLWs. The best guiding performance was with PLs of 1.2 dB/cm single mode for TM polarisation and 0.2 dB/cm fundamental mode for TE polarisation; obtained by the CLW: 750_wg8 which was fabricated with 2.31 µJ pulse energy and 750 µm/s scan speed. This result is significantly better than all other reported works on CLWs at the mid-IR [1, 2, 4]. However, there is still another issue needed to be solved is the anisotropy. In order to minimise the anisotropic behaviour, a suggested

approach is to reduce the anisotropic stress-induced effect by a thermal post-process which is investigated in the next section.

6.3.5.2. Properties of CLWs with respect to thermal treatments

It is known that the thermal post-process helps to enhance performance of CLWs [1, 9, 10]. However, the underlying mechanism of the thermal treatment with regard to a reduction of the residual stress and other physical and optical properties is not yet understood. In this section, a comprehensive study on this matter is carried out with the help of the simulation model built in chapter 5.

In this set of experiment, the CLWs were thermally treated with a series of peak temperatures (from 573 K to 1173 K) for 3 hours each. The PL results of the CLWs after the thermal treatments are shown in Fig. 6.8. [recited from Fig.2, Paper II]. As discussed in chapter 5, the stress-induced RI change between the modified tracks is negative for ordinary RI ($-\Delta n_{o/y}^{stress}$), and positive for extraordinary RI ($+\Delta n_{e/z}^{stress}$), thereby, the residual stress theoretically favours the guiding of TE polarised light and worsens the guiding of TM polarised light. For this, it was expected that the thermal annealing would help to improve TM light guidance. However, the results show the contrary, and a rather un-expected trend.

For TM mode [Fig. 6.8, upper graph], the PLs unexpectedly increased when the CLWs were sequentially annealed to the peak temperature of 873 K. However, up to the sequential annealing at 973 K, the trend of the PL values is reversed: the PLs dropped to a value that is close to the PL level of the non-annealed CLWs. At higher peak temperatures of the sequential annealing, the PLs started to increase again. The CLWs vanished or stopped guiding after the sequential heat treatments at peak temperature higher than 1173 K.

For TE mode [Fig. 6.8. lower graph], the purpose of thermally treating the CLWs was to clean the higher order modes and leave the waveguides mono-mode. This was achieved when the CLWs was sequentially annealed up to 773 K. Additionally, as expected the steadily increasing trend of PLs was observed until the heat treatment at 1073 K. At higher temperature of annealing, the CLWs stopped guiding for TE light. This value is lower than the one for TM mode as it was expected that the change of ordinary and extraordinary RI is the anisotropic behaviour.

Overall, the best guiding performance was obtained by the CLW: 500_wg5 after the sequential thermal post-process at peak temperature of 773 K. It shows mono-mode guiding for both TE and TM polarisations with lowest PLs of <1.5 dB/cm.

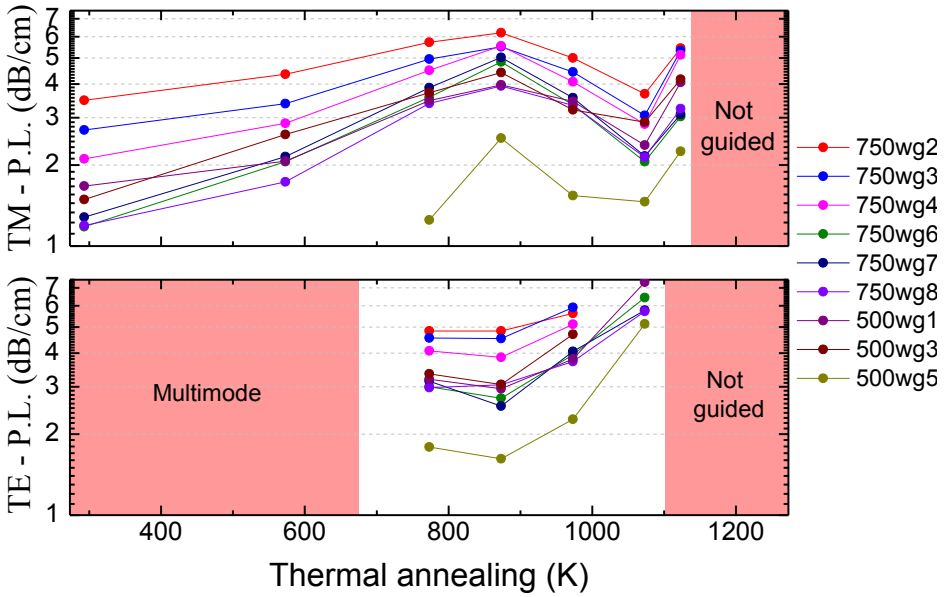

Fig. 6.8. PLs of CLWs with respect to thermal annealing conditions for TE (upper graph) and TM (lower graph) polarisations.

Complex RI profiles of the CLW2R_50

In order to study the guiding behaviour, it is paramount to understand the complex RI profiles of this particular CLW structure. Using the simulation model described in chapter 5, RI profiles of both ordinary index ($\Delta n_{o/y}$) and extraordinary index ($\Delta n_{o/y}$) were numerically calculated (Fig. 6.9).

In the $\Delta n_{o/y}$ profile [Fig. 6.9(a)], both the depressed-RI change inside the tracks ($-\Delta n^{local}$) and the stress-induced RI component at their surrounds ($-\Delta n^{stress}$) are negative (the blue area) which makes the CLW performance is linearly proportional to the magnitude of the residual stress. It should be noted that there are also some parts of positive RI change (the red area) generated between each layers of tracks in the vertical. This might partly weaken the RI confinement of the cladding, though it is not very critical in this case of TE guiding (also confirmed by experimental results).

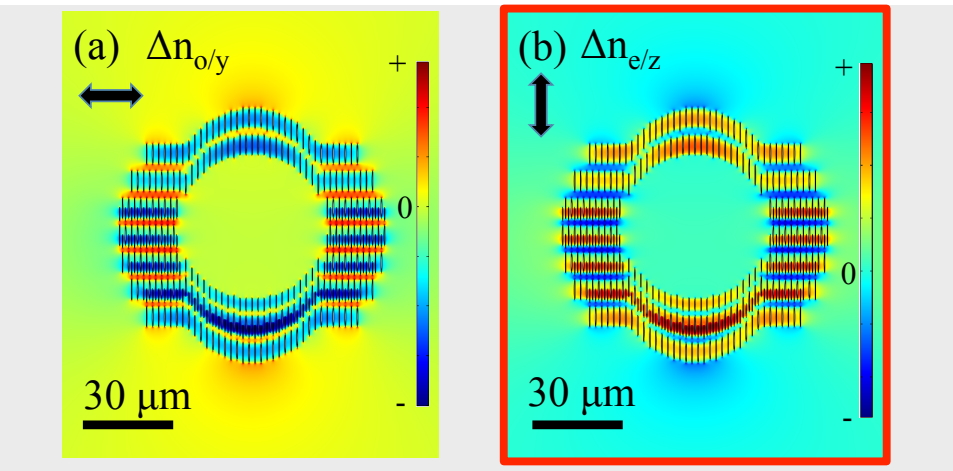

Fig. 6.9. Ordinary (a) and extraordinary (b) RI profiles of CLW2R_50

In the case of the $\Delta n_{e/z}$ profile [Fig. 6.9(b)], the positive stress-induced RI component ($+\Delta n^{stress}$) combines with the negative depressed-RI change ($-\Delta n^{local}$) to form a complicated profile of the whole structure. It seems that the CLW performance can be improved if the stress effect is reduced. However, when taking into account the negative RI change (the blue area) occurred between then track layers in the vertical, the reduction of the stress magnitude could lose this advantage. Therefore, the guiding behaviour for TM polarisation is a compromise of all the negative and positive proportions and hard to predict without a progressive study of stress effect.

The stress effects on TM mode guiding

As it was observed in the experiment, the thermal annealing which is assumed to reduce the residual stress resulted a non-linear behaviour of the CLW performance for the TM mode. Moreover, it is also reported that the thermal treatments leads to a reduction not only in depressed-RI [12], but also in the cross-sectional size of the modified tracks. Therefore, three variables which must be taken into account when the laser-written structure is subjected to thermal treatment are (1) the decrease of stress-induced effect, (2) the decrease of depressed-RI change and (3) the decrease of cross-sectional size.

Shown in Fig. 6.10 are the results from a series of simulation performed by varying the three variables. The maximum stress magnitude has a range from 250 MPa to 0 MPa as the stress is reducing during the thermal annealing process. The range of depressed-RI change is from 0.022 to 0.014 as an estimation. Reduction of the cross-sectional track

size was from 300 nm to 200 nm (measured by AFM) along the minor axis. The reduction of track size along the major axis is in sub-micron scale which is too little compared to the micro-length of the track, hence it is negligible.

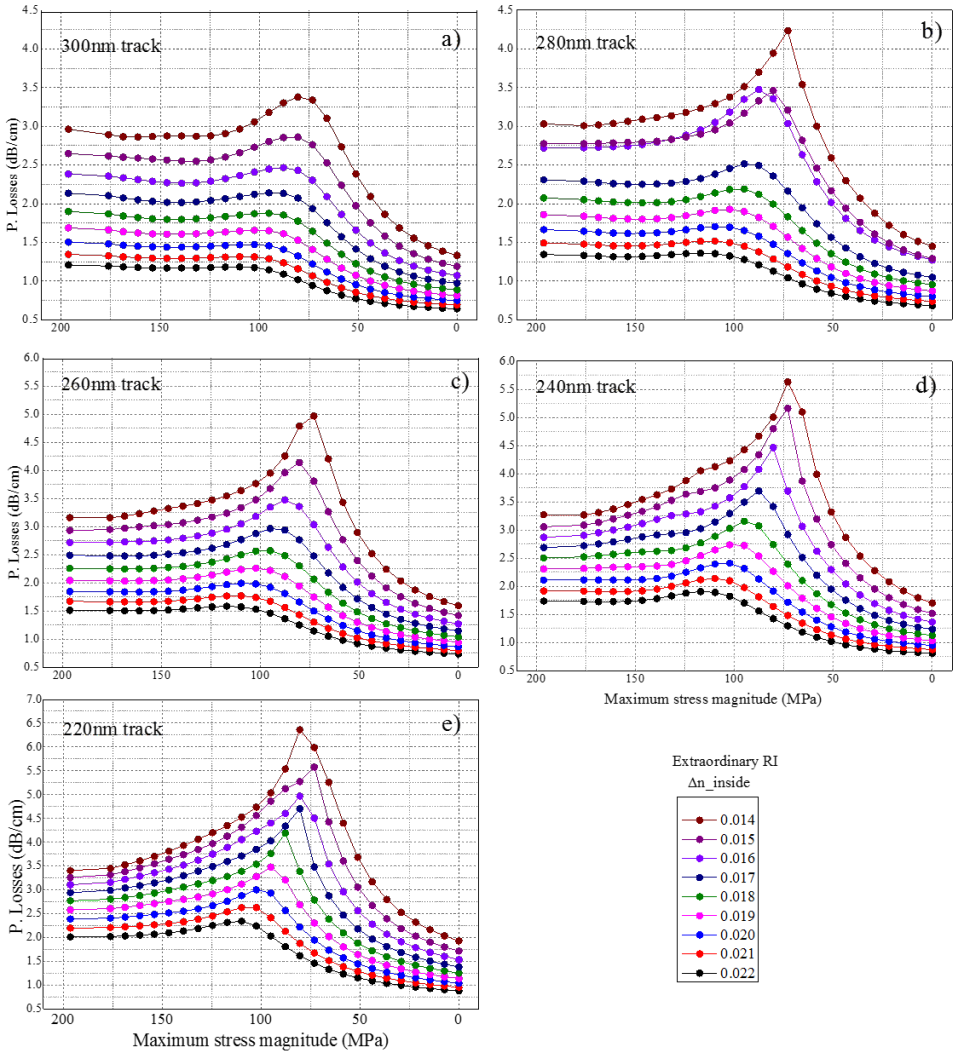

Fig. 6.10. TM-PLs of CLW2R_50 with respect to maximum stress magnitude for the case of track width of 300 nm (a), 280 nm (b), 260 nm (c), 240 nm (d), and 220 nm (e).

Assuming that the cross-sectional size of track is constant [300 nm, Fig. 6.10(a)], the PLs do not decrease (or no improvement of the guiding), but increase instead, when the stress is brought down to ~70 MPa. The increment is more significant if the depressed-RI in the tracks are smaller. The decrease of PLs only happens when the stress is

reduced from the point ~70 MPa down to 0 MPa. In the case of smaller tracks (280 nm – 220 nm) [Fig. 6.10(b-e)], the trend becomes more evident as the increasing peak is significantly sharper. This is understandable because the smaller tracks result more space between them, hence more proportions of the stress field.

In this scenario, in order to reduce the PLs down <1 dB/cm, either the track size or the depressed-RI has to remain constant when the CLW experiences the heat treatments which is not the case occurred in reality. Therefore, practically it is not possible to reduce the PLs for TM mode by applying thermal annealing; as it was observed in the experiment above.

Estimations of the CLW properties with respect to thermal treatments

During the annealing, all the changes of the three variables are believed to simultaneously take place, however, the slope/rate of each changes is unknown. In order to explain the non-linear behaviour observed in the experiment, an iterative mode-matching process must be carried out. Experimental results of the CLWs after each step of the annealing processes is subjected to matching of both PLs and MFDs, using the same heuristic procedure described in chapter 5. Since there are three dependent variables needed to be solved, the matching of both PLs and MFDs is performed by means of root-mean-square error and an elimination rule. The variables which have a smallest error of matching were initially chosen, and later refined by the elimination rule. In the elimination rule, as it is clear that all the variables have to decrease their values associating to the annealing process, thereby the variables of the later annealing cannot be higher than the values obtained from the previous annealing.

For convenient, the matching was carried out for the CLW: 750_wg8, then the common trend can be established for other CLWs since they have the same structure. Details and results are presented in Paper II.

6.3.6. Propagations of CLWs in straight and s-bend paths

As discussed in the previous sections, in order to offer high optical guiding performance, the CLW structure should have large cladding layers of ~16 μm and core diameter of ~50 μm. In this section, propagation of this CLW structure is simulated by FD-BPM so that its PLs and BLs can be estimated. Results of RI profiles, mode analysis, propagation of straight CLW, propagations of s-bend CLWs are illustrated in parts (a), (b), (c), (d)

and (e) of Fig. 6.11 and Fig 6.12, respectively. Here, the RI profiles were initially generated from FEM simulation and then loaded to FD-BMP model for propagation simulations. It should be noted that in this simulation the depressed-RI values (Δn^{local}) and the stress-induced RI changes (Δn^{stress}) was assumed from the values described in chapter 5, as they are typical values obtained by our experiments.

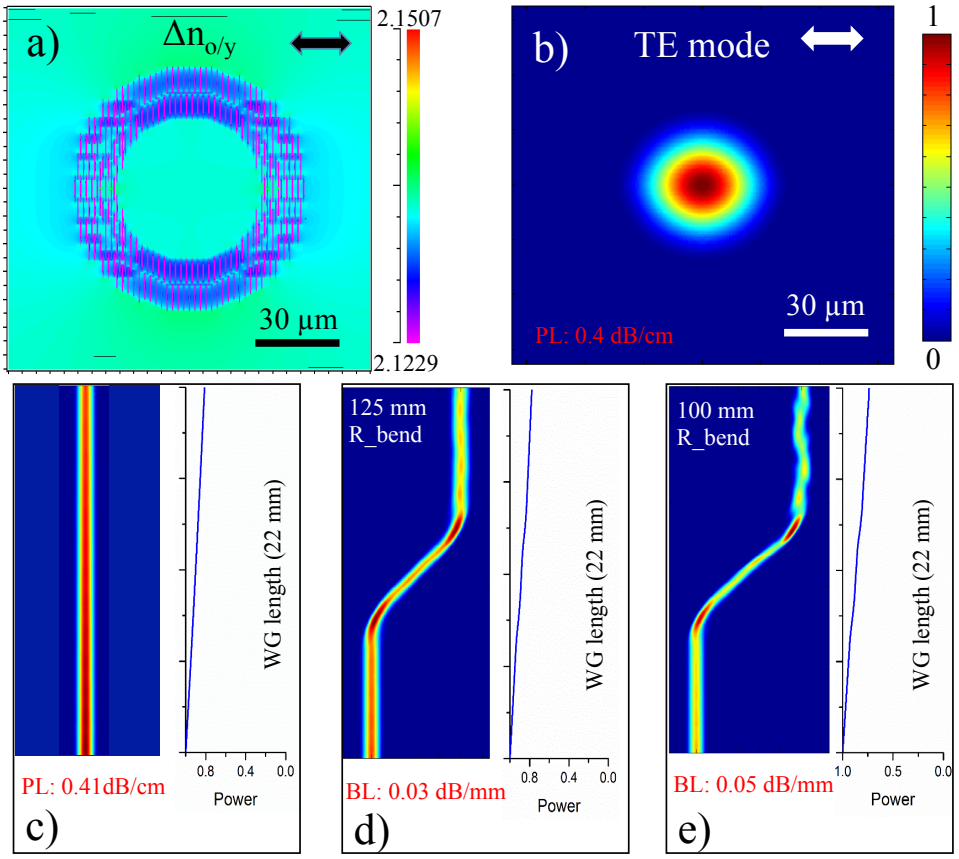

Fig. 6.11. Propagation simulation of straight (c), and s-bends (d) and (e) CLWs for TE polarisation

For TE polarisation (Fig. 6.11), the fundamental mode of the CLW was found to have low PLs of 0.4 dB/cm. As expected, its propagation in straight path shows very little loss of the power [Fig. 6.11(c)]. Two s-bend CLWs were examined with bend-radii of 125 mm and 100 mm, showing BLs of 0.03 dB/mm and 0.05 dB/mm, respectively, which are extremely low [Fig. 6.11(d) and (e)].

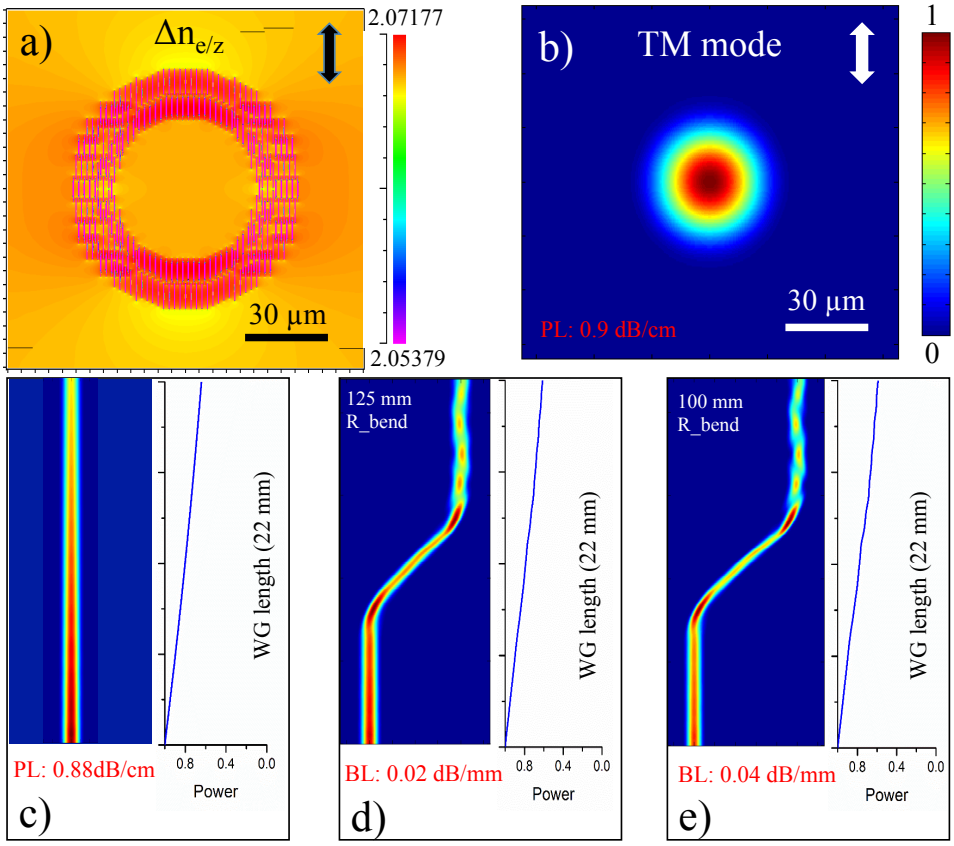

Fig. 6.12. Propagation simulation of straight (c), s-bends (d) and (e) CLWs for TM polarisation

For TM polarisation (Fig.6.12), the obtained PL is 0.9 dB/cm which is higher than the value for TE mode (as expected from the inherent anisotropy of the CLW). The bend losses are 0.02 dB/mm (125 mm bend) and (0.04 dB/mm (100 mm bend), which are comparable with those values for TE mode, suggesting that the losses at the bend are not affected by the optical polarisation.

The PL values however, are still not <0.5 dB/cm which is the condition for realistically implementing integrated photonic devices at the mid-IR. There are still a need of improving the design or fabrication conditions so that lower PLs can be achieved.

6.3.7. Directional beam splitters and MZ structures

One important component of integrated photonic devices is a beam splitter. In this section, design of a 50:50 beam splitter by means of evanescent coupling is investigated. In order to couple the light by evanescent field, it is of importance to ensure that the

waveguide is mono-mode. Several designs with a variety of core sizes have been considered. It was found that the CLW with core diameter of 36 µm and cladding thickness of 22 µm (named CLW2R_36) matches the condition of remaining mono-mode during the evanescent coupling.

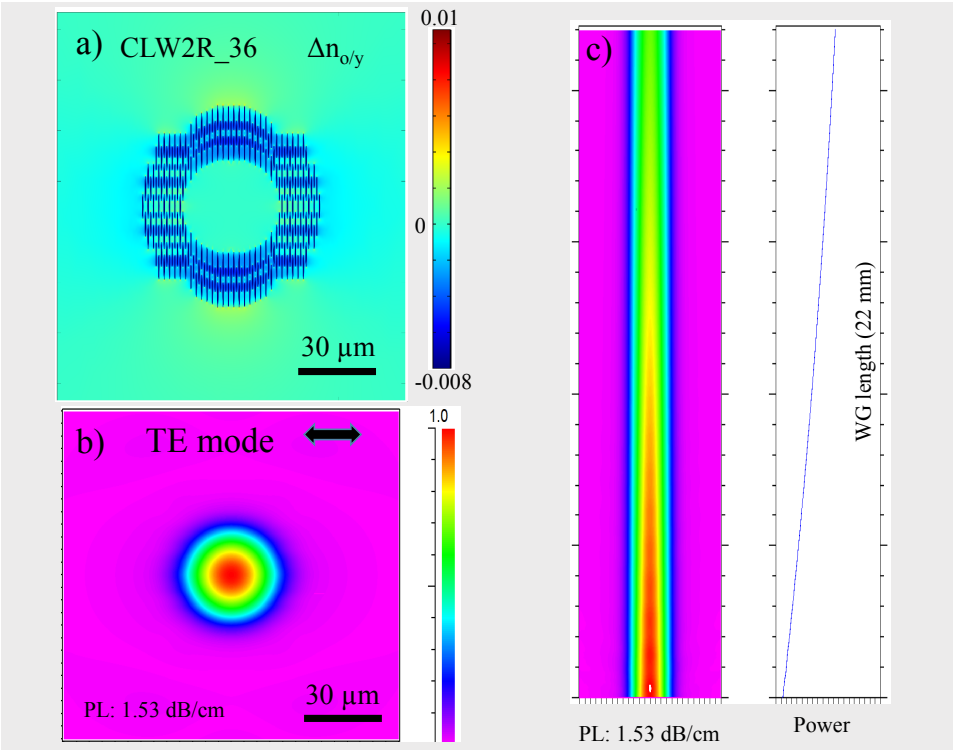

Fig. 6.13. FD-BPM simulation of straight CLW2R_36: refractive index profile with y-component (a), fundamental guided mode (b), and propagation profile (c).

Propagation of the CLW2R_36 was initially simulated [Fig. 6.13], showing low-loss mono-mode guiding for TE polarised light. The PLs was found ~1.5 dB/cm which is relatively low, and can be further improved by increasing RI contrast of the cladding. The CLW2R_36 however, does not guide for TM polarisation. This might be due to either the contrast of the extraordinary RI is not high enough, or size of the CLW is small which leads to a strong laser-induced stress field in the core and hence deteriorating the TM mode.

Evanescent couplings of CLW2R_36

Considering two waveguides placed in a proximity, the propagation of light in one waveguide will transfer parts of it to the other through the so-called evanescent field. Once the contact length is long enough, light can be totally transferred from one to the other. The contact length required to have the total light transfer is typically referred to as the coupling length which is an important factor needed to be considered for having effective 50-50 splitters. Since the coupling length is determined by the contact area between the coupled waveguides, several configurations of coupling structure have been considered.

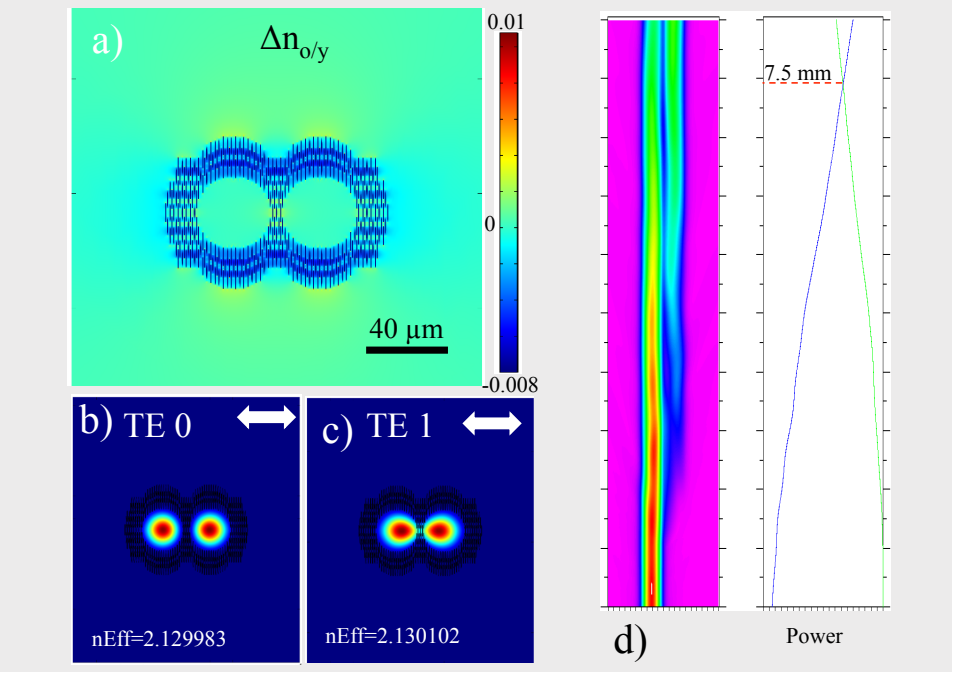

Fig. 6.14. Simulations of evanescent coupling of CLW2R_36s with a separation of 42 µm: refractive index profile with y-component (a), first and second order modes (b) (c), and propagation profile (d). 50/50 splitting occurs at the half coupling length of 7.5 mm.

In the first configuration, the two CLWs are placed at the distance of 42 µm (from centre to centre) which leaves three tracks in between them [Fig 6.14]. By performing the FEM calculation, two coupled modes were found along with discrete effective indices [Fig. 6.14 (b) and (c)]. Theoretical coupling length ($L_{100\%}$) can be estimated by the formula [13]:

$$L_{100\%} = \frac{\lambda}{2(nEff1 - nEff2)}$$

Where nEff1 and nEff2 are the effective indices of first and second modes, respectively. λ is the radiation wavelength which is 3.68 μm in this case. The coupling length at which 50:50 splitting occurs can be readily calculated by: $L_{50\%} = L_{100\%}/2$.

In the case of 42 μm separation of the two CLWs, by applying the computed effective index values, the coupling length is obtained: $L_{100\%}$ = 15462 μm, or the coupling length for 50:50 splitting is ~7.5 mm. As shown in Fig. 6.14 (d), the FD-BPM propagation simulation also agreed with this value. This coupling length is however too long for practically making a splitter usually embedded in a compact photonic device of cm's size.

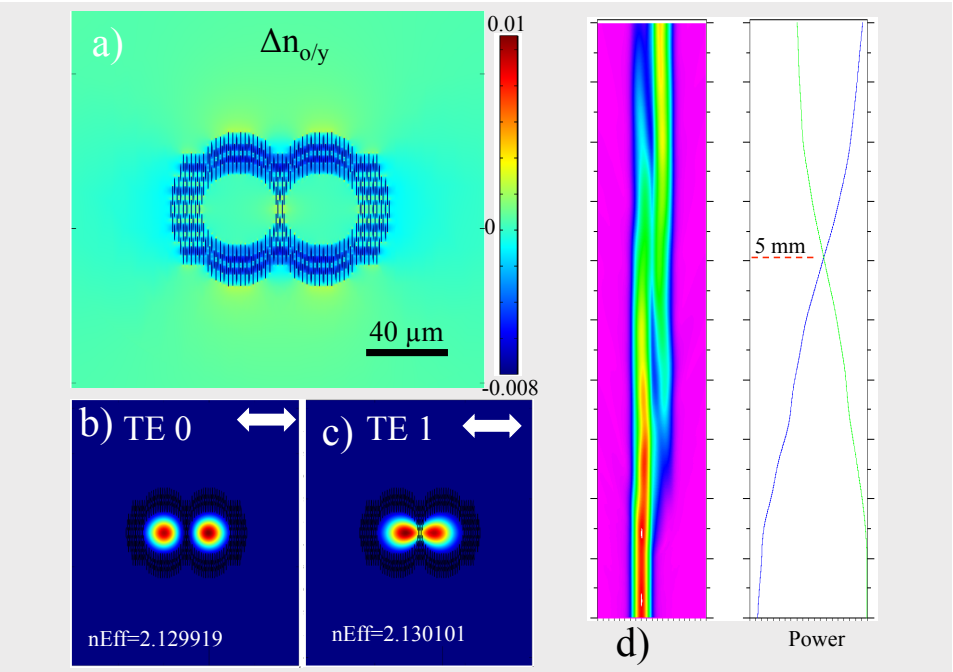

Fig. 6.15. Simulations of evanescent coupling of CLW2R_36s with a separation of 40 μm: refractive index profile with y-component (a), first and second order modes (b) (c), and propagation profile (d). 50/50 splitting occurs at the half coupling length of 5 mm.

In the second configuration, a distance of 40 μm is kept between the two CLWs or 2 tracks are left between them [Fig. 6.15]. Again, the FEM simulation results the coupled modes together with their effective indices [Fig. 6.14 (b) and (c)]. As theoretically

calculated and further confirmed in the FD-BPM propagation [Fig. 6.15 (d)], the coupling length at 50:50 splitting is reduced to 5 mm. However, this length still has not reached the ideal requirement for having a compact device.

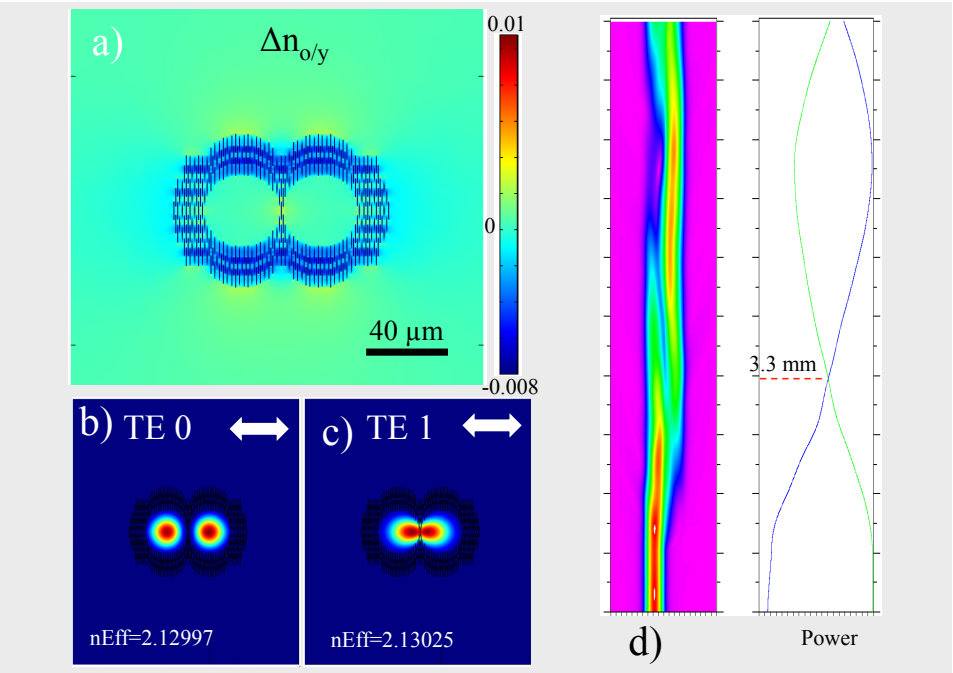

Fig. 6.16. Simulations of evanescent coupling of CLW2R_36s with a separation of 38 µm: refractive index profile with y-component (a), fundamental guided modes (b) (c), and propagation profile (d). 50/50 splitting occurs at the half coupling length of 3.3 mm.

In the last configuration, only one track is remained between the two CLWs which leaves the distance from the two waveguide centres to 38 µm. The results from both FEM mode analysis [Fig. 6.16(b) and (c)] and FD-BPM propagation [Fig. 6.16(d)] shows the coupling length of 3.3 mm for 50:50 splitting. This length is suggested to be short enough for a compact design of a splitter and long enough to easily handle the 50:50 splitting of the two branches.

Design of a 50:50 directional splitter

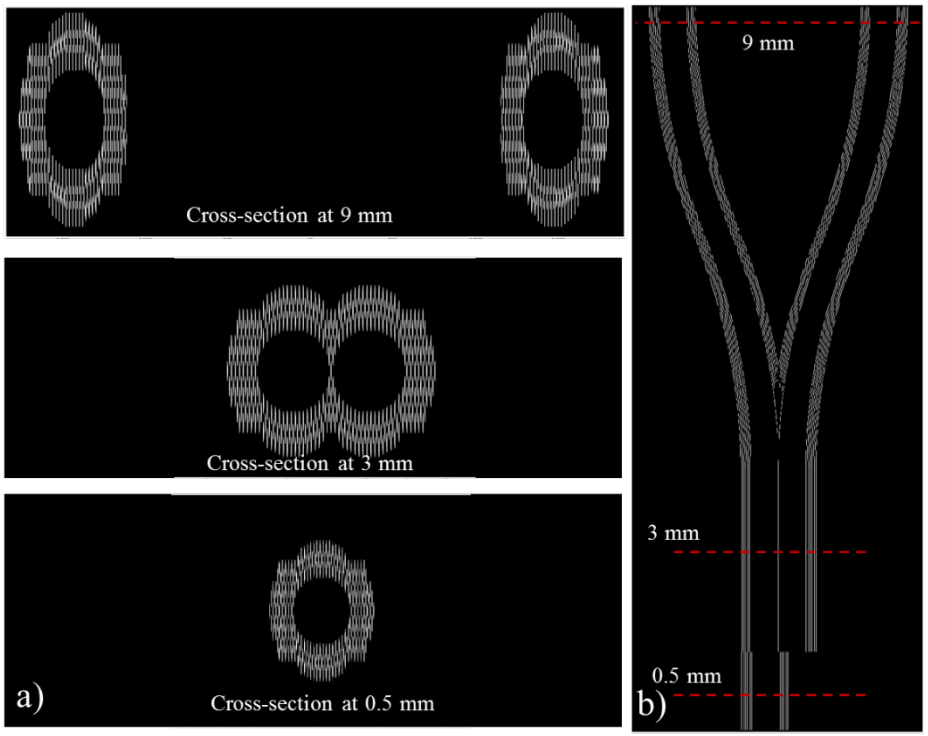

Fig. 6.17. Cross-sections (a) and structure (b) of a directional beam splitter on CLWs.

In the splitter configuration, the 50:50 directional splitting is achieved by placing two s-bends to the two coupled waveguides at the place where half of the coupling length has reached. The CLWs are separated from the initial distance of 38 µm to 290 µm by s-bends with bend-radius of 74.1 mm after 6 mm length of propagation [Fig. 6.17]. The cross-sections at 0.5 mm, 3 mm and 9mm are illustrated in Fig. 6.17 (a). It is worth noticing that at the intersection of the two s-bends and the two coupled CLWs some tracks must be systematically designed to join and expand for a proper configuration without leakage of the cladding. For fabrication, this configuration can be achieved by defining discrete joints where tracks are either overlapped or diverted (can be done with G-code on Aerotech Motion stages).

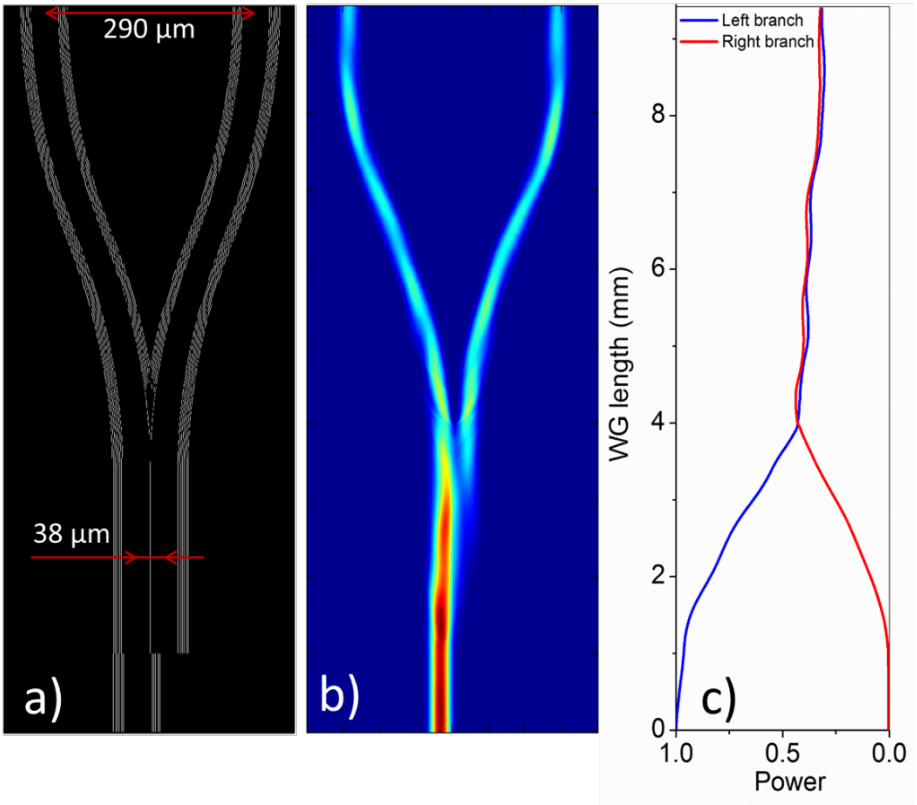

Fig. 6.18. Structure (a), propagation simulation (b) and power graph (c) of a directional beam splitter using mid-IR $LiNbO_3$ CLWs.

Performance of the splitter was carried out by launching a fundamental mode to the input waveguide, while recording the power losses on each waveguide branches [Fig. 6.18]. The 50:50 splitting was clearly observed after the beam leaves the half coupling length of 3.285 mm and separated equally to the two s-bends. The total excess loss [$=10*\log(P_{in}/(P_{out1}+P_{out2})$] of 1.9 dB was observed for the chosen length of 9.4 mm. This result demonstrates the possibility of implementing beam splitting waveguide circuits capable of operating at the mid-IR range, for the first time to our knowledge, in $LiNbO_3$ crystals.

Design of a Mach-Zehnder structure

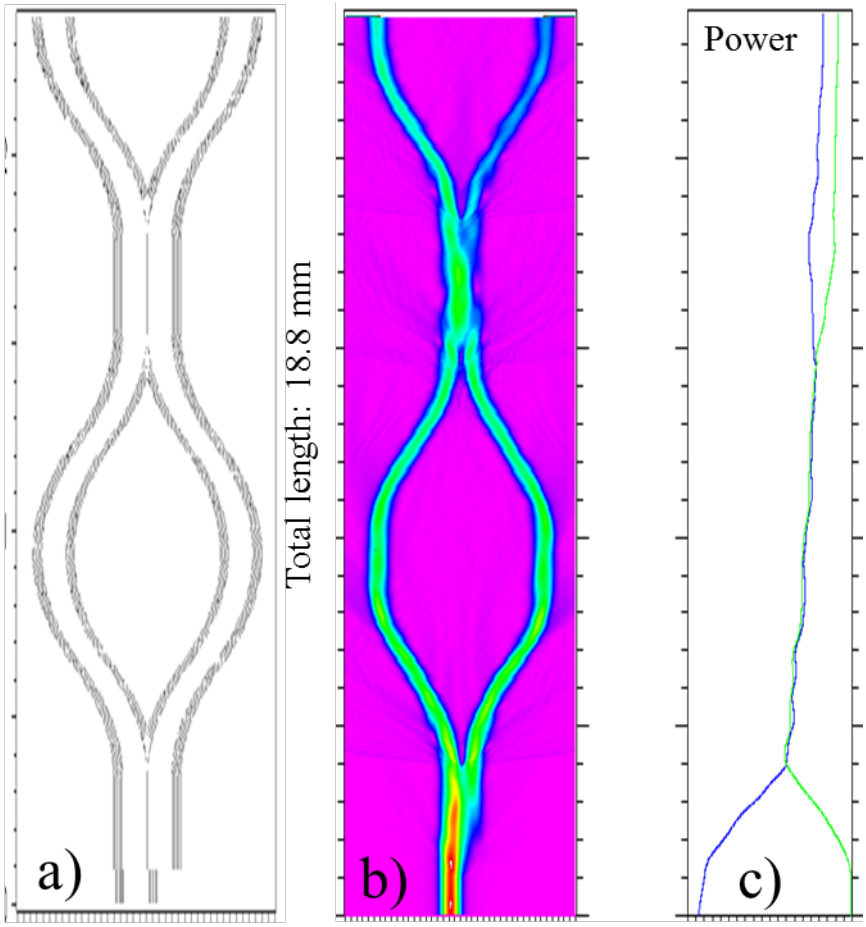

Fig. 6.19. Structure (a), propagation simulation (b) and power graph (c) of a Mach-Zehnder configuration in mid-IR $LiNbO_3$ CLWs.

Following the desirable performance of the directional beam splitter, a Mach-Zehnder configuration is designed simply by combining two splitters in reversed directions. The configuration with total length of 18.8 mm, propagation result and power graph are demonstrated in Fig. 6.19 (a) (b) and (c) respectively. It can be seen that the beam is equally split, re-joined at the second evanescent interaction junction and split again to two branches at the end. However, it has been noticed that the lights coming out of the two arms at the end are not equal; suggesting a small phase shift occurred at the optical

splitting/ joining parts. This means that either the splitter might not give exactly 50:50 splitting, or the joining junction might induce a phase shift. The result demonstrates highly sensitivity of this MZ structure with respect to the change of light properties; which is crucial for application in sensing devices, light modulators and interferometers.

Reference

1. R. He, Q. An, Y. Jia, G. R. Castillo-Vega, J. R. Vázquez de Aldana, and F. Chen, *Femtosecond laser micromachining of lithium niobate depressed cladding waveguides.* Optical Materials Express, 2013. **3**(9): p. 1378-1384.
2. Q. An, Y. Ren, Y. Jia, J. Rodríguez Vázquez de Aldana, and F. Chen, *Mid-infrared waveguides in zinc sulfide crystal.* Opt. Mat. Express, 2013. **3**: p. 466-471.
3. A. Rodenas, G. A. Torchia, G. Lifante, E. Cantelar, J. Lamela, F. Jaque, L. Roso, and D. Jaque, *Refractive index change mechanisms in femtosecond laser written ceramic Nd:YAG waveguides: micro-spectroscopy experiments and beam propagation calculations.* Applied Physics B, 2009. **95**(1): p. 85-96.
4. H. Karakuzu, M. Dubov, S. Boscolo, L. A. Melnikov, and Y. A. Mazhirina, *Optimisation of microstructured waveguides in z-cut $LiNbO_3$ crystals.* Opt. Mat. Express, 2014. **4**(3): p. 541-552.
5. A. Rodenas, *Direct femtosecond laser writing of 3D photonic structures in rare-earth doped lithium niobate*, in *Departamento de Física de Materiales*. 2009, Universidad Autónoma de Madrid.
6. R. Osellame, G. Cerullo, and R. Ramponi, *Femtosecond Laser Micromachining: Photonic and Microfluidic Devices in Transparent Materials*. 2012: Springer Berlin Heidelberg.
7. S. Gross, N. Jovanovic, A. Sharp, M. Ireland, J. Lawrence, and M. l. J. Withford, *Low loss mid-infrared ZBLAN waveguides for future astronomical applications.* Opt. Express, 2015. **23**: p. 7946-7956.
8. J. Hu and C. R. Menyuk, *Understanding leaky modes: slab waveguide revisited.* Advances in Optics and Photonics, 2009. **1**(1): p. 58-106.
9. R. He, Q. An, J. R. Vázquez de Aldana, Q. Lu, and F. Chen, *Femtosecond-laser micromachined optical waveguides in $Bi_4Ge_3O_{12}$ crystals.* Applied Optics, 2013. **52**(16): p. 3713-3718.
10. J. Martınez de Mendıvil, D. Sola, J. R. Vazquez de Aldana, G. Lifante, A. H. de Aza, P. Pena, and J. I. Pena, *Ultrafast direct laser writing of cladding waveguides in the $0.8CaSiO_3$-$0.2Ca_3(PO_4)_2$ eutectic glass doped with Nd^{3+} ions.* J. Appl. Phys., 2015. **117**: p. 043104.
11. J. Hu and C. R. Menyuk, *Understanding leaky modes: slab waveguide revisited.* Adv. Opt. Photonics, 2009. **1**: p. 58–106.
12. J. Burghoff, H. Hartung, S. Nolte, and A. Tünnermann, *Structural properties of femtosecond laser-induced modifications in $LiNbO_3$.* Applied Physics A, 2007. **86**(2): p. 165-170.
13. W. P. Huang, *Coupled-mode theory for optical waveguides: an overview.* J. Opt. Soc. Am. A 1994. **11**(3): p. 963-983.

7

Development of $LiNbO_3$-CLWs with intermediate repetition rate regime

This chapter describes the process for obtaining low-loss single mode mid-IR $LiNbO_3$-CLWs using the intermediate repetition rate laser pulses.

Contents

7.1. Introduction

Some previous reports has demonstrated that the increase of laser pulse repetition rate provides substantial effects on the laser modifying process in the 3DLW technique [1-5]. The first associated effect comes with the heat accumulation generated after a number of pulses. This makes the volume of modification become larger than the geometrical size of the laser focal spot [1, 3, 6]. Secondly, the thermal cycles of the medium during the laser processing reduce [1, 3], leading to a reduction of the generated stress as a result of annealing effect. Thirdly, the presence of more pulses per unit of time speeds up the processing time, which is crucial for developing complex optical circuits containing thousands of laser-written elements [7, 8]. Additionally, greater refractive index contrast can be obtained by laser modification in the high repetition rate regime [9].

As studied in chapter 6, the low repetition rate (1 kHz) laser processing results in a strong stress-induced effect at surrounds of the laser-irradiated volume in $LiNbO_3$. This strong anisotropic stress fields causes the laser-written $LiNbO_3$ CLWs to have highly anisotropic behaviours which are not ideal for many applications. Therefore, the CLWs are usually post-processed with thermal treatments to improve their optical properties.

In this chapter, with the goal to reduce the generation of anisotropic stress, and increase the contrast of the RI modification, the CLWs are investigated in an intermediate repetition rate (100 kHz) regime. In the first part, the laser processing in the transversal writing scheme is studied towards development of straight and s-bend CLWs capable of single-mode low-loss guiding for both polarised lights at the mid-IR range. In the second part, the longitudinal laser writing scheme is also explored. The new approach is targeted to offer symmetric profile of the laser modification. The CLW structures therefore can be symmetrically arranged in circular, lattice-like (hexagonal), and helical geometries, resulting in minimal effects of the anisotropic stress, and better optical performance.

7.2. CLWs in transversal writing scheme

In this first part, the CLWs are developed by the traditionally transversal writing scenario. The laser modifying process is thoroughly studied in the 100 kHz repetition rate regime to optimise most appropriate parameters for constructing CLW structures. Both straight and s-bend waveguide geometries are developed with optimised fabrication

conditions. As the main stream of the thesis, the single-mode low-loss optical performance of the waveguides at the mid-IR wavelength is targeting.

7.2.1. Design and modelling

The CLW structures and numerical modal analysis are carried out by the fundamental FEM model that has been described in chapter 5 and using throughout this thesis. The optimised CLW designs are taken from the previous studies in chapter 6. Waveguiding core diameters are ranging between 40 and 50 µm, while cladding spatial widths/ thicknesses are in the range from 30 to 40 µm. Light propagation of both straight and s-bend CLWs are modelled by FD-BPM simulation that is also presented in chapter 5.

7.2.2. Experimental details

General information of the transversal writing geometry has been described in chapter 4, and in a particular case in chapter 6. In this section, the laser processing is compared between two orientations of the $LiNbO_3$ sample (Fig. 7.1). In the first study [Fig. 7.1 (a)], the laser beam is propagated along the z-axis and focused on the xy plane of the sample. This is a typical orientation of fabrication on z-cut $LiNbO_3$ sample. Fig. 7.1 (b) shows the second case when the laser beam is propagated along the y-axis and focused on the xz plane of the sample. The case is associated with orientation of y-cut $LiNbO_3$ sample.

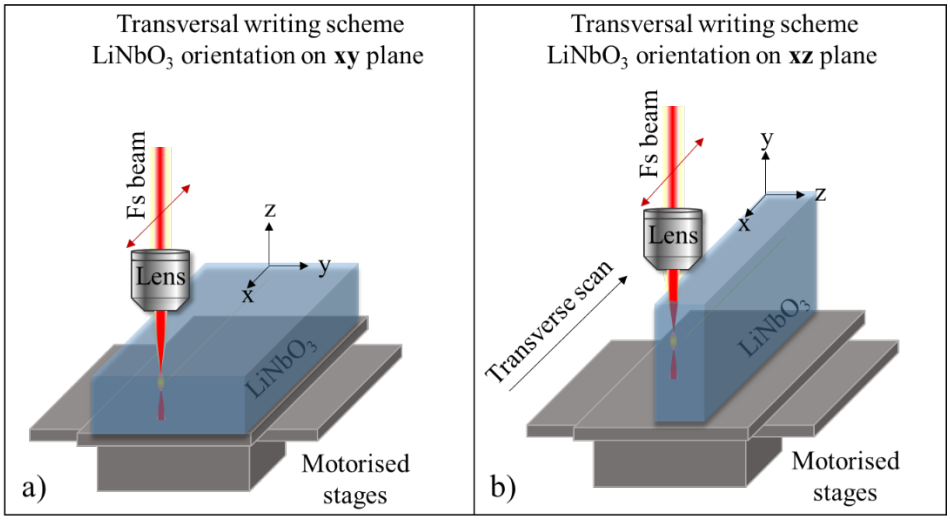

Fig. 7.1. Schematic of transversal laser writing scheme on z-orientation (a) and y-orientation (b) of $LiNbO_3$ sample.

In both cases, the laser polarisation and scanning direction are made along the x-axis. The laser beam is focused at ~300 μm depth inside the bulk material. A high-resolution three-axis motorised stage – Aerotech Motion was used to mount the sample and precisely move the positions corresponding to a programmed script.

The ultrafast laser beam was generated by a Ti:Sapphire regenerative amplified laser system (RegA 9000) which was set to the intermediate repetition rate of 100 kHz, at a central wavelength of 800 nm. The pulses are temporally chirped by an external pulse shaping unit. Pulse energies are adjusted by a motorised half-wave plate. During experiments, a variety of laser fabrication parameters: e.g. pulse duration, energy, scan speed and focusing lenses was used. The parameters are specified in each case, corresponding to specific sets of experiments.

Thermal post-processing

Thermal treatments of fabricated CLWs were additionally processed, with the aim to remove the unwanted TypeI-modified regions which might occur along with the Type II modification. The waveguides were thermally treated in a furnace with open-air condition. The thermal annealing conditions were set at peak temperature of 473 K, for 2 hours and with ramp of 2 K per minute.

Characterisation

The structures modified by static shots of the laser pulses were instantaneously observed by a built-in phase contrast microscope. The laser-written CLW structures were qualitatively analysed by a transmission microscope before and after the thermal treatments. Optical characterisation and loss measurement were then performed at the mid-IR wavelength of 3680 nm. Details are described in chapter 4.

7.2.3. Parametric investigation

A recent report has demonstrated that a significant difference in the modification is observed when the laser processing pulses are focused on different orientations of the $LiNbO_3$ crystal [10]. The effect originates from the strong birefringence of the material and associates to the orientation of the pulse propagation direction with respect to the optical axis of the $LiNbO_3$ crystal. In this section, dependence of laser modification on the two common orientations of the $LiNbO_3$ sample is studied with identical laser

fabrication conditions. Static shots of the laser pulses are made on the sample with typical exposure time of 1 second. In the 100 kHz repetition rate system, it is equivalent to arrival of 100 $\times 10^3$ pulses within the unit time of 1 second.

Z-orientation of $LiNbO_3$ sample

As previously illustrated in Fig. 7.1 (a), in this case the pulses are propagated parallel to the optical z-axis of the sample, and focused at a constant depth of ~300 μm. Laser parameters were systematically studied with a fixed pulse energy of 3 μJ and varying values of temporal pulse durations (table 7.1).

Table 7. 1. Laser fabrication parameters for static shots on z-orientation of $LiNbO_3$ sample

Repetition rate	100 kHz
Central wavelength	800 nm
Pulse duration	1000 fs – 350 fs
Pulse energy	3 μJ
Polarisation	**Linear, perpendicular to optical z-axis**
Pulse propagation	**Parallel to the optical z-axis**
Exposure time	1 s
Pulse per second	100 $\times 10^3$ pulses
Focusing optics	Aspheric lens NA 0.5
Depth of focused beam	~300 μm
Sample orientation	z-cut $LiNbO_3$ sample: z-orientation

In this laser processing geometry along z-orientation of the sample, the cross-sectional structures were observed in the zy plane or zx plane, both presenting the same profiles. Phase contrast images of the modified regions (filaments) are shown in the Fig. 7.2. It is noticed that the exposure of the pulses results in Type II modification (a decrease of RI), while TypeI modification was not observed at all. Specifically, at pulse durations of longer than 800 fs, the material resulted in void-like structures with two separated regions of modification. This is a result of micro-explosion when the material is exposed to near picosecond regime. The pulses at this long range therefore are not desirable for developing CLWs in which homogeneous laser-modified tracks are required for efficient cladding arrangements. The modifying process became less efficient when the pulse durations were shorter than 600 fs. In particular modified regions were not noticeable

when pulses of shorter than 350 fs were exposed. This can be recognised as the pulse duration threshold for this particular laser processing along z-orientation.

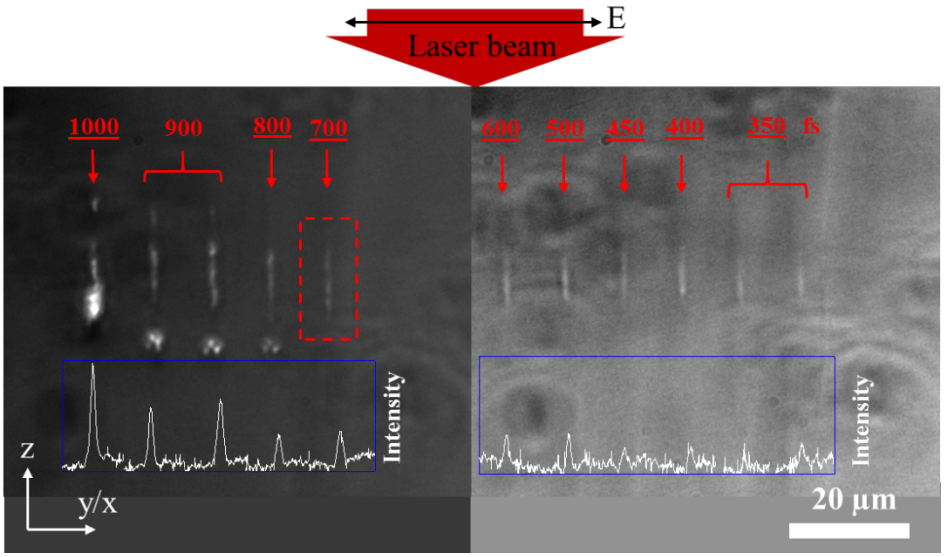

Fig. 7.2. Phase contrast images of filaments created by single-shot irradiation of different pulses. The laser beam was propagated parallel to the optical z-axis of the $LiNbO_3$ sample.

The inset graphs in Fig. 7.2 show cross-sectional intensity of the laser-modified area. By comparing all the laser-modified filaments, the filament irradiated by 700 fs pulses clearly demonstrates the highest RI contrast, and no amorphous void-like formation.

Y-cut orientation of $LiNbO_3$ sample

It is worth to recall here the geometry of the laser processing in this orientation of the $LiNbO_3$ crystal as illustrated in Fig. 7.1 (b). In particular, the laser pulses were propagated perpendicular to the optical z-axis of the crystal. The polarisation direction and other laser parameters remains the same as those used in the previous experiment (table 7.2).

Table 7. 2. Laser fabrication parameters for static shots on y-cut orientation of $LiNbO_3$ sample

Repetition rate	100 kHz
Central wavelength	800 nm
Pulse duration	1500 fs – 200 fs
Pulse energy	3 µJ

Polarisation	**Linear, perpendicular to optical z-axis**
Pulse propagation	**Perpendicular to the optical z-axis**
Exposure time	1 s
Pulse per second	100 $\times 10^3$ pulses
Focusing optics	Aspheric lens NA 0.5
Depth of focused beam	~300 µm
Sample orientation	z-cut $LiNbO_3$ sample: y-orientation

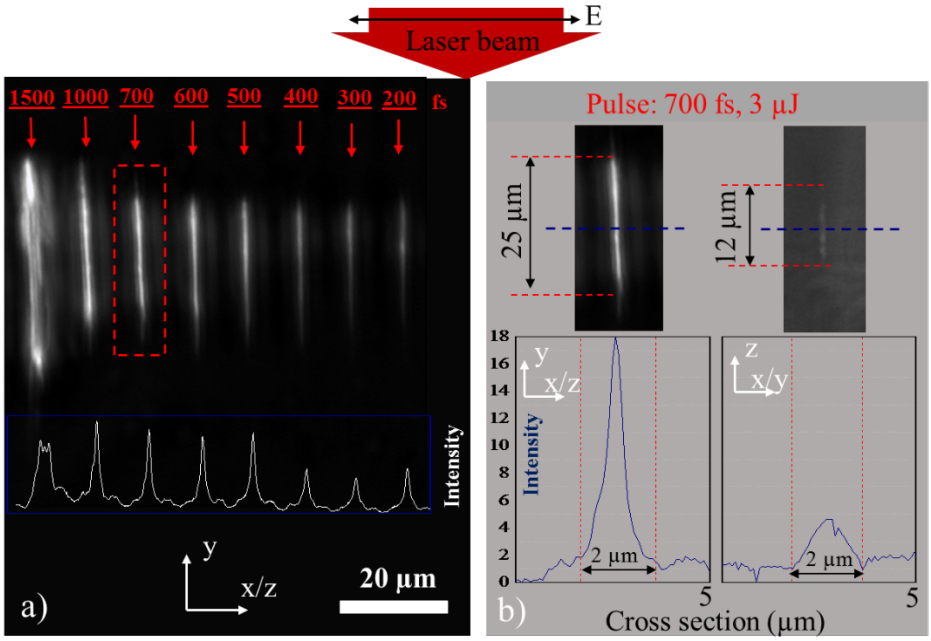

Fig. 7.3. Phase contrast images of filaments created by single-shot irradiation of different pulses. The laser beam was propagated perpendicular to the optical z-axis of the $LiNbO_3$ sample (a). and Comparison of the two filaments obtained by laser processing along two different orientation of the sample (b).

Results of the laser modification are shown in a phase contrast image [Fig. 7.3 (a)]. Due to the symmetry of the focused Gaussian beam, cross-section observation of the laser-modified filaments on the yx plane and yz plane are almost identical. Similar to the process along the z-orientation, there was no Type I modification was observed. The image shows a strong Type II modification occurred during the laser processing in this y-cut orientation. As expected, a decreasing trend of RI contrast with respect to the decrease of pulse duration was recorded. The noticeable modification was obtained using the temporal pulses of as short as 200 fs which was not observed in the case of the

process along z-orientation. It is believed that pulses of < 200 fs are still able to effectively modify the $LiNbO_3$ in this orientation, though shorter pulses were not available to carry out more tests for confirmation.

The effectiveness of the laser modification between the processes along the two orientations was examined by comparing RI contrast of the two filaments that were obtained by the same laser pulses of 700 fs and energy of 3 μJ. As shown in Fig. 7.3 (b), the filament processed along y-cut orientation clearly provides significantly higher RI contrast (~4-fold higher) than the one obtained in the case of z-orientation. Additionally, it has been seen that the filament processed along y-orientation was more elongated than the other (25 μm compared to 12 μm). The width of the two filaments however was measured to be the almost same size of ~2 μm.

The optimised laser parameters therefore were concluded with 700 fs and μJ. These parameters are used to fabricate CLW structures in both y- and z-orientations. Results are presented in the next sections.

7.2.4. Straight and s-bend CLWs

It was obvious that the laser modifying process in y-orientation of the sample has a huge advantage over the other in terms of the resultant RI contrast. However, the strong modification results in strong damages, leading to fragility of the laser-fabricated microstructures. Evidently, large cracks were observed on the surface of the sample. These cracks further propagated during the polishing process, causing all the laser-written CLWs broken, and not able to characterise.

Therefore, only CLWs fabricated by the laser processing along the z-orientation are reported in this section. The fabrication parameters are listed in table 7.3. The chosen pulse duration is 700 fs as studied in the previous section. Scan speed of 0.7 mm/s was used, for comparing with the conditions in low 1 kHz repetition rate regime. It should be noted that in this 100 kHz repetition rate system, the scan speed can be increased 100 times faster for equivalent effect of the laser modification.

Table 7. 3. Laser fabrication parameters for writing CLWs in $LiNbO_3$ sample

Repetition rate	100 kHz
Central wavelength	800 nm
Pulse duration	700 fs

Pulse energy	3 µJ
Polarisation	**Linear, perpendicular to optical z-axis**
Pulse propagation	**Parallel to the optical z-axis**
Scan speed	0.7 mm/s
Focusing optics	Aspheric lens NA 0.5
Depth of focused beam	~300 µm
Sample orientation	z-cut $LiNbO_3$ sample: z-orientation

Straight CLWs

The first CLW structure (namely CLW1) was designed with core diameter of 44 µm, and spatial cladding thickness of 40 µm (Fig. 7. 4). As investigated in the previous section, the individual laser-written track has elliptical shape with dimensions of 2 µm × 12 µm. The horizontal spacing between the tracks is kept at 2 µm. This CLW geometry contains 176 tracks which takes 1-2 hours to fabricate the complete waveguide length of 20 mm with scan speed of 0.7 mm/s. For future reference, this processing time can be speeded up to time scale of tens of minutes by scanning the laser with speed of 70 mm/s.

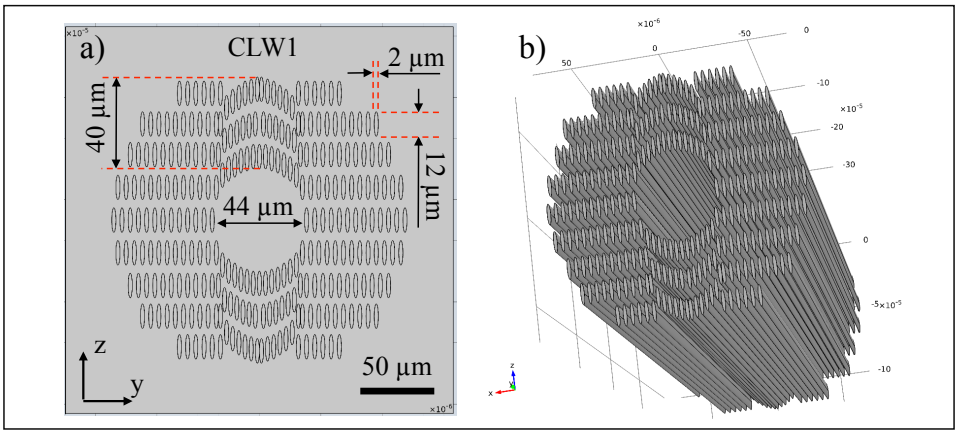

Fig. 7.4. Geometrical design of the CLW1 in 2D (a) and 3D (b).

The CLW1 was characterised for its structure and optical guiding at the wavelength of 3.68 µm. Structure of the as-fabricated CLW1 is shown in Fig. 7.5 (a), indicating a well-match with the design. However, apart from the Type II depressed-cladding structure, it looks like that Type I modification (the brighter area) additionally occurred at the lower part of the depressed-cladding structure. The thermal annealing post-process at peak temperature of 473 K for 2 hours was performed with the intension to reduce/remove the unwanted Type I modified regions. As shown in Fig. 7.5 (b), the bright area below the

depressed cladding structure almost disappeared, indicating that the removal of the Type I regions was clearly achieved. Regarding to the optical guiding performance, the as-fabricated CLW1 supports single-mode guiding with very low PL of 0.4 dB/cm for TE polarised light. For the TM mode, the CLW1 has PL of 2.6 dB/cm which is significantly higher than the value for TE mode. This anisotropic behaviour commonly obtained in the $LiNbO_3$ CLWs. On the other hand, the annealed CLW1 did not seem to improve the guiding performance. No significant change of the PLs was recorded. This indicates that the effect of the Type I modified in this CLW was not critical.

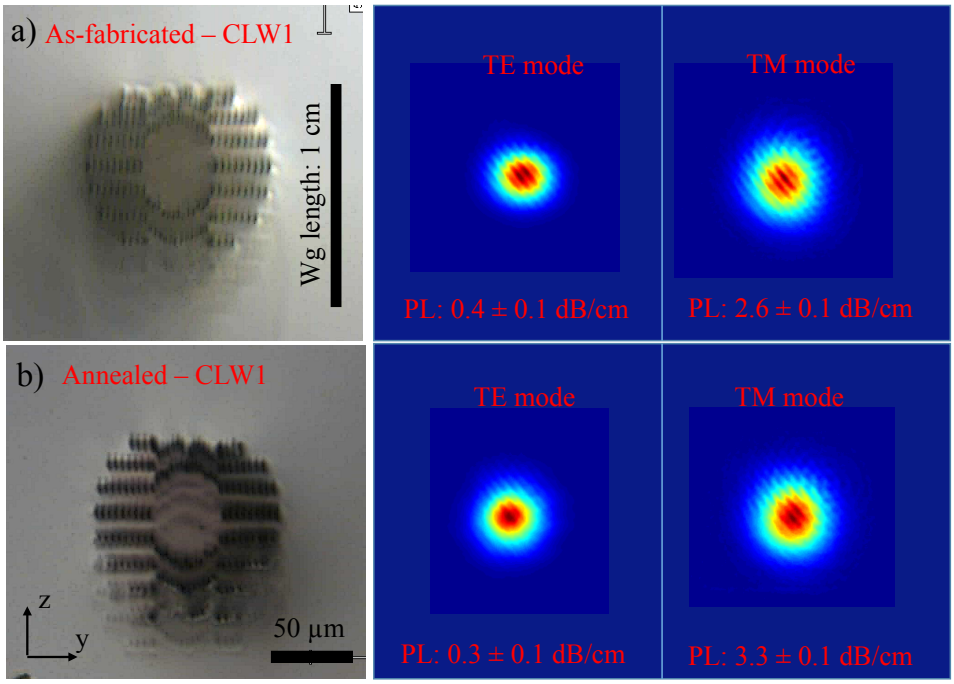

Fig. 7.5. Transmission images of the transversally laser-written CLW structures and near-field guided modes of the as-fabricated CLW1 (a) and the annealed CLW1 (b).

As discussed in chapter 6, the anisotropic behaviour can be corrected by applying appropriate designs: such as the increase of the spatial cladding thickness. The second design (namely CLW2) was investigated. It contains 270 tracks forming a core diameter of 44 µm and spatial cladding thickness of 55 µm (Fig. 7.6). Other parameters: i.e. spacing between the tracks and individual track dimensions are kept the same as those parameters in the design of the CLW1.

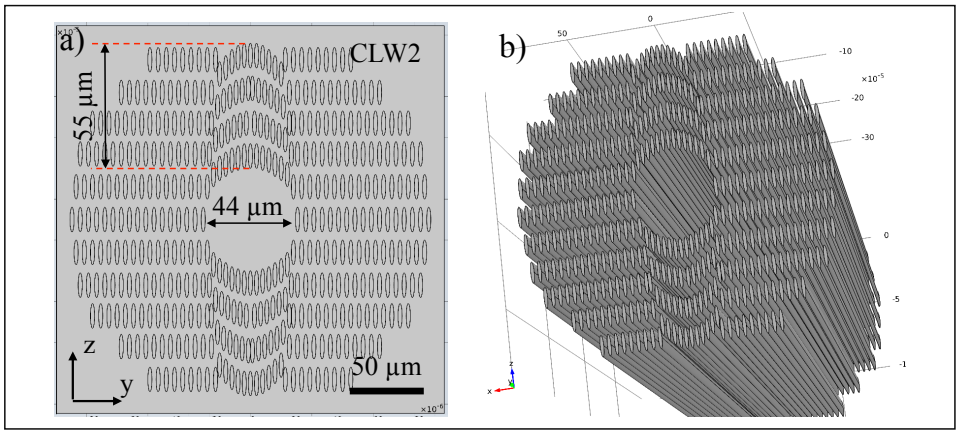

Fig. 7.6. Geometrical design of the CLW2 in 2D (a) and 3D (b).

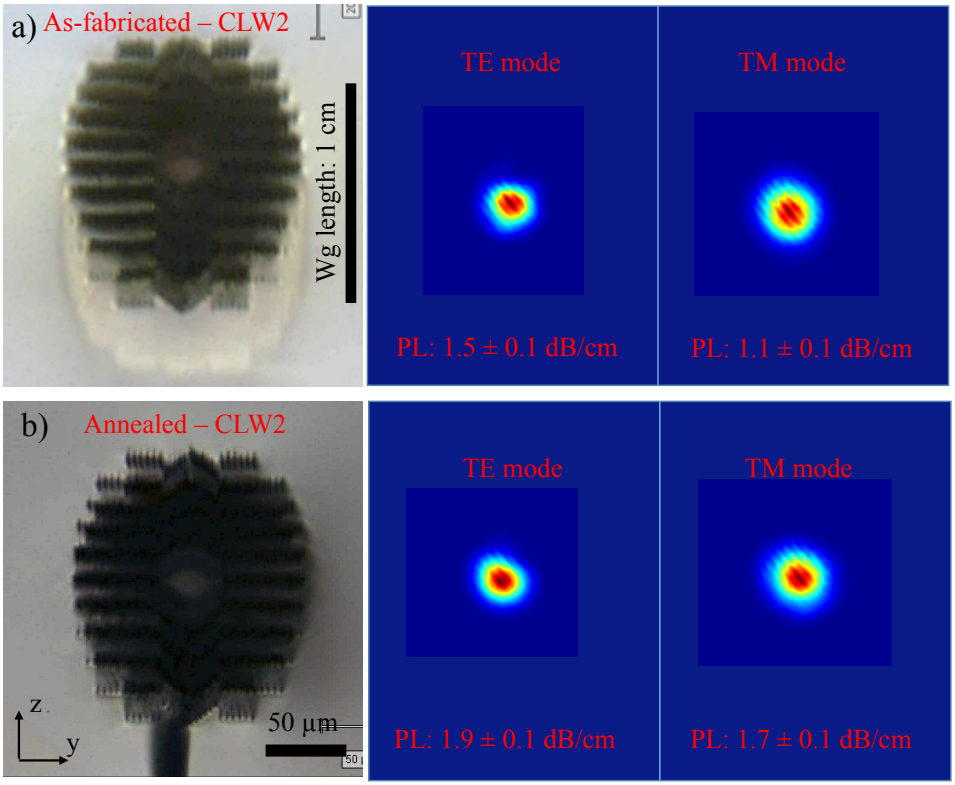

Fig. 7.7. Transmission images of the transversally laser-written CLW structures and near-field guided modes of the as-fabricated CLW2 (a) and the annealed CLW2 (b).

The laser fabrication of the CLW2 was processed with the same parameters used for the CLW1. As expected, the overall fabricated structure of the CLW2 has a good agreement with the structural design [Fig. 7.7 (a)]. The presence of Type I modified area was also

observed. In terms of the optical guiding quality, the CLW2 offers mid-IR guiding with relatively low PLs of ~1 dB/cm for both polarisations. This significant reduction of the anisotropic behaviour is credited to the appropriate arrangement of the cladding. The CLW2 was further annealed at peak temperature of 473 K for 2 hours. The annealed CLW2 no longer has the presence of the Type I modified region. However, its guiding quality did not improve, but got worse instead. As shown in Fig. 7.7 (b), the PLs increased to ~1.7 dB/cm after the CLW2 was thermally treated.

S-bend CLWs

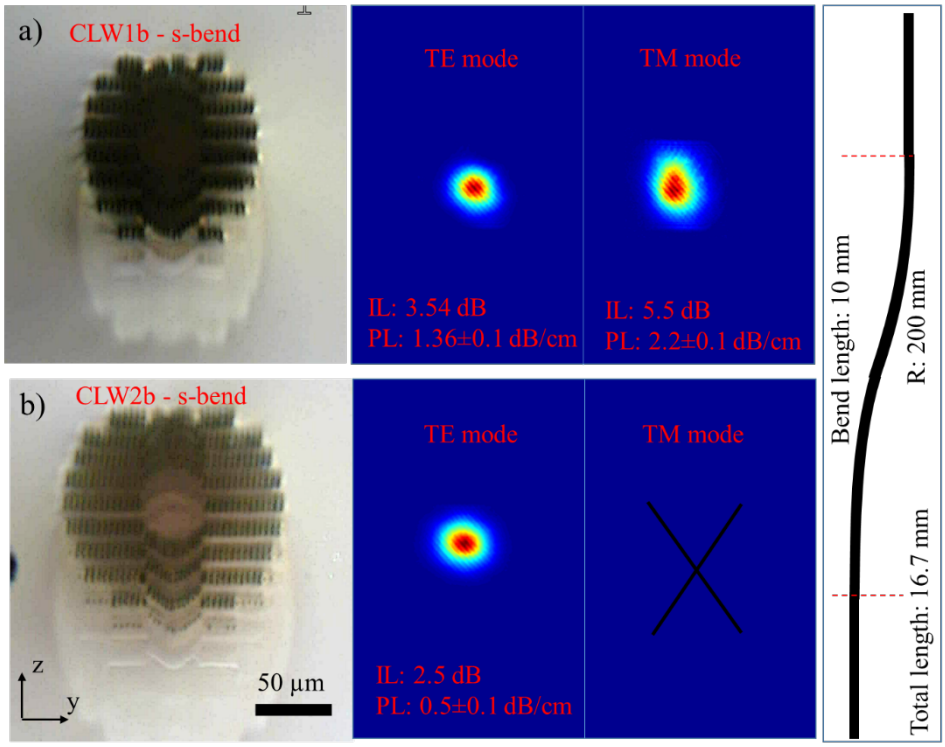

Fig. 7.8. Transmission images of the s-bend CLW structures and near-field guided modes of the as-fabricated CLW1b (a) and the CLW2b (b).

S-bend structures were laser-fabricated, using the designs of the CLW1 and CLW2. The s-bend CLWs denoted as CLW1b and CLW2b have a total length of 16.7 mm, in which length of the s-bend section is 10 mm, and bending radius of 200 mm (Fig. 7.8). Though laser fabrication parameters of the s-bend CLWs were set at the same as those used in the straight CLWs, the resulted structures of the s-bend CLWs look different from the

straight CLWs previously obtained. This is due to the un-stability of the laser system occurred at the time of fabrication. For this reason, the losses at the bending structures were not determined. The CLW1b has the geometrical design of the CLW1. It offers mid-IR for both polarisations with PLs ranging between 1 and 2 dB/cm. In the case of the CLW2b which was designed with geometrical CLW2 arrangement, it only supports TE mode guiding at the mid-IR. This behaviour is believed to be related to the unstable laser operation as previously mentioned. In this case, the low PLs of <0.5 dB/cm were achieved by the s-bend structure - CLW2b, implying the bend-loss is extremely low, though exact number was not confirmed.

Overall, the CLWs fabricated in this transversal writing geometry and intermediate repetition rate regime offers single-mode mid-RI guiding for both polarisation with relatively low-PLs of ~1 dB/cm, without the requirement of thermal annealing post-process. This is a clear sign of less anisotropic effect obtained by this intermediate repetition rate regime. It is a big improvement when compared to CLWs fabricated by the low-repetition rate system, in which strong anisotropic stress effects were observed.

7.3. CLWs in longitudinal writing scheme

Longitudinal laser writing geometry in 3DLW technique is defined by parallel scanning of the sample relative to the direction of laser beam propagation. It was initially introduced to offer symmetric profiles of modification which is a result of the transversely symmetric intensity profile of the focused Gaussian beam [11]. However, in this longitudinal writing geometry, the waveguide length is physically limited (typically up to 5 mm) by the focal working distance of the laser focusing objective [12]. More importantly, this limitation is due to the requirement of the high laser power to reach the intensity required for optical breakdown at such long travel inside the material [13]. To date most experimental works by the longitudinal writing geometry have been reported mainly for glass material [13, 14].

In the section, the longitudinal laser writing scheme is explored for fabrication of $LiNbO_3$ crystal. The new approach is expected to face big challenges due to the birefringence of the crystal, which complicates the laser modifying process, particularly at such long distance inside the material. The goal of using this approach is to obtain symmetric profile of the laser modification. The laser-modified CLW structures

therefore are symmetrically arranged in circular, lattice-like/ hexagonal, and helical geometries, resulting in minimal effects of the anisotropic stress, and better optical performance

7.3.1. Design and modelling

Similar to other works in this thesis, the CLW structures and numerical modal analysis are performed by the FEM model introduced in chapter 5. Several cladding geometries are designed as following:

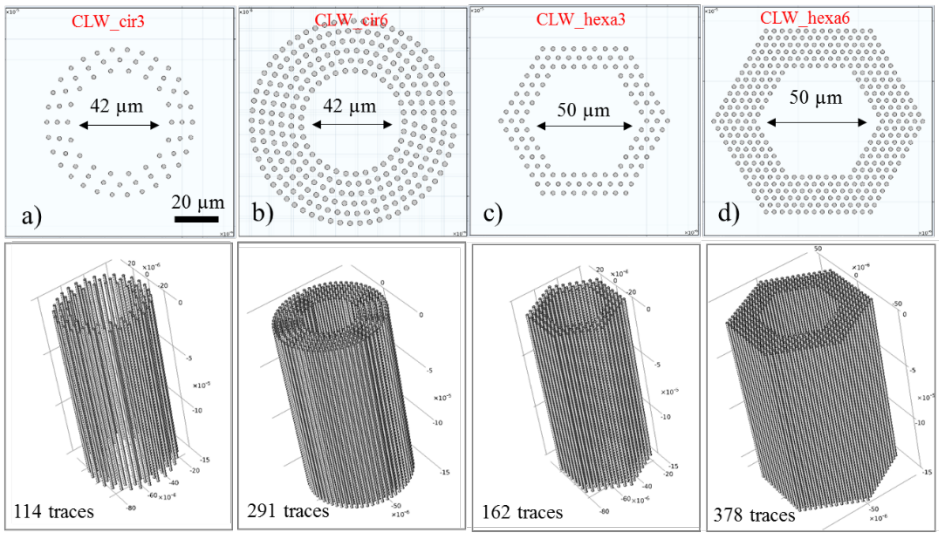

Fig. 7.9. CLW designs for longitudinal writing scheme: circular geometries with 3 layers of traces – CLW_cir3 (a), 6 layers of traces – CLW_cir6 (b); and hexagonal geometries with 3 layers of traces –CLW_hexa3 (c) and 6 layers of traces –CLW_hexa6 (d); along with their 3D visualisation.

The CLWs were designed with tubular arrangements of circular cross-sectional traces. Specifically, in the circular geometry, the CLW_cir3 and CLW_cir6 were arranged with the same core diameter of 42 µm and contains 114 traces and 291 traces respectively. In the lattice-like structures, the CLWs are arranged in hexagonal geometry containing 162 traces (CLW_hexa3) and 378 traces (CLW_hexa6), and with the same core diameter of 50 µm. It should be noted that the traces are assumed to have circular shape with diameter of 2 µm, as it was measured for the filament fabricated by 700 fs pulse, 3 µJ energy, and at the depth of ~300 µm inside the $LiNbO_3$ sample.

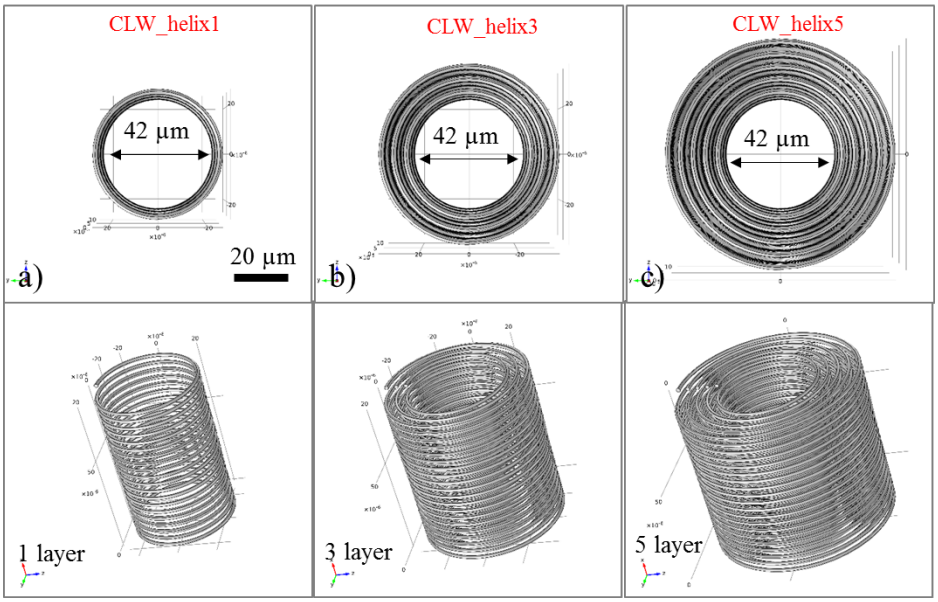

Fig. 7.10. CLW designs for longitudinal writing scheme: helical geometries with 1 layer of traces – CLW_helix1 (a), 3 layers of traces – CLW_helix3 (b), and 5 layers of traces –CLW_helix5 (c); along with their 3D visualisation

Another set of designs was made with helical structures. In this geometry, the laser focus is moved in helical trajectories, resulting continuous RI change along the irradiated path. Three designs have been made, including 1 layer, 3 layer and 5 layer structures (Fig. 7.10).

7.3.2. Experimental details

The laser fabrication system in this experiment was used the same as the previous one in section 7.3.2, except it is translated in the longitudinal scanning path. The longitudinal laser writing geometry is described in Fig. 7.11. In this setup, the laser is focused/propagated along the y-axis and perpendicular to optical z-axis of the sample. The polarisation was linearly aligned perpendicular to the z-axis. Longitudinal movements with complex trajectories are controlled by a programmable Aerotech Motion stage.

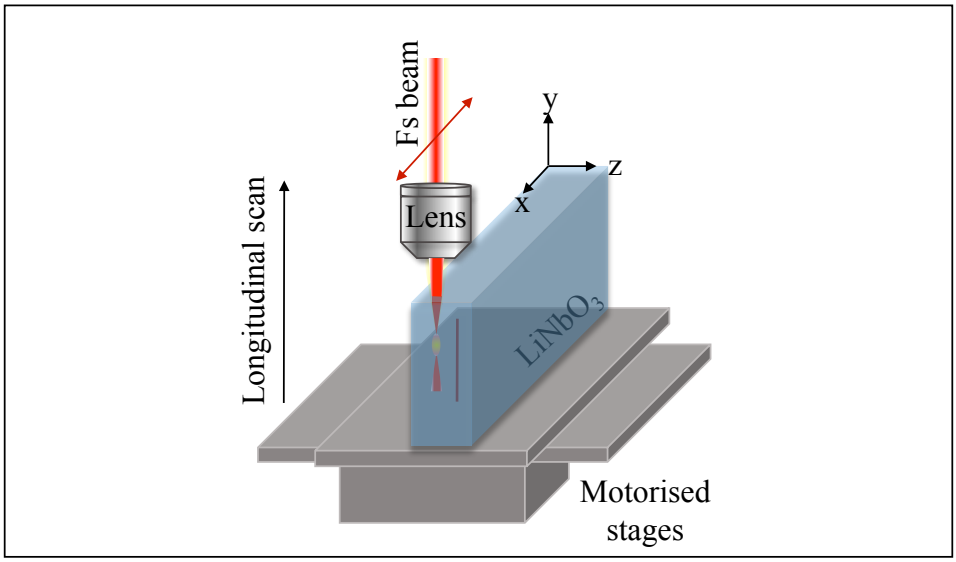

Fig. 7.11. Schematic illustration of 3DLW technique in longitudinal writing scheme.

7.3.3. Parametric investigation

Laser modification in the longitudinal scanning geometry is typically limited to a certain depth inside the material. Therefore, it is of paramount importance to choose appropriate focusing objective which allows long-distance focusing of laser beam inside the material without distortion of its path.

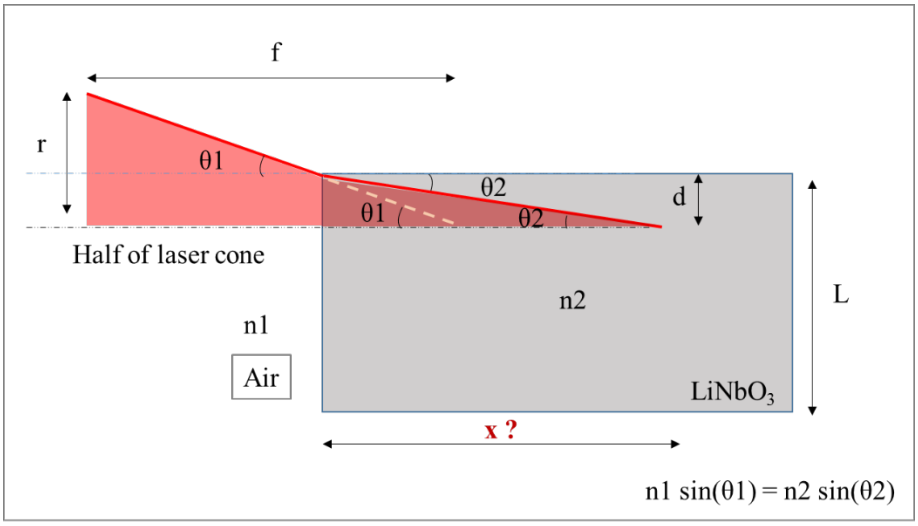

Fig. 7.12. Illustration of optical train of laser cone upon entering the $LiNbO_3$ sample: A base for calculation of maximum focusing depth corresponding to the use of objective lens.

Fig. 7.12 illustrates a simplified optical train when a laser beam is focused into the $LiNbO_3$ crystal. Due to the RI difference between the two mediums air-crystal, the laser beam is diffracted upon arriving in the crystal. The depth of focus (x) can be evaluated using simple calculations:

$$\tan(\theta 1) = \frac{r}{f}\ ; \tan(\theta 2) = \frac{x}{d}; \tag{7.1}$$

$$n1\ sin(\theta 1) = n2 \sin(\theta 2)\,; \tag{7.2}$$

Where n1 is the refractive index of air (n1 = 1), n2 is the refractive index of $LiNbO_3$ (n2 ≈ 2.1), r is radius of the laser beam (r ≈ 3 mm, measured), f is the focal length of the focusing lens and d is the distance from the laser focal point to the edge of the sample. Assuming the laser beam is focused at the distance (d) of 0.5 mm to the sample edge, and an aspheric lens with focal distance (f) of 8 mm is used, the maximum depth of the laser focus (x) inside the sample without aperturing the beam is calculated around 8 mm. By increasing the distance (d, up to 1 mm) to the sample edge, the focusing depth can be scaled up to 20 mm. This depth is long enough for the laser processing of long waveguides, typically 5mm. Another way to increase this focusing depth is the use of objective lens with low NA< 0.2, and long focal length >20mm. However, this is not ideal, since the laser intensity is decreased proportionally to the low NA lenses, therefore higher laser power is required to reach the optical breakdown of the material.

Laser modification at the 5 mm depth inside the $LiNbO_3$ crystal

This approach was designed to establish laser parameters for modification of the $LiNbO_3$ crystal at a maximum depth. It involves static shots of the laser pulses at the depth of 5 mm inside the material. The laser parameters are listed in table 7.4. The process was done using maximum available laser power delivered by an aspheric lens with NA of 0.5.

Table 7. 4. Laser fabrication parameters for static shots on z-orientation of $LiNbO_3$ sample at the depth of 5 mm

Repetition rate	100 kHz
Central wavelength	800 nm
Pulse duration	0.5 ps – 4.5 ps
Pulse energy	4.5 μJ

Polarisation	**Linear, perpendicular to optical z-axis**
Pulse propagation	**Parallel to the optical z-axis**
Exposure time	1 s
Pulse per second	100×10^3 pulses
Focusing optics	Aspheric lens NA 0.5
Depth of focused beam	~5 mm
Sample orientation	z-cut $LiNbO_3$ sample: z-orientation

At this depth, it was observed that the $LiNbO_3$ was not modified by laser pulses in the femtosecond regime. The negative Type II modification occurred when pulses of longer than 1ps were used (Fig. 7.13).

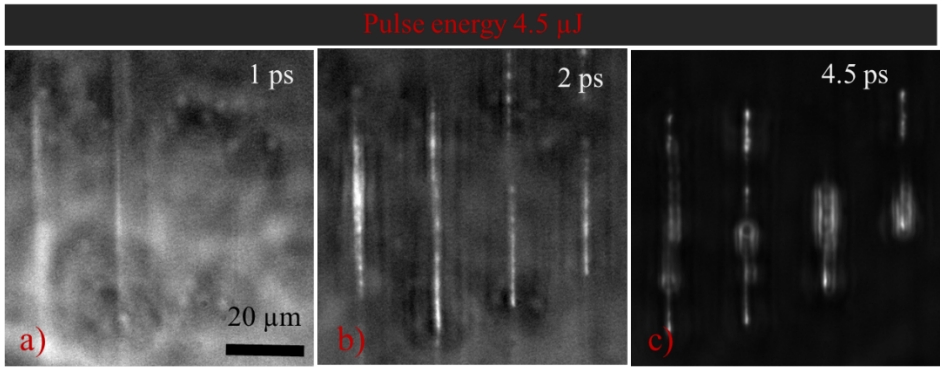

Fig. 7.13. Phase contrast images of filaments fabricated by 3DLW at depth of 5 mm inside $LiNbO_3$ sample.

It was however noticed that at long pulses of >2 ps, the void-like structures appeared, e.g. in the case of 4.5 ps. The appropriate condition therefore lies within the range of 1 and 2 ps.

Laser modification at the 0.3 mm depth inside the $LiNbO_3$ crystal

The previous examination has concluded that the RI modification at the 5 mm depth is feasible using the pulses within the range of 1 ps to 2 ps. It is of parallel importance to find suitable conditions for modification of $LiNbO_3$ at low depth of several hundred microns. The parameters must match a criterion of creating laser-modified region with high RI contrast, but not causing serious damage. Strong damages are typically induced by high laser power at the low focused depth. They can expand several micrometers, and usually come along with strong heat accumulation. These strong damaged structures therefore might distort the upcoming close-by beam, and limit the fabrication of

micrometric structures. For this reason, the laser processing was studied at 300 µm depth using low pulse energies of < 2 µJ (Fig. 7.14).

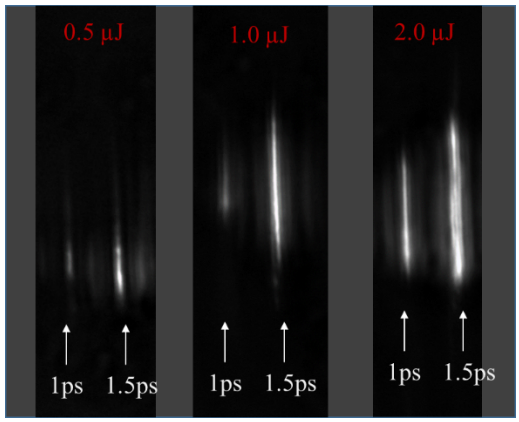

Fig. 7.14. Phase contrast images of filaments fabricated by 3DLW at depth of 0.3 mm inside $LiNbO_3$ sample: a comparison of different pulse energies.

Results show that the appropriate conditions were met when the laser pulses were used within the range of 1-1.5 ps and 0.5- 1.0 µJ.

Formation of laser-written traces with 5 mm length

Using the optimised parameters, the $LiNbO_3$ crystal was laser-inscribed with fixed pulse duration of 1.5 ps, and decreasing pulse energies from 3.5 µJ to 1 µJ on the fly. The laser pulses were focused at depth of 5 mm inside the crystal, and scanned upward to the surface with a constant velocity of 0.2 mm/s.

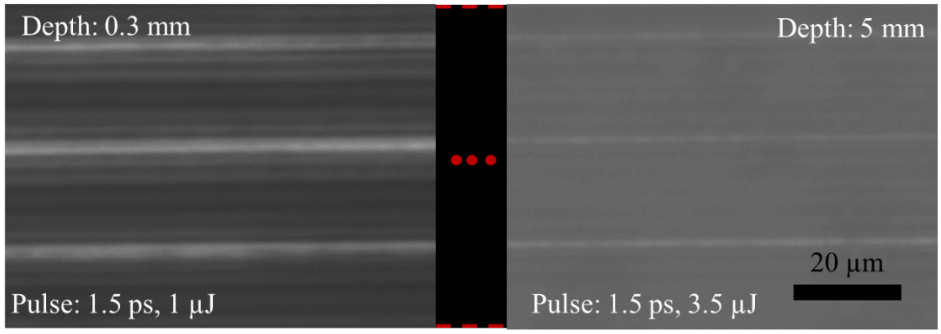

Fig. 7.15. Phase contrast images of traces laser-inscribed by 1.5 ps pulses, at a constant scan speed of 0.2 mm/s, and with varying the energy on the fly

Fig. 7.15 shows top-view phase contrast images of the modified traces. Three traces were repeated to confirm the reproducibility of the modifying process. At the close surface (0.3 mm) strong RI contrast of the modified region was observed, along with broaden width of the traces. The traces at the 5 mm depth appeared to have lower RI contrast and thinner in its spatial thickness. This inhomogeneity might have strong impact on overall profiles of CLWs.

Dependence of laser-written traces on scan speed

Another important parameter in 3DLW technique is the scan speed. The velocity of the scanning laser beam is directly related to the number of pulses arrived on a spatial unit. The $LiNbO_3$ sample was studied with varying scan speed, while keeping other parameters constant. As observed in Fig. 7.16, the laser modification is strongly sensitive to the scan speed: strong Type II change of RI was obtained with low scan speed of 0.1 mm/s, while at high scan speed of 1.0 mm/s the resultant RI change was much weaker.

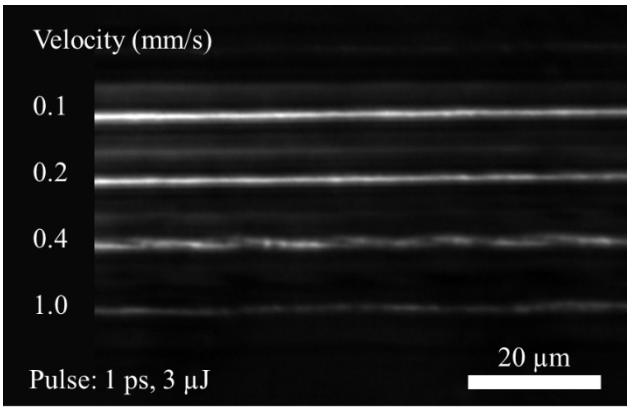

Fig. 7.16. Phase contrast image of traces fabricated with different laser scanning velocities.

On the whole, there are two options for choosing laser parameters which enable laser-transcription of traces up to 5 mm length. (1) The first option involves keeping the fixed pulse duration of 1.5 ps and constant scan speed of 0.2 mm/s, while changing the pulse energy from 3 μJ to 1 μJ on the fly, upon moving the laser up to the sample surface. (2) the second option is to keep both pulse duration and energy constant at 1.5 ps and 3 μJ respectively, while vary the scan speed from 0.2 mm/s to 1.0 mm/s on the fly.

For convenience/ availability of the technology, the option 2 was chosen for translating CLW structures in this longitudinal writing scheme.

7.3.4. Circular and lattice-like cladding structures

All the CLW designs described in section 7.3.1, were fabricated with the laser parameters listed in table 7.5.

Table 7. 5. Laser fabrication parameters for photoinscription of $LiNbO_3$ CLWs in the longitudinal writing geometry

Repetition rate	100 kHz
Central wavelength	800 nm
Pulse duration	1.5 ps
Pulse energy	3 μJ
Polarisation	Linear, perpendicular to optical z-axis
Pulse propagation	Parallel to the optical z-axis
Scan speed	0.2 – 1.0 mm/s
Focusing optics	Aspheric lens NA 0.5
Depth of focused beam	Up to ~5 mm
Sample orientation	z-cut $LiNbO_3$ sample: z-orientation

Results of the CLWs fabricated in the longitudinal writing geometry are shown in fig. 7.17. The structures of all the four designs were laser-inscribed for a length of 5 mm. However, due to the inhomogeneity and complication of the modifying process, many of the traces were not complete until the whole length of 5 mm. Apparently, complete structures were observed only up to 3.5 mm length. The optical performance of the CLWs is shown in Fig. 7.17. It is un-expecting that they only support guiding for mid-IR TE polarised light. It has been suggested that this behaviour might be due to the presence of nanograting structures occurred during the laser processing. The periodic nanopatterns aligned perpendicular to the laser polarisation might preferably scatter the vertically polarised (TM) light rather than the horizontally polarised (TE) light. However, in order to confirm this effect, further studies are required. These studies are set as the future research line of this thesis due to the limit of time within the recent work.

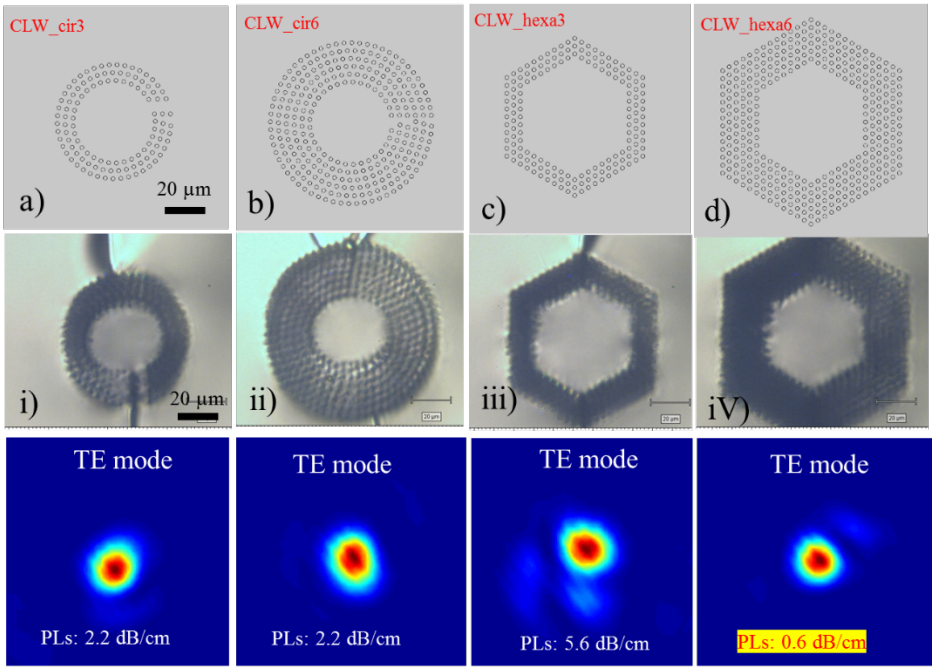

Fig. 7.17. Circular and hexagonal designs (a) (b) (c) (d), and transmission images (i) (ii) (iii) (iv) of CLWs optimised for 3DLW in longitudinal writing scheme; along with their characterised nea-field modes.

It is noticed that among the fabricated CLW structures, the hexagonal geometry – CLW_hexa6 resulted in the lowest PLs of 0.6 dB/cm which is in line with most results previously obtained by the 3DLW in transversal writing scheme. The advantage of the hexagonal structures might be associated to the role of periodic arrangement of the traces in the lattice-like form.

7.3.5. Helical cladding structures

The helical cladding structures were developed by translating the laser pulses along a designated helical trajectories. To our knowledge, it is the first time the $LiNbO_3$ CLWs were explored in this advanced geometry. Two design with one layer and three layers were investigated (Fig. 7.18).

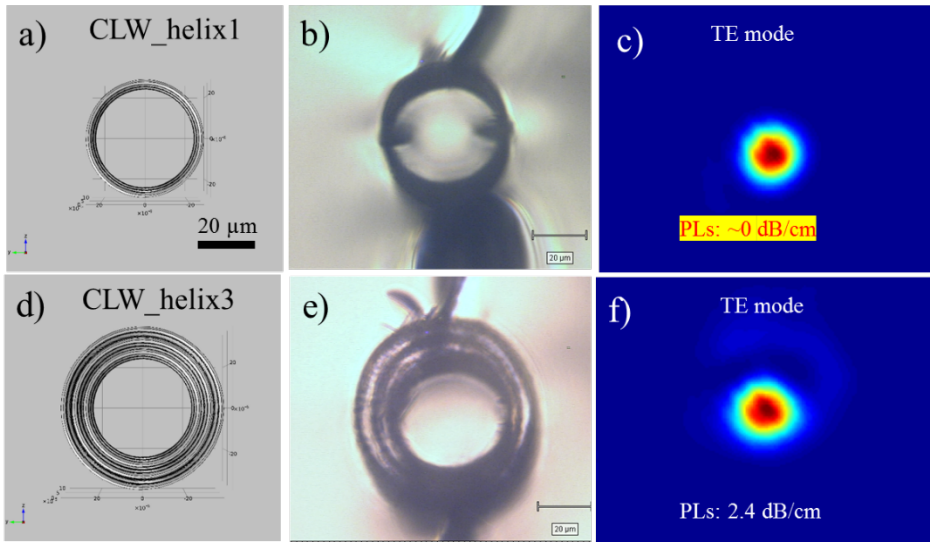

Fig. 7.18. Designs, transmission image, and characterised near-field mode of helical structures with 1 layer of trace –CLW_helix1 (a) (b) (c), and 3 layers of traces (d) (e) (f), respectively.

The results show that the helical CLWs support guiding for TE polarisation with low PLs. It is noticed that the PLs of the CLW_helix1 are almost zero. However, since it was observed that the structure was not complete throughout the sample, the guided mode was collected inside the material, and therefore measurement of the PLs might not surely correct. Though only approximated losses were recorded, it is believed that the real PL values are still well below 0.5 dB/cm. On the whole, the advantages of these structures are (1) the capacity of low-loss single mode guiding for the mid-IR light, (2) the use of concise proportion of the material, as much smaller cladding thickness are required, and (3) efficient time of fabrication. This approach provides a fundamental foundation for high performance light generation/conversion devices, though further development is still needed.

Reference

1. C. B. Schaffer, A. Brodeur, J. F. Garcia, and E. Mazur, *Micromachining bulk glass by use of femtosecond laser pulses with nanojoule energy.* Opt. Lett., 2001. **26**(2): p. 93-95.
2. R. Osellame, N. Chiodo, V. Maselli, A. Yin, M. Zavelani-Rossi, G. Cerullo, P. Laporta, L. Aiello, S. De Nicola, P. Ferraro, Finizio, A., and G. Pierattini, *Optical properties of waveguides written by a 26 MHz stretched cavity Ti:sapphire femtosecond oscillator.* Opt. Express, 2005. **13**(2): p. 612-620.
3. S. M. Eaton, H. Zhang, P. R. Herman, F. Yoshino, L. Shah, J. Bovatsek, and A. Y. Arai, *Heat accumulation effects in femtosecond laser-written waveguides with variable repetition rate.* Opt. Express, 2005. **13**(12): p. 4708-4716.
4. S. Nolte , M. Will , J. Burghoff, and A. Tünnermann, *Ultrafast laser processing: New options for three-dimensional photonic structures.* Journal of Modern Optics, 2004. **51**(16): p. 2533-2542.
5. S. Juodkazis, H. Misawa, and I. Maksimovb, *Thermal accumulation effect in three-dimensional recording by picosecond pulses.* Appl. Phys. Lett., 2004. **85**(22): p. 5239-5241.
6. M. Will, J. Burghoff, J. Limpert, T. Schreiber, S. Nolte, and A. Tunnermann, *High-speed fabrication of optical waveguides inside glasses using a high-repetition-rate fiber CPA system*, in *Photon Processing in Microelectronics and Photonics III*. 2004, Proc. SPIE. p. 168-174.
7. K. Minoshima, A. M. Kowalevicz, E. P. Ippen, and J. G. Fujimoto, *Fabrication of coupled mode photonic devices in glass by nonlinear femtosecond laser materials processing.* Opt. Express, 2002. **10**(15): p. 645-652.
8. V. G. Della, R. Osellame, N. Chiodo, S. Taccheo, G. Cerullo, P. Laporta, A. Killi, U. Morgner, M. Lederer, and D. Kopf, *C-band waveguide amplifier produced by femtosecond laser writing.* Opt. Express, 2005. **13**(16): p. 5976-82.
9. L. Shah, A. Y. Arai, S. M. Eaton, and P. R. Herman, *Waveguide writing in fused silica with a femtosecond fiber laser at 522 nm and 1 MHz repetition rate* Opt. Express, 2005. **13**(6): p. 1999-2006.
10. P. Karpinski, V. Shvedov, W. Krolikowski, and C. Hnatovsky, *Laser-writing inside uniaxially birefringent crystals: fine morphology of ultrashort pulse-induced changes in lithium niobate.* Opt. Express, 2016. **24**(7): p. 7456-7476.
11. R. Osellame, G. Cerullo, and R. Ramponi, *Femtosecond Laser Micromachining: Photonic and Microfluidic Devices in Transparent Materials*. 2012: Springer Berlin Heidelberg.
12. D. Liu, Y. Li, R. An, Y. Dou, H. Yang, and Gong., Q., *Influence of focusing depth on the microfabrication of waveguides inside silica glass by femtosecond laser direct writing.* Appl. Phys. A, 2006. **84**(3): p. 257–260.
13. K. Yamada, W. Watanabe, T. Toma, K. Itoh, and J. Nishii, *In situ observation of photo induced refractive-index changes in filaments formed in glasses by femtosecond laser pulses.* Opt. Lett., 2001. **26**(1): p. 19-21.
14. C. Mauclair, A. Mermillod-Blondin, N. Huot, E. Audouard, and R. Stoian, *Ultrafast laser writing of homogeneous longitudinal waveguides in glasses using dynamic wavefront correction.* Opt. Express, 2008. **16**(8): p. 5481-5492.

8

Conclusions and future works

This chapter describes the general conclusions of the thesis and the possible future work.

Contents

8.1. Conclusions

The main achievements of the thesis are briefly summarised in the following.

Heuristic model for obtaining realistic information of the laser-written CLWs in $LiNbO_3$

In this thesis, a comprehensive heuristic simulation model is built, taking into account both the depressed-RI changes and the anisotropic stress-induced RI fields. The efficient evaluation of both of them is important for developing high performance mid-IR cladding waveguides, and reliable laser manufacturing of photonic circuits. Full mid-IR RI profiles of $LiNbO_3$ CLWs microstructured under a given 3DLW conditions are reported for the first time to our knowledge. We developed a novel heuristic modelling approach based on the use of standard optical characterisation data (near-field mode diameters -MFDs and propagation losses -PLs), along with standard numerical methods (finite element method –FEM). The approach offers a satisfactory solution to the problem of designing realistic laser-written circuit building-blocks, such as straight waveguides, bends and evanescent splitters.

Achievement of high performance $LiNbO_3$ CLWs by 3DLW technique at low-repetition rate regime

The CLWs were fabricated by 3DLW technique in the low-repetition rate regime (1 kHz) in which complete heat diffusion occurs between two consecutive pulses and therefore the residual laser-induced stress as well as the lattice defects within the laser-written structures are significantly high. As evaluated in the simulation model, these highly anisotropic stress-induced RI fields favour guiding for one polarised mode, while deteriorate guiding for the other. Based on the extracted values of the complex RI profiles, CLWs were designed towards a single-guided mode low-loss performance for both transverse electric (TE) and transverse magnetic (TM) polarised lights.

Cladding arrangements with core diameters of 40 - 100 μm, and cladding thicknesses of 10 - 20 μm were studied for a given laser writing parameters, resulting in optical guiding of 3680 nm mid-IR light with the lowest PLs of <0.5 dB/cm for the first time to our knowledge. Evidence of the inherent anisotropic behaviour is clearly observed, as the CLWs support single-mode guiding for TM polarised light, whereas they are multimode for TE light. In order to diminish the anisotropy of the RI profiles, the CLWs were

further treated with different thermal annealings. We compared the guiding properties of the CLWs both in as-fabricated samples and annealed samples. More importantly, we inferred how the sub-micron laser written tracks change its size and index of refraction, and also how the stress-fields reduce as a function of annealing temperature and time. Results reveal that by performing a sequential thermal annealing until a peak temperature of 773 K, single mode guiding at 3680 nm wavelength for both polarisations could be achieved, with a minimum obtained PLs of 1.25 dB/cm and 1.79 dB/cm for TM and TE polarisations, respectively.

Achievement of high performance $LiNbO_3$ CLW devices by 3DLW in the intermediate-repetition rate regime

In this set of studies, the fabrication of the CLWs was processed by 3DLW in the intermediate repetition rate regime (100 kHz). In this regime, the arrival time between two consecutive pulses is equivalent to the time for the heat diffusion out of the focal volume, so that the heat begins to moderately accumulate, potentially erasing lattice defects and diminishing the generation of surrounding stress fields. Additionally, the use of a 100-fold higher repetition rate than in the previous writing squeme allows to fabricate waveguides at a 100-fold faster speed, thereby dramatically reducing the processing time. This is practically important for microstructuring complex waveguide circuits which involves thousands of written elements. The dependence of the CLW properties with respect to various 3DLW parameters, i.e. pulse duration and pulse energy was additionally investigated. In this regime, performance of CLWs with single-mode low-PLs of ~1 dB/cm for both TE and TM polarisation was directly obtained without the need of thermal annealing post-process, as it was needed for the low-repetition rate 3DLW waveguides.

Based on the high-performance straight-CLWs, s-bend CLW structures were further developed under various laser parameters, also showing losses of as low as ~0.5 dB/cm configured with bending-radius of up to 200 mm. Following the success of the straight and s-bend CLWs, finite difference beam propagation method (FD-BPM) was used to numerically investigate the practical development of directional beam splitters. Configuration of the splitters was based on the concept of evanescent coupling waveguides combined with s-bend structures. The achieved directional beam splitters are the building blocks of a Mach-Zehnder (MZ) structure which was further numerically

examined. This MZ structure in $LiNbO_3$ makes possible promising applications for light modulators and interferometers at the mid-IR range, and potentially for broader fields ranging from mid-IR sensing to astrophotonic instrumentation.

Development of longitudinal laser writing scenario – a new approach for more isotropic laser-written $LiNbO_3$ CLWs

In order to overcome the anisotropic issue, we explored another approach which offers more symmetric profile of the laser-modified volume. In this approach, the sample is laser-inscribed along the longitudinal/parallel direction to the laser propagation and waveguiding direction propagation. The 3DLW results in laser-written structures with circular cross-section which can minimise the anisotropic effect of the laser-induced stress. However, this requires a deep focusing of the laser beam inside the crystal (>2 mm), and thereby complicates the lattice modification process, due to strong refraction effects, aberrations, and non-linear processes. We found that the laser modification in this longitudinal writing scheme is extremely sensitive to the alignment between the laser beam and the sample, the surface quality of the crystal, the laser polarisation, and more importantly the pulse temporal duration and energy. Recognisable type II modification was achieved at depths of up to 5 mm inside the crystal once the fabrication conditions were finely adjusted. The $LiNbO_3$ CLWs were demonstrated for the first time by this longitudinal writing geometry. Single-guided mode mid-IR performance at 3680 nm wavelength with low PLs of 0.5 dB/cm was achieved. The cladding structures were designed with several two-dimensional track arrangements: concentric circular rings, lattice-like hexagonal rings and with helical continuous tracks. Among these cladding geometries, the helical structure shows big advantages over the conventional structures, due to its fast processing time, three-fold faster than it is required for the others. The best waveguiding performance was however obtained by the hexagonal track arrangements.

8.2. Future works

High optical performance with PLs <0.5dB/cm was successfully achieved. However, the mid-IR $LiNbO_3$ CWLs still can be improved by better adjustment of the designs, 3DLW conditions, and appropriate thermal treatments. Specifically, in the transversal laser writing scheme, the straight and bend-CLWs were not fabricated by identical conditions due to a technical problem: the laser operation was unstable at the time. Once the laser

equipment is fully serviced, it is believed that the CLWs can be further improved. In the longitudinal writing scheme, the CLWs were still limited by lengths, as the difficulty in the laser modification at depths of longer than 5 mm inside the $LiNbO_3$ crystal. This problem can be solved by using high power laser, and properly adjusting both energy and scan speed on the fly. Multi-scanning process is also worth to try for possible modification of higher refractive index contrast, which therefore improves the guiding performance of waveguides.

Fabrication of mid-IR directional beam splitters in $LiNbO_3$ is highly feasible with the fundamental foundation of the highly achieved CLWs in both straight and s-bend geometries. Implementation of the splitters can be done by properly designing the laser writing trajectories in a programed sub-micron precision motion stage. The next step is to fabricate fully functional MZ devices which basically consist of beam splitters and combiners. Electrodes can be embedded on the MZ platform for light modulators, and interferometers which are the fundamental base for applications in mid-IR sensing and astrophotonics. Other potential work is to fabricate the low-loss CLWs in periodically poled Lithium Niobate (PPLN) for on-chip mid-IR light generation/conversion.

A. Publications and presentations

A.1 Publications

Paper I

Heuristic modelling of laser written mid-infrared $LiNbO_3$ stressed-cladding waveguides

Huu-Dat Nguyen,[1] Airán Ródenas,[1,*] Javier R. Vázquez de Aldana,[2] Javier Martínez,[1] Feng Chen,[3] Magdalena Aguiló,[1] Maria Cinta Pujol[1] and Francesc Díaz[1]

[1]*Física i Cristal·lografia de Materials i Nanomaterials (FiCMA-FiCNA-EMAS), Departament de Química Física i Inorgànica,, Universitat Rovira i Virgili, (URV), 43007, Tarragona, Spain*

[2]*Grupo de Investigación en APLsicaciones del Láser y Fotónica (ALF-USAL), Facultad de Ciencias, Universidad de Salamanca, 37008 Salamanca, Spain*

[3]*School of Physics, State Key Laboratory of Crystal Materials and Key Laboratory of Particle Physics and Particle Irradiation, Ministry of Education, Shandong University, Jinan 250100, China*

[*]*arodenas@gmail.com*

Abstract: Mid-infrared lithium niobate cladding waveguides have great potential in low-loss on-chip non-linear optical instruments such as mid-infrared spectrometers and frequency converters, but their three-dimensional femtosecond-laser fabrication is currently not well understood due to the complex interplay between achievable depressed index values and the stress-optic refractive index changes arising as a function of both laser fabrication parameters, and cladding arrangement. Moreover, both the stress-field anisotropy and the asymmetric shape of low-index tracks yield highly birefringent waveguides not useful for most applications where controlling and manipulating the polarization state of a light beam is crucial. To achieve true high performance devices a fundamental understanding on how these waveguides behave and how they can be ultimately optimized is required. In this work we employ a heuristic modelling approach based on the use of standard optical characterization data along with standard computational numerical methods to obtain a satisfactory approximate solution to the problem of designing realistic laser-written circuit building-blocks, such as straight waveguides, bends and evanescent splitters. We infer basic waveguide design parameters such as the complex index of refraction of laser-written tracks at 3.68 μm mid-infrared wavelengths, as well as the cross-sectional stress-optic index maps, obtaining an overall waveguide simulation that closely matches the measured mid-infrared waveguide properties in terms of anisotropy, mode field distributions and propagation losses. We then explore experimentally feasible waveguide designs in the search of a single-mode low-loss behaviour for both ordinary and extraordinary polarizations. We evaluate the overall losses of s-bend components unveiling the expected radiation bend losses of this type of waveguides, and finally showcase a prototype design of a low-loss evanescent splitter. Developing a realistic waveguide model with which robust waveguide designs can be developed will be key for exploiting the potential of the technology.

OCIS codes: (220.4000) Microstructure fabrication; (160.4330) Nonlinear optical materials; (230.7370) Waveguides; (000.4430) Numerical approximation and analysis.

References and links

1. Y. Ren, G. Brown, A. Ródenas, S. Beecher, F. Chen, and A. K. Kar, "Mid-infrared waveguide lasers in rare-earth-doped YAG," Opt. Lett. **37**(16), 3339–3341 (2012).

#258038 Received 26 Jan 2016; revised 4 Mar 2016; accepted 13 Mar 2016; published 1 Apr 2016

2. R. He, Q. An, Y. Jia, G. R. Castillo-Vega, J. R. Vázquez de Aldana, and F. Chen, "Femtosecond laser micromachining of lithium niobate depressed cladding waveguides," Opt. Mater. Express **3**(9), 1378–1384 (2013).
3. Q. An, Y. Ren, Y. Jia, J. R. V. de Aldana, and F. Chen, "Mid-infrared waveguides in zinc sulfide crystal," Opt. Mater. Express **3**(4), 466–471 (2013).
4. J. R. Macdonald, S. J. Beecher, P. A. Berry, G. Brown, K. L. Schepler, and A. K. Kar, "Efficient mid-infrared Cr:ZnSe channel waveguide laser operating at 2486 nm," Opt. Lett. **38**(13), 2194–2196 (2013).
5. J. Hu and C. R. Menyuk, "Understanding leaky modes: slab waveguide revisited," Adv. Opt. Photonics **1**(1), 58–106 (2009).
6. A. Ródenas, G. Zhou, D. Jaque, and M. Gu, "Direct laser writing of three-dimensional photonic structures in Nd:yttrium aluminum garnet laser ceramics," Appl. Phys. Lett. **93**(15), 151104 (2008).
7. A. Ródenas, G. A. Torchia, G. Lifante, E. Cantelar, J. Lamela, F. Jaque, L. Roso, and D. Jaque, "Refractive index change mechanisms in femtosecond laser written ceramic Nd:YAG waveguides: micro-spectroscopy experiments and beam propagation calculations," Appl. Phys. B **95**(1), 85–96 (2009).
8. A. Rodenas, "Direct femtosecond laser writing of 3D photonic structures in rare-earth doped lithium niobate", PhD Thesis 2009, ISBN 978–84–693–3869–8, *http://hdl.handle.net/10486/4167*
9. A. Ródenas, L. M. Maestro, M. Ramirez, G. A. Torchia, L. Roso, F. Chen, and D. Jaque, "Anisotropic lattice changes in femtosecond laser inscribed Nd^{3+}:MgO:$LiNbO_3$ optical waveguides," J. Appl. Phys. **106**(1), 013110 (2009).
10. B. McMillen and Y. Bellouard, "On the anisotropy of stress-distribution induced in glasses and crystals by non-ablative femtosecond laser exposure," Opt. Express **23**(1), 86–100 (2015).
11. H. Karakuzu, M. Dubov, S. Boscolo, L. A. Melnikov, and Y. A. Mazhirina, "Optimisation of microstructured waveguides in z-cut $LiNbO_3$ crystals," Opt. Mater. Express **4**(3), 541–552 (2014).
12. J. Burghoff, C. Grebing, S. Nolte, and A. Tünnermann, "Efficient frequency doubling in femtosecond laser written waveguides in lithium niobate," Appl. Phys. Lett. **89**(8), 081108 (2006).
13. A. Rodenas, A. Benayas, J. R. Macdonald, J. Zhang, D. Y. Tang, D. Jaque, and A. K. Kar, "Direct laser writing of near-IR step-index buried channel waveguides in rare earth doped YAG," Opt. Lett. **36**(17), 3395–3397 (2011).
14. S. Kroesen, W. Horn, J. Imbrock, and C. Denz, "Electro-optical tunable waveguide embedded multiscan Bragg gratings in lithium niobate by direct femtosecond laser writing," Opt. Express **22**(19), 23339–23348 (2014).
15. A. G. Okhrimchuk, A. V. Shestakov, I. Khrushchev, and J. Mitchell, "Depressed cladding, buried waveguide laser formed in a YAG:Nd^{3+} crystal by femtosecond laser writing," Opt. Lett. **30**(17), 2248–2250 (2005).
16. A. Okhrimchuk, V. Mezentsev, A. Shestakov, and I. Bennion, "Low loss depressed cladding waveguide inscribed in YAG:Nd single crystal by femtosecond laser pulses," Opt. Express **20**(4), 3832–3843 (2012).
17. T. Gorelik, M. Will, S. Nolte, A. Tuennermann, and U. Glatzel, "Transmission electron microscopy studies of femtosecond laser induced modifications in quartz," Appl. Phys., A Mater. Sci. Process. **76**(3), 309–311 (2003).
18. M. Will, J. Burghoff, S. Nolte, A. Tünnermann, F. Wunderlich, and K. Goetz, "Detailed investigations on femtosecond-induced modifcations in crystalline quartz for integrated optical applications," Proc. SPIE **5714**, 261–270 (2005).
19. J. Burghoff, S. Nolte, and A. Tunnermann, "Origins of waveguiding in femtosecond laser structured $LiNbO_3$," Appl. Phys. A **89**(1), 127–132 (2007).
20. Y. S. Kim and R. T. Smith, "Thermal expansion of lithium tantalate and lithium niobate single crystals," J. Appl. Phys. **40**(11), 4637–4641 (1969).
21. A. Ródenas, J. A. Sanz Garcia, D. Jaque, G. A. Torchia, C. Mendez, I. Arias, L. Roso, and F. Agullo-Rueda, "Optical investigations of femtosecond laser induced microstress in neodymium doped lithium niobate crystals," J. Appl. Phys. **100**(3), 033521 (2006).
22. A. S. Andrushchak, B. G. Mytsyk, H. P. Laba, O. V. Yurkevych, I. M. Solskii, A. V. Kityk, and B. Sahraoui, "Complete sets of elastic constants and photoelastic coefficients of pure and MgO-doped lithium niobate crystals at room temperature," J. Appl. Phys. **106**(7), 073510 (2009).
23. D. E. Zelmon, D. L. Small, and D. Jundt, "Infrared corrected Sellmeier coefficients for congruently grown lithium niobate and 5 mol.% magnesium oxide –doped lithium niobate," J. Opt. Soc. Am. B **14**(12), 3319–3322 (1997).
24. Y. Tsuji and M. Koshiba, "Guided-mode and leaky-mode analysis by imaginary distance beam propagation method based on finite element scheme," J. Lightwave Technol. **18**(4), 618–623 (2000).
25. H. Karakuzu, M. Dubov, and S. Boscolo, "Control of the properties of micro-structured waveguides in lithium niobate crystal," Opt. Express **21**(14), 17122–17130 (2013).
26. R. Scarmozzino and R. M. Osgood, "Comparison of finite-difference and Fourier-transform solutions of the parabolic wave equation with emphasis on integrated-optics applications," J. Opt. Soc. Am. A **8**(5), 724–731 (1991).
27. R. Scarmozzino, A. Gopinath, R. Pregla, and S. Helfert, "Numerical techniques for modeling guided-wave photonic devices," IEEE J. Sel. Top. Quantum Electron. **6**(1), 150–162 (2000).
28. G. R. Hadley, "Transparent boundary condition for the beam propagation method," IEEE J. Quantum Electron. **28**(1), 363–370 (1992).
29. S. Gross, N. Jovanovic, A. Sharp, M. Ireland, J. Lawrence, and M. J. Withford, "Low loss mid-infrared ZBLAN waveguides for future astronomical applications," Opt. Express **23**(6), 7946–7956 (2015).

#258038 Received 26 Jan 2016; revised 4 Mar 2016; accepted 13 Mar 2016; published 1 Apr 2016

1. Introduction

The three-dimensional laser writing (3DLW) of mid-infrared (mid-IR) depressed-index cladding waveguides (CLW) in crystals has received considerable attention in recent years, thanks to the easiness with which mid-IR waveguiding can be achieved, and to the potential of the 3DLW technique for fabricating waveguide circuits which are free from the limitations of planar designs and therefore enable the design of circuit architectures hitherto not possible [1–4]. The development of these type of mid-IR waveguides inside the volume of crystalline non-linear optical materials has a wide range of straight applications ranging from novel integrated laser sources to integrated nonlinear frequency conversion chips and electro-optic interferometric spectrometers all exploiting the mid-IR range.

A laser written CLW basically consists on a depressed-index two-dimensional (2D) optical cladding inside which different propagating leaky modes can be sustained depending on the magnitude of the negative refractive index change in the cladding, as well as on the spatial thickness and size of the cladding structure [5]. The exact microstructure of the cladding is made by arranging laser-written tracks, where the permanent refractive index decrease has its origin in the degree of crystal amorphization that results from the strong and spatially localized ionization of the dielectric material and the irreversible lattice damage which is entailed in the energy relaxation processes [6,7]. To achieve an effective sub-micron resolution in the 3DLW process the laser pulse duration is typically kept in the sub-picosecond regime (~0.2 ps) so as to minimize heat affected zones, and the photon energy is usually chosen sub-bandgap ($E_g \approx 3.9$ eV in $LiNbO_3$) so as to attain a laser fluence above the threshold for modification only at the center of the tight focal volume inside the dielectric material, enabling the 3D writing [8].

Although the 3DLW technique is naturally fast and relatively easy to use as compared to clean-room lithography techniques, its transfer to industry as a manufacturing process of anisotropic crystals such as lithium niobate is still far from attainable, due to various bottlenecks regarding the fabrication speed, the reliability of the process as well as the fundamental understanding of the laser interaction processes. One of the challenges which is still to be resolved is the correct understanding of the strong anisotropic stress fields that unavoidably appear alongside any laser-written structures and therefore have to be taken into account when developing laser manufacturing processes of photonic circuits [6–10]. Since the design of mid-IR CLWs involves the microfabrication of structures with sizes in the ~50 μm scale, tens or hundreds of low-index single tracks have to be written to achieve such a large volume. Due to this, the optical properties of fabricated waveguides are typically difficult to predict and very far from what would be expected if no stress-optic index changes are supposed. Since each individual track is a source of anisotropic stress-fields, the overall stress field built up in the full cladding structure will depend on the exact 2D track arrangement and therefore the final optical properties of the waveguides cannot be reliably predicted, unless a comprehensive stress-optic waveguide model is built in advance. This difficulty implies that up until now all experimental reports on CLWs have been performed following a trial and error methodology where the exact processes involved in the fabrication of the guiding structure are not well understood, and as a result the development of a comprehensive model on which to build a reliable manufacturing process has not been achieved. In this sense, a systematic study on CLWs with the aim of developing a realistic model on how both the laser-written depressed index map and the stress-optic index maps form and combine as a function of the basic laser parameters has hitherto not been performed. Furthermore, such a knowledge is deeply required for the development of specifically mid-IR waveguides, since at this larger wavelength range the confinement losses of CLWs are larger than at the near-IR or visible ranges [11], and therefore the cladding microstructure design has to be necessarily optimized in a comprehensive way so as to obtain low propagation losses below the 0.5 dB/cm level typically required for optical circuits of cm's size.

#258038 Received 26 Jan 2016; revised 4 Mar 2016; accepted 13 Mar 2016; published 1 Apr 2016

Up until the first report on the use of a laser-written crystalline CLW for guiding in the mid-IR range [1], the longest operating wavelength in a crystalline 3DLW waveguide was limited to around ~1.5 μm, and was obtained by using the standard double-track stress-optic waveguiding approach (see Fig. 1 below), first reported by Burghoff et al. in $LiNbO_3$ crystals for ~1 μm wavelength light [12]. The stress-optic double-track approach was however proven to be insufficient for confining 1.9 μm near-IR light [13], and recently Kroesen et al. experimentally showed how at 1.55 μm the CLW design gives comparatively much better waveguiding performance (in terms of propagation losses and waveguide anisotropy) than the two-track approach [14]. Although the seminal introduction of the CLW approach was performed by Okhimchuck et al. a decade ago with the intention of developing compact and efficient Nd:YAG waveguide lasers at 1.06 μm [15,16], only recently the approach has been used for demonstrating efficient crystalline channel waveguide lasers at longer wavelengths (waveguide lasing in Tm:YAG crystals at 1.9 μm as well as Cr:ZnSe crystals at 2.5 μm [1,4]). In this sense, the CLW is indeed advantageous for laser applications due to the fact that both the mode spatial distribution and size can be easily tailored for achieving optimal input coupling and efficient lasing and also because the core is made of pristine material. However, besides laser applications the fabrication of low-loss mid-IR $LiNbO_3$ CLWs is also highly desirable for developing high-performance and monolithic mid-IR non-linear chips.

1.1. Difficulties in achieving laser-written crystalline low-loss mid-IR cladding waveguides

The development of low propagation loss (~0.5 dB/cm) laser-written LiNbO3 CLWs for the mid-IR range is strongly limited by the reported difficulty of achieving propagation losses below 3 dB/cm at wavelengths larger than ~3 μm. In the first report on $LiNbO_3$ mid-IR CLWs only insertion losses (IL) were reported, with a value of ~5 dB for a 1 cm long single mode CLW at 4 μm wavelength [2]. Recently, An et al. reported single mode CLWs on ZnS crystals with PLs ~4 dB/cm at 4 μm [3]. Beyond these experimental reports, Karakuzu et al. recently performed a systematic confinement-loss numerical calculation on $LiNbO_3$ crystals, concluding that only PLs ≥1 dB/cm are theoretically possible at 3.5 μm wavelength [11]. This theoretical work however did not take into account the characteristic stress-fields which affect guiding structures fabricated by 3DLW [7–11], and was also built on a different CLW design composed of seven ring layers with circular rod shapes. At the light of these results, achieving low-loss (PLs<0.5 dB/cm) mid-IR CLWs in $LiNbO_3$ is undoubtedly a challenge which needs to be tackled and whose solution requires a deeper understanding of the real refractive index changes that occur at the mid-IR range. Moreover, there has been no study to our knowledge on the expected bend radiation losses of this type of crystalline CLWs in the mid-IR range, which is also a fundamental issue which needs to be optimized for achieving mid-IR on-chip circuits. Achieving a general understanding of how to model these type of waveguides would allow to perform realistic numerical calculations towards their optimization.

In this work we report on a heuristic approach for the modelling of mid-IR $LiNbO_3$ CLWs, i.e. a method for achieving satisfactory solutions to the complex problem of predicting the optical behavior (modal properties, birefringence, propagation losses and bend radiation losses) of mid-IR CLWs. We use experimental data such as the waveguide mode near field intensity distributions and the PLs of fabricated waveguides, together with stress field values from previous studies, and compare this measured data with that obtained from a first waveguide model using standard computational tools as the finite element method (FEM) and the finite difference beam propagation method (FD-BPM). Iterations of the waveguide parameters are then run until the model results match the experimentally measured data. Once the waveguide parameters match the experimental data obtained with our laser system, we then subsequently explore different cladding designs in the search for a low-loss behavior for both transverse magnetic (TM) and electric (TE) polarized modes. For each cladding design we also evaluate the expected overall losses of s-bend components, and finally we showcase a 3.68 μm wavelength 50:50 low-loss evanescent splitter based on low-loss CLWs.

#258038 Received 26 Jan 2016; revised 4 Mar 2016; accepted 13 Mar 2016; published 1 Apr 2016

2. Numerical simulation models

2.1 Finite Element Method (FEM) simulation of anisotropically stressed cladding waveguides

2.1.1 Stress field simulation

The numerical analysis of the waveguides was performed with commercial COMSOL Multiphysics® software. The tight focusing of femtosecond laser pulses inside $LiNbO_3$ is well known to induce a micrometric volume change, which resembles the laser focus ellipsoid, and consists on lattice damaged crystal where slight amorphization occurs and is surrounded by a characteristic anisotropic stress field [9,17–19]. The local volume changes surrounding a longitudinal and straight laser-written track can therefore be simulated with a 2D thermal expansion model, supposing that the amorphized volume expands and elastically distorts the surrounding unmodified crystal, simplifying the problem to a 2D cross-sectional calculation. This approach was first validated for two-track waveguide designs in the visible and near-IR range by Gorelik et al. and Will et al. in quartz crystals [17,18], and subsequently by Burghoff et al. in $LiNbO_3$ crystals [19]. Due to the fact that real track shapes strongly vary depending on the type of laser writing system used as well as crystal composition and crystallographic orientation [8,19], these simulations need to be performed with a well characterized sample and under well specified 3D laser fabrication system parameters. In our case, the laser-written tracks were simulated to have elliptical shape with length of 20 μm along the incident direction of laser beam (z-axis, vertical) and width of 1 μm along the perpendicular direction (y-axis, horizontal). These dimensional values were obtained from arrays of fabricated tracks and waveguides and characterized with back-scatter SEM imaging (not shown here for the sake of brevity). The experimental set up is described in Section 3. The simulation is governed by the Hooke's law [Eq. (1)] which reflects the relation between strain (ε), stress (σ), tensors and temperature difference in linear thermal expansion model.

$$\sigma_{ij} = \sigma_0 + C_{ijkl} : \left(\varepsilon_{kl} - \varepsilon_0 - \alpha_{kl}\theta\right). \tag{1}$$

where C_{ijkl} is the fourth order elasticity tensor, ":" stands for the double-dot tensor product, σ_0 and ε_0 are initial stress and strain, θ is the temperature change parameter controlling the expansion $\theta = T - T_0$, and α_{kl} is the second order linear thermal expansion tensor. The elasticity tensor can be completely represented by a known symmetric 6x6 matrix [20], and the thermal expansion coefficients were taken from [21]. For the case of the strain tensor, it is written in terms of the point displacement gradient ∇u :

$$\varepsilon = \frac{1}{2}\left(\nabla u + \nabla u^T\right); \varepsilon_{mn} = \frac{1}{2}\left(\frac{\partial u_m}{\partial u_n} + \frac{\partial u_n}{\partial u_m}\right). \tag{2}$$

A fixed constraint is set at an outer boundary of circular shape and domain size of 0.6 mm diameter, and a displacement constraint is assigned to the laser-written track domains where the expansion starts. The temperature difference θ is used as a primary control parameter that can be set to match experimental data, for example simulating a pair of written tracks (see Fig. 1) where the stress field has been experimentally studied [8,19]. In this first study, we have used available micro-stress data from previous laser-written waveguides in $LiNbO_3$ crystals with the same fabrication parameters to those of the present work. These works revealed that the range of induced stress field magnitudes between a pair of tracks that are separated by several micrometers (~10-50 μm) and that are fabricated using chirped pulse amplified laser systems delivering near-IR (~800 nm) sub-picosecond (~200 fs) low-repetition rate (~1 KHz) pulsed laser trains, and written with standard focusing lenses (~0.2-0.6 NA), is of the order of 10-500 MPa depending on the selected laser pulse energy (typically ~0.1-0.8 μJ) [8,19,21]. We nonetheless notice that a more detailed stress-field distribution study is still lacking for the case of laser-written $LiNbO_3$ crystals, which could be done by using novel rapid stress analysis methods such as those reported by McMillen et al [10].

#258038 Received 26 Jan 2016; revised 4 Mar 2016; accepted 13 Mar 2016; published 1 Apr 2016

2.1.2 Mode analysis simulation

The obtained 2D stress distribution is assumed as the only responsible field for refractive index (RI) changes surrounding the laser inscribed low-index tracks. The relationship between stress-induced RI changes and stress tensor is governed by the piezo-optic effect:

$$\Delta\left(\frac{1}{n^2}\right)_{ij} = \sum_{k,l} \pi_{ijkl}\sigma_{kl}. \tag{3}$$

where the piezo-optic tensor π_{ijkl} of the material is taken from [22].

Inside the tracks, a decrease of the real part of the $LiNbO_3$ RI of around 0.01-0.001 is known to occur as a result a $LiNbO_3$ crystalline lattice damage and amorphization [8,19]. The precise knowledge of these values is however still subject of research, due to the fact that the exact physical processes that the $LiNbO_3$ lattice undergoes when exposed to different types of tightly focused fs laser pulsed beams are not known, and there is a clear lack of available techniques capable of directly measuring the refractive index values of high index materials with a sub-μm spatial resolution, as required for this type laser written structures. Moreover, it is also of paramount importance to differentiate among the RI change values measured at the visible, near-IR, or mid-IR wavelength ranges, since these ranges involve fundamentally different resonance effects, such as the bandgap absorption at the UV-vis and impurities, lattice defects absorptions, and multiphonon absorptions in the mid-IR, so that RI values measured using visible light instruments may not be valid for characterizing mid-IR waveguides. Nevertheless, due to the lack of direct RI measurements of laser-written $LiNbO_3$ structures in the mid-IR range, in this work we start the model using already reported RI values at visible light experiments as input parameters [19], and later refine these values in iterative steps to match our experimental mid-IR waveguide characterization results. It is pertinent to recall here the fundamental difference between guided modes in RI increased core waveguides (such as in the case of double-track stress-optic waveguides) where waveguiding of a confined mode is achieved in the high RI $LiNbO_3$ volume, and the leaky modes of depressed index CLWs, where light propagation takes place within a core volume which has the same RI as the rest of the crystalline material and only a continuum of radiation modes exists inside the low RI cladding. In this sense, while confined modes rely on the magnitude of the positive RI increase at the core, the leaky modes of CLWs are very sensitive to the magnitude of the negative RI change inside the tracks conforming the cladding [5]. It is in this regard that choosing CLWs as object for studying the unknown mid-IR RI change values of laser micro-processed $LiNbO_3$ can be a powerful indirect method.

The electromagnetic-wave frequency-domain model was applied for the analysis of mode guiding. All simulations in this work are computed for a free space wavelength of 3.68 μm and the $LiNbO_3$ refractive indices of n_z = 2.0700 and n_y = 2.1309 for extraordinary and ordinary polarized modes, respectively [23]. In order to truncate the computational domain and minimize light reflections from the boundary, isotropic and circular perfectly matched layers (PML) where applied surrounding the cladding waveguide structure. The PML light absorber is defined as a function of refractive index n_{PML} [24,25]:

$$n_{PML}(r) = n_{o,e} - ik_{\max}\left(\frac{r-r_{in}}{L}\right)^2, r_{in} < r \le r_{in} + L. \tag{4}$$

where r is the radial coordinate, r_{in} and L are the inner radius and thickness of the PML, and k_{max} is the maximum absorption value. All these parameters have been carefully chosen so as to give reliable waveguide modes [5]: k_{max} = 0.002 has been chosen as giving the most effective absorption for the structure, and r_{in} = 150 μm and L = 150 μm are chosen to effectively reduce the computational domain while not affecting the computed modes. Since the laser-written tracks were simulated to have a considerably elliptical shape with width of

#258038 Received 26 Jan 2016; revised 4 Mar 2016; accepted 13 Mar 2016; published 1 Apr 2016

~1 μm along the perpendicular direction (y-axis, horizontal) and ~20 μm along the incident (writing) direction of the laser beam (z-axis, vertical), the finite elements mesh of elliptical tracks was defined with a free triangular mesh of size around 40 nm in the horizontal and 450 nm for the vertical. Inside the cladding area a free triangular mesh of size around 1 μm in both horizontal and vertical directions was used. The rest of domains were defined with free triangular meshes of minimum size 50 nm and maximum size 10 μm. The initial refractive index changes (Δn) assumed at the tracks for the mid-IR range, were of $\Delta n = -5 \times 10^{-3}$ for both polarizations. TM and TE modes were studied separately, and iteratively computed varying the Δn values, to match experimental results by varying the Δn values of the laser-written tracks. In the first mode analysis we typically searched for as many modes as possible (~500 modes). From this first simulation it was then possible to refine the effective index and use this value for further simulations in which only 20 modes were looked for and the time consumption for simulation could be reduced.

2.2 Light propagation simulation

Light propagation was simulated by BeamPROP software which is a part of the RSoft Photonic Component Design Suite®. The computational simulation is based on FD-BPM and a transparent boundary condition was applied, following previous works [26–28]. For a straight waveguide, a simple segment was created with total length of 22 mm. The segment was assigned to the complex RI profile of the designed cladding structure previously generated by COMSOL model and which was processed in Matlab to create a readable BeamPROP matrix file. This methodology allowed to apply any specific designated complex index profile which cannot be done by using simple built-in drawing tools. For large radii bend waveguides (R ≥100 mm) the same procedure was applied and a circular s-bend was added between the input and output straight sections. Scaling and grid sizes were thoroughly considered to assure that correct computations were obtained. Mode solving was performed by launching a gaussian field in the waveguide input and using correlation method. The use of a correlation method is suitable for finding lossy or leaky modes. For the simulation of light propagation, the obtained fundamental mode (FM) was launched in the waveguide input, while the output power was monitored along the waveguide pathway, using a square monitor of the size of the corresponding waveguide core. All beam propagation Figs. in this work show a 2D intensity distribution across the waveguides, i.e. the near-field intensity distribution inside the CLWs, and the integrated power across the monitor surface, which represents the actual power flux at each point along the waveguide path length. This allowed us to compare the propagation losses (PLs) of different cladding designs. Bend losses (BLs) were also estimated by subtracting the PLs of straight waveguides to the total loss obtained in an s-bend waveguide of equal length. By knowing the total extra radiation loss due to bends we then normalize this value to the total arc length of the s-bend in mm, obtaining a BLs value in dB/mm. Besides this method, we also estimate the straight waveguide mode PLs by assuming an exponential decay with propagation length with the effective medium attenuation coefficient $\alpha = 4\pi \cdot Im(n_{\text{eff}})/\lambda$, so that:

$$PLs(dB/cm) = \frac{40\pi}{\ln 10.\lambda(\mu m)} Im(n_{eff}) \times 10^4. \quad (5)$$

and which gave equivalent numerical results.

3. Experimental and technical details

3.1 Laser fabrication of the cladding waveguide structures

Cladding structures were formed by transversally writing tracks to form a depressed-index circular tubular array that can sustain leaky modes. Due to the high anisotropy of the track cross section, the dimension of the resulting cladding is much larger in the vertical than the

#258038 Received 26 Jan 2016; revised 4 Mar 2016; accepted 13 Mar 2016; published 1 Apr 2016

horizontal cross section, therefore extra lines of tracks were added to the lateral sides of the circular shape structure so that this asymmetry can be minimized within this simple laser writing setup (see Fig. 2). Single tracks were first written so as to obtain the track sizes as a function of laser power and focusing depth for a fixed scanning speed of 0.7 mm/s. Subsequently, CLWs with diameter core sizes of 40 μm, 70 μm and 110 μm were designed in COMSOL and the tracks coordinates where then used in the laser inscription process. In this paper we only report the smallest fabricated waveguides (diameter core of 40 μm, named as 40-CLW), since the others were multimode and therefore out of the interest of the present work.

A Z-cut MgO:$LiNbO_3$ sample was cut with dimensions of 20(x) × 10(y) × 1(z) mm^3 and optically polished. 3DLW was performed along the z-axis of the sample. A Ti:Sapphire regenerative amplifier laser system (Spitfire and Tsunami systems, Spectra-Physics) was used. The system produces linearly-polarized pulses of about ~120 fs duration, with a repetition rate of 1 kHz at a central wavelength around 795 nm. A calibrated neutral density filter, a half-wave plate and a linear polarizer were used to precisely control the value of the pulse energy. The sample was mounted on a high-resolution three-axis motorized stage. The laser beam was focused through the xy plane of the sample at a minimum depth of 300 μm using a microscope objective (20x, N.A = 0.4). Waveguides were written along the 20 mm x-axis long dimension of the crystal. Track separation in the y-direction was fixed to 2 μm. The writing speed was of 0.7 mm/s and the pulse energy was set to 0.6 μJ. Laser polarization was kept perpendicular to the scanning direction. After fabrication the end facets of the sample were polished.

3.2. Optical waveguide characterization

The mid-IR guiding properties of CLWs were characterized using a linearly polarized ICL diode-laser (Nanoplus) emitting at the wavelength of 3.683 μm. The sample was mounted on a Thorlabs stage with 5-axis microcontrollers. Input and output laser coupling was performed using aspheric lenses (C021TME-E, NA = 0.18) from Thorlabs. Imaging was performed on a FLIR SC7000 mid-IR camera. In order to optimize the CLW mode excitation and minimize the excitation of cladding modes, a pinhole was used before the input lens to finely adjust the beam diameter. The input coupling efficiency was calculated by the overlap integral method for ten different pinhole diameters, using the measured laser input focal spots and the waveguide output mode. The insertion losses were measured for all pinhole diameters to verify the optimum coupling, and a minimum of 4.1 dB was achieved when the input spot field diameter closely matched the 40-CLW mode field diameter (MFD). PLs were calculated by subtracting the coupling losses and the Fresnel losses to the insertion losses. To obtain calibrated MFDs a calibration target was used (R1DS1P - Positive 1951 USAF Test Target, Ø1").

4. Results

4.1 Simulated total stress field of two adjacent parallel tracks

The simulation for two adjacent parallel tracks was performed as starting step because these type of waveguides are very well known and studied, and the main features of the total stress fields, such as anisotropy and the typical experimental levels of stress field magnitudes can be obtained from literature [8,19,21]. Running this first simple array allows to obtain a starting value for the main parameter of the CLWs simulation, which is the temperature difference (θ), which controls the stress level, and can be set to obtain a value that matches previously reported values. The simulation results of the obtained stress field built up around 2 elliptical parallel adjacent tracks with a separation of 10 μm are shown in Fig. 1.

#258038 Received 26 Jan 2016; revised 4 Mar 2016; accepted 13 Mar 2016; published 1 Apr 2016

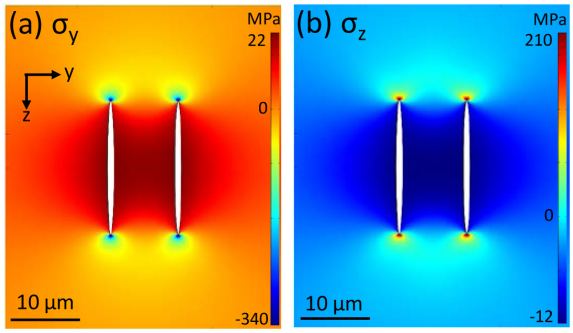

Fig. 1. Simulated stress field of the 2-track structure. (a) for the σ_y component (b) for the σ_z component.

It can be seen that for the σ_y stress component, compressive stress is distributed along the lateral side of the tracks, while tensile stress takes place at the apexes. For the σ_z stress component, the stress is tensile between the tracks and compressive at the tracks apexes. The temperature difference (θ) parameter was set to 100 K, which produces a compressive stress value (σ_y) of around 20 MPa between tracks, in a good agreement with previous work using the same experimental setup [8].

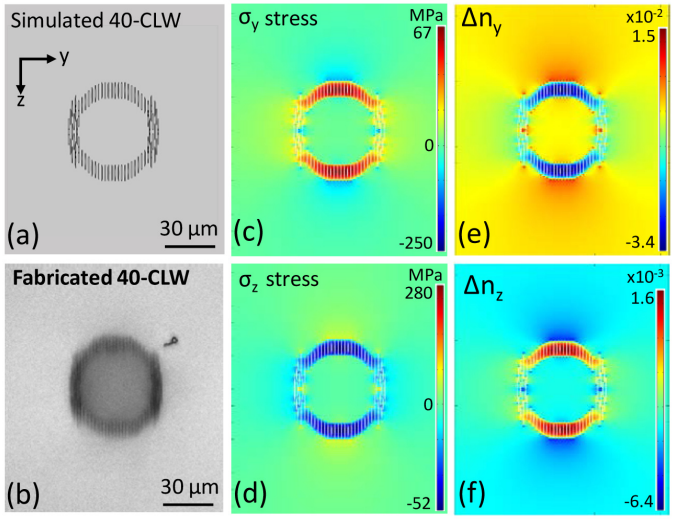

Fig. 2. Profiles of 40 µm diameter core cladding waveguides: (a) geometry, (b) fabricated result, (c)(d) stress fields σ_y and σ_z, (e)(f) stress-optic refractive index change distributions n_y and n_z.

4.2 Stress field in the cladding structures

The 40-CLW cladding geometry is displayed in Fig. 2(a), being very well matched with the real cladding fabricated by 3DLW shown in Fig. 2(b). The cladding ring is formed by 79 elliptical tracks (with horizontal track separations of 2 µm) including extra lines of tracks at

#258038 Received 26 Jan 2016; revised 4 Mar 2016; accepted 13 Mar 2016; published 1 Apr 2016

the sides which aim to "strengthen" the cladding wall. As it can be seen in Fig. 2(c) and (d), a biaxial tensile/compressive $\sigma_{y/z}$ stress field develops at the top and bottom sides of the cladding. This stress field will produce a strongly anisotropic waveguide behaviour. The maximum compressive and tensile stress is of about 67 MPa and 280 MPa, respectively. RI change profiles resembling the stress fields are shown in Fig. 2(e) and (f). It is also observed that changes of RI in the inside of the cladding ring are smaller than those outside. This is explained by the fact that the stress field originating from the inside apexes is partly cancelled by the opposite stress from the neighbour tracks due to the circular geometry. From this first analysis it is clear that the cladding confinement will be more efficient for TE-polarized modes, than for TM. This effect does not depend on the $LiNbO_3$ crystallographic axial alignment; it is an anisotropic effect arising solely by the highly asymmetric shape of the tracks. By placing the tracks closer together this effect can be mitigated, however at the cost of duplicating the fabrication time, and also increasing the risk of sample cracking. To avoid these two issues and maintain flexible fabrication parameters which do not entail cracking, in this work we have fixed the distance between tracks to 2 μm for all the studied cladding designs.

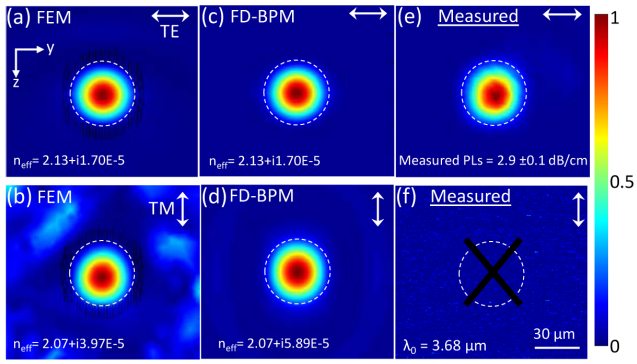

Fig. 3. Fundamental mode near field intensity distribution of the 40 μm diameter core CLW as obtained by FEM (a and b), FD-BPM (c and d), and experiments (e, and f).

4.3. Optical mode analysis and propagation losses in the cladding structures

A first mode analysis was performed both with FEM and FD-BPM software, using the initial parameters (see Section §2 for details), and compared with the real optical measurement of the fabricated 40-CLW. Fig. 3 shows a summary of results comparing the simulated TE and TM fundamental modes by the FEM method [Fig. 3(a) and (b)], FD-BPM method [Fig. 3(c) and (d)], and experimental results [Fig. 3(e) and (f)]. The effective index of the modes was obtained by both FEM and FD-BPM giving a TE mode with an effective refractive index of $2.13 + i1.7 \times 10^{-5}$. The imaginary part of the effective refractive index gives an estimated PLs of 2.5 dB/cm, which is slightly lower than the measured value (2.9 ± 0.1 dB/cm). In the case of vertically polarized light no TM mode was observed experimentally, while the PLs of the TM mode is calculated to be around 8.7 dB/cm. The reason why the 40-CLW does not guide TM light could be either that the losses are too high for this polarization and/or that the index change inside the tracks for vertically polarized (n_e) light is significantly lower than that for horizontally polarized light, so that the minimum index contrast for sustaining a leaky mode at 3680 nm wavelength is not attained. The 40-CLW seems to guide well TE polarized light. The measured propagation losses of 2.9 dB/cm is a value comparable with previous reported values [2,3,11], and in line with the observation described in Section §1.1 that losses below 1

#258038 Received 26 Jan 2016; revised 4 Mar 2016; accepted 13 Mar 2016; published 1 Apr 2016

dB/cm at mid-IR wavelengths appear to be hardly achievable so far, by the 3DLW technique in crystals.

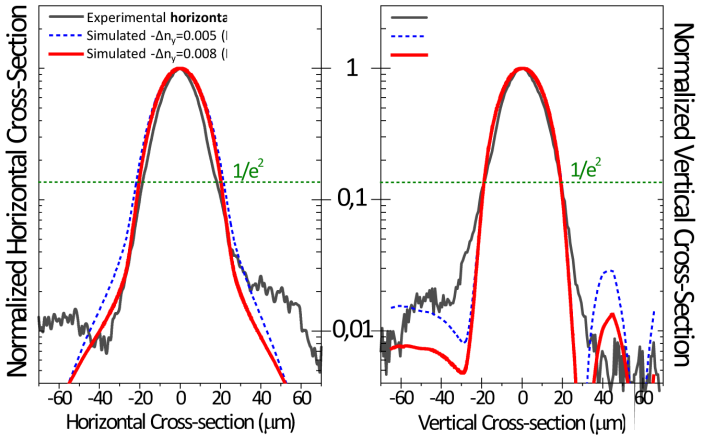

Fig. 4. Comparison of near field TE mode cross sections of simulations and experiment. Horizontal cross sections are shown on the left and vertical cross sections are shown on the right. The best matching between simulated and measured cross sections was obtained for an index change inside tracks of $\Delta n = -0.008$.

4.4. Refinement of the model: the complex index of refraction of laser modified $LiNbO_3$

Since the experimental characterisation of the 40-CLW showed no TM mode, only TE modes were used for further improving the model parameters. In the following we compare the cross sections of the experimental TE mode near field with the simulated ones, with the aim of obtaining the refractive index of laser modified depressed index tracks which give a best fit of the model. Fig. 4 shows the horizontal cross sections on the left, and vertical cross sections on the right. As it can be seen, the initial assumption that the Δn inside the tracks $\Delta n = -0.005$ gives a good matching between the simulated and the measured vertical MFD of the TE mid-IR mode. However, in the following we evaluate its optimization using the model and the experimental measurements. A set of different TE modes was computed for varying Δn_y values inside tracks from –0.001 to –0.01, so as to obtain the best overall fit to the measured near field mode. The best MFD matching was obtained for a Δn inside tracks of –0.008 (red line in Fig. 4). In this case, the vertical MFD is of 38.2 µm for both simulation and experiment, and of 40.6 µm (simulation) and 37.0 µm (experiment) along the horizontal direction. From this experiment we therefore conclude that the ordinary Δn_y of laser modified $LiNbO_3$ which forms the cladding has a reduced index of –0.008, at 3.68 µm wavelength. For the case of extraordinary light, since we did not obtain experimental data we will use the same value as a first approximation. In this regard, it is worth noticing that small variations in the Δn of ± 0.002 at tracks do not significantly affect the MFDs, so that this parameter is not highly critical for designing this type of CLWs.

#258038 Received 26 Jan 2016; revised 4 Mar 2016; accepted 13 Mar 2016; published 1 Apr 2016

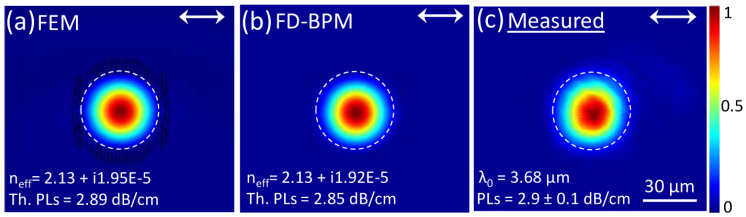

Fig. 5. Simulated (a and b) and measured (c) TE modes of the 40-CLW. (a) FEM, (b) FD-BPM and (c) experiment. Using complex RI change inside the cladding tracks: Δn_y = –0.008 + i0.0007. Scale bar in (c) is 30 µm and it is the same for the three Figs.

Since the simulation was performed in a purely refractive structure and the obtained waveguide losses are purely confinement losses, adding an imaginary component to the index of refraction (extinction coefficient associated to the absorption and scattering at the tracks volume) of damaged $LiNbO_3$ at cladding tracks will allow to better predict the real losses from the model. A set of ten different complex refraction indexes inside the tracks was run, with varying imaginary part from 10^{-4} to 10^{-5}. The final theoretical propagation losses of the TE modes were obtained both from formula (5), and from BeamPROP calculations. The optimized RI change value at the tracks was found to be $\Delta n_y = -0.008 + i7 \times 10^{-4}$, which gives a TE mode effective refractive index of $2.13 + 1.95 \times i10^{-5}$. This TE mode effective index gives a propagation loss of 2.89 dB/cm, in excellent agreement with the measured value of 2.9 ± 0.1 dB/cm. The final results of the simulated TE and the measured mode are shown in Fig. 5.

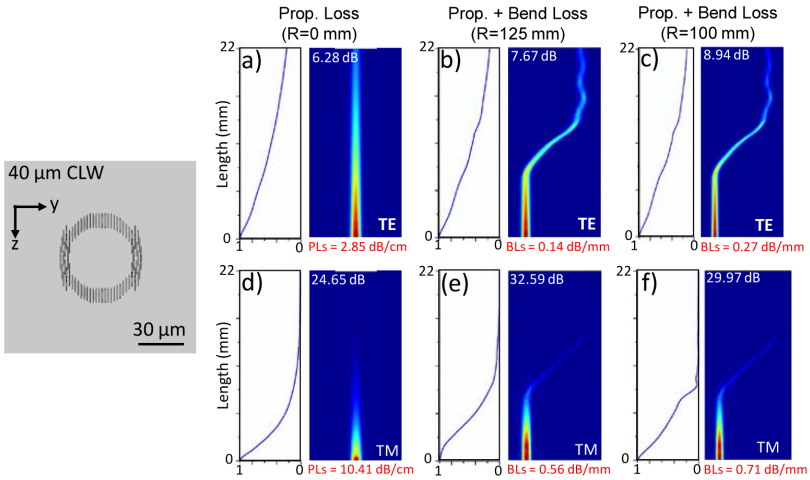

Fig. 6. Straight waveguide propagation losses (a and d), s-bend with R = 125 mm (b and e), and s-bend with R = 100 mm (c and f). Propagation losses (PLs, dB/cm straight length) and bend losses (BLs, dB/mm arc length) are evaluated for TE and TM modes.

#258038 Received 26 Jan 2016; revised 4 Mar 2016; accepted 13 Mar 2016; published 1 Apr 2016

4.5 Simulation of s-bend losses of mid-IR $LiNbO_3$ cladding waveguides

4.5.1 Simulation of s-bend losses of 40 μm diameter core cladding (40CLW)

The 40 μm core diameter waveguide 40CLW with a 22 mm length was first simulated. All results are shown in Fig. 6. The waveguide index profiles are taken from COMSOL results along with the Δn = –0.008 + 0.0007i at laser written tracks. The bend waveguides have 0.2 mm offsets to the sides, and radii of 125 and 100 mm are evaluated. For TE polarization, PLs are of 2.85 dB/cm close to the measured value (2.9 dB/cm). We obtain a TE mode BLs of 0.14 and 0.27 dB/mm for 125 and 100 mm radii, respectively. For the TM mode, we obtain a PLs of 10.41 dB/cm, and BLs of 0.56 and 0.71 dB/mm for 125 and 100 mm, respectively.

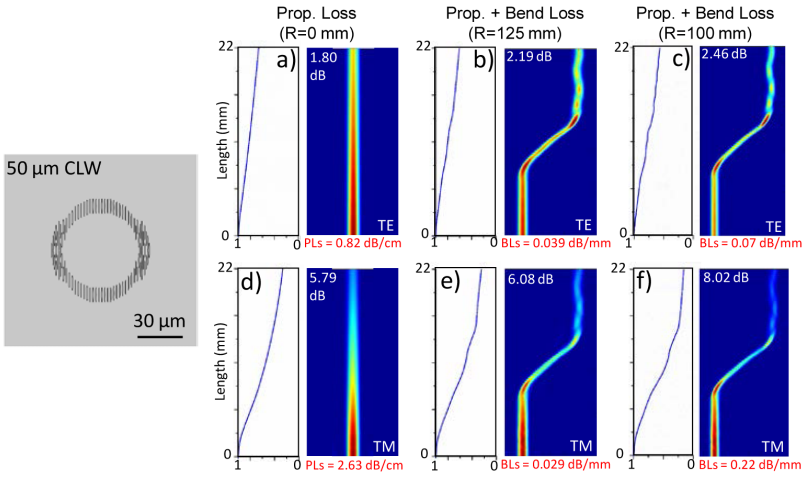

Fig. 7. Straight waveguide PLs (a and d), s-bend with R = 125 mm (b and e), and with R = 100 mm (c and f).

4.5.2 Simulation of 50 μm diameter core cladding (50-CLW)

A simulation of 50 μm diameter core diameter cladding waveguide was also performed. Fig. 7 shows all results. Only one higher mode was observed with a high imaginary effective index of ~3×10^{-4} and which therefore we expect to be not relevant for the present analysis. The PLs of the fundamental mode are of 0.82 dB/cm and 2.63 dB/cm for TE and TM modes, respectively. The bend losses are also improved in both cases: TE mode BLs of 0.039 and 0.07 dB/mm for 125 and 100 mm radii, respectively; and TM mode BLs of 0.029 and 0.22 dB/mm for 125 and 100 mm, respectively. The threshold of 0.5 dB/cm PLs that we established for considering acceptable device losses is however not achieved. Furthermore, the waveguide is still highly anisotropic with high PLs for TM light. A much wider cladding design is therefore required.

4.5.3 Simulation of a 50 μm diameter core double ring cladding (50-CLW2R)

The attenuation of leaky modes is known to be exponential with a rate rapidly decreasing as the thickness of the depressed index cladding increases [5]. Therefore, it is straightforward to fabricate lower PLs CLWs by just increasing the number of tracks conforming the cladding layer. This procedure is however at the cost of greatly increasing the fabrication time. Therefore, our model proves to be useful in this regard allowing one to first test a low-loss CLW design with a minimized number of tracks. Recently, Gross et al. reported the lowest

#258038 Received 26 Jan 2016; revised 4 Mar 2016; accepted 13 Mar 2016; published 1 Apr 2016

loss so far mid-IR CLWs fabricated by means of 3DLW (to the best of our knowledge), using ZBLAN glass [29]. Low PLs of 0.29 dB/cm were experimentally measured for a 47 µm diameter core and 59 µm thickness circular depressed CLW at the wavelength of 4 µm. To further decrease the PLs of $LiNbO_3$ CLWs we therefore increase the cladding thickness wall, but limited it to 14 µm so as maintain a reasonably low chip fabrication time. The thickness enlargement was obtained by incorporating a second ring of tracks to the cladding design, and obtaining a circular cladding similar to the one fabricated in ZBLAN glass by Gross et al. [29]. Fig. 8 shows all results of this 50-CLW2R design. The simulation of this 50-CLW2R cladding yields a TE mode PLs of 0.41 dB/cm, and a TM mode PLs of 0.88 dB/cm, therefore achieving low enough PLs for device developments. Regarding the BLs, for 125 mm and 100 mm radii, the TE mode BLs are of 0.03 and 0.05 dB/mm, and the TM mode BLs are of 0.02 and 0.04 dB/mm, respectively.

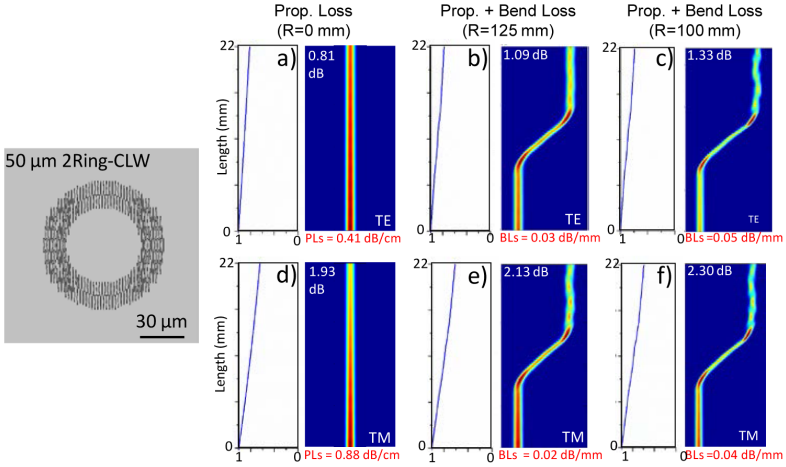

Fig. 8. Simulation of light propagation in the 50 µm diameter core straight waveguide and s-bend double ring CLW. Straight waveguide propagation losses (a and d), s-bend with r = 125 mm (b and e), and s-bend with r = 100 mm (c and f). Propagation losses (PLs, dB/cm straight length) and bend losses (BLs, dB/mm arc length) are evaluated for TE and TM modes.

4.6 Simulation of a 50:50 directional splitter

Finally, we have studied the evanescent coupling behavior of double ring CLWs at 3.683 µm wavelength, and simulated a 50:50 directional splitter for TE modes. In order to ensure single mode profile along the evanescent coupling section, waveguides are designed with core diameter of 36 µm and double cladding structure for this splitting section. The separation of the two waveguides in the coupling region is maintained to 38 µm from center to center which leaves only 1 low index track between them [see Fig. 9(a)]. The 50:50 directional splitting is achieved by introducing two s-bends to the two waveguide branches once a half coupling length has been reached. The 290 µm separation of the waveguides is achieved with bend radius of 71.4 mm after 6 mm length of propagation [see Fig. 9(a)]. Fig. 9(b) and (c) show the behavior for the TE polarized mode: the directional coupling region has a half coupling length (50% power transmission) of 3.285 mm, and the total element including the straight input and output regions has a total excess loss [= $10*\log(P_{in}/(P_{out1} + P_{out2})$] of 1.9 dB for the chosen length of 9.4 mm. This result demonstrates that it is possible to design beam splitting waveguide circuits capable of operating at the mid-IR range, for the first time to our knowledge, in $LiNbO_3$ crystals.

#258038 Received 26 Jan 2016; revised 4 Mar 2016; accepted 13 Mar 2016; published 1 Apr 2016

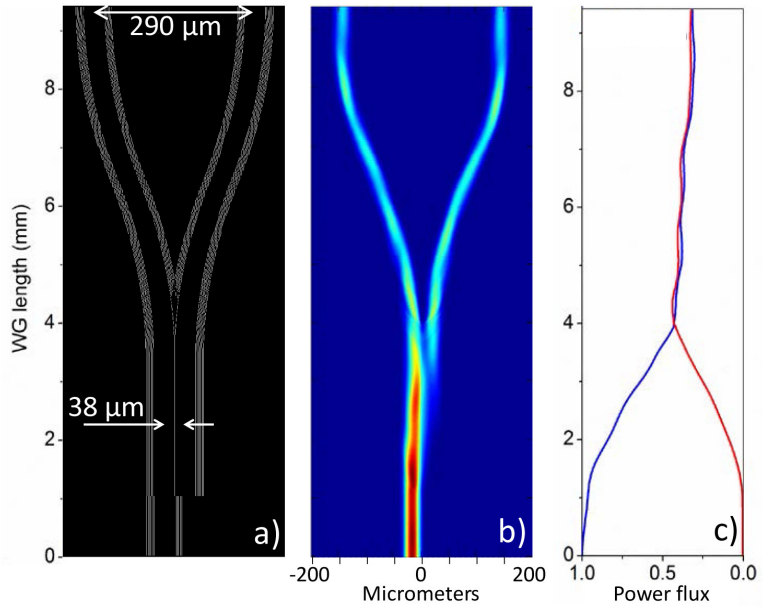

Fig. 9. a) cladding design of the splitter, b) light propagation simulation showing the field intensity distribution, and c) integrated power flux monitor of the two branches along the splitter length, blue and red curves show the left and right branches, respectively.

5. Conclusions

In this work we have used a heuristic approach for finding an effective simulation model of 3D laser fabricated anisotropically stressed depressed cladding waveguides in $LiNbO_3$ crystals for the wavelength of 3.683 µm. We have first developed our model so as to match the modal behavior of a single mode fabricated waveguide, and later used it to investigate for the first time how to decrease the mid-IR losses of cladding waveguides from the around 3 dB/cm currently reported, to the lower losses required for fabricating full on chip instruments using these type of waveguides. We have specifically evaluated how the anisotropic stress fields arising from the laser writing approach produce a difficulty to overcome intrinsic waveguide birefringence, and we have shown how one can address this problem in a realistic way by using a simulation model which includes the stress-optic dynamics into the leaky modes generation and predicts basic functions such as the bend losses and coupling lengths. We believe this study throws new light into the femtosecond laser writing dynamics in crystalline media and it can prove a valuable contribution to the development of mid-IR 3D waveguide devices inside $LiNbO_3$ non-linear crystals.

Acknowledgments

This work was supported by the Spanish MINECO under project MAT2013-47395-C4-4-R, TEC2014-55948-R and FIS2013-44174-P. Catalan Government 2014SGR1358. European Commission (ACP2-GA-2013-314335-JEDI ACE). F. D. acknowledges additional support 2010-ICREA-02 for excellence in research.

#258038 Received 26 Jan 2016; revised 4 Mar 2016; accepted 13 Mar 2016; published 1 Apr 2016

Paper II

Research Article | Vol. 25, No. 4 | 20 Feb 2017 | OPTICS EXPRESS 3722

Optics EXPRESS

Low-loss 3D-laser-written mid-infrared $LiNbO_3$ depressed-index cladding waveguides for both TE and TM polarizations

HUU-DAT NGUYEN,[1] AIRÁN RÓDENAS,[1,2,*] JAVIER R. VÁZQUEZ DE ALDANA,[3] GUILLERMO MARTÍN,[4] JAVIER MARTÍNEZ,[1] MAGDALENA AGUILÓ,[1] MARIA CINTA PUJOL,[1] AND FRANCESC DÍAZ[1]

[1]*Física i Cristal·lografía de Materials i Nanomaterials (FiCMA-FiCNA-EMAS), Departament de Química Física i Inorgànica, Universitat Rovira i Virgili, (URV), 43007, Tarragona, Spain*
[2]*Istituto di Fotonica e Nanotecnologie - Consiglio Nazionale delle Ricerche, Piazza Leonardo da Vinci, 32, I-20133 Milano, Italy*
[3]*Grupo de Investigación en Aplicaciones del Láser y Fotónica (ALF-USAL), Facultad de Ciencias, Universidad de Salamanca, E-37008 Salamanca, Spain*
[4]*UJF-Grenoble 1 / CNRS-INSU, Institut de Planétologie et d'Astrophysique de Grenoble (IPAG), Grenoble, France*
[*]*arodenas@gmail.com*

Abstract: We report mid-infrared $LiNbO_3$ depressed-index microstructured cladding waveguides fabricated by three-dimensional laser writing showing low propagation losses (~1.5 dB/cm) at 3.68 μm wavelength for both the transverse electric and magnetic polarized modes, a feature previously unachieved due to the strong anisotropic properties of this type of laser microstructured waveguides and which is of fundamental importance for many photonic applications. Using a heuristic modeling-testing iteration design approach which takes into account cladding induced stress-optic index changes, the fabricated cladding microstructure provides low-loss single mode operation for the mid-IR for both orthogonal polarizations. The dependence of the localized refractive index changes within the cladding microstructure with post-fabrication thermal annealing processes was also investigated, revealing its complex dependence of the laser induced refractive index changes on laser fabrication conditions and thermal post-processing steps. The waveguide modes properties and their dependence on thermal post-processing were numerically modeled and fitted to the experimental values by systematically varying three fundamental parameters of this type of waveguides: depressed refractive index values at sub-micron laser-written tracks, track size changes, and piezo-optic induced refractive index changes.

OCIS codes: (220.4000) Microstructure fabrication; (160.4330) Nonlinear optical materials; (230.7370) Waveguides; (000.4430) Numerical approximation and analysis; (130.0130) Integrated optics; (130.3730) Lithium niobate.

References and links

1. R. R. Thomson, S. Campbell, I. J. Blewett, A. K. Kar, and D. T. Reid, "Optical waveguide fabrication in z-cut lithium niobate ($LiNbO_3$) using femtosecond pulses in the low repetition rate regime," Appl. Phys. Lett. **88**(11), 111109 (2006).
2. R. Osellame, M. Lobino, N. Chiodo, M. Marangoni, G. Cerullo, R. Ramponi, H. T. Bookey, R. R. Thomson, N. D. Psaila, and A. K. Kar, "Femtosecond laser writing of waveguides in periodically poled lithium niobate preserving the nonlinear coefficient," Appl. Phys. Lett. **90**(24), 241107 (2007).
3. J. Burghoff, C. Grebing, S. Nolte, and A. Tünnermann, "Efficient frequency doubling in femtosecond laser-written waveguides in lithium niobate," Appl. Phys. Lett. **89**(8), 081108 (2006).
4. R. He, Q. An, Y. Jia, G. R. Castillo-Vega, J. R. Vázquez de Aldana, and F. Chen, "Femtosecond laser micromachining of lithium niobate depressed cladding waveguides," Opt. Mater. Express **3**(9), 1378–1384 (2013).
5. J. Burghoff, S. Nolte, and A. Tünnermann, "Origins of waveguiding in femtosecond laser structured $LiNbO_3$," Appls. Phys. A Mater. Sci. Process. **89**(1), 127–132 (2007).

#281205 https://doi.org/10.1364/OE.25.003722
Journal © 2017 Received 2 Dec 2016; revised 26 Jan 2017; accepted 27 Jan 2017; published 13 Feb 2017

Optics EXPRESS

6. H. Karakuzu, M. Dubov, and S. Boscolo, "Control of the properties of micro-structured waveguides in lithium niobate crystal," Opt. Express **21**(14), 17122–17130 (2013).
7. R. S. Weis and T. K. Gaylord, "Lithium niobate: Summary of physical properties and crystal structure," Appl. Phys., A Mater. Sci. Process. **37**(4), 191–203 (1985).
8. S. Heidmann, N. Courjal, and G. Martin, "Double polarization active Y junctions in the L band, based on Ti:$LiNbO_3$ lithium niobate waveguides: polarization and contrast performances," Opt. Lett. **37**(16), 3318–3320 (2012).
9. G. Martin, S. Heidmann, J.-Y. Rauch, L. Jocou, and N. Courjal, "Electro-optic fringe locking and photometric tuning using a two-stage Mach-Zehnder lithium niobate waveguide for high-contrast mid-infrared interferometry," Opt. Eng. **53**(3), 034101 (2014).
10. F. Thomas, S. Heidmann, M. de Mengin, N. Courjal, G. Ulliac, A. Morand, P. Benech, E. Le Coarer, and G. Martin, "First Results in Near and Mid IR Lithium Niobate-Based Integrated Optics Interferometer Based on SWIFTS-Lippmann Concept," J. Lightwave Technol. **32**(22), 3736–3742 (2014).
11. D. Jaque, E. Cantelar, and G. Lifante, "Lattice micro-modifications induced by Zn diffusion in Nd:$LiNbO_3$ channel waveguides probed by Nd^{3+} confocal micro-luminescence," Appl. Phys. B **88**(2), 201–204 (2007).
12. D. Castaldini, P. Bassi, S. Tascu, P. Aschieri, M. P. De Micheli, and P. Baldi, "Soft-proton-exchange tapers for low insertion-loss $LiNbO_3$ devices," J. Lightwave Technol. **25**(6), 1588–1593 (2007).
13. G. B. Montanari, P. De Nicola, S. Sugliani, A. Menin, A. Parini, A. Nubile, G. Bellanca, M. Chiarini, M. Bianconi, and G. G. Bentini, "Step-index optical waveguide produced by multi-step ion implantation in $LiNbO_3$," Opt. Express **20**(4), 4444–4453 (2012).
14. S. Juodkazis, V. Mizeikis, and H. Misawa, "Three-dimensional microfabrication of materials by femtosecond laser for photonics applications," J. Appl. Phys. **106**(5), 051101 (2009).
15. S. Nolte, M. Will, J. Burghoff, and A. Tünnermann, "Femtosecond waveguide writing: a new avenue to the three-dimensional integrated optics," Appl. Phys., A Mater. Sci. Process. **77**(1), 109–111 (2003).
16. R. Osellame, G. Cerullo, and R. Ramponi, eds., Femtosecond Laser Micromachining: Photonic and Microfluidic Devices in Transparent Materials, Topics in Applied Physics 123 (Springer-Verlag, 2012).
17. A. Ródenas, G. Zhou, D. Jaque, and M. Gu, "Direct laser writing of three-dimensional photonic structures in Nd:yttrium aluminum garnet laser ceramics," Appl. Phys. Lett. **93**(15), 151104 (2008).
18. A. Ródenas, G. A. Torchia, G. Lifante, E. Cantelar, J. Lamela, F. Jaque, L. Roso, and D. Jaque, "Refractive index change mechanisms in femtosecond laser written ceramic Nd:YAG waveguides: micro-spectroscopy experiments and beam propagation calculations," Appl. Phys. B **95**(1), 85–96 (2009).
19. A. Ródenas, "Direct femtosecond laser writing of 3D photonic structures in rare-earth doped lithium niobate," (Universidad Autónoma de Madrid, 2009).
20. H. D. Nguyen, A. Ródenas, J. R. Vázquez de Aldana, J. Martínez, F. Chen, M. Aguiló, M. C. Pujol, and F. Díaz, "Heuristic modelling of laser written mid-infrared $LiNbO_3$ stressed-cladding waveguides," Opt. Express **24**(7), 7777–7791 (2016).
21. A. Rodenas and A. K. Kar, "High-contrast step-index waveguides in borate nonlinear laser crystals by 3D laser writing," Opt. Express **19**(18), 17820–17833 (2011).
22. H. Liu, Y. Jia, J. R. Vázquez de Aldana, D. Jaque, and F. Chen, "Femtosecond laser inscribed cladding waveguides in Nd:YAG ceramics: Fabrication, fluorescence imaging and laser performance," Opt. Express **20**(17), 18620–18629 (2012).
23. J. Hu and C. R. Menyuk, "Understanding leaky modes: slab waveguide revisited," Adv. Opt. Photonics **1**(1), 58–106 (2009).
24. Q. An, Y. Ren, Y. Jia, J. R. Vázquez de Aldana, and F. Chen, "Mid-infrared waveguides in zinc sulfide crystal," Opt. Mater. Express **3**(4), 466–471 (2013).
25. A. Ródenas, L. M. Maestro, M. Ramirez, G. A. Torchia, L. Roso, F. Chen, and D. Jaque, "Anisotropic lattice changes in femtosecond laser inscribed Nd^{3+}:MgO:$LiNbO_3$ optical waveguides," J. Appl. Phys. **106**(1), 013110 (2009).
26. B. McMillen and Y. Bellouard, "On the anisotropy of stress-distribution induced in glasses and crystals by non-ablative femtosecond laser exposure," Opt. Express **23**(1), 86–100 (2015).
27. H. Karakuzu, M. Dubov, S. Boscolo, L. A. Melnikov, and Y. A. Mazhirina, "Optimisation of microstructured waveguides in z-cut $LiNbO_3$ crystals," Opt. Mater. Express **4**(3), 541–552 (2014).
28. R. He, Q. An, J. R. Vázquez de Aldana, Q. Lu, and F. Chen, "Femtosecond-laser micromachined optical waveguides in $Bi_4Ge_3O_{12}$ crystals," Appl. Opt. **52**(16), 3713–3718 (2013).
29. D. E. Zelmon, D. L. Small, and D. Jundt, "Infrared corrected Sellmeier coefficients for congruently grown lithium niobate and 5 mol.% magnesium oxide –doped lithium niobate," J. Opt. Soc. Am. B **14**(12), 3319–3322 (1997).
30. S. Gross, N. Jovanovic, A. Sharp, M. Ireland, J. Lawrence, and M. J. Withford, "Low loss mid-infrared ZBLAN waveguides for future astronomical applications," Opt. Express **23**(6), 7946–7956 (2015).
31. J. Martínez de Mendívil, D. Sola, J. R. Vázquez de Aldana, G. Lifante, A. H. de Aza, P. Pena, and J. I. Peña, "Ultrafast direct laser writing of cladding waveguides in the $0.8CaSiO_3$-$0.2Ca_3(PO_4)_2$ eutectic glass doped with Nd^{3+} ions," J. Appl. Phys. **117**(4), 043104 (2015).
32. A. Benayas, D. Jaque, B. McMillen, and K. P. Chen, "Thermal stability of microstructural and optical modifications induced in sapphire by ultrafast laser filamentation," J. Appl. Phys. **107**(3), 033522 (2010).

Optics EXPRESS

33. J. Burghoff, H. Hartung, S. Nolte, and A. Tünnermann, "Structural properties of femtosecond laser-induced modifications in $LiNbO_3$," Appl. Phys., A Mater. Sci. Process. **86**(2), 165–170 (2006).
34. A. M. Prokhorov and Y. S. Kuz'minov, *Physics and Chemistry of Crystalline Lithium Niobate* (Taylor & Francis Ltd, 1990).
35. A. Benayas, W. F. Silva, C. Jacinto, E. Cantelar, J. Lamela, F. Jaque, J. R. Vázquez de Aldana, G. A. Torchia, L. Roso, A. A. Kaminskii, and D. Jaque, "Thermally resistant waveguides fabricated in Nd:YAG ceramics by crossing femtosecond damage filaments," Opt. Lett. **35**(3), 330–332 (2010).

1. Introduction

Lithium niobate ($LiNbO_3$) has been established as a versatile material for integrated electro-optic devices and nonlinear optical applications due to its high electro-optical and non-linear coefficients, its well-developed industrial manufacturing quality, and its large transparency window from the UV to the mid-IR [1–4]. The large developments on $LiNbO_3$ devices for the telecom range in the last three decades enable $LiNbO_3$ crystals to be a promising material for the mid-IR photonics as well, with wide applications in chemical and bio-medical fields, in atmospheric research, high-resolution on-chip vibrational spectroscopy, and astrophotonic instrumentation [2–10]. Conventionally, lithographic techniques such as ion in-diffusion, ion implantation and soft proton exchange have been employed to manufacture optical waveguide structures in $LiNbO_3$ [11–13]. However, the lithographic approach is limited to a two-dimensional (2D) layout which does not allow to fully exploit three-dimensional circuit architectures, which are compulsory for multi-channel beam combination, in particular in the field of astrophotonics and stellar interferometry. The direct femtosecond (fs) laser writing has emerged as a versatile and efficient tool which enables the three-dimensional (3D) laser writing (3DLW) of complex waveguide designs within a short timescale of minutes [14–16]. However, $LiNbO_3$ still poses various serious challenges for the 3DLW technique to be reliable and efficient for photonic fabrication: its birefringence induces aberration of the writing focal volume when using high numerical aperture lenses, and its photo-refractive, piezo-optic and non-linear properties further complicate the 3DLW fabrication process to a very high degree [2,7].

The tight focusing of fs near-IR laser pulses inside the host material are known to induce a non-linear absorption which results in a spatially localized lattice change in the sub-micron scale [14–21]. The structural changes involve electronic defects or lattice defects, so that in general a change in the material involves modified refractive and absorptive properties through a change in the complex refractive index ($\Delta n^* = \Delta n + i\Delta\kappa$, where Δn is the change in the real part of the index of refraction and $\Delta\kappa$ is the change in the extinction coefficient). It is important to note that index changes can vary significantly if measured at the visible, near-IR or mid-IR ranges, since the material polarizability and defects absorption in these ranges have distinctive origins. However, these effects are difficult to know due to the difficulty in measuring index changes in nanostructured volumes at different wavelengths, and only a few works have reported on the dispersion of Δn at different wavelengths in laser written waveguides [21]. In general, two fundamental types of index modification Δn have been reported with the 3DLW technique in $LiNbO_3$, which are the so called Type I (increased refractive index at the laser writing focal volume) and Type II (negative index change at the laser writing focal volume, and strong stress field surrounding the track due to lattice amorphization and defect generation, involving collateral piezo-optic index changes) [1,3]. Depressed-index cladding waveguides, hereafter CLWs, are normally written by drawing two-dimensional tubular structures in the regime for Type II index changes, and which therefore act as depressed cladding (see inset in Fig. 1). The guiding properties depend on the magnitude of the negative Δn change produced at the written tracks, and on the size and spatial width of the cladding arrangement [20]. The final refractive index profiles of a whole cladding structure are dependent on (1) the local Δn at the modified tracks and on (2) the anisotropic piezo-optic index changes in the surroundings of tracks, which strongly depend on

Optics EXPRESS

the chosen 3DLW parameters: i.e. pulse duration, pulse energy, repetition rate, scanning speed, wavelength, polarization, and focusing optics.

Recently, the mid-IR refractive index profile of 3DLW $LiNbO_3$ microstructured cladding waveguides was reported for the first time [20]. The refractive index estimations were performed by means of a combination of experimental characterizations and detailed finite element method (FEM) based simulation models of the microstructures taking into account both refractive index changes due to direct fs laser modification and also the stress-induced birefringent index changes [20]. However, single mode optical guiding was only demonstrated for TE horizontally polarized light and not for TM polarization, due to the strong anisotropy of the cladding structures, this implying that the Δn profiles of the waveguides for TM modes could not be assessed, and also no guiding for both TE/TM light could be achieved. Moreover, the demonstrated propagation losses for single mode TE waveguides was of 2.9 dB/cm, far from being low losses. There exists therefore a fundamental bottleneck for obtaining CLWs in $LiNbO_3$ for mid-IR applications, capable of single mode guiding with low propagation losses for both orthogonal polarizations. Not in vain, single mode $LiNbO_3$ CLWs with propagation losses (PLs) lower than ~3 dB/cm at wavelength longer than 3 μm are still to be demonstrated [6,20–27]. In the search for improving the optical performance of CLWs, thermal treatments have been also performed to remove the anisotropic micro-stress fields induced during the laser writing process [4,27,28], since this induced stress is considered as one of the major factors causing the birefringent behavior of the CLWs. However, a clear understanding of the changes in waveguide profiles under different annealing conditions is also still missing, and 3DLW mid-IR $LiNbO_3$ single mode CLWs in particular have not yet been studied in combination with post-fabrication annealing treatments, mainly due to the high difficulties in assessing refractive index changes in this long wavelength range.

The goal of this work is to further understand the micro- and nano-structural refractive index changes, which take place in 3DLW $LiNbO_3$ CLWs, with the aim of achieving single mode low-loss propagation for both TE/TM polarizations. By means of refining the microstructural designs of CLWs, and studying their guiding properties both in as-fabricated samples and annealed samples, we infer how the sub-micron laser written tracks change in both size and index of refraction, and also how the stress-fields are reduced as a function of annealing temperature and time. Results reveal that by performing thermal annealings until a cladding design dependent temperature, single mode guiding for both polarizations can be achieved, with a minimum obtained propagation losses of 1.25 dB/cm and 1.79 dB/cm for TM and TE polarizations, respectively.

2. Materials and technical details

2.1 Design and numerical modelling

Cladding waveguide design and numerical analysis were done by using a finite element computational method (FEM hereafter) using commercial COMSOL package, and which takes into account both constant refractive index changes inside the laser written tracks and its surrounding piezo-optic index changes, supposing a thermal expansion of the laser written tracks, as previously reported [20]. The micrometric volume changes induced by the localized femtosecond pulse ionization inside $LiNbO_3$ were simulated with a 2D thermal expansion model which yields the stress distribution in the expanded track surroundings. The inside of laser written tracks is approximated to be constant and have a negative index change. The studied 2D stress fields are responsible for anisotropic refractive index changes surrounding the laser-modified low-index tracks due to the piezo-optic effect. Once a full cladding waveguide refractive index profile is obtained, the mode analysis is performed with an electromagnetic-wave frequency-domain model. All simulations are calculated for a free space wavelength of 3.68 μm where ordinary and extraordinary index values of $LiNbO_3$ are $n_{y(o)} = 2.1309$ and $n_{z(e)} = 2.0700$, respectively [29]. The numerical mode calculation gives the

Optics EXPRESS

near-field distributions of the guided waveguide modes and their corresponding effective indices which are used to obtain the theoretical mode field diameters (MFDs) and propagation losses (PLs), respectively (for further details see [20]).

Previously reported single-mode mid-IR waveguides [20] were fabricated with a core of 40 μm and cladding width of 10 μm (vertical size of a single track) and were experimentally found to support guiding only for TE polarized light with high PLs of around ~3 dB/cm [20]. Increasing the core diameter and the width of the cladding structure is known to result in reduction of PLs of the fundamental mode, although avoiding the excitation of higher order modes for any polarization can be difficult [20,27,30]. Therefore, in this work the waveguides are designed with a two-fold widened cladding arrangement consisting of two rings of tracks, with a core diameter of 50 μm (hereafter CLW2R) aimed to offer low-loss optical guiding for both polarizations with minimized birefringent effect. In order to get an initial approximation, the waveguide design and computation take as starting parameters the refractive index contrast and induced-stress magnitudes obtained in our previous study [20], and develops towards better optical performances using a minimized number of tracks given the double-ring structure. The initial cladding structure consists of 174 laser-written tracks spaced by 2 μm, forming an unmodified circular core of 50 μm in diameter (see inset of Fig. 1). However, due to aberration effects of the focal volume inside $LiNbO_3$, 117 extra tracks were added to the model replicating the experimentally observed appearance of secondary focal points of the writing laser beam around 8 μm above the primary focus and for focusing depths higher than 300 μm. By means of atomic force microscopy (AFM) and scanning electron microscopy (SEM) imaging, the laser-inscribed tracks were measured to have elliptical shapes with a length of 7 μm along the incident direction of the laser beam (z-axis, vertical) and a width of 300 nm along the perpendicular direction (y-axis, horizontal). The measured sizes of the extra tracks were around 66% of the primary tracks. The fabricated cladding layer is almost uniform with an approximate width of 16 μm except in its the lower part where it is thicker due to the extra tracks created by the focal volume aberrations.

Following previous works [18], it is expected that under the processes of thermal annealing the laser-modified depressed-index tracks will reduce in size and in refractive index change magnitude with respect to the bulk, and the stress fields will be relaxed. These microstructural changes will result in complex changes of optical guiding performance, since depressed index tracks conform the cladding and the stress-induced index changes reinforce or weaken it depending on the sign of the piezo-optic induced refractive index change. The study of these three variables (depressed-refractive indices, stress-induced refractive indices and track dimensions) is therefore carried out for each different thermal annealing process, by matching both the theoretical MFD and PL values to the experimental results (discussed in section §3.2), this allowing to unveil how these mid-IR waveguides change their properties with annealing temperatures above 573 K (300°C).

2.2 Femtosecond laser fabrication

The laser fabrication involves the transversal inscription of tracks to construct a depressed-Δn circular array which supports leaky modes along the tubular channel [23]. Geometrical coordinates of each individual track were extracted from the 2D design and loaded to a script used in the laser inscription process. Trial of writing single tracks was initially conducted in order to specify the track sizes as a function of laser energy and focusing depth.

The femtosecond laser beam used for waveguide fabrication was linearly polarized along the y-axis of the crystal (perpendicular to the scanning direction). A 90° rotation of the polarization direction did not produce significant differences in the fabricated structures. Such independence, to our knowledge, is due to the fact that the propagation direction of the femtosecond laser is along the z-axis of the crystal (z-cut sample) and thus the polarization is mainly contained in the isotropy plane.

Optics EXPRESS

The 3D laser writing (3DLW) was processed along the z-axis of a z-cut $LiNbO_3$ sample with dimensions of 20(x) × 10(y) × 1(z) mm^3 (include the commercial source of the crystal). All faces of the sample were optically polished with high quality before starting the fabrication processes. The optical fabrication setup includes a Ti:Sapphire regenerative amplified laser system (Spitfire and Tsunami systems, Spectra-Physics) which produces linearly-polarized pulses of ~120 fs duration, with a repetition rate of 1 kHz at a central wavelength of 795 nm. A series of pulse energies were adjusted by using a calibrated neutral density filter, a half-wave plate and a linear polarizer. A high-resolution three-axis motorized stage was used to mount the sample and precisely move the positions corresponding to the programmed script. A microscope objective (40 × , NA = 0.65) was used to focus the laser beam through the xy plane of the sample at a central depth of 300 μm. The laser scanning direction was along the long dimension (20 mm, x-axis) of the crystal. Separation of the tracks in the y-direction was fixed to 2 μm. Laser polarization was kept perpendicular to the scanning direction. In the first set of waveguides, a series of eight pulse energy values (0.84 μJ to 2.31 μJ, with increment of 0.21 μJ) was performed along with a fixed scan velocity of 750 μm/s. The second set of waveguides was done with three values of pulse energy (0.84 μJ to 1.68 μJ, with increment of 0.42 μJ) and a fixed scan velocity of 500 μm/s.

2.3 Optical waveguide characterization

Microscope optical imaging of the cladding structure was done with a blue-LED confocal optical microscope (Sensofar PLμ 2300). In order to obtain high resolution images of the tracks, SEM characterisation was also performed. In addition, AFM was also used to investigate the nanometric widths of the single tracks, after the sample was slightly chemically etched with nitric acid at room temperature for 30 seconds so that the laser-damage tracks were revealed.

The waveguides were characterised at the wavelength of 3.68 μm with a linearly polarized interband cascade laser. The collimated laser beam was directed with two mirrors to undergo a change in height so that its final polarization was linear at 45° with respect to both the vertical and horizontal polarization axes. Two linear polarizers were then used to select either horizontal (TE) or vertical (TM) polarizations, one polarizer before the input lens, and the second after the output lens. A micro-positioning stage with 5-axis manual microcontrollers was used to align the sample. Input light was launched in the waveguides with an aspheric lens of 0.18NA, and the waveguides output modes near fields were imaged with a FLIR SC700 mid-IR camera and an aspheric lens with 0.56 NA. A pinhole was placed before the input lens so as to finely adjust the beam diameter and optimize the input coupling into waveguides. The coupling efficiency was calculated by means of overlap integral between the optimal input spot size and each waveguide output mode. PLs were calculated by subtracting the input coupling losses and double Fresnel losses to the measured total insertion losses at the optimal input spot size.

2.4 Thermal annealing

Thermal treatments of the waveguides were performed in a furnace with open-air condition. A series of seven annealing processes at different maximum temperatures was carried out. The first annealing was done at a maximum temperature of 573 K (300°C) for 3 hours, with a 2 K per minute ramp for heating up and cooling down. The same processes were repeated with increasing maximum temperatures of 773, 873, 973, 1073, 1123 and 1173 K (900°C). Since the annealing was repeatedly done on the same sample, the final result is an accumulation of heat treatments from all the preceding processes. The sample was analysed by SEM and the waveguides were fully characterized after each annealing step.

Optics EXPRESS

3. Results

3.1 Mid-IR optical guiding properties of waveguides

All propagation losses obtained from the guiding characterization of as-fabricated (no annealings) are listed in Table 1 and shown in Fig. 1.

Group A consists of 8 waveguides fabricated with a fixed scan speed of 750 μm/s (hereafter named 750_wg#) and different pulse energy values chosen within the range that provided enough power to cause depressed-Δ*n* damage and observable guiding, and did not induce cracks within the CLWs. Waveguide 750_wg5 had a surface damage and therefore could therefore not be precisely characterized. Group B has three waveguides fabricated with three different pulse energies and a fixed scan velocity of 500 μm/s (hereafter 500_wg#). All the waveguides showed guiding for both TE and TM modes. However, while all CLWs were observed to be single mode for TM polarized light, multimode guiding was observed for TE polarization. This behavior shows how strong is the role of the anisotropic stress-induced Δ*n* profiles.

Table 1. Propagation losses of the CLW2Rs fabricated with different laser conditions

	Group A 750 μm/s scan velocity								Group B 500 μm/s scan velocity		
	750_ wg1	750_ wg2	750_ wg3	750_ wg4	750_ wg5	750_ **wg6**	750_ wg7	750_ **wg8**	500_ wg1	500_ wg3	500_ wg5
Pulse energy (μJ)	0.84	1.05	1.26	1.47	1.68	1.89	2.10	2.31	0.84	1.26	1.68
TE-PLs (dB/cm)	MM	MM	MM	MM	MM	MM	MM	MM	MM	MM	MM
TM-PLs (dB/cm)	4.59	3.48	2.70	2.11	x	**1.18**	1.28	**1.19**	1.67	1.49	MM

MM: multimode; x: not guided

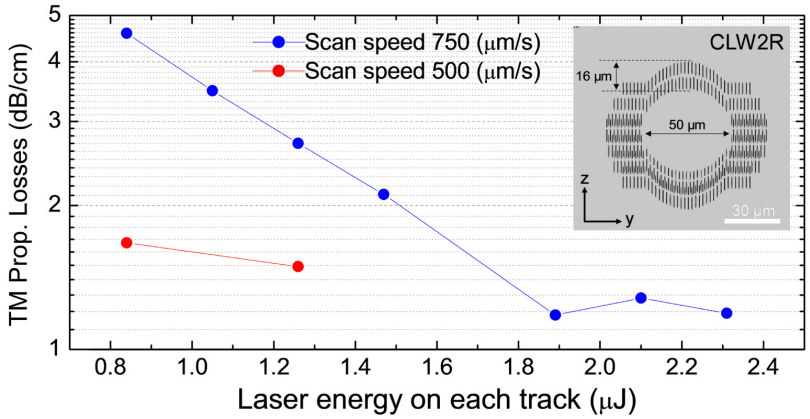

Fig. 1. Propagation losses for TM mode of CLW2Rs fabricated by different pulse energies and scanning velocities. Lines joining experimental points are added only as visual help.

Since the waveguides are multimode for the TE polarized light, PLs were not measured for this case, since our goal is to have single mode waveguides and characterize their losses. For the case of TM polarized light, a clear trend is observed that the higher the pulse energies by which the waveguides were fabricated, the better guiding performance they have in terms of lower PLs, however this at the cost of having increasing number of modes for the

Optics EXPRESS

orthogonal polarization (TE). As it can be expected, this could be due to the increasing Δn magnitude of the depressed cladding tracks. The lowest PL of 1.19 dB/cm was obtained by the waveguide 750_wg8 written by the highest laser pulse energy of 2.31 μJ and scanning speed of 750 μm/s. Waveguides fabricated with lower scanning speeds were measured to have lower losses (Fig. 1. Red line), although no CLWs could be fabricated at pulse energies above 1.3 μJ due to lack of space within the $LiNbO_3$ sample. Lower writing speed produce a larger pulse overlap along the scanning direction which in turn results in more homogeneous depressed index tracks, therefore producing a better confining region. However, this is also at the cost of increased fabrication times.

3.2. Guiding performance of waveguides under heat treatments

The main goal of treating the waveguides with thermal annealing was to reduce the level of the anisotropic stress which might benefit the optical performance for one polarization and deteriorate the other, due to the fact that piezo-optic induced refractive index changes have opposite sign for orthogonal polarizations. Improvements of optical properties with the help of heat treatments have been reported for laser-written cladding waveguides on different materials, although no work has yet been performed for the mid-infrared range. He et al. have demonstrated a 30% decrease of PLs when CLWs on bismuth germanium oxide (BGO) crystal were treated at 533K for 2 hours [28]. However, the BGO waveguides increased the losses at the annealing temperature of 633K, and started to disappear at higher temperatures. Another work was done with the study of CLWs on neodymium doped wollastonite tricalcium phosphate glass as a function of annealing temperature [31]. The transmitted optical power of these glass CLWs was improved as a factor of 3 when treated at up to 873K. With the heat treatment higher than 923K, a dramatic increase of PLs was observed. For the case of CLWs on $LiNbO_3$, single mode CLWs were enhanced in transmission with PLs from 5.3 to 4.3 dB/cm for 4 μm wavelength by annealing at 533K for 1 hour [4]. It should be noted however, that neither of these works was performed for mid-IR light, and therefore the effects and dependences of high temperature annealing processes with the material refractive index changes can be different to our present analysis.

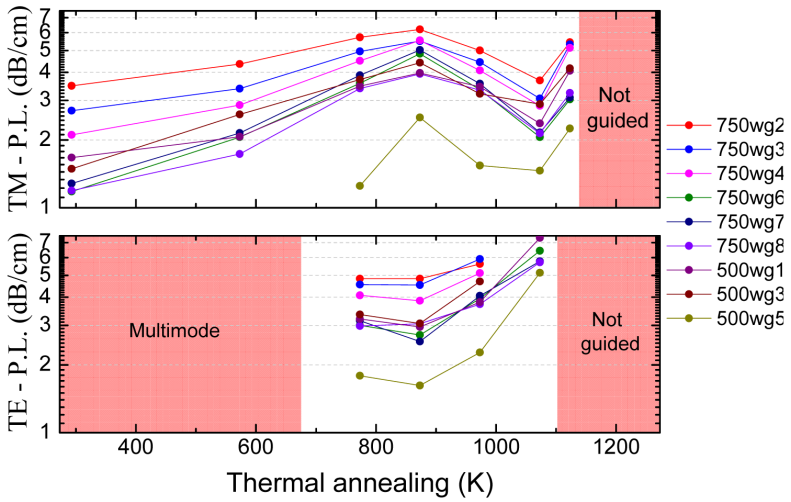

Fig. 2. Waveguide performances with respect to different heat treatments. PLs of the waveguides for TM polarization (upper graph) and TE polarization (lower graph). Lines joining experimental points are added only as visual help.

Optics EXPRESS

In our work, the behavior of this type of waveguide was revealed to be complicated when studied with a broad range of annealing temperatures (573K to 1173K). The initially non-annealed waveguides clearly showed a strong birefringent characteristic with mono-mode behavior for TM polarized light, while multimode was observed for TE light. The annealing treatment helped to clean the higher order modes of the TE polarization and left the CLW2Rs to have single mode behavior after sequential heating treatments of 573 and 773K for 3 hours each (see Fig. 2, lower graph). With higher annealing temperatures and longer annealing times, the PLs of these TE modes steadily increased. The same trend happened to all the waveguides, and all stopped guiding light when annealed at peak temperature of higher than 1073K. Here, the waveguide 750_wg1 was not included in the figure due to an accidental break during a manual handling of the sample.

For TM modes, the guiding performance was deteriorated during the first heat treatments of 573, 773 and 873 K, with a clear increase of the PLs (see Fig. 2, upper graph). The trend of PLs was reversed when the temperature was raised to 973K and at the annealing of 1073K the PLs dropped to a bottom which is around the PL levels of the non-annealed waveguides. Consequently, at higher temperature than 1123K the waveguides started to have more losses and vanished after temperature of 1173K. In conclusion, the TM polarized CLWs transmission did not benefit from the annealing treatments. This is a counterintuitive effect, since for TM (vertical) polarization it is well known that a compressive stress between the tracks produces a positive index increase which therefore deteriorates the depressed cladding effect of the tracks microstructure, so that erasing this stress should improve the optical guiding. Contrary to this, the guiding behavior is worsened for TM polarization, so that other microstructural changes must be taking place besides stress field erasure. Overall, as it can be seen in Fig. 2, the CLW 500_wg5, which was fabricated with high pulse energy (1.68 μJ) and slow scan speed (500 μm/s), provides the best optical performance after several heat treatments. This was indeed the only multimode CLW for TM light, so that thermal treatments also allowed to tailor it to be single mode. Details of this waveguide performance will be discussed in section §3.4.

3.3. Heuristic numerical modeling of waveguide properties with respect to thermal treatments

It has been suggested that the effects of the thermal annealing on laser-written waveguides involve several factors: one is a general decrease of induced color centers which increase the absorption of the material within the laser-damaged tracks and its surroundings (although this effect may not be of relevance within the mid-IR range as compared to visible of near-IR ranges where optical centers typically have absorption bands), and the other is a partial erasure of the depressed Δn change [3,5,18,31–33]. Depressed index tracks therefore not only change in optical properties but also in cross-sectional size, becoming smaller as thermal annealings are performed with higher temperatures [18–20]. The residual stress generated during the fs-laser fabrication process is additionally erased, which might be beneficial to the guiding properties of CLW if they are designed as pure depressed refractivd index structures.

In order to closely study these effects, an heuristic simulation model which iteratively feeds from experimental measurements of the mode field diameters and propagation losses (details reported in [20]) was used to estimate the hypothetical changes of the three variables: magnitude and spatial dimensions of the depressed- refractive index regions, and the level of residual stress in their surroundings. The exact values of these variables are strongly dependent on particular conditions of the laser fabrication, so that only once a first test of CLWs is fabricated and characterized under specific 3DLW conditions, modelling has to be done for these CLWs and the use of simulations to optimize the cladding microstructure will only be correct for subsequent CLWs fabricated under exactly the same 3DLW experimental conditions.

Optics EXPRESS

A detailed study was performed for the waveguide 750_wg8 which was laser-inscribed with pulse energy of 2.31 μJ and scanning speed of 750 μm/s, for which 8 different pulse energies were tested and therefore further analysis can be undertaken for this writing speed. Before annealing, the 750_wg8 supports monomode guiding for TM polarization and multimode guiding for TE polarization. The fundamental TM mode persisted during annealing of up to 1123K and vanished at higher temperature treatment. In the case of TE mode guiding, higher order modes were cleaned up and the CLW2R started to be single mode after annealed at 773K. The waveguide stopped guiding TE light after 1073K annealing. The measured PLs of these modes are shown in Fig. 3 (solid lines) which resembles the trend of all other waveguides as stated in the previous section §3.2 (Fig. 2). In order to simulate this unique behavior, initial numerical assumptions are made on the three core variables which are used in our model to perform analysis of theoretical guided modes: track sizes, refractive index, and magnitude of induced stress fields surrounding the tracks. The refinement of initial numerical assumptions is then based on optimal matching between theoretical and measured values of MFDs and PLs.

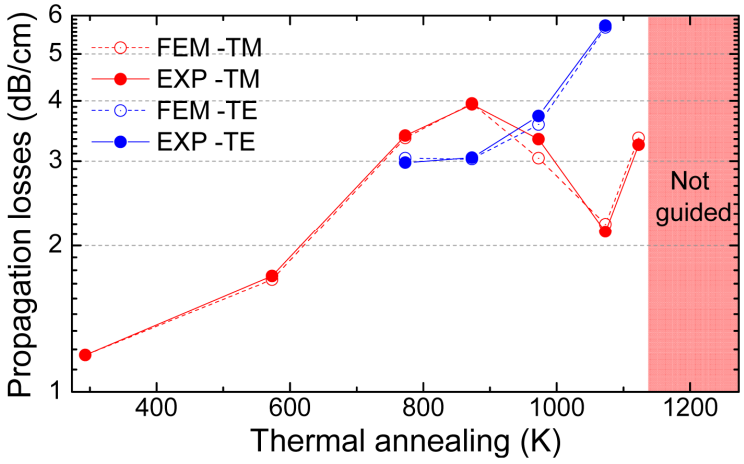

Fig. 3. Theoretical FEM and experimental PL values of the waveguide 750_wg8 versus the thermal annealing temperature. TE (blue graphs) and TM (red graphs) are both considered. The waveguide does not guide after treatment at 1173K. Lines joining experimental points are added only as visual help.

As a starting point, simulation was solved for the as-fabricated waveguide which consists on a double ring tubular microstructure of elliptical tracks with a width of 300 nm and a length of 7 μm (obtained from SEM and AFM characterization). The two other variables to define are the complex index of refraction at laser written tracks (including the extraordinary and ordinary index changes, Δn_z and Δn_y separately) and the value of stress field (σ) induced in the surrounding. In a previous report on mid-IR CLW by authors (using the same 3DLW setup) it was concluded that a maximum compressive stress (σ_y) of ~67 MPa and a complex index change of $\Delta n_y^* = -0.008 + i0.0007$ for the single-cladding waveguide (fabricated with low pulse power of 0.6 μJ and writing speed of 700 μm/s) was a best match to experiments for TE polarization (while no TM guiding was observed for a single ring CLW in this previous work) [20]. In the present work, the waveguide has a double-ring wider cladding (see inset of Fig. 1) and was written with a 4 times higher pulse energy of 2.31 μJ, therefore the values of stress and the magnitude of index changes are expected to be higher than those measured in the previous report. Our model however could only be applied for the

Optics EXPRESS

polarization for which the CLW is single mode, i.e. TM (vertical) polarization. Several iterations on the CLW modal properties were made with varying numbers of index and stress magnitude.

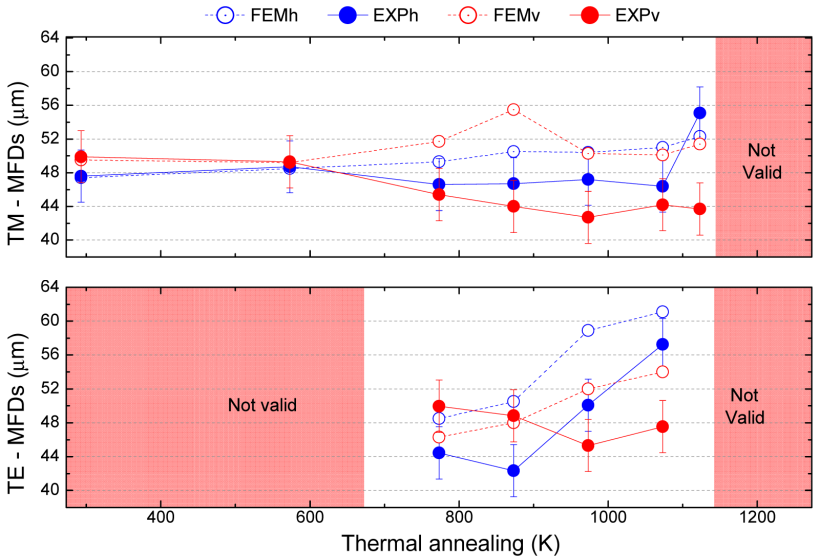

Fig. 4. Theoretical FEM and experimental MFD values of the waveguide 750_wg8 versus the thermal annealing temperature. TE (blue graphs) and TM (red graphs) are both considered. The MFD values are not calculated when either the waveguide is multimode or not guided. The error bar is ± 3 µm. Lines joining experimental points are added only as visual help.

The best matching values of PLs and MFDs were obtained with $n_{e(z)}$ index changes inside tracks of $\Delta n_z^* = -0.022 + i0.007$, which is almost a 3-fold increase with respect to previously reported values of mid-IR CLW. The maximum compressive stress was estimated to be around 180 MPa which is also a 3-fold increase in maximum stress with respect to the value of the single-ring low-pulse energy written CLW. This large increase of the generated stress is also expected as a result of the double-ring cladding. The same procedure was then carried out with all CLWs as a function of the thermal treatments with increasing temperatures. As mentioned above, it is expected that the thermal annealing will facilitate the erasure of the defects which means that the Δn magnitude, the cross-sectional sizes of the tracks and the residual stress levels are expected to decrease. Iterative calculations and comparisons with experiments were therefore made to establish the realistic conditions that best-match experimental measures. As shown in Fig. 3, simulated PLs are almost identical to experimental values. The theoretical MFDs were also matched as best as possible with the experimental values as shown in Fig. 4, within our statistical maximum error of ± 3 µm, which our experimental error in determining the mode near-field diameters, by means of imaging at λ = 3.68 µm wavelength. As shown in Fig. 4, for each polarization for the horizontal (h) and vertical (v) mode near-field cross-section were measured in the experimental modes and simulated modes. As it can be seen a qualitative agreement can be achieved while perfectly matching propagation losses (see Fig. 3).

Optics EXPRESS

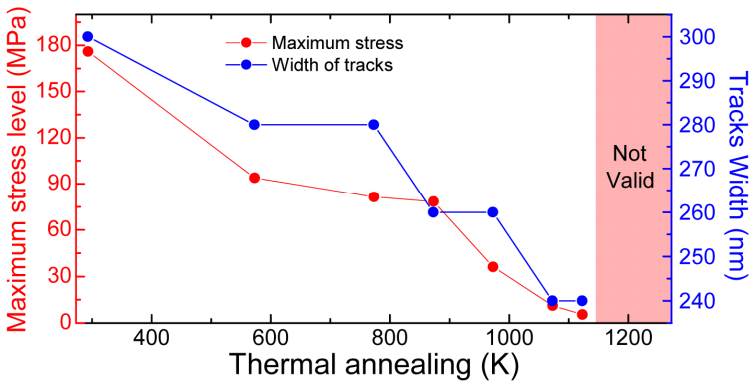

Fig. 5. Width of the laser-damage tracks and the induced stress in the cladding structure under different thermal annealing for waveguide 750_wg8.

3.3.1. Changes of the track dimensions and the induced stress by thermal annealing

Once the best matching of PLs and MFDs was obtained, the resulting changes in tracks dimensions can be studied. The width of the modified tracks shows to experience a linear reduction with increasing annealing temperature (see Fig. 5, blue graph). This was additionally confirmed by SEM and AFM characterisations (results not shown here for the sake of brevity). The width of the tracks is observed to be reduced about a 20% from 300 nm to 240 nm after several annealing steps, and finally a dramatic disappearance was observed at the temperature higher than 1173K, which is close to the melting point of $LiNbO_3$ at 1500K [34]. The vertical length of these tracks also experienced changes, although they were on the nanometer scale which compared to their large length was considered as negligible. The reduction of the residual stress followed the same tendency which fell from 180 MPa down to almost level of 10 MPa and disappeared with the loss of the filaments (Fig. 5, red graph). Previous work had reported these effects on ultrafast laser-written YAG waveguides which addressed similar tendency [35].

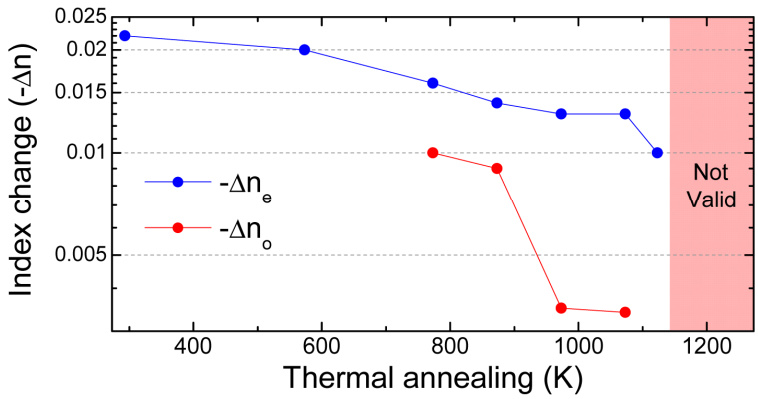

Fig. 6. Index contrast Δn_y (red line) and Δn_z (blue line) between the fs laser-modified tracks and the bulk material of the waveguide 750_wg8 when experienced thermal annealing process.

Optics EXPRESS

3.3.2. Changes of the index of refraction

A strongly anisotropic behavior of the two ordinary index Δn_y and extraordinary index Δn_z of laser-modified tracks had been reported for Type I and Type II regimes, under heat treatments of up to 573 K (300°C) and characterized in the visible range (633nm) [33]. Burghoff *et al.* reported no significant change in Type II Δn_y, while the positive Type I Δn_z completely vanished after the laser-written tracks were treated to 573 K [33]. However, our work which has been done on Type II damage tracks at the mid-IR range and under a much wider range of heat treatments (up to 1173K), shows a very different behavior. The decrease of the refractive index contrast between the tracks and the bulk material is displayed in Fig. 6 as a function of the annealing temperatures. The index change Δn_z between the tracks and the bulk material gradually fell from –0.022 to –0.01 when the waveguide was thermally treated. Regarding to the index change Δn_y, it was not measured until the CLWs were single mode, for the thermal treatment of 773K. At this point the measured Δn_y is –0.01 which is around a 62% of the Δn_z values (–0.016). A dramatic drop of the Δn_y is also observed at 973K and keeping stable until 1073K. Overall, these observations match well with the known anisotropy of $LiNbO_3$ and the large differences between the effects on the ordinary or extraordinary index of the crystal when subjected to laser irradiation.

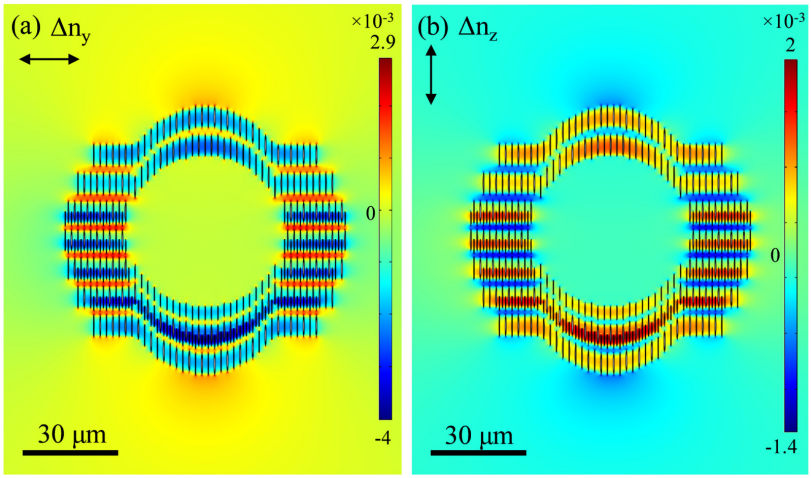

Fig. 7. Index profiles including the changes of ordinary Δn_y (a) and extraordinary Δn_z (b) indices of the waveguide 750_wg8 after thermal treatment of 773K. The refractive index changes inside tracks are $\Delta n_y = -0.01$ and $\Delta n_z = -0.016$.

3.3.3. Profile of the waveguide after 773K annealing

It is interesting to notice that although the magnitude of all the depressed-Δn tracks and the induced stress steadily dropped from the beginning to the end of the annealing steps, the waveguiding performance in terms of PLs oscillated and did not follow a simple trend, as seen on Fig. 3. To showcase the complexity and interplay between tracks and stress fields, in Fig. 7 we show the 2D computed index profiles CLW 750_wg8 after annealed at 773K. In the case of TE guiding, the Δn_y profile shows that some areas with increased index (red) come in between the vertical layers of low-index tracks, introducing a complex inhomogeneity to the cladding microstructure. This interference might not be significant, as the TE measured guided light always increased in PLs with the annealing steps. The TM index profile appears

Optics EXPRESS

also complicated, with an induced positive stress-optic index change (Δn_z) in the lateral sides (red regions) of the low-index tracks across the whole cladding structure.

Using these obtained index profiles, TE and TM modes are compared with the measured mode fields. As Fig. 8 shows, both simulated and measured are well-matched. The PLs also have good matching which is in order of <0.1 dB/cm error. The FEM design is obtained from the analysis of the SEM image of the cladding structure also shown.

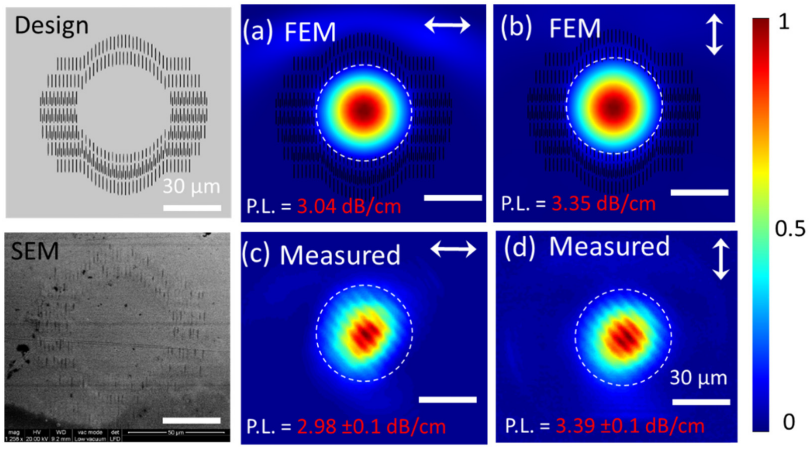

Fig. 8. Simulation and experiment of the CLW 750_wg8: Comparison of near field TE and TM modes at 3.68 µm wavelength. Interference fringes in the measured mode images are due to back-reflections in the optical guiding imaging system.

3.4 Optimal waveguide performance towards the lowest losses in both orthogonal polarizations

The section §3.1 has confirmed that low-speed laser inscription can offer low-loss waveguides even by using low levels of pulse energy. More homogenous damage tracks can be obtained when the overlapped areas are larger which significantly decreases the propagation losses at 3.68 µm in the mid-IR range. Our double ring cladding design has achieved low-loss waveguiding by using pulse energies of 1.68 µJ at scanning speed of 500 µm/s. This design and the use of laser conditions did not require a large amount of time (< 3h) to fabricate and provide a significant improvement of the waveguide. The reported CLW2R 500_wg5 with lowest losses showed multimode guiding for both TE and TM polarizations as fabricated. However, the higher order modes were shown to clean up by applying controlled thermal treatments. As studied in Section §3.3, the waveguide was measured to have single mode guiding with reasonably low losses of 1.25 dB/cm and 1.79 dB/cm for TM and TE polarized light, respectively. This is the first time (to our knowledge) that single mode guiding for both TE and TM polarizations is achieved, and with propagation losses around ~1.5 dB/cm which start to be within the range for instrumental developments.

4. Conclusions

In this work, we have designed a new double-widened cladding arrangement in search for improvements of the $LiNbO_3$ CLW performance in the mid-infrared. More specifically our goal was to achieve, for the first time to our knowledge, $LiNbO_3$ cladding waveguides for the mid-infrared being single mode, and guiding for both TE and TM orthogonal polarizations. The distinctive behavior of the waveguide under heat treatments has been explored with a

Optics EXPRESS

focus on optimizing the waveguide properties for both polarizations both in terms of achieving single modality and low losses. A complete set of the anisotropic $\Delta n_{y,z}$ changes of CLWs in the mid-IR has been revealed to understand the effects of the thermal annealing. Single mode guiding for TM and TE polarisations has been obtained with PLs of 1.25 dB/cm and 1.79 dB/cm, respectively. This significant improvement is of high potential for the implementation of integrated photonic devices working in the mid-IR range. This type of cladding waveguide takes advantages of maintaining the material properties (as the waveguiding core is considerably un-modified). Implementation of these cladding structures on lithium niobate which possesses high electro-optical and non-linear coefficients; opens a bright pathway for true high performance of real devices including non-linear frequency converters, interferometric spectrometers, interferometers, etc.

Funding

Spanish MINECO and FEDER under project MAT2016-75716-C2-1-R, TEC2014-55948-R and FIS2013-44174-P; Catalan Government 2014SGR1358 and Junta de Castilla y León (Projects UIC016, SA046U16); European Commission (ACP2-GA-2013-314335-JEDI ACE); F. D. acknowledges additional support 2010-ICREA-02 for excellence in research; G. Martin acknowledges support from ASHRA for mid-IR astrophotonic devices development in collaboration with international groups.

UNIVERSITAT
ROVIRA i VIRGILI